UNIVERSITY OF SOUTHAMPTON

Aeroacoustic Control of Landing Gear Noise using Perforated Fairings

by

Koen Boorsma

A thesis submitted for the degree of Doctor of Philosophy

School of Engineering Sciences
Aerodynamics and Flight Mechanics Research Group

June 2008

UNIVERSITY OF SOUTHAMPTON

ABSTRACT

SCHOOL OF ENGINEERING SCIENCES
AERODYNAMICS AND FLIGHT MECHANICS RESEARCH GROUP

Doctor of Philosophy

Aeroacoustic Control of Landing Gear Noise using Perforated Fairings

by Koen Boorsma

A study was performed to investigate and optimize the application of perforated fairings for landing gear noise control. The sparse knowledge about this new subject has necessitated a more fundamental study involving a basic fairing-strut configuration, followed by wind tunnel tests on a simplified landing gear configuration incorporating perforated fairings.

For the basic configuration, various exchangeable perforated half-cylindrical shells shrouding a circular cylinder were the subject of aerodynamic and acoustic tests. A qualitative and quantitative description has been given of the influence of perforated fairings on time averaged and unsteady flow and the related acoustics. The bled air through the shell prevents the formation of large scale vortices associated with the shell and thereby reduces low frequency noise. However, a test with a noisy H-beam replacing the circular cylinder has indicated that increasing porosity can result in adverse noise effects due to the bled mass flow washing the strut. Shearing flow past the perforate has been shown to create adverse self-noise of which both intensity and spectral content are dictated by the local velocity past the perforate.

The application of perforated fairings to the simplified landing gear model reduces the low frequency noise introduced by the solid fairings to values below the baseline landing gear configuration in both side and ground view directions. Exposing the perforate outside the stagnation area does not yield extra noise reduction but introduces perforate self-noise.

The synthesis of the conducted studies has shed new light on the application of perforated fairings for landing gear noise control. In particular the effects of porosity and perforation location have been clarified. However more research is needed for further optimization of these parameters.

Table of Contents

Abstract **i**

List of Figures **v**

List of Tables **viii**

Acknowledgements **ix**

Nomenclature **x**

1 Introduction **1**
1.1 Background and Aim 1
1.2 Outline of Thesis 3

2 Review of Previous Work **5**
2.1 Basic Principles of Aerodynamic Noise Generation 5
2.1.1 Unbounded flow 6
2.1.2 Effect of solid boundaries 8
2.1.3 Effect of source motion 9
2.2 Experimental Methods in Aeroacoustics 10
2.2.1 Wind tunnel measurements 10
2.2.2 Flyover measurements 12
2.3 Computational Methods in Aeroacoustics 14
2.3.1 Empirical and statistical methods 14
2.3.2 Computational modelling 15
2.4 Landing Gear Flow and Acoustics Research 17
2.4.1 Spectrum characteristics 17
2.4.2 Directivity 18
2.4.3 Noise sources 19
2.4.4 Effect of Reynolds number 20
2.4.5 Noise reduction means 20
2.5 Cylinder Flow and Acoustics Research 21
2.6 Aeroacoustics of Perforated Surfaces 23
2.6.1 Aerodynamics 24
2.6.2 Acoustics 31

3 Research Methodology **35**
3.1 Influential Parameters . . . 35
3.2 Research Plan . . . 37
3.3 Basic Model Experiment . . . 38
3.3.1 Model shape . . . 39
3.3.2 Model size . . . 40
3.3.3 Choice of perforate . . . 42
3.3.4 Experimental arrangement . . . 44
3.3.5 Apparatus . . . 51
3.4 Landing Gear Model Experiment . . . 59
3.4.1 Model . . . 59
3.4.2 Experimental arrangement . . . 62
3.4.3 Apparatus . . . 63

4 Basic Model Research **70**
4.1 Time-averaged Flow Features . . . 70
4.1.1 On surface . . . 70
4.1.2 Off surface . . . 72
4.1.3 Deflected velocities . . . 74
4.1.4 Bled mass flux . . . 75
4.1.5 Perforate flow . . . 76
4.2 Vortex Shedding . . . 78
4.2.1 Reynolds number effects . . . 81
4.2.2 Effect of exposure . . . 84
4.2.3 Effect of porosity . . . 86
4.3 High Frequency Noise . . . 88
4.3.1 Perforate noise . . . 88
4.3.2 Other sources . . . 91
4.4 Summary . . . 93

5 Landing Gear Model Research **95**
5.1 Fairing Flow . . . 96
5.2 Near Wake Flow . . . 99
5.3 Wheel Flow . . . 103
5.3.1 Wheel centerline . . . 103
5.3.2 Wheel shoulder . . . 107
5.4 Acoustics . . . 107
5.4.1 Microphone array . . . 107
5.4.2 On-surface microphones . . . 112
5.5 Summary . . . 115

6 Conclusions and Recommendations **117**
6.1 Basic Model Research . . . 117
6.2 Landing Gear Model Research . . . 119
6.3 Recommendations . . . 121

6.3.1 Application to landing gear 121
6.3.2 Future work 123

A Details of Computational Simulation 124
A.1 Preliminary Modelling Options 124
A.2 Computational Model 126
A.3 Geometry Construction 127
A.4 Grid Construction 128
A.4.1 Grid density 129
A.5 Temporal and Iterative Convergence 130
A.6 Validation 131

B Technical Drawings of the Basic Model Experiment 133

C Technical Drawings of the LG Model Experiment 141

References 149

List of Figures

1.1 The A340 Main Landing Gear. 2
1.2 Description of landing gear components (picture supplied by Airbus), wheels omitted 3

2.1 Normalized sideline spectra of components of a nose gear model: a=complete configuration; b=side support struts; c=lower drag-brace and actuator; d=wheel; e=door (U_0 = 100m/s), taken from Heller[1]. 17
2.2 Sections for describing flow past a perforated plate, taken from [2]. . 24
2.3 Dependence of ζ on σ as predicted by equation 2.20, $C_c = \frac{2}{3}$ 26
2.4 Reynolds number dependence of pressure drop (left) and Mach number dependence (right) after Idelchik [3]. 27
2.5 Dependence of ζ on r_{edge} for different values of σ after Idelchik [3]. . 28
2.6 Dependence of Tu on d_{or} (left) and σ (right) ($\frac{x}{d_{or}}$ = 20, $Re_{d_{or}} = 2.9 \times 10^4$) after Liu [4]. 30

3.1 Illustration of basic model and dimensions. 42
3.2 Different hole arrangements 44
3.3 Picture of the 4 different shells subject to experiments, from left to right: solid, perf33, perf42 and perf55. 45
3.4 Schematic diagram of the $3' \times 2'$ tunnel. 45
3.5 Test set-up in the $3' \times 2'$ tunnel. 47
3.6 Test set-up in the $7' \times 5'$ tunnel. 48
3.7 Air supply and nozzle in the anechoic chamber, taken from [5]. . . . 50
3.8 Test set-up in the anechoic chamber. 51
3.9 Numbering and location of on-surface microphones on the strut. . . 56
3.10 Landing gear wind tunnel model in comparison to the operational A340 gear. 60
3.11 Plain landing gear model and fairings. 61
3.12 Microscope view of the perforated sheet (d_{or}=2 mm, p_{or}=3 mm). . . 61
3.13 Model as suspended in the $7' \times 5'$ tunnel. 62
3.14 Location of pressure taps on the wheel 64
3.15 Visualization of the measurement set-up for the ZOC, taken from Scanivalve website. 65
3.16 Pressure sensor locations. 66
3.17 Set-up of microphone arrays in the $7' \times 5'$ tunnel. 68

4.1 Front and rear view of basic model oil flow visualization ($U_\infty = 40$ m/s). 71
4.2 Side view of basic model oil flow visualization at the shell trailing edge ($U_\infty = 40$ m/s, flow from top to bottom). 72
4.3 Time-averaged velocity contours and streamlines ($U_\infty = 30$ m/s, $z/D_f = 0$). 73
4.4 Lateral traverse of non-dimensional velocity in streamwise direction using pitot and PIV data ($U_\infty = 20$ m/s, $x/D_f = 0.26, z/D_f = 0$). . 74
4.5 Bled mass flux m_b for different configurations obtained by CFD ($U_\infty = 30$ m/s). 76
4.6 Time averaged velocity distribution and streamlines around orifices rounded off edges (perf42 ($\pm 45\,^\circ$)+cylinder, $U_\infty = 30$ m/s). 76
4.7 Time averaged velocity distribution around sharp edged orifices (perf33 ($\pm 45\,^\circ$)+cylinder, $U_\infty = 30$ m/s, legend in Figure 4.6). . . . 77
4.8 Snapshots of vorticity combined with velocity vectors in the downstream region ($U_\infty = 30$ m/s, $z/D_f = 0$). 78
4.9 Standard deviation of velocity in y-direction ($U_\infty = 30$ m/s, $z/D_f = 0$). 78
4.10 Transverse traverse of PSD of velocity ($U_\infty = 20$ m/s, $x/D_f = 1.44$ and $z/D_f = 0$). 79
4.11 Measured acoustics in $7' \times 5'$ tunnel ($U_\infty = 40$ m/s). 80
4.12 Measured acoustic in anechoic chamber (averaged over microphone 1 to 8, $d = 2$ m, $U_\infty = 40$ m/s). 81
4.13 Velocity traverse of isolated cylinder. 82
4.14 Velocity traverse of solid configuration. 83
4.15 Influence of exposure on PSD of velocity ($U_\infty = 20$ m/s, $x/D_f = 1.44$, $z/D_f = 0$). 84
4.16 Influence of exposure on measured acoustic in anechoic chamber (averaged over microphone 1 to 8, $d = 2$ m, $U_\infty = 40$ m/s). 85
4.17 Influence of porosity on PSD of velocity ($U_\infty = 20$ m/s, $x/D_f = 1.44$, $z/D_f = 0$). 86
4.18 Influence of porosity on measured acoustic in anechoic chamber (averaged over microphone 1 to 8, $d = 2$ m, $U_\infty = 40$ m/s). 87
4.19 Measured acoustics at high frequencies in $7' \times 5'$ tunnel ($U_\infty = 40$ m/s). 88
4.20 1/3 Octave band averaged beamforming plots ($U_\infty = 40$ m/s). . . . 89
4.21 Microphone array data ($U_\infty = 40$ m/s) 89
4.22 Relative atmospheric absorption according to ICAO [6] at a temperature of 15 ° C and humidity of 50%). 91
4.23 Acoustics of trailing edge noise ($U_\infty = 40$ m/s) 92
4.24 1/3 Octave band averaged beamforming plots 93

5.1 Front view of flow visualization of solid fairings ($U_\infty = 40$ m/s). . . 96
5.2 Side view of flow visualization of solid fairings ($U_\infty = 40$ m/s). . . . 97

5.3 Time-averaged velocity contours and streamlines in the xz-plane at y=0 (artlink area, $U_\infty = 40$ m/s). 97
5.4 Ground view of flow visualization of solid fairings ($U_\infty = 40$ m/s). . 98
5.5 Flow visualization on application of roughness strips to fairings ($U_\infty = 40$ m/s). 99
5.6 Time-averaged velocity contours and vectors in the xz-plane at y=0 (torque link area, $U_\infty = 40$ m/s). 100
5.7 Contours of velocity standard deviation (u'_t) combined with time-averaged velocity vectors in the xz-plane at y=0 (torque link area, $U_\infty = 40$ m/s). 100
5.8 Difference between solid and perforated fairings for contours an vectors in the xz-plane at y=0 (torque link area, $U_\infty = 40$ m/s). 101
5.9 PSD and mean surface pressure on the gear ($U_\infty = 40$ m/s). 102
5.10 Centerline surface pressures on landing gear wheels ($U_\infty = 40$ m/s). 104
5.11 PSD of surface pressure on landing gear wheels ($U_\infty = 40$ m/s). . . 105
5.12 Shoulder pressures on landing gear wheels ($U_\infty = 40$ m/s). 108
5.13 Beamforming plots at 2 kHz from ceiling array (above) and side wall array (below) ($U_\infty = 40$ m/s). 109
5.14 Beamforming plots at 10 kHz from ceiling array (above) and side wall array (below) ($U_\infty = 40$ m/s). 109
5.15 Comparison of levels from integrated beamforming plots (referenced to Solid configuration, $U_\infty = 40$ m/s). 111
5.16 Narrowband spectra of on-surface microphones on the gear ($U_\infty = 40$ m/s). 113
5.17 Subtracted tertsband averaged levels from microphone at bogie-artlink junction (referenced to Solid configuration). 114

A.1 Geometry of two simulated configurations. 128
A.2 Grid details 129
A.3 Grid convergence on time-averaged pressure distribution of the perf42 ($\pm 45\,^\circ$)+cylinder model, $U_\infty = 30m/s$. 130
A.4 Comparison of time-averaged velocity distribution between CFD (upper) and PIV (lower), $U_\infty = 30m/s$. 132

B.1 Drawing of parts and test set-up. 135

List of Tables

3.1 Survey of influential parameters for perforated fairings. 36
3.2 Summary of different shell configurations. 43
3.3 Position of far field microphones. 57

A.1 Settings for computational simulations. 126
A.2 Details of the simulated perforates. 127
A.3 Structured grid spacing for perf42 ($\pm 45\,^{\circ}$) case (medium refinement). 129

B.1 Parts list corresponding to Figure B.1 134

Acknowledgements

There are many individuals that I would like to thank for providing me with support during my PhD. Foremost, I would like to thank my supervisor, Professor Xin Zhang, for his guidance and encouragement and making the PhD possible.

In addition to that I would like to thank Airbus for their financial support and industrial liaison. I would also like to thank my colleagues and office mates Dave, Sammie, Martijn, Benjamin and Matthew for fruitful discussions, help during experiments and many moments of laughter.

Finally, I would like to thank the university technicians that supported and assisted in preparation of and during the multitude of experiments, especially Mike Tudor-Pole for his attitude and humour.

Nomenclature

List of Symbols

symbol	unit	description
α	$[-]$	linear term constant for ∇p dependence on U_∞
β	$[-]$	quadratic term constant for ∇p dependence on U_∞
Δf	$[\frac{1}{s}]$	frequency resolution
Δt	$[s]$	time step
δ	$[m]$	boundary layer thickness
δ_{ij}	$[-]$	Dirac delta function
γ	$[-]$	ratio of specific heats
μ	$[\frac{kg}{ms}]$	dynamic viscosity
ν	$[\frac{m^2}{s}]$	kinematic viscosity
$\tilde{\nu}$	$[\frac{m^2}{s}]$	modified turbulent kinematic viscosity
ν_t	$[\frac{m^2}{s}]$	turbulent kinematic viscosity
φ	$[^\circ]$	polar angle from shell leading edge
ρ	$[\frac{kg}{m^3}]$	density
σ	$[-]$	porosity (open-area coefficient) of a perforated material
θ	$[rad][^\circ]$	angle
ω	$[\frac{1}{s}]$	vorticity
χ	$[-]$	reactance, complex part of specific acoustic impedance
$\zeta_{\mathbf{c}}$	$[m]$	Lagrangian version of $\mathbf{y}$ vector
ζ	$[-]$	pressure loss coefficient

A	$[-]$	aspect ratio
a	$[\frac{m}{s}]$	speed of sound
C_c	$[-]$	contraction coefficient of screen
C_D	$[-]$	drag force coefficient
C_L	$[-]$	lift force coefficient
Cp	$[-]$	pressure coefficient
Cp_b	$[-]$	base pressure coefficient
D_f	$[m]$	fairing diameter
D_s	$[m]$	strut diameter
d	$[m]$	distance
d_h	$[m]$	distance of H-beam center to shell center
d_{or}	$[m]$	orifice diameter
f	$[\frac{1}{s}]$	frequency
f_i	$[\frac{1}{s}]$	midpoint of frequency band
f_l	$[\frac{1}{s}]$	lower limit of frequency band
f_s	$[\frac{1}{s}]$	sample frequency
f_u	$[\frac{1}{s}]$	upper limit of frequency band
h	$[m]$	tunnel height
i	$[-]$	$\sqrt{-1}$
k_M	$[-]$	coefficient for influence of M on ζ
L	$[m]$	shell length
L_c	$[m]$	correlation length
L_{eq}	$[-]$	equivalent sound pressure level
l	$[m]$	typical length scale
M	$[-]$	Mach number
m_b	$[-]$	bled mass flux referenced to freestream flux
$\mathbf{n}, n_i$	$[-]$	unity normal vector
n	$[-]$	number of samples in data acquisition
n_f	$[-]$	velocity increase over landing gear components by application of fairings
P_{ij}	$[\frac{kg}{ms^2}]$	stress tensor
p	$[\frac{kg}{ms^2}]$	static pressure
p_{atm}	$[\frac{kg}{ms^2}]$	atmospheric pressure
p_e	$[\frac{kg}{ms^2}]$	effective sound pressure
p_{or}	$[m]$	pitch of orifices (distance between the orifice centrepoints)

p_{ref}	$[\frac{kg}{ms^2}]$	reference pressure
p_t	$[\frac{kg}{ms^2}]$	total pressure
q	$[\frac{kg}{ms^2}]$	dynamic pressure
Re	$[-]$	Reynolds number
$Re_{d_{or}}$	$[-]$	orifice Reynolds number
r	$[-]$	resistance, real part of specific acoustic impedance
r_{edge}	$[m]$	edge radius of orifice
S	$[m^2]$	surface area
S_f	$[\%]$	percentage of landing gear covered by fairings
Str	$[-]$	Strouhal number
T	$[s]$	period
T_{ij}	$[\frac{kg}{ms^2}]$	Lighthill stress tensor
Tu	$[\%]$	turbulence intensity
t	$[s]$	time
t_D	$[-]$	non-dimensional time
t_f	$[m]$	fairing thickness
$\mathbf{U}, U_i$	$[\frac{m}{s}]$	velocity of acoustic source in motion
U	$[\frac{m}{s}]$	typical velocity scale
U_∞	$[\frac{m}{s}]$	freestream velocity
$\mathbf{u} = (u, v, w), u_i$	$[\frac{m}{s}]$	velocity vector
u_c	$[\frac{m}{s}]$	velocity in vena contracta
u_n	$[\frac{m}{s}]$	acoustic velocity normal to a surface
u_{or}	$[\frac{m}{s}]$	average velocity in an orifice
u_t	$[\frac{m}{s}]$	time averaged velocity magnitude ($\lvert\overline{\mathbf{u}}\rvert$)
u'_{RMS}	$[\frac{m}{s}]$	RMS value of velocity fluctuations in x-direction
u'_t	$[\frac{m}{s}]$	average of RMS of velocity fluctuations in two directions
V	$[m^3]$	integration volume
$\mathbf{V}, V_i$	$[\frac{m}{s}]$	velocity of integration surface S
v'_{RMS}	$[\frac{m}{s}]$	RMS value of velocity fluctuations in y-direction
$\mathbf{x} = (x, y, z), x_i$	$[m]$	position vector in Cartesian axis system
$\mathbf{y}$	$[m]$	position vector of acoustic source
y^+	$[-]$	coordinate without dimension in the wall boundary layer
Z_a	$[\frac{kgm^2}{s}]$	acoustic impedance
z_a	$[-]$	specific acoustic impedance

Conventions

$\mathbf{s}, s_i$	,	vector form of s in vector and tensor notation respectively
T_{ij}	,	tensor notation for tensor T
$\overline{s}$	,	mean value of s
s'	,	perturbation on the mean of s, $s - \overline{s}$
s_0	,	unperturbed value of s outside the acoustic source region
s_∞	,	freestream value of s
$\lvert\mathbf{s}\rvert$	,	magnitude of vector $\mathbf{s}$ after component summation
$\lvert s\rvert$	,	absolute value of complex variable s
$[s]$	,	value of s evaluated at retarded time $t - \dfrac{\lvert\mathbf{x}-\mathbf{y}\rvert}{a_0}$
Δs	,	absolute increment of s
$\nabla\mathbf{s}$	,	gradient of vector $\mathbf{s}$

Most commonly used acronyms

BL	Boundary layer
CAA	Computational Aeroacoustics
CAD	Computer Aided Design
CFD	Computational Fluid Dynamics
CNC	Computer Numerical Control
DES	Detached Eddy Simulation
DNS	Direct Numerical Simulation
EAL	Equivalent A-Weighted Sound level
EPNL	Effective Perceived Noise Level
FFT	Fast Fourier Transform
FV	Finite Volume
FW-H	Ffowcs Williams-Hawkings
HW	Hot wire
LE	Leading edge
LES	Large Eddy Simulation
MLG	Main Landing Gear
N-S	Navier-Stokes
OASPL	Overall Sound Pressure Level
PIV	Particle Image Velocimetry
PSD	Power Spectral Density
RANS	Reynolds Averaged Navier Stokes
RMS	Root Mean Square
SPL	Sound Pressure Level
STDEV	Standard Deviation
TE	Trailing edge
ZOC	Zero, Operate and Calibrate (pressure scanner)

Chapter 1

Introduction

1.1 Background and Aim

A steady increase in the number of flights and airports around likewise growing urban areas has increased research into aviation noise for large commercial aircraft. A more stringent legislation [6] and increased environmental awareness on this subject [7] has led to an extra push. Research started with tackling the most dominant component, engine noise. As a result, jet engine noise has significantly been reduced over the past decades, using for example high bypass ratio engines. This increased the relative importance of airframe noise for noise certification and environmental considerations. A 15-20 dB reduction in jet noise between 1970 and 1997 has reduced the average effective perceived noise level (EPNL, definition in section 2.2.2) for large commercial aircraft from approximately 110 to 90 EPNdB [7].

During final approach, throttled back engines, deployed high-lift devices and landing gears often make airframe noise the major contributor to overall aircraft noise [8]. The relative low fly altitude for an extended distance increases the noise affected area, thereby making the approach phase even more relevant. Landing gear noise can be the dominant component of airframe noise [9], especially for larger aircraft [10]. However, often none of the various airframe noise sources are dominant [11]. In this case the total airframe noise can only be reduced significantly if all components are reduced by a similar amountt, which makes reduction of landing gear noise essential. Although the aerodynamic drag of the undercarriage influences take off and landing performance, landing gear design is primarily aimed at its main mechanical function of supporting the aircraft above the runway. Con-

sequently, landing gear arrangements can feature components with unfavourable aerodynamic features. The interaction of airflow with protrusions and cavities gives rise to unsteady flow phenomena constituting a potent sound generating mechanism.

Shielding landing gear components with fairings and thereby preventing this interaction has been considered before [8, 10]. High speed flow deflection onto other components and fairing self-noise are disadvantages of these fairings. Bleeding air through fairings by making them porous can result in a redistribution of the air flow. Flight tests using perforated fairings have been conducted before [12, 13] and demonstrated a noise decrease. The effect of porous fairings on aeroacoustic performance of landing gear is a relatively new topic. Recent research on the subject [14, 15] has confirmed the flight test results, although the corresponding flow behavior has not been investigated. The main aim of the present research is to investigate and optimize the noise reduction potential by perforating these fairings.

Airbus, as main sponsor of this PhD programme, requested that the primary focus of the research be on the acoustic signature of a generic landing gear based upon the Airbus A340 main landing gear (MLG). An example of this landing gear and its fairings is given in Figure 1.1. A description of various landing gear components is

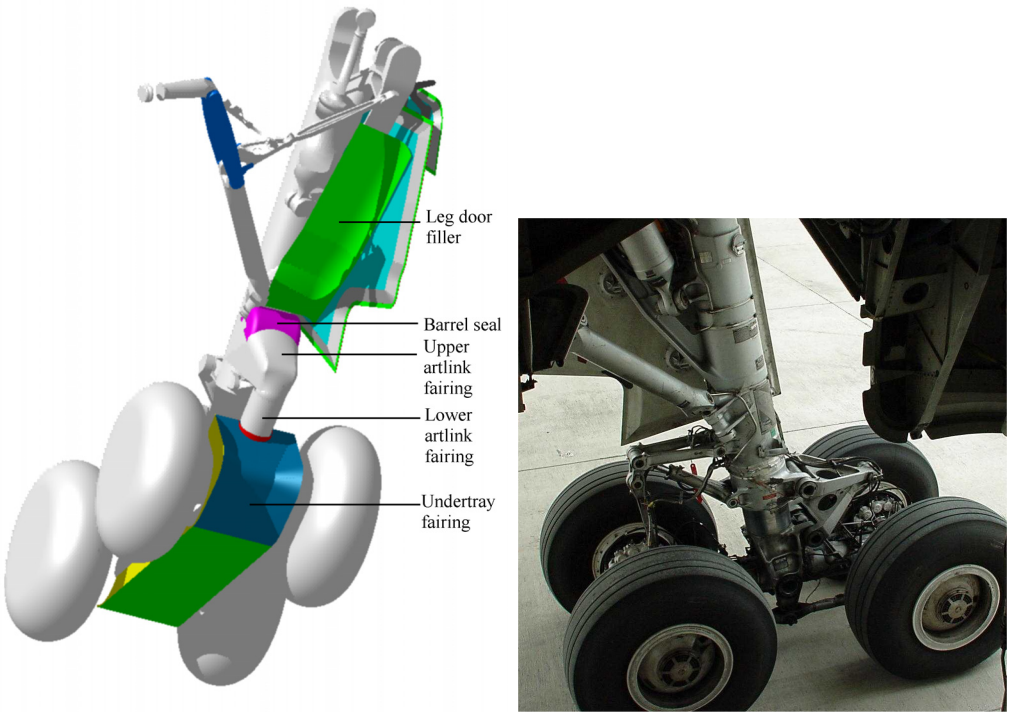

(a) CAD representation of A340 MLG and fairings (b) A340 MLG in operation

FIGURE 1.1: The A340 Main Landing Gear.

given in Figure 1.2. Typical parts being covered by fairings are the bogie beam and

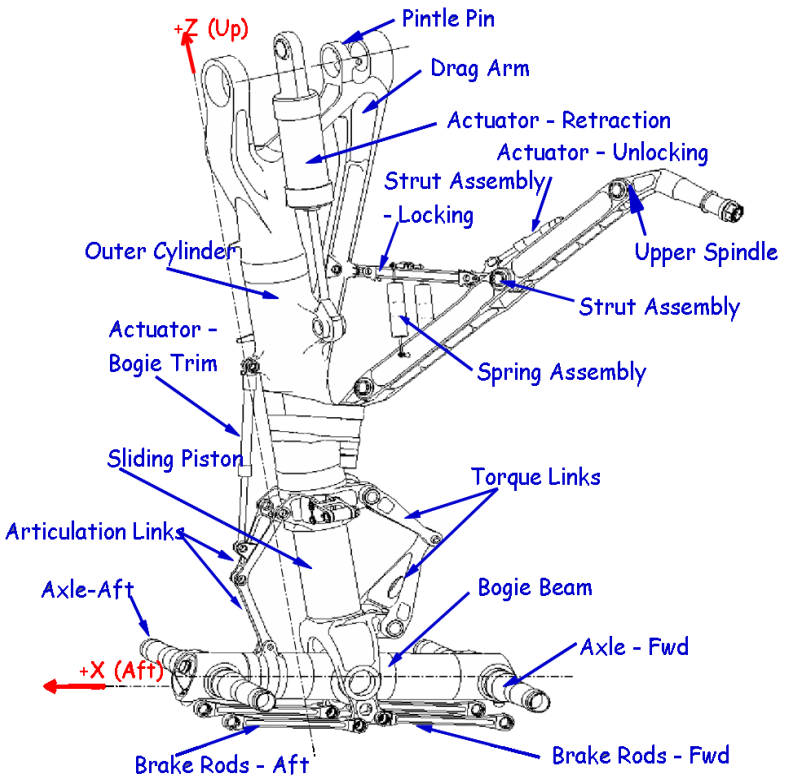

FIGURE 1.2: Description of landing gear components (picture supplied by Airbus), wheels omitted

wheel axles (undertray fairing), articulation link, side stay and the gap between leg door and drag arm. It was required to incorporate wind tunnel tests on a scaled landing gear model within the framework of the PhD. For this study, only landing gear components and fairings below the leg door are to be considered. This implies that only the undertray and upper- and lower articulation link fairings are relevant for the present investigation. The shape of the fairings was predefined by Airbus and hence this parameter was not eligible for modifications.

1.2 Outline of Thesis

Firstly, chapter 2 gives a review of previous research in the field. This includes basics of aerodynamic noise generation, experimental and computational methods in aeroacoustics, landing gear research and aerodynamics and acoustics of perforated surfaces. The research methodology inspired by the literature survey is addressed in chapter 3. This results in the design of a basic model for the research. Research

on this model is then discussed in chapter 4. Following the research on the basic model, experiments on the generic landing gear model are discussed in chapter 5.

Finally, the total work is discussed and the conclusions that can be drawn are summarized. Future work that is apparent from these conclusions is highlighted as well. This can be read in chapter 6.

Chapter 2

Review of Previous Work

In this chapter, previous work related to the topic of the present research is reviewed. To start with, the basics of noise generation by aerodynamic flow is treated. Research on the basics of aerodynamic noise generation is discussed in section 2.1.

Obtaining aeroacoustical information on transportation vehicles is a relatively new field of interest compared to obtaining conventional aerodynamic characteristics. In addition to that, the extremely complicated geometry of landing gear has troubled wind tunnel experiments and computational methods and thereby prevented a detailed understanding of the flow physics on this component. Advances in both fields have opened up the possibility to gain a better understanding of landing gear flow and acoustics. These advances are discussed in sections 2.2 and 2.3.

A shape frequently appearing in landing gear assemblies is a cylinder. The aerodynamic and acoustic research on this topic is briefly summarized in section 2.5. The findings on aerodynamics and acoustics of landing gear so far will be discussed in section 2.4. A review of previous research into the aerodynamics and acoustics of perforated surfaces is presented in section 2.6.

2.1 Basic Principles of Aerodynamic Noise Generation

In this section, the basic principles of aerodynamic noise generation will be addressed. The research on this subject is summarized, starting with an analysis

of noise generation in unbounded flow. From this starting point, extensions are made regarding presence of solid boundaries and source motion.

2.1.1 Unbounded flow

Lighthill [16] developed a theory for aerodynamic noise generation for unbounded flow. For this analysis, a fluid flow area (noise generation area) is decoupled from a uniform medium at rest (wave propagation area). It is argued that sound is a very small component of the whole motion and that therefore the properties of the flow in the source region can be determined by neglecting the production and propagation of sound. The exact equations of motion are compared with the equations of sound propagation in a medium at rest. The exact equations of motion for an arbitrary continuous medium under no external forces in tensor notation are given by

$$\frac{\partial \rho}{\partial t} + \frac{\partial}{\partial x_i}(\rho u_i) = 0 \quad , \quad \frac{\partial}{\partial t}(\rho u_i) + \frac{\partial}{\partial x_j}(\rho u_i u_j + P_{ij}) = 0 \quad , \tag{2.1}$$

where x_i represents the Cartesian coordinate, u_i the flow velocity, ρ the density and P_{ij} the stress tensor which for a Stokesian fluid equals

$$P_{ij} = p\delta_{ij} + \mu[-\frac{\partial u_i}{\partial x_j} - \frac{\partial u_j}{\partial x_i} + \frac{2}{3}(\frac{\partial u_k}{\partial x_k})\delta_{ij}] \quad , \tag{2.2}$$

where p is the pressure, δ_{ij} is the Dirac delta function (1 for $i = j$, 0 for $i \neq j$) and μ the dynamic viscosity coefficient.

The propagation of sound in a uniform medium at rest is governed by the following equations

$$\frac{\partial \rho}{\partial t} + \frac{\partial}{\partial x_i}(\rho u_i) = 0 \quad , \quad \frac{\partial}{\partial t}(\rho u_i) + {a_o}^2 \frac{\partial \rho}{\partial x_i} = 0 \quad , \quad \frac{\partial^2 \rho}{\partial t^2} - {a_0}^2 \nabla^2 \rho = 0 \quad , \tag{2.3}$$

where a_0 is the speed of sound in the medium and ∇ is the gradient operator $\frac{\partial}{\partial x_i}$. The third equation of (2.3) is called the wave equation and can be deduced by taking the time derivative of the first equation and subtracting the spatial derivative of the second one.

Rewriting the second equation of (2.1) in a similar form as the second equation of (2.3) and transforming (2.1) to a wave equation in a similar way as done for (2.3)

yields

$$\frac{\partial \rho}{\partial t}+\frac{\partial}{\partial x_i}(\rho u_i)=0 \quad , \quad \frac{\partial}{\partial t}(\rho u_i)+{a_0}^2\frac{\partial \rho}{\partial x_i}=-\frac{\partial T_{ij}}{\partial x_j} \quad , \quad \frac{\partial^2 \rho}{\partial t^2}-{a_0}^2\nabla^2\rho=\frac{\partial^2 T_{ij}}{\partial x_i \partial x_j} \quad , \tag{2.4}$$

where T_{ij} is called the Lighthill stress tensor

$$T_{ij}=\rho u_i u_j + P_{ij} - {a_0}^2\rho\delta_{ij} \quad . \tag{2.5}$$

These equations can be interpreted as the equations of propagation of sound in a uniform medium at rest due to externally applied fluctuating stresses. Since the origin of these stresses lies in fluid motion, this inhomogeneous wave equation describes the theory of aerodynamic noise generation.

It can be shown that outside the flow, the Lighthill stress tensor will approach zero. The velocity u_i then corresponds to very small acoustic perturbations, and its quadratic appearance in equation (2.5) will make this term negligible. Viscous stresses in P_{ij} and heat transfer (which makes p different from $(a_0)^2\rho$) are both very small negligible effects, because gradients are small without the presence of a solid body. Therefore (2.4) will become the same as equation (2.3) outside the airflow. Therefore (2.3) can be seen as the linearized inviscid version of (2.1) in an unbounded quiescent medium at constant temperature.

In most flows, the momentum flux $\rho u_i u_j$ will greatly exceed viscous stresses and for low Mach number M flow, heat transfer can be neglected as well. Therefore T_{ij} in the flow field area can often be approximated by $\rho u_i u_j$. It is shown that the sound produced by T_{ij} corresponds to a quadrupole field. Using Green's functions, the acoustic density perturbation at position $\mathbf{x}$ due to a quadrupole at position $\mathbf{y}$ with strength T_{ij} can be written as

$$\rho-\rho_0=\frac{1}{4\pi {a_0}^2}\frac{\partial^2}{\partial x_i \partial x_j}\iiint_V T_{ij}\Big(\mathbf{y},t-\frac{|\mathbf{x}-\mathbf{y}|}{a_0}\Big)\frac{d\mathbf{y}}{|\mathbf{x}-\mathbf{y}|} \quad , \tag{2.6}$$

where V is the integration volume of the flow area and ρ_0 the non-perturbed density in the uniform medium.

When differentiating the integrand in equation (2.6) with respect to x_i for large distances $|\mathbf{x}|$, the spatial derivative of the term inversely proportional to $|\mathbf{x}-\mathbf{y}|$ can be neglected. Differentiation of T_{ij} with respect to x_i can be thought of a time derivative divided by a_0. Time fluctuations of T_{ij} are roughly proportional to $\frac{U}{l}$,

yielding an estimate [16] for the squared density variations

$$(\rho-\rho_0)^2 \propto \Big(\frac{1}{{a_0}^2}\Big)^2\Big(\frac{1}{a_0^2}\Big)^2\Big(\frac{U}{l}\Big)^4(\rho_0U^2)^2\Big(\frac{l^3}{|\mathbf{x}|}\Big)^2 = {\rho_0}^2\Big(\frac{U}{a_0}\Big)^8\Big(\frac{l}{|\mathbf{x}|}\Big)^2 \quad , \qquad (2.7)$$

where l is a typical dimension and U a typical velocity. It is assumed that the momentum flux is the dominating contribution to T_{ij}. Thus quadrupole sound is shown to scale with the 8^{th} power of flow speed.

2.1.2 Effect of solid boundaries

Curle [17] modified Lighthill's theory to take the presence of solid boundaries into account. This modification is often referred to as the Lighthill-Curle theory. Lighthill's quadrupole sound will be reflected and diffracted by the solid boundaries. Also the quadrupoles will not be distributed over the whole space, but only throughout the region exterior to the solid boundaries. Therefore a dipole source distribution due to fluctuating aerodynamic forces with which the solid boundaries are found to act on the body is added. Incorporating this theory into the equations leads to

$$\rho-\rho_0 = \frac{1}{4\pi{a_0}^2}\frac{\partial^2}{\partial x_i\partial x_j}\iiint_V T_{ij}\Big(\mathbf{y}, t-\frac{|\mathbf{x}-\mathbf{y}|}{a_0}\Big)\frac{d\mathbf{y}}{|\mathbf{x}-\mathbf{y}|}+$$

$$\frac{1}{4\pi{a_0}^2}\frac{\partial}{\partial x_i}\iint_S n_jP_{ij}\Big(\mathbf{y}, t-\frac{|\mathbf{x}-\mathbf{y}|}{a_0}\Big)\frac{dS(\mathbf{y})}{|\mathbf{x}-\mathbf{y}|} \quad , \qquad (2.8)$$

where S denotes the surface of the solid boundary and n_j is the unit outward normal (pointing towards the fluid) on S. Similar to the estimate of the quadrupole source in (2.7), a dimensional analysis [17] of the density fluctuations due to the dipole term in (2.8) gives

$$(\rho-\rho_0)^2 \propto {\rho_0}^2\Big(\frac{U}{a_0}\Big)^6\Big(\frac{l}{|\mathbf{x}|}\Big)^2 \quad . \qquad (2.9)$$

Comparing this to the result of equation (2.7) indicates that for low Mach number flow, dipole radiation will dominate the sound emanating from the quadrupole source.

In deriving equation (2.8), it is assumed that the normal fluid velocity u_jn_j on the integration surface S is zero. However, if mass is added at the surface S, this will cause the normal component of the fluid velocity u_i to depart from 0. Another

possibility is when the integration surface S is taken off the solid boundary, in which case we have a closed permeable integration surface. Assume that the integration surface is not stationary, but moves with surface velocity V_i. An addition will then have to be made to the term representing the dipole distribution and a new monopole term representing the unsteady mass addition will arise. The resulting equations yields

$$\rho - \rho_0 = \frac{1}{4\pi {a_0}^2} \frac{\partial^2}{\partial x_i \partial x_j} \iiint_V [T_{ij}] \frac{d\mathbf{y}}{|\mathbf{x}-\mathbf{y}|} + \frac{1}{4\pi {a_0}^2} \frac{\partial}{\partial x_i} \iint_S n_j [P_{ij} + \rho u_i (u_j - V_j)] \frac{dS(\mathbf{y})}{|\mathbf{x}-\mathbf{y}|}$$

$$+ \frac{1}{4\pi {a_0}^2} \frac{\partial}{\partial t} \iint_S n_j [\rho_0 V_j + \rho(u_j - V_j)] \frac{dS(\mathbf{y})}{|\mathbf{x}-\mathbf{y}|} \quad , \tag{2.10}$$

where the items between brackets [ ] are evaluated at retarded time $t - \frac{|\mathbf{x}-\mathbf{y}|}{a_0}$. If there is no solid body present, both integrals around the closed permeable surface will obviously be zero. Furthermore, if the integration surface in (2.10) is taken as the body (which is stationary), $V_j = 0$. If also there is no unsteady mass addition ($n_j u_j = 0$), equation (2.10) will simplify to (2.8).

2.1.3 Effect of source motion

Ffowcs Williams and Hawkings [18] extended the Lighthill-Curle theory to include the effects of arbitrary motion of the source. Most problems concerning aerodynamic noise generation involve motion of a transportation vehicle, e.g. an aircraft or a car. Forward motion of the source is found to influence its radiation pattern with respect to an observer. An observer will perceive an increase in density perturbations with a moving source approaching and a decrease when the source is moving away.

The integral variable y_j in equation (2.10) is not fixed in space. Therefore incorporation of this effect is easy when we switch to a moving coordinate frame. The Lagrangian coordinate $\zeta_\mathbf{c}$ is defined by

$$\zeta_\mathbf{c} = \mathbf{y} - \mathbf{U}t \quad , \tag{2.11}$$

where $\mathbf{U}$ is the velocity of the source. Taking the integration surface on the body of the moving source ($V_j = U_j$) yields

$$\rho - \rho_0 = \frac{1}{4\pi {a_0}^2} \frac{\partial^2}{\partial x_i \partial x_j} \iiint_V \frac{[T_{ij}]}{(1 - M\cos\theta)} \frac{d\zeta_\mathbf{c}}{|\mathbf{x}-\mathbf{y}|} +$$

$$\frac{1}{4\pi {a_0}^2}\frac{\partial}{\partial x_i}\iint_S n_j \frac{[P_{ij}+\rho u_i(u_j-U_j)]}{(1-M\cos\theta)}\frac{dS(\zeta_{\mathbf{c}})}{|\mathbf{x}-\mathbf{y}|}+$$

$$\frac{1}{4\pi {a_0}^2}\frac{\partial}{\partial t}\iint_S n_j \frac{[\rho_0 U_j+\rho(u_j-U_j)]}{(1-M\cos\theta)}\frac{dS(\zeta_{\mathbf{c}})}{|\mathbf{x}-\mathbf{y}|} \quad , \tag{2.12}$$

where $M=\frac{|\mathbf{U}|}{a_0}$ is the Mach number and $\cos\theta=\frac{\mathbf{U}\cdot(\mathbf{x}-\mathbf{y})}{|\mathbf{U}||\mathbf{x}-\mathbf{y}|}$.

2.2 Experimental Methods in Aeroacoustics

Although computers are becoming increasingly important, experimental methods are still the main tool for determination of flow behavior and acoustics. Wind tunnel measurements as well as fly-over measurements are discussed below.

2.2.1 Wind tunnel measurements

Wind tunnel size restricts model size to be tested. Therefore often a scale model of landing gear is tested. This often resulted in models without geometrical details present in real landing gear. Details such as dressings, hydraulic cables harnesses, brake cylinders and bolt holes are found to be responsible for high frequency noise. Full scale landing gear tests have been performed in the German Dutch Wind Tunnels (DNW) [8, 10] using a free jet configuration with a nozzle section of $6 \times 8\ m^2$. However, development of stereolithography techniques has allowed fabrication of high fidelity scale models incorporating full scale details [19]. Work on aerodynamics and aeroacoustics related to or useful for landing gear research is briefly summarized below.

2.2.1.1 Aerodynamics

Flow measurement techniques can assist in understanding underlying flow physics responsible for noise generation. Hot wire anemometry can be used to detect unsteadiness in a wake, thereby pointing out noise sources on the measured object [9]. Particle Image Velocimetry (PIV) can create an image of the mean flow field whereas a constant varying flow indicates unsteady pressures thus sound creation [20]. Wheels have previously been found suitable for installation of pressure taps [20], although size and complexity of other components have precluded a wider

use of this technique. Development of unsteady pressure transducers has aided in localization of unsteady surface forces.

2.2.1.2 Aeroacoustics

The first aeroacoustical measurements were performed using stationary open facilities [1]. A distinction has to be made between near-field and far-field measurements, where the latter have the microphones positioned more than one wavelength away from the source. The microphones are placed out of the flow to prevent noise generation by flow turbulence around them [21]. Development of such facilities into anechoic chambers enhanced acoustic wind tunnel experiments, preventing reflections of sound rays by the tunnel walls and other objects and reducing background noise. The presence of the open test section shear layer however necessitates corrections for shear layer refraction of the sound rays. The correction scheme of Amiet [22] is widely in use and has been validated many times. Employing microphones at different microphone positions can reveal the directivity pattern of the noise.

Application of an acoustical mirror enables source localization [23]. The focusing effect of the mirror amplifies the signal of the source, with a microphone placed in a nearby focal point. Amplification is maximal when the source is located in a focal point of the ellipsoid shaped mirror. Traversing the mirror will give an image of noise sources on the test rig. The unavoidable handicap of traversing the mirror and the large size necessary for capturing lower frequency signals made this instrument less popular.

Another way of noise source localization is by employing a phased microphone array [24]. Individual microphone outputs can be shifted by an amount equal to their propagation delay and then summed together. The result of this process called beamforming is a single output for the array. By adjusting the propagation delay, it is possible to steer the array to different points in space, thereby scanning a certain area for noise sources. The result is an image of relative importance of noise sources in a plane. The advantage of this technique is that physically moving the array is not a necessity. To reduce the number of microphones needed for scanning an area, cross- or spiral shaped arrays with improved signal processing are proposed instead of using a full grid of microphones.

A recent development is the application of phased microphone arrays in hard-walled tunnels. Recession of the array and applying a porous surface material

to act as aerodynamic surface flush to the tunnel wall, allows acoustic signals to pass through and prevents noise from turbulent flow past the microphones [25]. Employing a phased microphone array in a hard-walled tunnel opened up the possibility for pressurized tunnels and thereby Reynolds number scaling without velocity and model size changes. The fact that these pressurized tunnels are scarce combined with the usage of scale models and a non sufficient maximum speed for most tunnels, means most experiments do not satisfy Reynolds number requirements.

2.2.2 Flyover measurements

Before the development of phased microphone arrays, distinguishing between different noise source components for flyover measurements was not an easy task. Attempts include farfield microphone assessment of a landing gear attached to an aerodynamically very clean sailplane [1], hampered by glider self-noise. Measurement of airplane certification noise levels are generally performed with microphones attached to a pole at 1.2 meter height. Flyover tests with large civil aircraft (landing gear deployed but high lift devices retracted) using phased microphone arrays enabled a comparison with wind tunnel tests [10]. However to do so, corrections must be made for several effects summarized below.

- Atmospheric attenuation
  Propagation of a sound signal through the atmosphere reduces the amplitude of the acoustic pressure perturbation. This attenuation is proportional to distance between source and receiver. Knowledge of the sound attenuation coefficient, dependent on acoustic wavelength, temperature and humidity yields the sound level decrease. A quantitative impression of sound absorption by propagation through the atmosphere is given in Figure 4.22.

- Convective amplification
  This effect is defined as the difference between sound propagation through a quiescent medium or a medium without zero mean flow or the difference between a stationary source and one in motion. Observed sound waves for an approaching source are compressed and expanded for a source moving away, resulting in a Doppler shift of the frequency. The well known Doppler formula can be employed to calculate the corrected frequency. Formulae for correcting the sound pressure, dependent on source type (monopole, dipole or quadrupole), are presented in [26].

- Ground reflection and number of gears
  Ground reflection effects are very difficult to work out in detail. The gross effect can be assumed as a doubling of sound energy, hence a sound increase of 3 dB. The number of landing gears can be accounted for in a similar way.

- Inflow conditions
  It must also be taken into account that local flow velocity on main landing gear may be different from the freestream velocity due to the circulation around the wing or fuselage underneath which the gear is installed. For main landing gears on large civil aircraft this installation effect usually comes down to a velocity reduction of around 80 % [10, 27] in a typical approach configuration. Also of concern when comparing flyover data to separate landing gear wind tunnel tests are discrepancies of local flow direction with respect to freestream velocity because of wing dihedral and angle of attack. A first look into interference effects between center and main landing gear was published in [28]. This study revealed almost negligible interaction noise, probably because of already present turbulent inflow conditions on most components of the isolated gear due to solid body interaction effects on the complex gear.

For the purpose of certification and interpretation, several different noise measures exist that take into account the sensitivity of the ear for different frequencies. When dealing with noise from airplane flyovers, the perceived noise level is frequently used. The perceived noise level [26] has been designed to take into account that people are more sensitive to complex sounds containing high frequency components than they are to high frequency pure tones. For sound signals having a pronounced spectral irregularity, a tone-correction is available on top of the perceived noise level. Another well known and important descriptor for the subjective loudness of airplane flyover noise is the A-weighted sound level [26], measured in dBA. To obtain the overall sound pressure level (OASPL) [26] from the corrected values, the contributions are integrated or summed over all resolved frequencies.

During the flyover of an airplane, the noise level observed at a point on the ground gradually intensifies until it reaches its maximum and gradually falls off again. To take into account the effect of duration, the total amount of sound energy delivered to the recipient is considered, divided by the measurement time period. This results in the equivalent sound pressure level L_{eq}, obtained by integration of

overall sound pressures during flyover, normalized using a time constant:

$$L_{eq} = 10log[\frac{1}{T}\int_0^T \frac{{p_e}^2(t)}{{p_{ref}}^2}dt] \quad . \tag{2.13}$$

For perceived noise levels, this results in the effective perceived noise level (EPNL), which includes pure tone correction and a normalizing constant of 10 seconds. For A-weighted levels, the equivalent A-weighted sound level (EAL) is used.

2.3 Computational Methods in Aeroacoustics

Understanding the physics of sound generation by aerodynamic flow is a necessity to develop computational methods for noise prediction. First empirical methods are discussed based on simple analytic formulae of noise generation. Thereafter the focus will be on numerical simulations of the landing gear flow and its acoustics.

2.3.1 Empirical and statistical methods

Computational Aeroacoustics (CAA) for airframe noise analysis started off with empirical methods, hence only working for similar geometrical configurations. Finks method [29] is known not to take into account small details responsible for high frequency noise, and thereby underestimating EPNL by 8 dB.

Landing gear can be thought of to be composed from several struts, wheels and dressings. Chow et al [30, 31] assumed a haystack (roughly parabolic shaped) spectrum (based on Curle's equation [17]) with a peak centered at the natural vortex shedding frequency for each component and fitted the model with data from full scale landing gear tests [10].

An alternative empirical method for landing gear noise prediction [27] divides the frequency domain into a low, mid and high frequency part consistent with contributions from the wheels, struts and small scale details (dressings, hoses). The sound pressure level for each spectral component is estimated by addition of a frequency dependent function to the overall sound pressure level (OASPL). The OASPL scales with distance to the source, velocity, directivity, number of struts and wheels and a complexity factor. Test results indicate that the number of struts and wheels can be accounted for simply by energy addition, i.e. noise in terms of squared pressure is proportional to the number of components. This means

that 2 identical components make 3 dB more noise than 1 similar component. Counting small scale details for high frequency noise estimation is considered impractical. Therefore a complexity factor is introduced (complexity of the gear is found to scale with takeoff weight) to account for the aggregate effect of these details. Model coefficients are fitted with full scale landing gear wind tunnel tests resulting in a consistent trend of the prediction with test data. For geometrically non-similar landing gear configurations these methods will be inaccurate, because local flow conditions, Reynolds number dependency and interaction effects can not be accounted for properly. Additionally, noise radiation is often modified by diffraction of the wing, which is usually not incorporated in the model. Although these empirical models do not give a detailed image of the acoustic field, they can be useful engineering tools.

Guo [32] proposed a statistical method, dividing the noise spectrum into very low, low, and high frequency parts. The Ffowcs Williams-Hawkings (FW-H) equation [18] can be used to predict farfield noise when nearfield pressure fluctuations are prescribed either from a surface surrounding the gear or from the solid surface of the gear itself. By making the frequency decomposition assumption, the input needed for a FW-H analysis reduces the need for a complete description of surface pressures to sectional forces and only a few surface pressures.

2.3.2 Computational modelling

One emerging method for landing gear noise prediction is to use computational fluid dynamics (CFD) to gain a detailed description of the flow field as an input to the Williams and Hawkings equation. The extremely complicated three-dimensional geometry of landing gear has made detailed computational studies very expensive. Rapid advances in computer power allowed the first reported unsteady RANS-Computations on a rather detailed landing gear flow field in 2002 [33]. The number of grid nodes to be solved (> 10 million) for a Reynolds Averaged Navier Stokes (RANS) simulation [33] requires a large number of parallel processor high performance (fast processor) computers. It appears that even routine flow simulations on simplified geometries are not an easy task, due to the occurrence of massively separated flow. Turbulence closure models often fall short in predicting the right flow behavior in this case, although they perform well for simulating the mean flow. For unsteady flow calculations, the small-scale turbulence needs to be resolved because it governs larger-scale turbulence through the energy cascade process and is responsible for high frequency broadband noise. Detached-Eddy

Simulation (DES, a mixture of Large Eddy Simulation (LES) employed in separated regions away from solid surfaces and RANS used near solid surfaces) was reported to lead to better results compared to unsteady RANS-computations [34], but further proof is needed. Direct Numerical Simulation is still computationally too expensive.

Although CFD has been used to calculate the flow in the near field of the landing gear, simulation of wave propagation necessitates high accuracy in order to resolve the small length and time scales (up to 10 kHz) associated with detailed parts. A typical minimum of 6 to 8 mesh points per wavelength is needed to resolve acoustic particle velocities that are about 4 orders of magnitude smaller than mean velocities. Numerical dispersion and dissipation in unsteady RANS simulations using low order schemes is known to drive an inherently unsteady flow to a steady state [35]. Numerical dissipation will suppress the amplitude of acoustic fluctuations, while dispersion tends to spread out a local solution over a wider area. High order numerical methods must be employed to obtain the desired accuracy. Computational aeroacoustics (CAA) schemes are emerging, but are computationally expensive. For landing gear applications, curved solid boundaries will result in highly stretched grid cells instead of uniform cells necessary for resolving isotropic wave propagation. Hence unacceptable dispersion and dissipation is induced unless grid spacing is further reduced. Unstructured grids have an advantage over structured grids in terms of ease of production. However, it is questionable if wave propagation is properly resolved along oblique cell boundaries of unstructured grids. Also, the large amount of storage and time required for resolving a mesh point has made unstructured grids less popular than structured ones.

Integral methods for far field noise calculation are not subject to numerical dispersion. For low Mach numbers, it is believed that the effect of the acoustic wave field on noise source calculation is negligible, allowing simulation of acoustic sources independent of the acoustic field. Therefore unsteady RANS computations coupled to an integral formulation for the far field are still believed to be a viable alternative [35]. Allocation of noise sources is less difficult than for experiments, because the contribution of different solid integration surfaces is easily quantified. Care should be taken if porous surfaces are used as input to an integral solver, especially if they encounter strong wakes. Comparison of FW-H analysis from the same CFD data with a solid vs. a porous surface input indicates that strong vortices across the porous surface can corrupt the noise radiation prediction [36].

2.4 Landing Gear Flow and Acoustics Research

2.4.1 Spectrum characteristics

The first experiments were performed on simple landing gear scale models in an open jet facility. They showed a haystack-shaped spectrum with a fairly well defined peak at Strouhal numbers between 0.8 and 8 (referenced to freestream velocity U_∞ and wheel diameter D) depending on dimension and configuration (nose vs. main) of the gear [1]. An example of the normalized spectra is shown in Figure 2.1. Wheel-well cavity tones appeared to be heavily damped with the gear

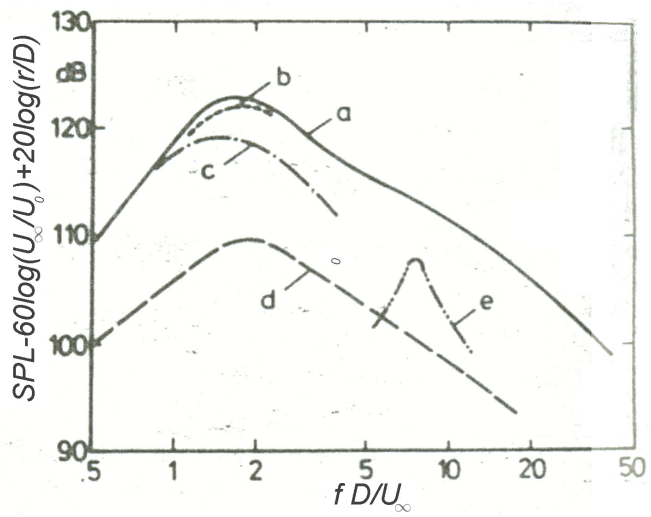

FIGURE 2.1: Normalized sideline spectra of components of a nose gear model: a=complete configuration; b=side support struts; c=lower drag-brace and actuator; d=wheel; e=door ($U_0 = 100$m/s), taken from Heller[1].

in place. The landing gear noise exhibited broadband features, usually without tones present. A potential source of tonal noise is cavity resonance in tube-type pins linking different gear components [8]. The onset of resonance is found to be highly dependent on inflow velocity, turbulence and direction. Cavity caps can be an effective noise reduction treatment. Other potential tonal sources include tire tread noise [19]. Diagonal flow over squared off tread edges can result in large tones distorting the spectrum. Because the tread edges on real landing gears are rounded off, this phenomenon is not likely to appear.

Usually spectral data are presented in the form of sound pressure level vs. frequency. In order to compare measurements for different flow speeds, a non-dimensional noise spectrum can be used like in Figure 2.1. Instead of frequency,

a Strouhal number is used. To characterize the frequency domain, it is often decomposed into a low, mid and high frequency range as explained in section 2.3. There is no official guideline stating the limits of these ranges. In the present work, low frequencies are below $f = 500$ Hz, the mid frequency ranges from this value to $f = 5$ kHz and the high frequencies exceed above $f = 5$ kHz. The sound pressure level can be adjusted by assuming a 6^{th} power scaling law of SPL with velocity. This approach leads to coinciding spectra for different flow speeds [8], indicating dominance of dipole type noise for aircraft landing gear (dipole noise scales with 6^{th} power of flow velocity, see equation (2.9)). However, it has been argued that for high frequencies, an estimate based on quadrupole terms (equation (2.7)) should be used to make spectra non-dimensional [27]. It is hypothesized that the radiation from fluctuating surface pressures cancels because of significant phase variation within the area of a wavelength. The body being non-compact in relation to the wavelength degrades the dipole to a quadrupole source, which indicates noise generation by turbulence. This hypothesis is supported by experimental noise source localization and measurement of a high frequency spectrum fall-off rate typical for turbulence (proportional to the inverse square of frequency). A velocity exponent of 8 makes the spectra coincide better in the frequency range above 2 kHz [27].

The above presented scaling laws for landing gear noise are obtained from isolated undercarriage configurations. Lilley [37] argues that the noise significantly changes when the landing gear is mounted on the airplane. The unsteady flow generated by the undercarriage suffers interference with the airframe and the noise is scattered at doors in the vicinity of the undercarriage legs and the wing trailing edge. Therefore scaling with the 5^{th} power of flow velocity seems to be more appropriate for the total configuration.

2.4.2 Directivity

Increased radiation to the sides [1] shows the dominance of dipole type sound resulting from vertically (or near vertically) oriented struts. Polar radiation (i.e. in a vertical plane containing the velocity vector) for landing gear noise is almost omnidirectional at low Strouhal-numbers, showing increasingly pronounced level maxima in the rear and forward arc with increasing Strouhal number [8]. This contradicts the theory that landing gear noise is dominated by large scale vortex shedding (thus a dipole-type source) for which the maximum noise should appear perpendicular to the flow direction (overhead position). The relevant disturbance

scales for intermediate Strouhal numbers is several millimeter, which corresponds to the dimensions of various dressings attached to the basic gear. Oblique local velocities responsible for the dressing noise generation can be an explanation for the earlier mentioned directivity trend [8]. Another possible explanation is the suspected dominance of noise from wake interaction with downstream gear components.

2.4.3 Noise sources

Several attempts have been made to identify the noise sources of landing gear. Based on natural vortex shedding, larger components are expected to be responsible for lower frequencies and small-scale details for high frequency noise. Regular vortex shedding is often distorted by interaction effects due to the complexity of the gear. Lockard [36] performed a high resolution calculation of a simplified gear and was able to address the relevance of the different noise sources using the FW-H equations. It appeared that gear boxes and wheels are an important contributors dominant over the total frequency range.

Interaction between wheels as a possible source has received attention in [20]. A translating mid-wheel vortex is identified that has the potential to produce significant ground-directed noise, as it distorts upon collision with one wheel and then the other. However, validation of the energy addition principle to account for the number of wheels [27] suggest that to omit tire wake-tire interaction is justified.

Struts exhibit a low frequency spectral peak governed by the overall component diameter [38] and a high frequency spectrum generated by small attached dressings, joints etc. Tests with and without these small scale components indicate that they can be responsible for up to 10 dB of the high frequency noise [19], thereby pointing out their importance. A possible explanation for the high relative importance of high frequency noise on landing gear is given in [10]. High local flow velocities around small-scale components caused by blockage are hypothesized to relatively enhance high frequency sources to low frequency sources for a given freestream velocity.

2.4.4 Effect of Reynolds number

A first survey into Reynolds number dependence [39] showed airframe noise sources can depend on Reynolds number, although tests with a simplified 4-wheel landing gear seem to be largely independent of Reynolds number. An attempt to correct for Reynolds number discrepancies is presented by Iida *et al* [40]. By incorporating experimental results (showing a relationship between characteristic length scale and Reynolds number) into the Lighthill-Curle equation, it is shown that the sound pressure level (SPL) is inversely proportional to the square root of Reynolds number. However, this theory has only been validated by experiments in the published paper.

2.4.5 Noise reduction means

2.4.5.1 Fairings

High velocity impingement on small scale and sharp edged components can be responsible for high frequency noise. Therefore there is a potential for noise reduction by flow control around these components. A non-practical fairing covering a total landing gear showed a 10 dB noise reduction potential [10]. Several tests employing more practical fairings [8, 10] demonstrated a noise reduction of about 3 dB. Retraction of the gear, free movement on the landing strip and the need for a cooling flow around the brakes prevent further noise reduction. Examples of possible practical fairings are the undertray fairing (shielding the wheel axles and undertray assembly), wheel caps (covering the rim) and leg door filler (covering the gap between leg door and drag arm).

High speed flow deflection onto other components by fairings must be avoided, preventing the promotion of noise generation by other components. Effectiveness of fairings including high speed flow deflection on other components can be modelled by $\Delta dB = 10log(1 - S_f){n_f}^6$, where S_f is the percentage of gear covered by fairings (flow speed over these components is assumed zero) and $n_f = \frac{<U^6>^{\frac{1}{6}}}{U_0}$ denotes the velocity increase over the remaining components. This equation demonstrates that high speed deflection can easily make the gain of fairings disappear.

Making the fairings porous and bleeding part of the flow through them can lead to an additional noise decrease as shown by flight tests[12, 13]. Recent wind tunnel tests [14, 15] have shown that the overall noise reduction by application of

impermeable fairings can be overshadowed by an increase in low frequency noise. The tests confirmed a noise decrease by application of porous fairings relative to solid surface fairings. However, the exact mechanism responsible for the noise effects remain unclear, since a thorough corresponding aerodynamic investigation has not been performed.

2.4.5.2 Other noise reduction means

Cavity caps are an effective and simple noise reduction measure to attenuate pin cavity tones [8]. Alignment of the bogie beam undertray in the flow direction was found to result in a 1 dB noise reduction [41]. The effect of bogie beam length and lateral wheel spacing (axle length) has been investigated in [14]. By incorporating noise requirements in the design phase, it was shown that a broadband landing gear noise reduction of 5 to 6 dB on source level can be achieved[42].

2.5 Cylinder Flow and Acoustics Research

The complex shape of landing gear complicates fundamental aeroacoustic research. A shape frequently applied in landing gears are cylinders, used as struts. To understand landing gear flow and acoustics, one must be well acquainted with flow around circular cylinders. Fortunately, a large amount of work has been done to understand the flow physics associated with this particular structure. The part of this work that is relevant for this study is summarized below.

A good collection of previous research can be found in [43] and [44]. The flow around circular cylinders is often characterized into three distinct flow regimes: subcritical, supercritical and transcritical. Subcritical flow indicates purely laminar boundary layer separation at a polar location of $\varphi \approx 80\,^\circ$ and regular vortex shedding at a Strouhal number of about 0.20 is observed over a range of Reynolds numbers (based on cylinder diameter) roughly between $Re_D \in [2 \times 10^2, 1 \times 10^5]$. The supercritical regime, roughly $Re_D \in [1 \times 10^5, 4 \times 10^6]$, is characterized by either a dramatic rise in the Strouhal number or else a loss of organized vortex shedding altogether. Transition to turbulence begins to occur on the body. Since a turbulent boundary layer is less susceptible for positive pressure gradients, separation is delayed to $\varphi \approx 120\,^\circ$. Therefore the wake is noticeably narrower causing a sudden drop in drag approximately at $Re_D = 3 \times 10^5$. After this critical state, the boundary layer turns fully turbulent, and increasing Re_D results in gradual

upstream movement of separation, causing a slight increase in drag again. In the transcritical regime, above a Reynolds number of roughly $Re_D = 4 \times 10^6$, periodic vortex shedding re-establishes at a higher Strouhal number of $0.26 - 0.30$. Hoerner [45] showed a relationship exists between drag and Strouhal number for Reynolds numbers between $10^3 < Re_D < 10^6$. By fitting a curve through available experimental data, he defines an empirical function for various bluff bodies in two-dimensional flow,

$$Str = \frac{0.21}{C_D^{\frac{3}{4}}} \quad . \tag{2.14}$$

For the present investigation, Reynolds numbers will exceed $Re_D = 1 \times 10^5$ and approach speeds below 80 m/s prevent the Reynolds number exceeding $Re_D = 4 \times 10^6$. This means the sub- and transcritical regions are not of interest and we focus on the supercritical regime. Experiments at these Reynolds numbers are known to show widely different behavior due to differences in experimental flow conditions such as tunnel boundary layer, cylinder aspect ratio and external sound. A large aspect ratio is necessary to create nominally two-dimensional flow behavior. Wake and separated flow regions are known to exhibit three-dimensional flow behavior, i.e. spanwise flow features. A measure to quantify spanwise flow structure is the correlation length L_c, which can be defined by [46]

$$L_c = \int_0^\infty \frac{\overline{u(0)u(z)}}{\sqrt{\overline{u(0)^2 u(z)^2}}} dz \quad , \tag{2.15}$$

where $u(0)$ and $u(z)$ are the fluctuating velocities in general flow directions at two points z apart. Typical values of L_c are smaller than $10D$. It represents the spanwise length along which the velocity fluctuations in the near-wake are still correlated. Values of L_c depend on experimental arrangement and Re_D.

The main contribution of aerodynamic sound from cylinder flow is related to the fluctuating forces acting on its body [47]. For low Reynolds numbers Re_D in the subcritical regime, an Aeolian tone is present corresponding to the regular vortex shedding. The contribution from the second term in equation 2.8 (dipole term) diminishes the relative importance of the quadrupole term. Perot el al. [48] emphasize that the dipole source term is merely quadrupole sound diffracted by the solid body.

The fluctuating lift generally is dominant resulting in a dipole sound field directed perpendicular to the undisturbed flow and obeying the intensity scaling law of equation 2.9. Likewise, the fluctuating drag results in a dipole sound field 90°

opposite. For increasing Reynolds number the fluctuating forces become more chaotic, resulting in a more broadband spectrum instead of the distinct peak of the Aeolian tone. Values of fluctuating lift and drag amplitude vary significantly with experimental conditions. Aspect ratio and endplate size seem to be the main experimental factors influencing the whole vortex shedding process and the associated values of fluctuating lift and L_c [49]. However ratios of fluctuating lift to drag have been reported around 4 for regular vortex shedding [44]. In the subcritical regime, the frequency corresponding to oscillating drag is 2 times the lift frequency, corresponding to vortices being shed from alternate sides of the cylinder.

Revell et al [50] attempted to determine a quantitative relationship between far field noise and drag coefficient for $4.5 \times 10^4 < Re_D < 4.5 \times 10^5$ and $0.1 < M < 0.5$. A spanwise distribution of lift and drag dipoles is assumed to develop an expression for the mean squared far-field acoustical pressure, using L_c to determine their spacing. Lift- and drag dipole strength are related to the mean squared pressure fluctuation, which in its turn is related to C_D. Frequency is estimated using equation 2.14. The constants are then determined experimentally, showing a strong dependence of SPL on drag coefficient varying as to 50 to 90 times $log(C_D)$ depending on directivity angle and bandwidth. Both smooth and rough cylinders are subject to experiments and show pure Strouhal tones in farfield noise spectra. However, the reader is cautioned that impingement of upstream turbulence can alter the results considerably, destroying the tonal behavior.

Additional to the work on stand alone circular cylinders is an increasing amount of work on elements of different cross-sectional shape and tandem cylinder configurations, for example in [51, 52].

2.6 Aeroacoustics of Perforated Surfaces

Perforated surfaces are well known for their acoustic absorption characteristics, especially in combination with porous materials [53]. In addition to that, perforated plates are often used in fluid dynamics for modification of aerodynamic or hydrodynamic flow characteristics. Both aerodynamic and acoustic research involving perforated surfaces are summarized below.

2.6.1 Aerodynamics

Perforated plates have been used in fluid motion for the production or reduction of turbulence and either for the creation or elimination of large-scale velocity or pressure uniformities. In the first case, the mixing capacity of a given flow is increased which can be useful in chemical applications (e.g. fluidized beds [54]). For the second category one can think about application in wind tunnels to minimize flow turbulence and enhance flow uniformity. In the field of hydraulics, perforated plates are often used for flow control. Therefore most previous research on this subject stems from this background. For these applications the most important parameters to look at are pressure drop across the plate, modification of velocity distribution and the induced turbulence. Most investigations deal with perforated plates at a 90 ° angle with the oncoming flow spanning an entire cross section, of which pressure drop and turbulence characteristics will be discussed firstly. Influence of porosity on aerodynamics of a plate of finite size is discussed thereafter.

2.6.1.1 Pressure drop and velocity distribution

To analyze flow past a perforated plate, Figure 2.2 distinguishes three sections: *(a)* A cross section of the freestream well ahead of the screen, *(b)* the cross section at which the jets issuing from the holes are fully contracted but still essentially undiffused, and *(c)* a cross section of the free stream well beyond the screen.

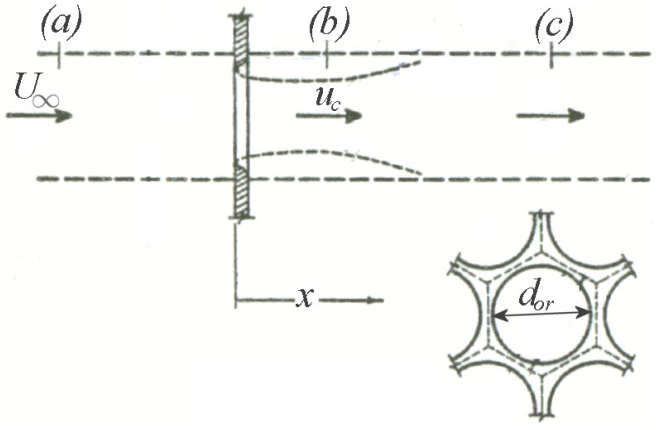

FIGURE 2.2: Sections for describing flow past a perforated plate, taken from [2].

Pressure drop between the first and last section can be quantified by means of the

pressure loss coefficient (coefficient of fluid resistance)

$$\zeta = \frac{\Delta p}{\frac{1}{2}\rho {U_\infty}^2} \quad , \tag{2.16}$$

where U_∞ is the undisturbed velocity upstream of the perforate. Generally, the pressure gradient can be expressed as the sum of two terms [55], which are proportional to the first and second power of velocity

$$\nabla p = \frac{\mu U_\infty}{\alpha} + \beta \frac{1}{2} \rho {U_\infty}^2 \quad . \tag{2.17}$$

The first term represents frictional losses, mainly due to momentum transfer (viscous shear stress) in boundary layers. The second term is associated with inertial losses, mainly due to flow separation. For small plate thickness t, $\nabla p = \frac{\Delta p}{t}$, which gives

$$\zeta = \frac{t}{\alpha} \frac{\mu}{\rho U_\infty} + \beta t \quad . \tag{2.18}$$

For plates with a small thickness and sufficiently high Reynolds numbers the frictional contribution to the pressure loss can be neglected compared to the inertial losses. Because fairings generally have a small thickness and Reynolds numbers are large, it is expected that indeed frictional contributions are negligible.

A good analysis of the afore mentioned parameters is given by Baines [2], where both lattices and perforated plates are studied experimentally and compared to a theoretical analysis. A one-dimensional analysis for high Reynolds numbers without compressibility effects is given. Pressure and velocity at cross sections *(a)*, *(b)* and *(c)* are considered to derive an expression for ζ. A theoretical analysis is possible, because frictional losses are small and the relative extent of the jets can be predicted since the orifice edges determine the points of jet formation. The location of full contraction of the jets in section *(b)* is also called the *vena contracta*. Using the continuity equation between section *(a)* and *(b)*, the contraction coefficient C_c is defined by

$$C_c = \frac{1}{\sigma} \frac{U_\infty}{u_c} \quad , \tag{2.19}$$

where u_c is the velocity in the vena contracta. Values of C_c have been reported between $\frac{2}{3}$ and 1 , depending on screen geometry. Conservation of momentum and energy then yields

$$\zeta = [\frac{1}{C_c \sigma} - 1]^2 \tag{2.20}$$

An illustration of equation 2.20 is given in Figure 2.3.

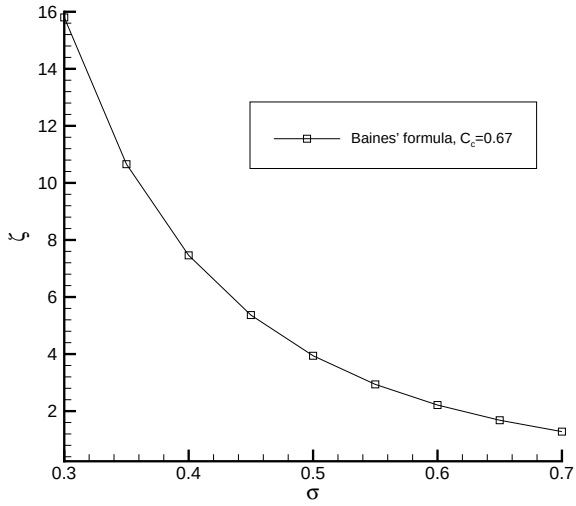

FIGURE 2.3: Dependence of ζ on σ as predicted by equation 2.20, $C_c = \frac{2}{3}$.

Morgan [56] argues that this equation should be modified for high values of the open area ratio σ, where the flow reduces to that around a series of isolated shapes. Values of C_D for a screen can be deduced by multiplying ζ with $\frac{1}{1-\sigma}$, however for $\sigma \rightarrow 1$ this formula does not approach the value that is supposed to represent the flow physics for flat plates. This is confirmed by experiments that show physical values of ζ to depart from equation 2.20 at $\sigma > 0.7$ for thin plate screens.

Pressure drop over a wide variety of perforated plates is documented by Idelchik [3], which combines the results of many previous investigations on this subject. The numerous parameters that are taken into account are Reynolds and Mach numbers, perforate shape, plate thickness, hole diameter and porosity. The data presented is for perforated plates spanning an entire wind tunnel cross section, perpendicular to the undisturbed velocity.

The Reynolds number of the perforate is defined as

$$Re_{d_{or}} = \frac{u_{or} d_{or}}{\nu} \quad , \tag{2.21}$$

where u_{or} is the velocity in the orifice and d_{or} the orifice diameter. Three specific flow regions can be distinguished:

- $Re_{d_{or}} < 10$
  The purely laminar regime, in which ζ depends linear with $Re_{d_{or}}$ on a logarithmic scale.

- $10 \leq Re_{d_{or}} < 1 \times 10^4$
  The transition regime, in which the linear dependence is violated.

- $Re_{d_{or}} \geq 1 \times 10^4$
  The turbulent regime, in which an effect of $Re_{d_{or}}$ on ζ is virtually absent and the quadratic resistance law of equation (2.16) is valid. The boundary layer has become turbulent and the separation pockets behind the screen become stable. Therefore further increase of $Re_{d_{or}}$ has no effect on ζ.

The regions are illustrated in Figure 2.4. Reynolds numbers for the present inves-

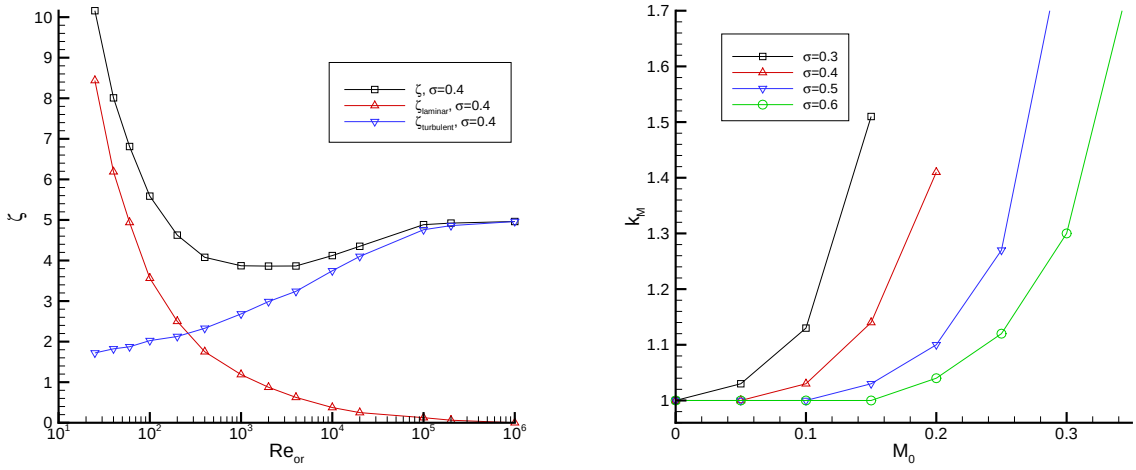

FIGURE 2.4: Reynolds number dependence of pressure drop (left) and Mach number dependence (right) after Idelchik [3].

tigation are in the turbulent region.

Dependence of ζ on Mach number M_0 for subsonic speeds is illustrated in the right hand side of Figure 2.4 by plotting k_M which is defined by

$$\zeta = k_M \zeta_{M_0=0} \tag{2.22}$$

Compressibility effects transfer kinetic energy into heat and thereby increases the pressure drop. However, it should be noted that the difference between M_0 and M_{or} is different between perforated plates spanning the tunnel or perforates on a fairing, since the flow can deflect away in the latter case. Therefore compressibility effects are expected to play a role for higher values of M_0 than indicated in Figure 2.4.

Another parameter to take into account is the edge radius r_{edge} of the holes. Empirical research on this aspect has been summarized in [3] and is visualized in

Figure 2.5. A rounded instead of a sharp edge will increase the vena contracta

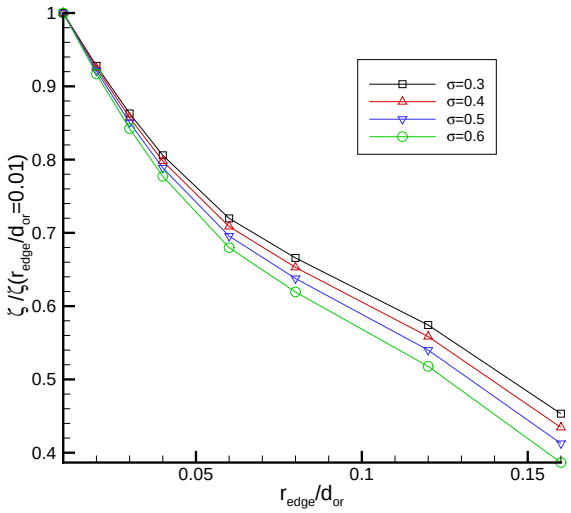

FIGURE 2.5: Dependence of ζ on r_{edge} for different values of σ after Idelchik [3].

and thereby reduce the pressure losses.

Modification of velocity distribution by perforated plates is treated in [2]. Non-uniformities in flow distribution are evened out more by passage through a perforated plate. A theory is developed to predict this modification, which agrees well with experiments for high open area ratios $\sigma > 0.5$. Screens with lower values of σ were found to yield unstable flow downstream. By varying the upstream velocity distribution approaching the plate, it was found that the velocity distribution downstream of the plate is almost invariant to the upstream profile for these values of σ. In this case downstream means sufficiently far away from the region affected by the individual jets. It is also argued that screens at an angle to the flow will tend to deflect the flow towards the normal of the plate, simply because the flow resistance is a minimum when the flow is at right angles to the plane of the screen. Therefore a curved perforated plate is expected to deflect the flow towards the center of the curve.

2.6.1.2 Turbulence

The flow through a screen can be represented by a number of jets that form independently and then gradually spread and coalesce with neighboring jets. The

energy of the mean flow is converted into turbulent energy by eddies produced in the zone of intense shear surrounding each jet. The eddies begin to decay immediately, changing their energy into heat by viscous dissipation. Further downstream the jets are fully mixed and turbulence will become isotropic. The length necessary for decay depends on the jet geometry and therefore scales with d_{or}.

Turbulence is often described by means of the turbulence intensity Tu which can be defined as the ratio of the Root Mean Square (RMS) of the velocity fluctuations over the mean velocity.

$$Tu = \frac{u'_{RMS}}{\overline{u}} \quad , \tag{2.23}$$

however in practice often the freestream velocity U_∞ instead of the mean velocity is taken as a reference. Checkel [57] did hot wire measurements along a hole centerline aft of various plates with $\sigma = 0.4$ spanning the tunnel. Varying hole diameter and tunnel speed, the Reynolds number range covers $Re_{d_{or}} \; \epsilon \; [1.0 \times 10^3, 1.3 \times 10^4]$. Turbulence intensity Tu is shown to reach a maximum of 50% at $\frac{x}{d_{or}} = 2.5$ for all combinations, illustrating dependence of production and decay on hole diameter. Since hole diameter varies between 2.5 and 20 mm for a constant plate thickness ($t = 5$ mm), influence of hole aspect ratio becomes noticeable. Apparently, a high aspect ratio produces smaller scale turbulence resulting in lower turbulence energy levels in the downstream flows.

A more recent investigation is presented by R. Liu [4]. Experiments are performed with perforated plates spanning the entire tunnel test section. Influence of the size and solidity of circular perforations on turbulence was measured for Reynolds numbers around 20×10^3 using a hot wire probe at different downstream distances. Turbulence intensity was shown to increase with solidity, i.e decrease with σ. Homogeneity (defined by uniformity of turbulence intensity) at a fixed downstream distance decreases with plate solidity. Physically, this can be explained by the larger pitch between jets leaving each perforation (for a constant diameter with increasing solidity), which causes the jets to take longer to mix. Values are illustrated in Figure 2.6. The normalized turbulence intensity was found to decrease with $\frac{x}{d_{or}}$ in the form of a power law relationship.

2.6.1.3 Screens of finite size

The above investigations focus on a screen fully obstructing the flow path, i.e. all flow is forced through the perforates. Research on a perforated plate of finite width spanning a wind tunnel has been performed by Castro [58] in the Reynolds

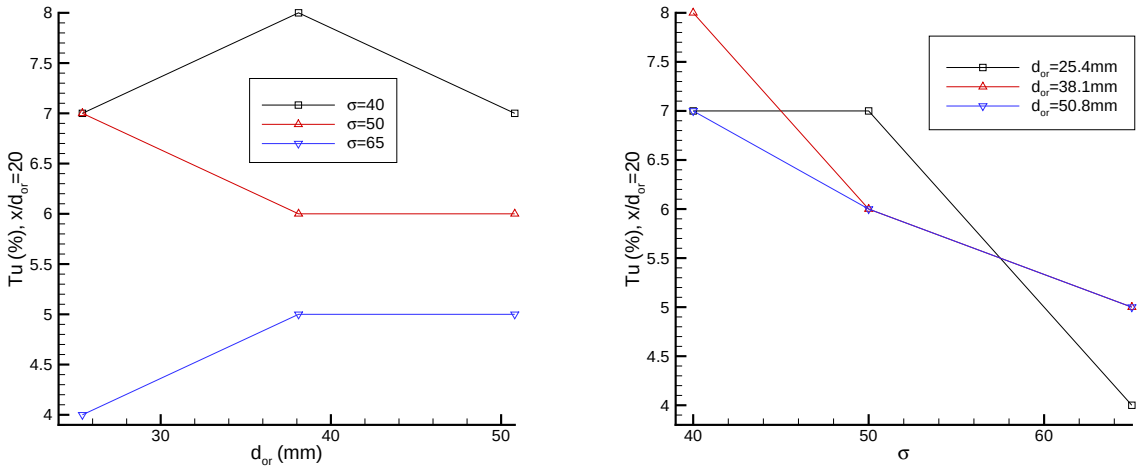

FIGURE 2.6: Dependence of Tu on d_{or} (left) and σ (right) ($\frac{x}{d_{or}} = 20$, $Re_{d_{or}} = 2.9 \times 10^4$) after Liu [4].

number range between 2.5×10^4 and 9.0×10^4 (based on plate width). Hot wire measurements in the wake of the plates with a porosity between 0 and 64.5% show that the effect of bled flow is to move the area of reversed flow further downstream. Above a porosity of approximately 40%, the reversed flow area disappears. For zero porosity ($\sigma = 0$), the two unstable shear layers interact in the near wake and roll up to form a vortex street. The bled flow prevents this interaction in the usual way and delays the vortex formation. This is accompanied by an increase in base pressure. At a porosity of 20% the vortex street suddenly ceases to exist. This is indicated by a sudden drop in plate drag and a sudden downstream movement of the point of maximum turbulence intensity along the plate centerline. The velocity spectrum measured sideways of the wake shows a distinct peak at a Strouhal number of 0.14 (based on plate width) for a solid plate. Above $\sigma = 0.2$ a distinct spectral peak is still visible, although the frequency suddenly drops. This periodicity is believed to be due to the 'flapping' of the unstable turbulent wake instead of vortex shedding. Above a porosity of 40% it is no longer possible to pinpoint a dominant frequency.

Oblique or normal incidence to a curved plate introduces pressure gradients along its surface, which will influence the aeroacoustic behavior of the fairing. Research on curved perforated fairings is a new field of interest. The above mentioned investigations can aid in creating a rough idea of the flow structure and factors involved. We want to be able to assess the influence of perforations on vortex shedding and air deflection for oblique or perpendicular flow on a curved thin walled surface of finite dimension.

2.6.2 Acoustics

Perforated plates are often used in acoustic liners as a facing sheet [53]. The facing sheet covers cavities designed to attenuate noise of a particular frequency. Noise that is radiated onto the perforated surface is attenuated due to viscous dissipation in the cavity defined by the perforated surface. Tailoring of the apertures with respect to the expected sound frequency can make for an effective absorption of narrow-band noise. Such perforated surfaces are commonly found in automobile exhaust systems, aircraft engines and compressors.

As mentioned, liners can be tailored to dissipate acoustic energy at certain frequencies by changing the flow resistance through variation of porosity. The radiation characteristics of a surface are defined by the acoustic impedance Z_a

$$Z_a = \frac{p'}{u_n} \quad . \tag{2.24}$$

This is the ratio of the complex acoustic pressure to the acoustic velocity normal to the surface. The specific acoustic impedance z_a is obtained by dividing Z_a with the characteristic impedance of the medium $\rho_0 a_0$ (the acoustic impedance of a plane wave in the direction of propagation)

$$z_a = \frac{Z_a}{\rho_0 a_0} = \frac{p'}{u_n}\frac{1}{\rho_0 a_0} = r + i\chi \quad , \tag{2.25}$$

where the real part is defined as the resistance r and the complex part as the reactance χ. For an impervious surface, $z_a = \infty$, indicating total reflection of impinging sound waves. The impedance can be tailored by varying parameters such as orifice diameter, plate thickness and depth of the backing cell.

A study on flow control using this principle is presented in [59]. Both experiments and computations are performed with a cylinder (Re = 6000 to 12000) using an optimized finite impedance on its surface to reduce the dipole noise term. An annular space behind the perforated cylinder surface creates the ideal impedance in the experiments. For the LES-computation, both a Helmholtz resonator model (approximating the phenomenon of air resonance in a cavity using a one-dimensional model) as well as a perforated shell model (actually modelling the flow in the annulus and the perforations by assuming laminar flow) are implemented to impose the impedance boundary condition. Because air deflection is not of interest here, hole diameters are around 0.06 mm, opposed to 3.2 mm for the earlier mentioned fairings that already have been used for flyover tests. Results of both experi-

ments and computations indicate that indeed the optimized impedance boundary condition leads to a reduction of the emitted noise level by attenuating the peak frequency associated with the shedding.

Another attempt to employ perforations for noise control is presented by Ikeda [60]. A pantograph horn as part of a train set produces an unwanted aeolian tone. Wind tunnel tests have been performed on a cylinder with large diameter perforations (1/5 cylinder diameter) from the leading edge through to the back face at $Re = 1.1 \times 10^5$. A suppression of the aeolian tone is shown by stabilization of the wake shear layers due to the jets emitted from the perforations at regular intervals. The flow field measurements agree with the earlier described research by Castro [58].

2.6.2.1 Shearing flow

Acoustic research on perforated surfaces mostly deals with parallel incidence of the undisturbed flow with respect to a flat plate [61]. An aspect to take into account is the generation of noise by the perforations itself. Turbulent fluctuations in the boundary layer give rise to a fluctuating volume flow through the apertures. This fluctuating volume flow creates two monopoles of equal and opposite strength located respectively just above and below each aperture. For acoustically transparent surfaces, both monopoles combine to produce a dipole sound field exhibiting a U_∞^6 dependence. More 'opaque' surfaces have monopoles only above the apertures which convert the turbulence into sound more effectively [62]. The turbulence induced noise described above has been shown to generate a substantial amount of broadband noise [61], concentrated between roughly $Str \in [0.20, 1.50]$, based on hole diameter. For transparent surfaces, the effective sound pressure p_e due to this phenomenon has been shown to obey the following scaling law

$$ {p_e}^2 \propto \frac{S}{\sigma} \frac{\rho_0 \cos\theta}{a_0 d} StrTu^2 {U_\infty}^6 \quad , \tag{2.26} $$

where d is the distance from the center of the screen area S with porosity σ to the observation point at an angle θ referenced to an axis normal to the screen.

More discrete frequency noise by perforates can occur whenever a feedback mechanism is present. In practice this mechanism can be provided by locking-in of the vortex shedding with an acoustic resonance whenever an enclosed cavity is present on the other side of the perforate. In the case of acoustic liners this can often be the case [63]. Another feedback mechanism is an edgetone type mechanism as

described in [64, 65]. The research investigates a jet of air impinging on a sharp edge. When the jet impinges the sharp edge, airflow is divided between the upper and lower side of the edge. When the stream spreads over the edge, it must pass up one side first creating an asymmetry. This asymmetry produces a periodicity in the velocity, causing a pulsation in the air supply. The resonance in the holes creates a discrete noise or 'singing' phenomenon. A sharp edge is more effective in spreading the flow hence creating the tonal noise.

However the situation is slightly different for grazing flow past perforations. In this case, eddies are shed from the orifice upstream edge. McCanless and Boone [66] state that interaction of eddies with the downstream edge of the perforation in which eddies are shed is important. It is posed that the vortices significantly increase in strength when they strike the aft edge of the hole because of the shearing induced by the sharp corner.

Porous wall wind tunnel test sections made of perforated plates have been given attention in [67]. They exist to give the air the opportunity to pass between flow stream and surrounding plenum chambers, thereby correcting for model blockage effects in the test section. The singing phenomenon caused by the edgetones has been reported to significantly disturb unsteady measurements.

2.6.2.2 Normal incidence

Noise generated by flow through a single circular orifice has been studied experimentally by Anderson [68, 69, 70, 71]. Primary tones and higher harmonics are observed when the ratio of thickness to diameter of the orifice t/d_{or} lay between 0.5 and 2. Greatest intensity was observed when orifice diameter equaled plate thickness. The frequency of the tone was found to depend on differential pressure Δp across the orifice, density of the gas ρ and thickness of the orifice plate t. Since $\Delta p/\rho$ is a measure for velocity, a value for Strouhal number based on plate thickness can be defined. Typical values are $Str_t = ft/U = 0.25$ and $Str_t = 0.6, 0.8$ for higher modes. For thick, pipe-like orifices amplitudes generally are much smaller and the frequency of the tones scale with orifice diameter d_{or} instead of plate thickness t.

For maximum efficiency in the production of tones it is important that the entrance edge of the orifice is sharp rather than the exit. Slightly rounding off the entrance edge makes the intensity of the tone more feeble if not entirely absent. Flow visualization clarifies the physics on this phenomenon. The tone is cre-

ated aerodynamically by the periodic vortex shedding of vortices from the orifice, which gives rise to a sound field in the surrounding medium. However, as the orifice Reynolds number approaches $Re_{d_{or}} = 1 \times 10^4$ the amplitude of the eigenfrequencies decrease, finally merging into the acoustic noise background into which all eigenfrequencies become transformed.

The turbulence created by a perforated plate can be an additional noise source in the case of impingement on a solid body downstream of the plate. Olsen [72] studied noise by impingement of turbulence on various solid bodies. It appeared that although the effect of body shape was small, solid bodies with blunt trailing edges generally are quieter.

Chapter 3

Research Methodology

This chapter discusses the methodology used in the present research. Firstly, the influential parameters that have become apparent from the literature review will be structured and ordered according significance. This process aids in constructing the research plan, which is discussed thereafter. Finally, model design and experimental arrangements for the models used in the present research will be discussed.

3.1 Influential Parameters

From the literature review, a number of parameters of influence for the present research have become apparent. A survey of the initial parameters of influence is presented in Table 3.1. The table distinguishes between parameters that can be varied on the real landing gear and parameters that are influential in wind tunnel experiments but fixed on the real landing gear. The parameters herein that tailor the perforate directly are porosity σ, pitch p_{or} (distance between orifice centerpoints, Figure 3.2), hole diameter d_{or}, hole arrangement, location of exposed perforations and hole edge radius r_{edge}. To vary and assess the influence of each of these parameters would be a task too elaborate within a PhD. Therefore a judgement had to be made on the relative importance of these parameters. Fortunately the literature survey brushes upon many of these issues. By engineering judgement, the amount of air that passes through the perforate is primarily determined by the porosity and the location of porosity. It is these aspects that are expected to dominantly influence fairing self noise at lower frequencies and the amount of high speed deflection onto other components. Therefore it is chosen to concen-

TABLE 3.1: Survey of influential parameters for perforated fairings.

Parameter	Variable on landing gear?	Comment
$Re_{d_{or}}$	yes	variation of orifice Reynolds number
M_{or}	yes	orifice Mach number effects
σ	yes	porosity of perforate
p_{or}	yes	pitch of orifices
d_{or}	yes	diameter of orifices (relative to fairing size)
r_{edge}	yes	edge radius of orifices
hole arrangement	yes	hexagonal or rectangular configuration (Figure 3.2)
location of perforate	yes	stagnation point area or towards fairing sides
aerodynamic drag	yes	landing gear drag variable by application of perforations
fairing shape	no	landing gear fairing shape is fixed
fairing location	no	relative positioning to other geometry
t_f	no	fairing thickness
inflow conditions	no	variation of α
Re_{D_f}	no	variation of fairing Reynolds number
M_0	no	Mach number effects
model stiffness	no	vibration effects

trate on porosity and its location instead of changing pitch, hole arrangement and hole diameter at a constant porosity. However especially from an acoustic point of view, it is expected that self-noise by the perforate will be highly influenced by d_{or}, r_{edge} and t_f. While the main focus is on porosity and its position, these aspects will have to be taken into account and assessed wherever possible, depending on the outcome of the experiments. Additionally, the parameters that are influential in wind tunnel experiments but not variable on the landing gear will have to be chosen with replication of flight conditions in mind.

The overall aerodynamic performance needs to be considered for a landing gear which incorporates perforated fairings. The undercarriage contributes to the aerodynamic drag which aids in slowing down the airplane during the approach phase. Additionally, the landing gear drag influences the take off performance for aircraft. In this respect, an increase in aerodynamic drag of the undercarriage would necessitate a larger thrust and hence result in an engine noise increase. Therefore one should be careful when making large modifications to landing gear configurations.

3.2 Research Plan

In order to develop guidelines for application of perforations to landing gear fairings, the following research plan is to be carried out. From the literature review it becomes clear that most previous research on perforated surfaces is focussed on flat plates with infinite dimensions. The two most important differences to landing gear fairings are the fairings being curved and finite, which allows for flow past the sides instead of solely through the perforate. The complex shape of the landing gear and the perforated fairings hamper detailed computational and experimental research of acoustics and flow behavior. The literature review has indicated that the currently available numerical methods and computers are not capable of dealing with the complex landing gear geometry. Experimentally, the readily complex landing gear flow full of interaction effects will complicate distinguishing and interpreting the influence of porosity on aeroacoustics. Additionally, experimental techniques preclude interrogation of the velocity field in the many semi-enclosed landing gear spaces (e.g. between torque link and main strut) and thereby mapping the total flow field.

Therefore an experiment is proposed to test a simplified fairing-strut combination. By simplifying the landing gear and fairing geometry, it is possible to interrogate the total velocity field around the fairing strut-combination. The relatively low

complexity of the configuration increases the signal to noise ratio between the various configurations. The effort lost for establishment of a database for the baseline configuration (without perforations) is less costly compared to a full landing gear model. The simplified fairing geometry enables easy manufacture of differently configurated fairings for an assessment of the various influential parameters. This way insight is gained in the underlying physics that determine aeroacoustic performance of perforated fairings. For clarification of time averaged flow behavior, the basic geometry used for this experiment can be subject to a computational study as well.

It is not expected that findings from the basic study are directly applicable to the landing gear fairings. Large discrepancies in geometry and flow conditions preclude transferring values from the basic study onto the landing gear. However the basic experiment will give a better understanding of the underlying flow physics of perforated fairings and of the sensitivity for influential parameters. This knowledge will enhance the engineering judgement that decides upon how to apply perforations to landing gear fairings and optimize the noise reduction potential.

Following the basic model experiment, a first step is made towards application on landing gear. A scaled landing gear model incorporating perforated fairing is examined experimentally as requested by Airbus. Since only the gear components below the leg door are studied, this model comprises of the undertray and articulation link fairings. Although the described research plan is not conclusive on all influential parameters, it is believed to be the best route towards satisfying industrial requirements within the framework of a PhD.

The rest of the chapter is dedicated to the design of the basic model and landing gear model experiment, including experimental arrangement and apparatus.

3.3 Basic Model Experiment

This section discusses the design of the basic model experiment. Firstly model aspects such as shape and size are addressed. Then the experimental arrangement including wind tunnels and test set-up is highlighted. Finally, the measurement apparatus including it's uncertainty is discussed.

3.3.1 Model shape

As explained in section 3.2, a simplified fairing-strut combination is the subject of investigation for these experiments. A thin walled half cylindrical shell with constant cross section is chosen for the fairing. A circular shape is chosen because it is a relatively known aerodynamic shape and comes close to the actual fairings used in practice, e.g. the lower articulation link cover. Ease of production is an added benefit that comes with this fairing shape. In flight the fairings shield the landing gear components. These components will often be struts. A cylindrical strut can be placed aft of the fairing to simulate this effect. Since a cylindrical strut does not feature small scale details and irregularities characteristic for landing gear geometry, a single acoustic test employing an H-beam instead of a cylinder is also performed. A representation of these shapes is shown in Figure 3.1.

To minimize the flow in the spanwise direction, the cross section of shell and strut is kept constant. This should gain a nominally two-dimensional flow, thereby simplifying the flow and the necessary measurements. Flow past the model ends has to be prevented by either endplates or tunnel walls. Cylinder flow literature [43] indicates the presence of three-dimensional flow behavior in the wake, depending on details of the experimental parameters such as tunnel wall boundary layer.

Strut size in reference to fairing size, i.e. cylinder over shell diameter is chosen to be 2/3. In practice it makes no sense to employ an excessively large and noisier fairing covering a relative small component. On the other hand, the mentioned value seems reasonable to fit the fairing comfortably around components that need shielding. The diameter of the square H-beam equals the cylinder diameter. Positioning of the strut with respect to the shell is another issue. It is chosen to coincide the cylinder origin with the shell origin. In order to create a similar blockage for the H-beam configuration, the H-beam center is positioned slightly downstream from the shell center. These locations are the most obvious choice, although it is realized that a change of strut location can alter the flow field significantly. Acceleration of the flow between shell and strut in the case of a perforated shell will depend greatly on the relative positioning of these components. Therefore different trends might be observed employing another strut location. However, in order not to loose the focus of the project and spend time on less relevant details it is chosen to keep this distance constant.

3.3.2 Model size

Parameters of influence for choosing model size can be divided between aerodynamic and practical considerations.

3.3.2.1 Aerodynamic considerations

The size of the model will influence the flow behavior around the model in combination with the experimental facility. The factors that should be taken into consideration are summarized below.

- Reynolds number
  The fairing Reynolds number at a approach speed of $M = 0.2$ ranges between $Re_{D_f} = 1 \times 10^6$ and $Re_{D_f} = 4 \times 10^6$, based upon dimensions of articulation link and undertray fairing respectively. This means that boundary layer flow will generally be turbulent. If we were to assume a flow speed between 30 and 45 m/s (which is the range of the maximum tunnel speeds in the available wind tunnels), the diameter of the model would be close to 1 metre. This size is regarded not as a viable option in the available wind tunnels at the university. The heavy structure needed to achieve the necessary stiffness and a relatively large area to map during the flow measurements make this option impractical (see also section 3.3.2.2). fairing Reynolds numbers will be of the order $Re_{D_f} = 1 \times 10^5$, in the transition between sub- and supercritical regime for cylinder flow depending on experimental conditions (see also section 2.5).

  For the flow around the perforated fairing, the perforate will most probably act as a trip, hence fairing Reynolds number requirements are not regarded very important. Once the flow is in the supercritial flow regime, Reynolds number effects are small. If necessary in the case of the solid shell and strut, transition strips can be used to trip the boundary layer and ensure turbulent separation.

- Wind tunnel blockage and model aspect ratio
  The constraint of the flow between the model, its wake and the tunnel walls will cause velocity field changes at the model compared to a model in free field. When comparing data to CFD, these effects must be corrected for. For a two-dimensional model spanning the tunnel, a blockage ratio of up to 6% seems to be acceptable for circular cylinders, depending on geometric aspect ratio [73]. More blockage will result in uncorrectable changes of

the pressure distribution (moving of cylinder separation point) and Strouhal number (Str). However, separation on the present model is less susceptible for blockage effects compared to a circular cylinder. The outcome of the experiment does not have to be compared to similar experiments. More important is the ability to distinguish a trend between the different configurations. Change in blockage effects should be negligible between different configurations (shell variation has a minimal effect on blockage), allowing for a comparison between them. However, blockage ratios should be kept as low as possible to achieve similar flow features as in real flight.

The geometric aspect ratio necessary to obtain a nominally two-dimensional cylinder flow is not quantified in [44] for the supercritical regime. Previous experiments in this regime [74] have been performed with $L/D = 5$, where L is the axial length of the cylinder. It should be noted however that a half-cylinder exhibits fixed separation at the edges, which can influence aspect ratio effects. Also, because balance measurements are to be performed, the model must not touch the tunnel walls or endplates. It is expected that the existing gap will influence spanwise flow behavior. From [44] it is concluded that endplate size must be around 5 times the diameter size for nominally two-dimensional flow.

3.3.2.2 Practical considerations

Next to aerodynamic factors, considerations of a practical nature influence model size. A larger model will increases the area that needs to be mapped during the flow measurements (e.g. PIV, HW). Various other issues are discussed below.

- Manufacture of the shell
  Diameter and thickness combinations are limited for extruded aluminium tubes. Tailoring thickness of a composite product is difficult. Rolling of a flat sheet enables machining of the holes in advance, but introduces tolerances in the eventual shape.

- Stiffness and mass
  The model should be as rigid as possible. Noise due to model vibration is unwanted and will corrupt aerodynamic noise measurements. Models with various degrees of stiffness due to perforations will induce different noise signatures. The aerodynamic noise variation due to perforations might therefore not be distinguishable.

The mass of the model must be kept low to guarantee valid unsteady force measurements. A high model mass will lower the natural frequency of the balance system, which is an unwanted effect. Additionally, a heavy model will make installation and configuration changes difficult.

Working with large endplates is not considered practical. To keep model length low for stiffness requirements and high enough for aspect ratio requirements, a model spanning the square cross section of the $3' \times 2'$ tunnel (which measures 0.9 m by 0.6 m) vertically is regarded a sound alternative. In that case, a shell diameter of 152 mm and total spanwise length of 600 mm satisfy aspect ratio requirements and result in a blockage of 17%. A visualization with dimensions is shown in Figure 3.1. For more details on construction and materials or dimensions

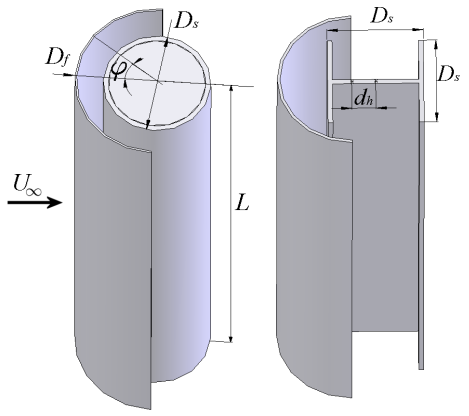

(a) Shrouded cylinder (b) Shrouded H-beam

Dimension	
Shell (outer) diameter (D_f)	152 mm
Strut diameter (D_s)	100 mm
Shell length (L)	514 mm
φ	Polar angle from shell leading edge
Cylinder center to shell center	0 mm
H-beam center to shell center (d_h)	25 mm

(c) Specification of dimensions

FIGURE 3.1: Illustration of basic model and dimensions.

of the basic model, the reader is referred to appendix B.

3.3.3 Choice of perforate

A number of differently perforated shells will be used in the investigation. As outlined before in section 3.1 the emphasis will be on varying porosity σ and the location of porosity (φ).

The orifice Reynolds number in flight is expected to be above $Re_{d_{or}} = 1 \times 10^4$ at earlier mentioned approach speeds for porosities between $\sigma \in [0.3, 0.6]$. This means that also for the flow in the orifice, we are in the turbulent regime and the separation pockets behind the perforate are stable. Orifice velocity will increase with decreasing σ. However, since flow can pass besides the fairings, the rate of

decrease should be lower than plates blocking a total cross section. To ensure that the orifice Reynolds number in the experiment exceeds the value of $Re_{d_{or}} = 1 \times 10^4$, orifice diameter d_{or} must not be lower than 2 mm.

A summary of the different shells is given in Table 3.2. The perforate configuration

TABLE 3.2: Summary of different shell configurations.

Shell	t_f (mm)	σ (%)	d_{or} (mm)	p_{or} (mm)	Location of perforate (φ)	Comments
solid	1.6	0	-	-	-	-
perf33	3	33	3	5	$\pm$ 90 $^\circ$	No hole edge radius, no margins
perf42	1.6	42	3.2	4.7	$\pm$ 45 $^\circ$	Hole edge radius of 0.3 mm, margins of 25 mm on both ends
perf55	3	55	7	9	$\pm$ 90 $^\circ$	No hole edge radius, no margins

of the perf42 shell is copied from the perforate already tested during Airbus fly-over measurements in Toulouse in 2004 [12, 13]. Drawings of this perforated shell can be found in Figure B.2(a). The perf42 and solid shell are both manufactured from full thin walled circular cylinders, which were cut in half. Perforations were then added afterwards, while the shell already had it's circular shape. The production of holes with the desired edge radius appeared to be impossible with the accuracy of the CNC-machine. Hence the holes had to be drilled manually, which was time consuming and therefore rather expensive. Although literature indicates that this edge radius is necessary to prevent edge tones [64, 65], two other shells featuring different porosities were employed without this edge radius. Budget constraints necessitated these shells to be pre-perforated sheets bent into the semicircular shape. This type of manufacture of the shells also necessitated a different fairing thickness than the first perforated shell.

All perforations are in a hexagonal pattern (illustrated in Figure 3.2), the straight line of holes in polar direction. Porosity of a plate with circular holes in a hexagonal

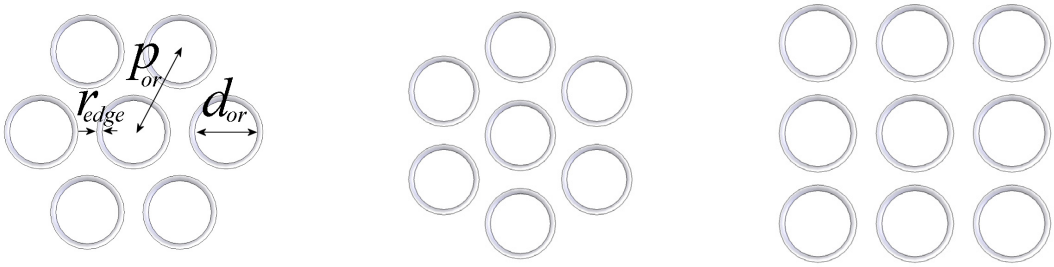

(a) Hexagonal with horizontal alignment

(b) Hexagonal with vertical alignment

(c) Square arrangement

FIGURE 3.2: Different hole arrangements

arrangement is governed by

$$\sigma = \frac{1}{6}\sqrt{3}\pi\left(\frac{d_{or}}{p_{or}}\right)^2 \quad . \tag{3.1}$$

When increasing porosity values at a constant hole diameter d_{or}, the small pitch p_{or} will create an unstable structure. Therefore a different hole diameter d_{or} is employed for the highest porosity shell. The perforations on the perf42 model do not cover the entire shell; this fairing has margins to its sides.

Pictures of the four different shells are shown in Figure 3.3. To determine the influence of perforation location, tape has been applied to the perforated shells. Tape is attached uniform in spanwise direction and symmetrical in radial direction with respect to the shell leading edge. In the current convention as defined in Figure 3.1, $\varphi = \pm 30\,^\circ$ means that $180 - 2 \times 30 = 120\,^\circ$ of the shell is covered with tape, while on the remaining area ($60\,^\circ$) the perforations are exposed to the flow. The exposed perforated area always includes the stagnation point and progresses from there. Hence $\varphi = 0\,^\circ$ is a fully taped model and $\varphi = \pm 90\,^\circ$ denotes full exposure of the perforations.

3.3.4 Experimental arrangement

Aerodynamic and acoustic measurements of the basic model are performed in the $3' \times 2'$, $7' \times 5'$ tunnel and an anechoic chamber respectively. The $3' \times 2'$ tunnel is solely used for flow measurements, while the $7' \times 5'$ tunnel is used for acoustic measurements and oil flow visualization. Acoustic measurements with microphones out of the flow were performed in the anechoic chamber. The arrangements in these facilities are discussed below.

FIGURE 3.3: Picture of the 4 different shells subject to experiments, from left to right: solid, perf33, perf42 and perf55.

3.3.4.1 $3' \times 2'$ tunnel

A schematic diagram of the $3' \times 2'$ tunnel (which actually measures 0.9 m by 0.6 m) is shown in Figure 3.4. Recently a 2 m extension has been added between

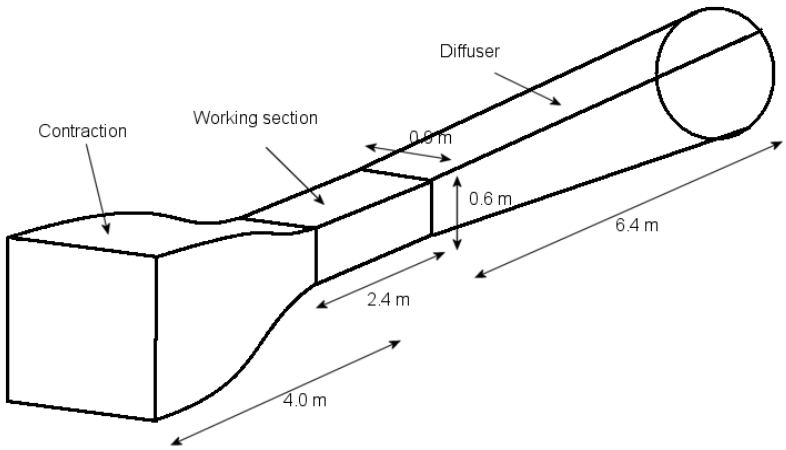

FIGURE 3.4: Schematic diagram of the $3' \times 2'$ tunnel.

original test section and diffuser. The fan is placed downstream of the working section which makes this a suction tunnel and adds the disadvantage of lower static pressure than atmospheric pressure in the working section. The maximum flow speed is $U_\infty = 30$ m/s, which results in a fairing Reynolds number around $Re_{D_f} = 3\times10^5$. The tunnel is easy to operate, seeding for PIV is not a problem and balance suspension underneath the floor is readily present. Disadvantage is the noisiness of this open circuit tunnel hampering acoustic measurements. The small hard walled test section acts as a reverberation chamber and therefore investigations in this tunnel will concentrate on the aerodynamics of the basic model.

Flow direction has been tested by using woollen tufts in [75] at unknown speed. Results were satisfactory and are not expected to change significantly with flow speed. Turbulence level between $U_\infty = 15$ m/s and $U_\infty = 30$ m/s has been reported in [76] to be around $Tu = 0.2$ %. The longitudinal pressure gradient caused by boundary layer growth is not regarded as important for the present experiment. Although there is no streamwise increase in test section area to compensate for this effect, pressure gradients have been at an acceptable level during previous experiments. A higher velocity (i.e. Reynolds number) 'flattens' the boundary layer which means longitudinal pressure gradients become even less. Average thickness of the boundary layer for the velocity range between $U_\infty = 15$ m/s and $U_\infty = 30$ m/s has been reported to be around $\delta = 20$ mm [77] at model location.

Flow speed is regulated by a manual operated frequency controller varying fan speed. This fan speed is set to give a constant pressure difference over the contraction. Flow speed is measured with a pitot-static tube, located upstream at $(x/D_f, y/D_f, z/D_f) = (-6.56, 1.41, 0.89)$ (refer to Figure 3.5 for coordinate system). The two tubes are connected to a Furness Controls FC012 digital micromanometer with a range of 199 mmH20 and a claimed accuracy of $\pm0.5\%$. The output of the micromanometer is read by a data acquisition computer after converting the signal using an AD-converter. By inputting atmospheric parameters (temperature, pressure and humidity), the pressure difference from the micromanometer is converted to velocity using Labview based software.

Test set-up The model is placed vertically in the 0.9 m × 0.6 m working section, resulting in a blockage of 17% based on frontal area. A visualization of the setup in the $3' \times 2'$ tunnel is shown in Figure 3.5. A right-handed Cartesian axis system originating in the model center is used to describe tunnel positions, as illustrated in Figure 3.5. In order to create a nominally two-dimensional flow, interference

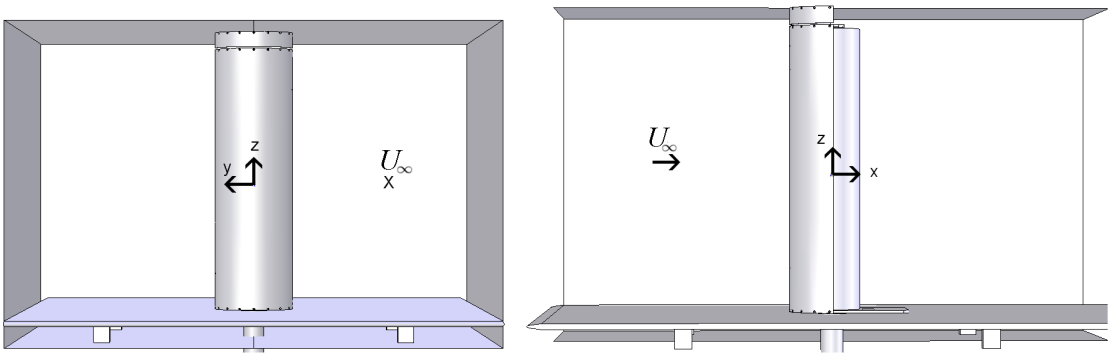

(a) Front view (b) Side view

FIGURE 3.5: Test set-up in the $3' \times 2'$ tunnel.

between model and the approximately 20 mm thick tunnel boundary layer must be prevented. A 20 mm thick flat plate (located 30 mm above the tunnel floor) is used. The plate has a rounded leading edge to prevent separation. A 12 mm wide roughness strip of 120 Grit Carborandum is used to trip the boundary layer 50 mm from the leading edge of the plate. Suspending a similar plate to the ceiling is more difficult, blocks the camera view for acquisition of PIV data and hampers traversing the hot wire. Therefore a 30 mm dummy section of the shell is used to create a similar blockage and to prevent the actual model to be contaminated with the ceiling boundary layer for eventual balance measurements. For both the groundplate and the dummy section, a small air gap of approximately 3 mm is present between them and the model brackets.

To aid suspension of the model, a 40 mm diameter solid aluminium bar is screwed in the model which can be suspended to a balance below the tunnel. Both ground plate and tunnel floor have a 50 mm diameter hole in them to enable the strut to pass through below. To prevent contamination of balance measurements, a thin aluminium sheet shrouds the bar between tunnel floor and groundplate. For more details the reader is referred to the drawings in appendix B.

3.3.4.2 $7' \times 5'$ tunnel

Acoustic measurements are performed in the $7' \times 5'$ wind tunnel, using the 2.1 m wide, 1.7 m high octagonal cross section (high speed section). The wind tunnel is a closed circuit and maximum flow speed is $U_\infty = 45$ m/s for relatively low blockage models, limiting the fairing Reynolds number to $Re_{D_f} = 4 \times 10^5$. The tunnel and its flow quality are described by Davies [78]. When originally built, the turbulence level was reported at less than Tu=0.1However, the validity of this

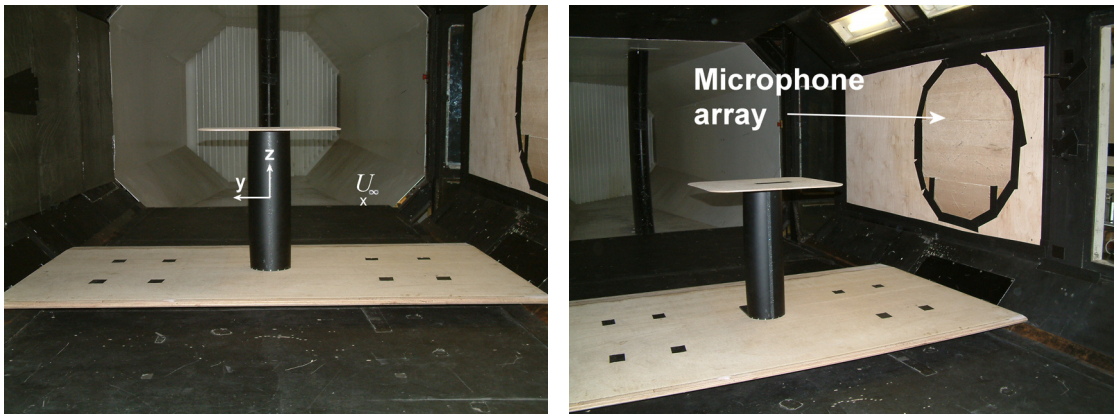

(a) Front view (b) Angled view

FIGURE 3.6: Test set-up in the $7' \times 5'$ tunnel.

report can be questioned since modification to screens over the years might have influenced turbulence levels and flow direction. The turning vanes that aid in cornering the tunnel flow are known to produce a distinct tone close to $f = 1000$ Hz at velocities close to $U_\infty = 30$ m/s depending on model blockage. This tone is audible in the control room, illustrating its loudness. Although the test section is considerably larger than the $3' \times 2'$ tunnel and reverberations are less significant, the background noise levels of the tunnel make acoustic measurements a challenge.

Test set-up The model is placed vertically on a 25 mm thick plywood ground-plate just above the tunnel floor, see Figure 3.6. Since there was no intention to perform balance measurements in this tunnel, there is no air gap present between model and ground plate. The plate is bolted onto two metal bars spanning the width of the tunnel. The length of the plate is 1150 mm and the width is 1750 mm, spanning the tunnel at a height of 60 mm above the tunnel floor. The ground-plate has a smoothed leading edge and thin (approximately 2 mm thick) trailing edge, to prevent much noise coming from the plate itself. To obtain a nominally two-dimensional flow, an endplate is present on the top end of the model. The plate is a 500 mm rectangle with edges rounded off, the plate center coinciding with the model center at this spanwise location. A larger endplate would prevent free propagation of sound waves from the model to the microphone array located in the tunnel side wall. The tunnel ceiling and one port side wall (opposite of the microphone array) are lined with foam to attempt to reduce reverberations inside the tunnel. Blockage ratio is 2.5%, based on model frontal area over tunnel empty cross section.

Similar to the $3' \times 2'$ tunnel, a coordinate system can be defined originating in the

model center as indicated in Figure 3.6(a). The x-coordinate is zero in the strut center and positive pointing in downstream direction. Flow speed is measured by a pitot-static tube, located upstream at $(x/D_f, y/D_f, z/D_f)$ = (-9.70, 6.56, 4.79). The dynamic pressure is measured by a Setra Model 239 pressure transducer with a range of 1.25×10^3 Pa and a quoted accuracy of 0.14% of this range. This gives a maximum uncertainty in the freestream velocity of ± 0.07 m/s at $U_\infty = 20$ m/s after input of tunnel temperature and pressure.

3.3.4.3 Anechoic chamber

Acoustic measurements with microphones placed out of the flow are performed in the large anechoic chamber at ISVR[79]. The bare chamber dimensions (without wedges) are 9.15 m × 9.15 m × 7.32 m, giving a volume of 611 m^3. The wall lining consists of over 8000 non-flammable glass-fibre cored wedges, extending 910 mm from the walls, floor and ceiling. Free-field conditions exist at frequencies above 80 Hz. A grid of floor panels (designed for minimum interference with the anechoic nature of the chamber, see Figure 3.7(b)) is mounted just above the tip of the floor wedges in order to rest the test set-up and facilitate access to the test rig.

The airstream is provided by a nozzle connected to a compressed air tank through piping as illustrated in Figure 3.7. More details about this configuration can be found in [5]. The nozzle has a contraction ratio of 10:1 and a rectangular exit of 500 mm high and 350 mm wide. Maximum achievable freestream velocity at the nozzle exit is $U_\infty = 45$ m/s, but since there is a limit to the compressed air this velocity can be maintained only for a short period of time (less than 30 s).

Test set-up The model was suspended horizontally in front of the nozzle exit using rigid steel struts that are bolted to the floor panels, depicted in Figure 3.8. Section 3.3.1 readily explained that for the anechoic chamber tests, an H-beam has been used as a strut next to the cylindrical strut used for the wind tunnel measurements. Similar to the wind tunnels, a coordinate system can be defined originating in the model center as shown in Figure 3.8(a). The x-coordinate is in streamwise direction (positive pointing downstream), the y-coordinate in transverse and the z-coordinate in spanwise direction. The nozzle exit is located in the yz plane at $x/D_f = -1.67$, while the nozzle center in the yz plane coincides with the model center at $y/D_f = 0$ and $z/D_f = 0$.

As shown in the Figure, endplates were constructed flush with the sides of the

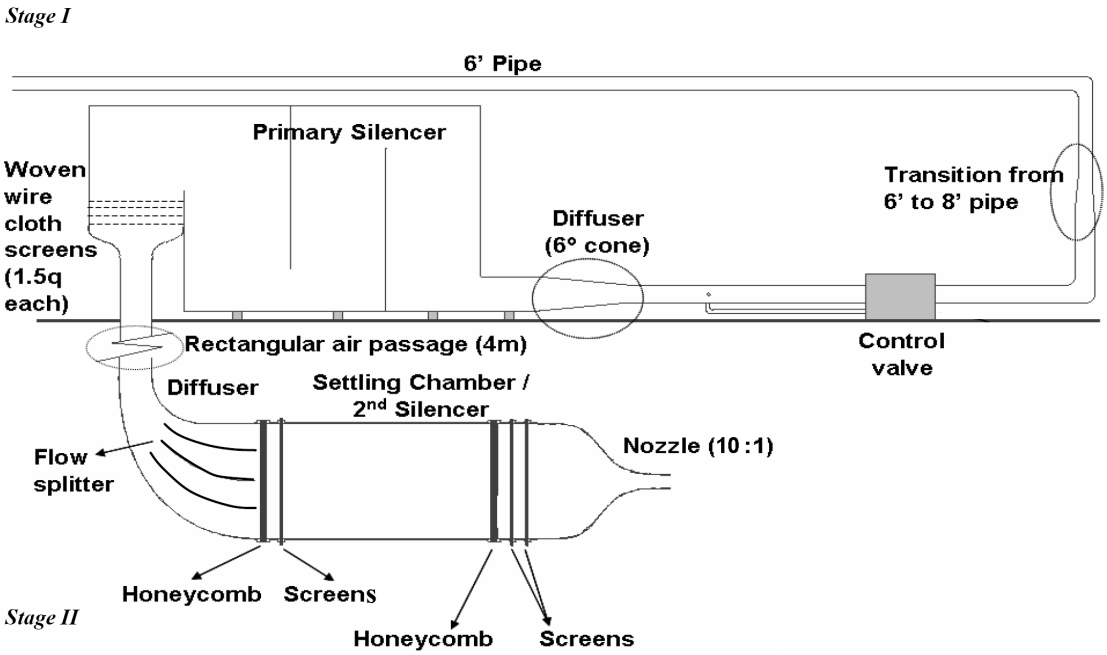

(a) Schematic of air supply

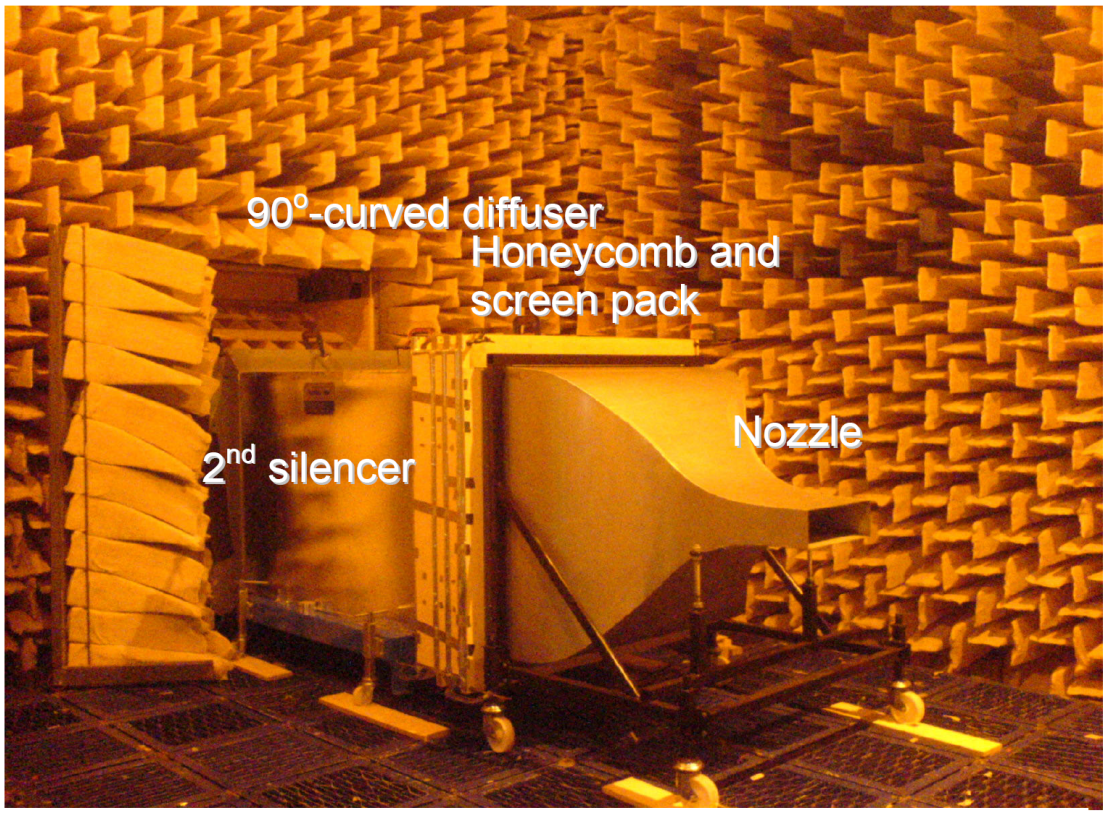

(b) Silencer and nozzle (different contraction from present nozzle) in the chamber

FIGURE 3.7: Air supply and nozzle in the anechoic chamber, taken from [5].

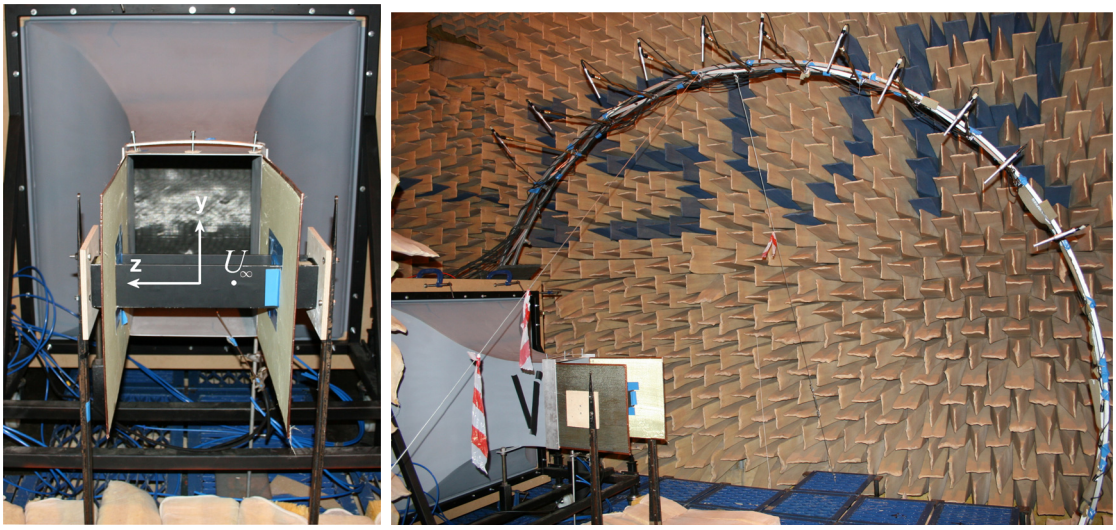

(a) Model suspension and location (b) Placement of the microphone arc

FIGURE 3.8: Test set-up in the anechoic chamber.

nozzle in order to prevent the jet from spreading in the spanwise direction and enforce nominally two-dimensional flow behavior. Holes were cut out in the endplates to facilitate placement of the 514 mm spanwise length of the model between the plates. Hence only the 350 mm spanwise length of the model fitted between the endplates was washed by the airflow. Tape was applied to prevent air leakage at the interface between endplate and model. The size of the endplates was cut to nozzle height and extended 850 mm in streamwise direction amounting to an endplate size of $3.28D_f \times 5.58D_f$.

Freestream velocity is measured by a pitot-static tube located at the nozzle exit, at a location of $(x/D_f, y/D_f, z/D_f)$ = (-1.67, -1.21, 0.36). The dynamic pressure is measured by a Comark C9551 pressure meter with a range of 14000 Pa and a quoted accuracy of 0.2% of this range. This gives a maximum uncertainty in the freestream velocity of ± 0.05 m/s at $U_\infty = 40$ m/s after input of temperature and pressure.

3.3.5 Apparatus

3.3.5.1 Oil flow visualization

A mixture of titanium dioxide, paraffin and oleic acid is used for oil flow visualization of both shell and strut of the basic model. A black background color is needed to be able to distinguish flow features. The shells readily have this color, the cylinder is covered with black self-adhesive plastic to fulfill this requirement.

The oil is transported along surface streaklines leaving an image of the time-averaged flow field after it has dried. Flow direction and separation are typical phenomena observed with this technique[80]. However, near to separation lines the oil may pile up to form a steep ramp affecting separation position[81]. The streakline pattern at separation lines depends on the initial condition due to the building up of the oil. In practice this means the pattern is dependent on how much oil was applied. Usually the built up oil leaves a line upstream of the actual separation line.

The flow pattern was photographed using a standard digital camera (FUJIFILM FinePix S602Zoom), with the model still present in the tunnel as removing it would disturb the flow pattern. To facilitate application of the oil and taking pictures, the visualization is performed in the more convenient environment of the $7' \times 5'$ tunnel.

3.3.5.2 Particle Image Velocimetry

Particle Image Velocimetry (PIV) was used to obtain information about the velocity field in an xy-plane at the model center. Readers unknown with the basic working principles of PIV are referred to the book by Raffel[82]. Measurements were performed using a Dantec FlowMap system. A 120 mJ Nd:YAG dual-cavity laser was fixed on a table to the side of the $3' \times 2'$ tunnel, shining through a perspex side window and illuminating a streamwise plane (xy-plane) halfway across the model. A water-based seed generator positioned outside the tunnel in front of the contraction was used to seed the flow. An 80C60 HiSense CCD camera (1280×1024 pixel resolution) was mounted on slides above the tunnel enabling a streamwise traverse. The camera looked through a 200 mm wide glass ceiling plate perpendicular to the laser sheet. Using a 24 mm lens, the image size of the planes was around 260x210 mm in the transverse and normal direction respectively. This necessitated 3 traverse positions of the camera to visualize $x/D_f \, \epsilon \, [-1.04, 2.15]$ with an overlap of around 15%. 500 image pairs were recorded per configuration. Time between recordings was kept constant at 0.5 s. The time between each pulse varied with flow speed in the order of 50 μs.

The images were post-processed using FlowManager software[83] provided by Dantec Dynamics. An adaptive correlation was performed with 2 refinement steps, starting with 128×128 and ending with 32×32 pixel interrogation area size. Vertical and horizontal overlap of the 2 images in each pair is set to 75%. Erroneous

vectors were removed using a range and peak validation and discarded vectors are substituted using interpolation. More information on the Dantec PIV-system and the post-processing methods can be found in [83]. The mean velocity field was obtained by averaging the 500 instantaneous vector maps.

Since the PIV resolves only the u- and v-components of velocity, the time averaged velocity magnitude u_t is defined here as

$$u_t = |\overline{\mathbf{u}}| = \sqrt{\overline{u}^2 + \overline{v}^2} \quad . \tag{3.2}$$

The RMS value of the x-velocity component fluctuations can be defined as

$$u'_{RMS} = \sqrt{\overline{u'^2}} = \sqrt{\overline{(u - \overline{u})^2}} = \mathrm{STDEV}(u) \quad , \tag{3.3}$$

and the same definition holds for the y-component v. For an impression of the total unsteadiness, values of u'_{RMS} and v'_{RMS} can be summed over the two dimensions yielding

$$u'_t = \sqrt{{u'_{RMS}}^2 + {v'_{RMS}}^2} \quad . \tag{3.4}$$

Uncertainty The accuracy of the instantaneous velocity fields can be estimated by assuming an accuracy in the correlation of 0.1 pixel displacement[82]. This corresponds to a maximum error in the velocity of 0.40 m/s. Using error analysis for multi-sample experiments as described by Moffat[84], the uncertainty in a time-averaged vector is 0.02 m/s.

3.3.5.3 Hot wire anemometry

A 2.5 μm diameter platinum-plated tungsten single wire was used as a sensor, supported in a cylindrical body. The body is suspended to a traverse post in the form of a 25 mm diameter metal rod, aligned in the vertical direction. The traverse moves through a slotted gap in the ceiling, sealed air-tight by a rubber strip. The gap permits the traverse to move along the span of the model (z-direction) and 200 mm in negative and positive y-direction. Streamwise (x-direction) traverse movement is facilitated by varying the position of the slotted ceiling panel. The traverse is supported by a framework mounted above the working section. A data acquisition computer drives stepper motors that feed lateral and spanwise traverse movement.

The probe was connected to a constant-temperature anemometer bridge circuit, manufactured by the University of Newcastle [76]. The output from the bridge was connected to an analogue to digital converter connected to a data acquisition computer. Labview based data acquisition software is used to document and control the hot wire measurements. To convert the voltage signal to velocity, a calibration was performed in an empty test section against the pitot-static tube. For more on the working principles of hot wire anemometry, the reader is referred to the book by Bruun[85]. The hot wire was aligned parallel to the z-direction. Therefore it reacted to the velocity components in the x- and y-directions. The measured magnitude of the velocity vector $|\mathbf{u}|$ thus consists solely of the u- and v-components, hence the time averaged velocity can be represented by equation 3.2. Since velocity fluctuations in the z-direction are expected to be largely absent outside the wake, these variables are accurately represented in this area.

In the wake region reversed flow and spanwise flow features complicate the measurements, and interpretation of absolute quantities should be avoided. This limits the wake data to interpretation of trends, since velocity magnitude is not believed to be represented accurately.

To inspect spectral characteristics of the velocity signal $|\mathbf{u}(t)|$, the Fast Fourier Transform (FFT) of $|\mathbf{u}(t)|$ is calculated. When the signal is sampled at f_s and T is the length of time of data acquisition (thus using $n = f_s \cdot T$ samples),

$$\mathrm{FFT}(|\mathbf{u}(t)|) = \int_0^T |\mathbf{u}(t)| e^{-i2\pi f t} dt \quad , \tag{3.5}$$

which is a discrete complex function of n frequencies, equally spaced with a resolution of $\Delta f = 1/T = f_s/n$. The Power Spectral Density (PSD) is then calculated using

$$\mathrm{PSD}(|\mathbf{u}(t)|) = |\mathrm{FFT}(|\mathbf{u}(t)|)|^2/n \quad , \tag{3.6}$$

and is a measure for the energy contained within each frequency band. Again this is a discrete function of n frequencies equally spaced at $1/T$. The integral of the PSD over f then yields the variance $\overline{|\mathbf{u}'(t)^2|} = \overline{|(\mathbf{u}(t) - \overline{\mathbf{u}(t)})^2|}$. Since the second half of the spectrum is redundant, values are plotted from $f = f_s/n$ till $f = f_s/2$. Current hot wire data are sampled at a rate of $f_s = 2000$ Hz and $n = 2048$, averaged over 75 blocks, giving a frequency resolution of $\Delta f = 0.98$ Hz. The frequencies in the PSD plots are made dimensionless using

$$Str_{D_f} = \frac{f D_f}{U_\infty} \quad . \tag{3.7}$$

Uncertainty The uncertainty of the hot wire measurements depends on a number of factors. The error estimation by Moffat[84] distinguishes fixed and variable sources, depending on whether the error it introduces is steady or changes during the time of one complete experiment. Employing this method, the fixed error consists of the accuracy of the calibration against the pitot-static tube and including the accuracy of the pitot tube itself this adds up to 0.20 m/s. Variable errors are estimated by comparing the mean values of the 75 acquired blocks. The average standard deviation at $U_\infty = 20$ m/s equals 0.35 m/s, indicating an uncertainty of 0.04 m/s for the 75 samples. Adding these values by calculating the root-sum-square[84] yields a total uncertainty in the velocity measurements of 0.21 m/s at $U_\infty = 20$ m/s. This value is valid outside the wake and shear layer. However, if the wire is traversed into reversed flow (wake) areas, the velocity magnitude of the measurements is not reflected accurately. A qualitative comparison of the velocity spectra is regarded as more suitable. The resolution of $\Delta f = 0.98$ Hz is a measure for the accuracy of frequencies of the velocity spectra.

3.3.5.4 Microphones

Two different sets of microphones were used in the $7' \times 5'$ wind tunnel and the anechoic chamber.

On-surface microphones The on-surface microphones used in the $7' \times 5'$ wind tunnel are Panasonic Omnidirectional Back Electret Condenser Cartridges, series WM-61A. The frequency response range of the cartridges is 20 Hz to 20 kHz. Since they are electret microphones, the signal was powered by preamplifiers built in-house.

The 6 mm diameter microphones were flush mounted at various positions on the strut. Numbering and location of microphones is illustrated in Figure 3.9. Microphones k1 to k6 are spaced equidistant in spanwise direction in the back face of the strut ($\varphi = 180\,^\circ$), while microphones k7 and k8 are located on the strut leading edge ($\varphi = 0\,^\circ$). Microphones k9 to k16 are spaced circumferentially around the strut with an increment of $\Delta\varphi = 20\,^\circ$. These microphones are also spaced apart in spanwise direction to prevent possible distortion of measurements by upstream placed microphones affecting the flow around the strut.

The data were sampled at a frequency of $f = 48$ kHz and a block size of $n = 16384$, averaged over 60 blocks, giving a resolution of $\Delta f = 2.93$ Hz.

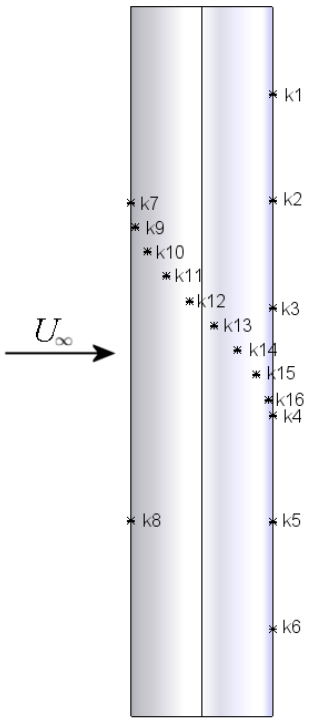

Microphone name	φ (°)	z-coordinate (mm)
k1	180	190
k2	180	114
k3	180	38
k4	180	-38
k5	180	-114
k6	180	-190
k7	0	114
k8	0	-114
k9	20	95
k10	40	78
k11	60	60
k12	80	43
k13	100	25
k14	120	8
k15	140	-10
k16	160	-27

FIGURE 3.9: Numbering and location of on-surface microphones on the strut.

Far field microphones For the anechoic chamber tests, Behringer ECM8000 omnidirectional electret microphones were used. Their response range is 15 Hz to 20 kHz and they are powered by two 8-Channel DIGIMAX FS preamplifiers, manufactured by PreSonus.

The microphones are suspended on a steel frame arc, placed 700 mm sideways from the xz-plane as depicted in Figure 3.8(b). Metal tube cross members enabled the microphones to be positioned in the xy-centerplane at z=0. The position of the microphones is summarized in Table 3.3. The angle is defined with respect to the model center, 90 ° right above the model and increasing from the upstream to the downstream quadrant. Using the linear scaling law of acoustic pressure with distance, data for all microphones were corrected to a distance of 2 m from the model center to enable comparison between individual microphones. The data were sampled at a frequency of $f = 44.1$ kHz and a block size of $n = 8192$, averaged over 60 blocks, giving a resolution of $\Delta f = 5.38$ Hz.

For both sets of microphones, analog to digital conversion was performed using a National Instruments' PXI-4472 24 bit data acquisition card, controlled by a PC using LabView software. Calibration was performed using a B&K pistonphone (type 4230) emitting a pure tone of 94 dB (1 Pa) at 995 Hz.

TABLE 3.3: Position of far field microphones.

Microphone number	Angle in xz-centerplane (°)	Distance from model center (mm)
1	56	1800
2	67	1730
3	83	1820
4	101	1830
5	110	1980
6	120	2050
7	130	2170
8	139	2200
9	150	2300
10	156	2340
11	166	2420

Using the calibration, the raw data in Volts were converted to instantaneous sound pressure $p'(t)$ and converted to SPL for each frequency band using

$$\mathrm{SPL}(f) = 20\log\frac{|\mathrm{FFT}(p'(t))|}{n \cdot p_{ref}} \quad , \tag{3.8}$$

where the reference pressure equals $p_{ref} = 2 \times 10^{-5}$ Pa. The dimension of this quantity is thus pressure per frequency band. The resulting narrowband spectra are useful especially for inspection of tonal noise features.

Using the narrowband spectra, 1/3-Octave band spectra can be calculated by summing the values over each passband. For 1/3-Octave bands, the spacing between upper (f_u) and lower frequency (f_l) of each band is defined by

$$f_u = 2^{1/3} f_l \quad , \tag{3.9}$$

and the center frequency of each tertsband, f_i, is the midpoint on a logarithmic scale, i.e.

$$log f_i = \frac{1}{2}[log f_u + log f_l] \quad \text{or} \quad f_i = \sqrt{f_u f_l} \quad . \tag{3.10}$$

In the present work, the 43 center frequencies between $f_i = 1.25$ Hz and $f_i = 20$ kHz as documented by Ruijgrok [26] were used.

Uncertainty The accuracy of the microphone measurements consists of many parts and is hard to estimate. The error due to the 24 bit finite resolution of the data acquisition hardware is negligible. The two sets of microphones used are both electrets with similar specifications, although the preamplifiers used are different. The pistonphone used to calibrate both sets of microphones is quoted to be accurate up to ±0.3 dB. For the Panasonics, an additional error is introduced since the microphone capsule doesn't have a perfect fit in the calibrator. Another source of error is the flat response over the frequency range assumed for the microphones. This assumption proved good enough for the present experiments after determination of the transfer function between a Panasonic and a calibrated 1/2" B&K microphone, both exposed to white noise.

Microphone levels are predominantly compared between different configurations (i.e. for the same microphone), discarding the importance of the fixed error. The variable error is estimated by comparing the values of the 60 acquired blocks and adds up to 0.5 dB for both sets of microphones, roughly constant for each frequency band.

3.3.5.5 Phased microphone array

The phased array used for the current experiment consists of 56 microphones, spirally placed in a circular wooden board with a diameter of 700 mm, flush with its surface. The array was placed in the starboard side wall of the wind tunnel, as visible on the right hand side of Figure 3.6(b). Because the microphones were placed flush with the tunnel wall, a porous cloth is fixed on the surface of the array board to reduce the impact of the noise due to the tunnel wall boundary layer. The distance between scan plane (model centre) and array is $6.9D_f$ in y-direction.

Microphones, data acquisition and microphone calibration were the same as for the on-surface microphone measurements in the $7' \times 5'$ wind tunnel. However sampling frequency is set to $f = 48$ kHz, block size $n = 4096$ and the data were averaged over 100 blocks. The beamforming code for the present experiments was written by Fenech [86] and is based on conventional frequency-domain beamforming. 1/3-Octave band averaged beamforming plots were calculated for comparison between configurations, however the finite aperture of the array prevented sufficient resolution for localization below 2 kHz. The scan plane used for calculation of the beamforming plots corresponds to the model side view, hence the xz-plane at $y = 0$. The absolute level of the contour plots is not physical, however the

difference in SPL between plots for the same frequency can be interpreted. For a more quantitative comparison between configurations, the levels of the beamforming plots were summed for each frequency band between $x/D_f = \pm 1.0$ and $z/D_f = \pm 1.7$ to give 1/3 Octave band averaged spectra. More details on the design of the array can be found in the report written by Fenech [86].

Uncertainty The fixed error of the beamforming plots and their integrated levels is not relevant since they are only used for a comparison between configurations. A rough estimate for the variable error is obtained from a comparison between two runs with identical configurations. This yields a maximum error of 1.5 dB for the beamforming plots and 0.45 dB for the integrated levels, which is believed to be on the boundary of acceptance.

3.4 Landing Gear Model Experiment

This section discusses the design of the landing gear model experiment. As highlighted in section 1.1, it was required to incorporate wind tunnel tests on a scaled landing gear model within the framework of the PhD. Firstly model aspects are addressed and then the experimental arrangement including wind tunnel and test set-up is highlighted. Finally, the measurement apparatus including it's uncertainty is discussed.

3.4.1 Model

As mentioned in section 1.1, the research focusses on application to a generic landing gear model, based on the A340 Main Landing Gear visualized in Figure 1.1. As driven by the industrial interests of Airbus the investigation was concentrated on the articulation link and undertray fairing. Therefore the components located above the articulation link such as the leg door are omitted. A visualization of the model compared to the operational gear is shown in Figure 3.10. Details on articulation, torque link and brake discs and links are accurately represented, although hoses are not present since these would be too difficult to manufacture. Further more the outside rim of the wheels are covered with hub caps, and tyre thread is omitted as requested by Airbus. The landing gear components are manufactured from metal except from the tyres which are made from carbon fibre impregnated

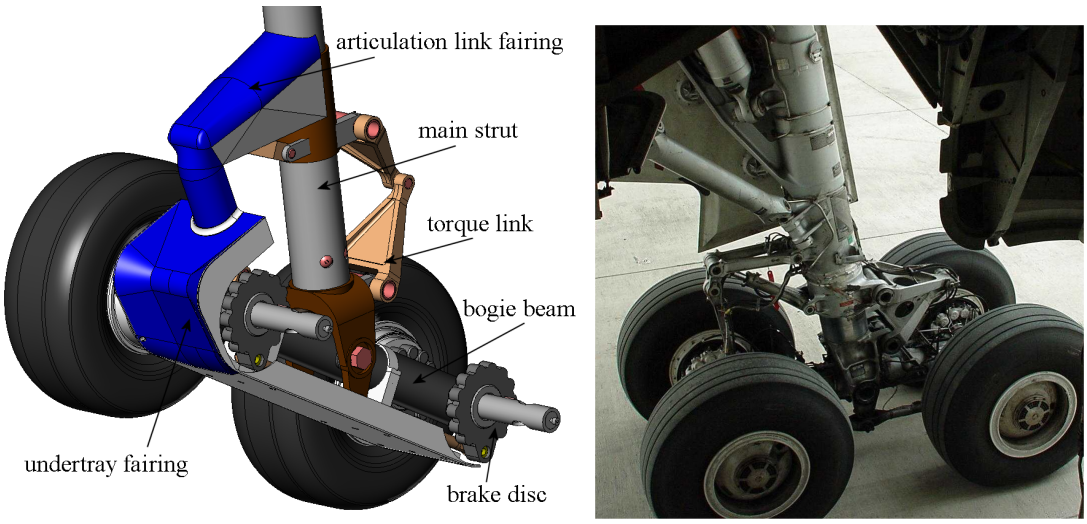

(a) Visualization of the landing gear model (2 wheels omitted for clarity)

(b) A340 MLG in operation

FIGURE 3.10: Landing gear wind tunnel model in comparison to the operational A340 gear.

with epoxy resin. For more details the reader is referred to the technical drawings of the model, enclosed in appendix C.

The size of the model is dictated by the experimental facility, which is the $7' \times 5'$ wind tunnel. The maximum flow speed of roughly 40 m/s against an approach flight speed of 80 m/s means twice the size of a real MLG is necessary to satisfy Reynolds number requirements. However, the largest size the tunnel can accommodate is dictated by blockage requirements. A 25% scale model has a blockage of 10% (with fairings on), which is regarded as a maximum for this test.

The fairings are a scaled copy of the fairings used in previous Airbus flyover tests [12, 13]. The shape of the fairings was predefined by Airbus and hence this parameter was not eligible for modifications. Manufacture of the perforated fairings has proven not to be an easy task. Perforated and solid metal sheets are bent into shape and welded together to form the desired fairing. This method requires a thin sheet with small diameter orifices to prevent a large portion of irregular truncated holes at the welding seems. For a measurable influence on flow and acoustics, engineering judgement dictates the porosity σ above 35 %. Bearing this in mind together with the commercial availability of the sheets has led to a 40% open area perforated sheet with a hole diameter d_{or} of 2 mm and pitch p_{or} of 3 mm. Following the basic experiment results, the location of the perforated subsurfaces is concentrated around the stagnation area. These surfaces are indicated by the blue color in Figure 3.10. A picture of the eventual model and fairings is shown in Figure 3.11. The drawings of the fairings are also included in appendix C.

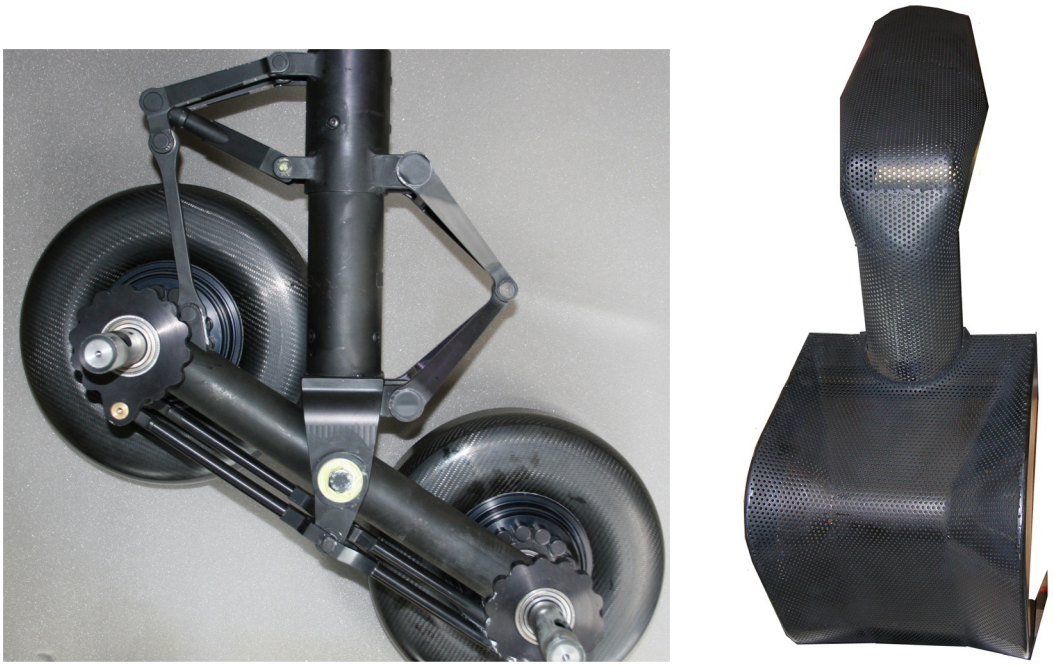

(a) Landing gear model (b) Landing gear model fairings

FIGURE 3.11: Plain landing gear model and fairings.

A parameter that has been given attention to following the basic model results (section 4.3.1) is the hole edge radius. Due to the punching process with which the perforations are created, one side of the sheet has a slight edge radius, while the other side has sharp edges. It was ascertained that the side with the edge radius is facing the flow. To give an estimate for the edge radius, a microscope is used to visualize the area of interest. Additionally, experiments involving high velocity impingement of sand on the sheet (various types of sandblasting) are performed to try and increase the hole edge radius. The results are shown in Figure 3.12. Based

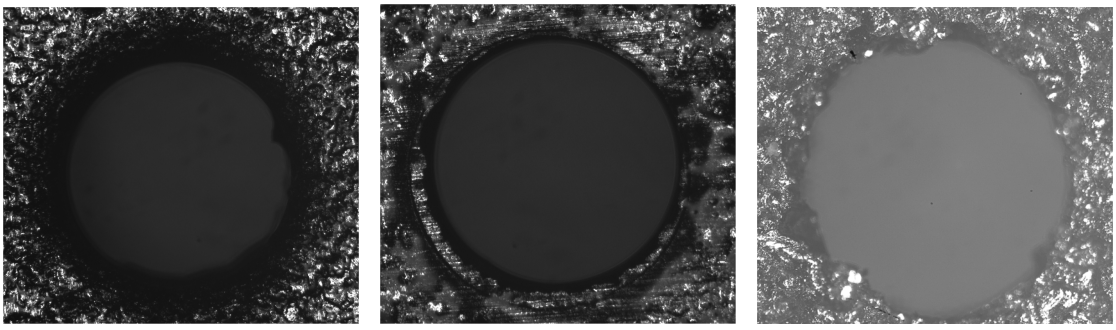

(a) Front of perforated sheet (b) Rear of perforated sheet (c) Front of perforated sheet after sandblasting

FIGURE 3.12: Microscope view of the perforated sheet (d_{or}=2 mm, p_{or}=3 mm).

on this Figure, the edge radius for holes at the front of the sheet is estimated to be roughly 8 % of the hole diameter d_{or}, while the rear side holes edges are confirmed

to be flat. Sand blasting of the sheet distorts the circle shape of the hole, but does not significantly increase the edge radius.

3.4.2 Experimental arrangement

As mentioned before, the facility for the landing gear model experiments is the $7' \times 5'$ wind tunnel. This facility is readily highlighted in section 3.3.4.2. The test set-up is described below.

3.4.2.1 Test set-up

The model is suspended from the port side tunnel side wall as depicted in Figure 3.13. A simplification compared to flight configuration is the fact that the wing

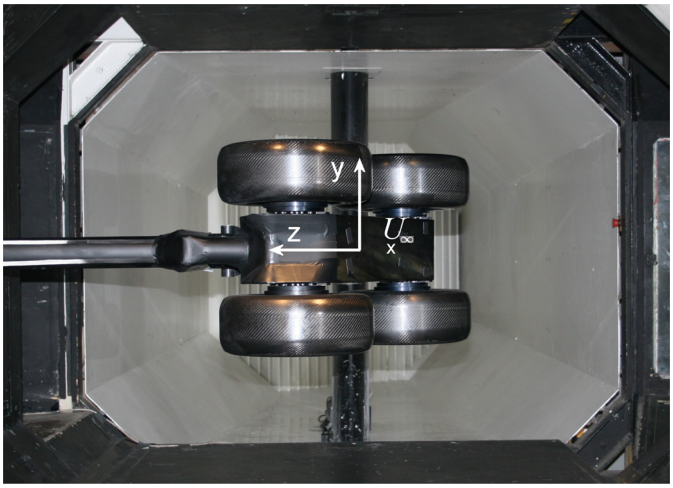

FIGURE 3.13: Model as suspended in the $7' \times 5'$ tunnel.

dihedral is not taken into account. The main landing gear deployed has the main strut in a vertical plain referenced to the aircraft, while the local wing surface is inclined upwards towards the wing tip. Therefore the angle between main strut and wing surface amounts up to 77.2 ° for the A340 MLG. This angle is discarded and the main leg is inclined perpendicular to the wind tunnel wall in this plane. Therefore the model and it's flow are symmetrical around the plane comprising of the main leg and bogie centerline.

During landing approach the aircraft typically operates at a 6.5 ° angle of attack with respect to the flow direction. Correcting for the local flow direction would result in an angle of 88 ° between the main leg and wind tunnel wall (main gear

leg inclined 2° backward). It is chosen to incline the main leg perpendicular to the wind tunnel wall in this plane, but correct for this angle by changing the angle of the bogie beam. Hence both in streamwise and transverse planes the main leg is inclined perpendicular to the tunnel wall. The angle between bogie beam and main leg is increased by 2° (55° to 57°) to achieve the 33° 'toe-up' angle of the bogie beam against the flow direction. A coordinate system can be defined originating in the center of the main strut-bogie beam junction. The x-coordinate is in streamwise direction, positive pointing downstream. The y- and z-coordinates are defined in Figure 3.13. During acoustic measurements, tunnel ground floor and port side wall are lined with foam to attempt to reduce reverberations inside the tunnel.

3.4.3 Apparatus

Most of the apparatus of landing gear model experiments has readily been used in the basic model experiments. Therefore section 3.3.5 can be used as a reference for the oil flow visualization. The extra clarification necessary for the remaining apparatus is given below.

3.4.3.1 Particle Image Velocimetry

The system as described in section 3.3.5.2 was used to obtain time averaged velocity contours in the xz-plane at the model center (y=0). Therefore the camera was positioned above a transparent part of the tunnel ceiling, looking down on the plane of interest. The laser is positioned outside the port side of the tunnel wall to illuminate a horizontal sheet (xz-plane) by firing through a small hole in the tunnel sidewall. The camera and laser were traversed in order to visualize the flow field upstream of the articulation link and the near wake downstream of the torque link and aft wheel. The acquisition parameters were the same as for the basic model experiment. An uncertainty analysis yields the same values as for the basic model experiment.

3.4.3.2 Pressure tappings

Static pressure was measured at various positions on the wheel surface. The location of the tappings are shown in Figure 3.14. In order to get a 360° centerline

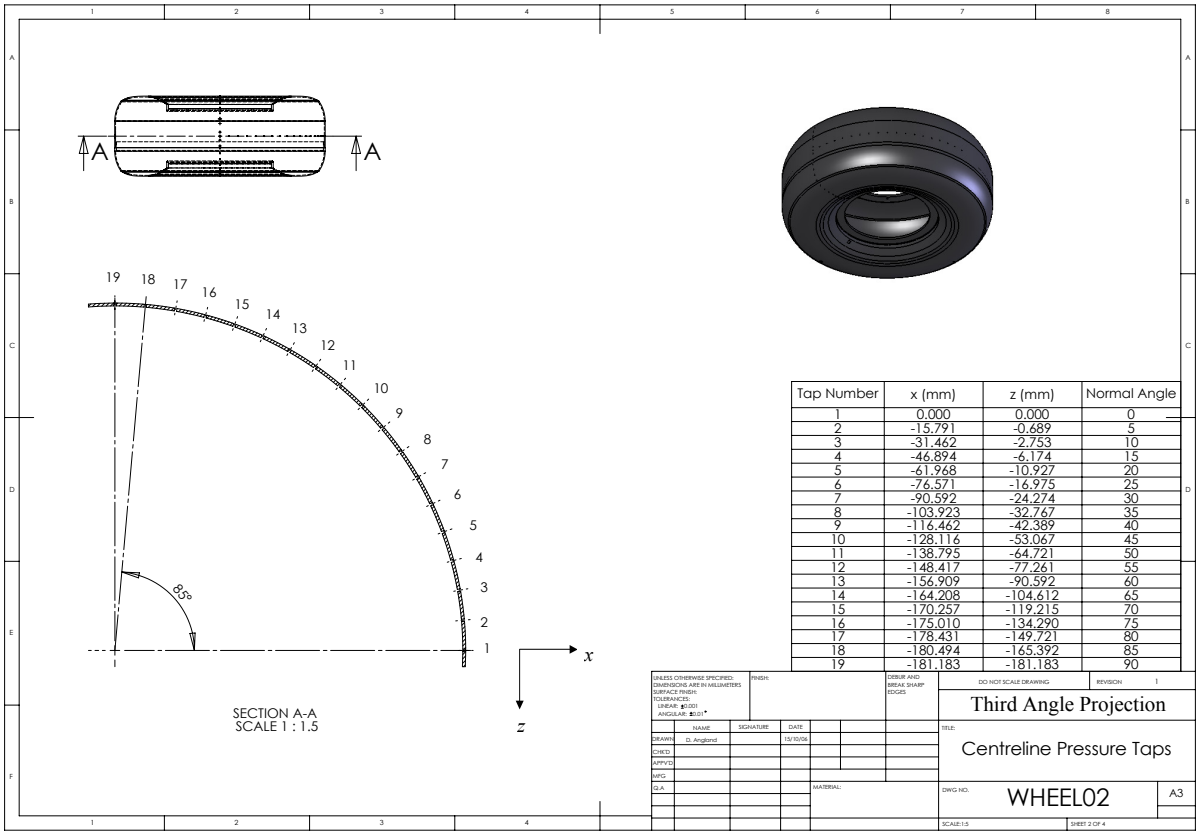

Tap Number	x (mm)	z (mm)	Normal Angle
1	0.000	0.000	0
2	-15.791	-0.689	5
3	-31.462	-2.753	10
4	-46.894	-6.174	15
5	-61.968	-10.927	20
6	-76.571	-16.975	25
7	-90.592	-24.274	30
8	-103.923	-32.767	35
9	-116.462	-42.389	40
10	-128.116	-53.067	45
11	-138.795	-64.721	50
12	-148.417	-77.261	55
13	-156.909	-90.592	60
14	-164.208	-104.612	65
15	-170.257	-119.215	70
16	-175.010	-134.290	75
17	-178.431	-149.721	80
18	-180.494	-165.392	85
19	-181.183	-181.183	90

UNLESS OTHERWISE SPECIFIED: DIMENSIONS ARE IN MILLIMETERS SURFACE FINISH: TOLERANCES: LINEAR: ±0.01 ANGULAR: ±0.01°
FINISH:
DEBUR AND BREAK SHARP EDGES
DO NOT SCALE DRAWING
REVISION 1
Third Angle Projection
TITLE: Centreline Pressure Taps
DWG NO. WHEEL02
A3
SCALE:1:5
SHEET 2 OF 4

	NAME	SIGNATURE	DATE
DRAWN	D. Angland		15/10/06
CHK'D			
APP'V'D			
MFG			
Q.A.			
MATERIAL:			

(a) Centerline pressure taps

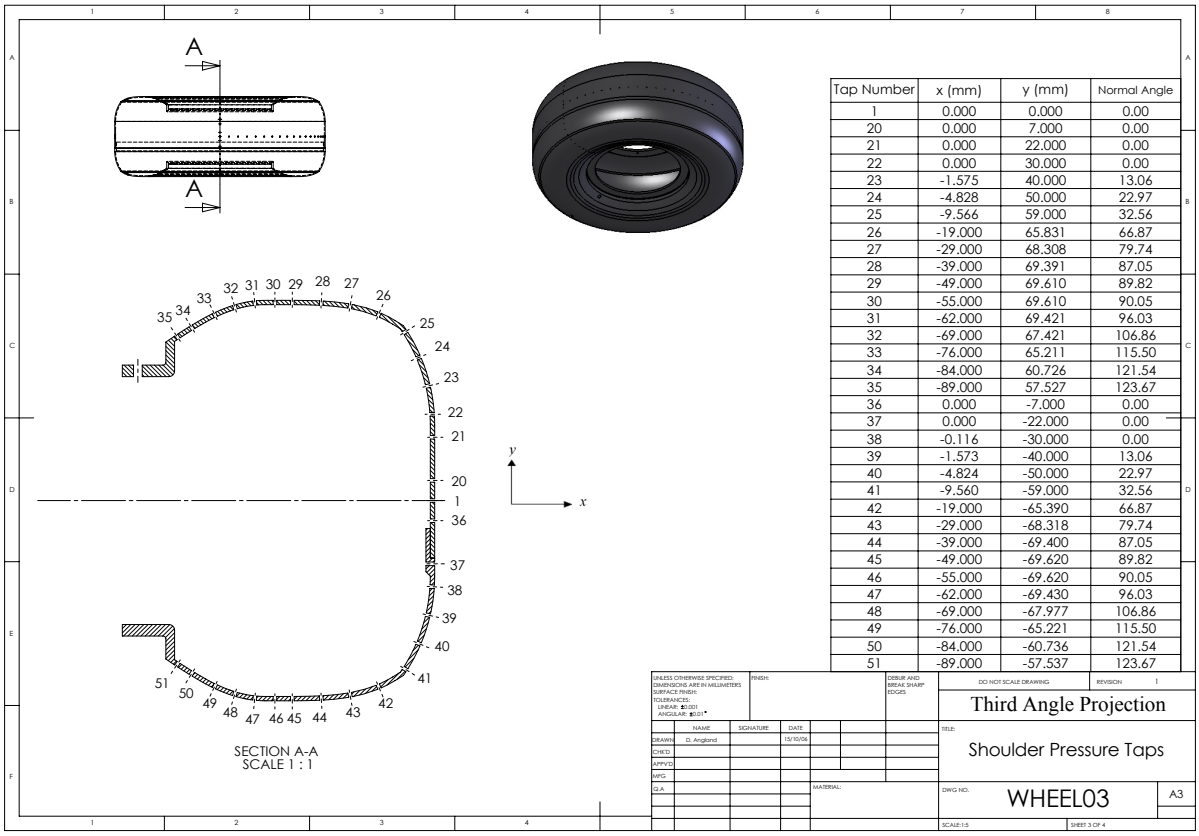

Tap Number	x (mm)	y (mm)	Normal Angle
1	0.000	0.000	0.00
20	0.000	7.000	0.00
21	0.000	22.000	0.00
22	0.000	30.000	0.00
23	-1.575	40.000	13.06
24	-4.828	50.000	22.97
25	-9.566	59.000	32.56
26	-19.000	65.831	66.87
27	-29.000	68.308	79.74
28	-39.000	69.391	87.05
29	-49.000	69.610	89.82
30	-55.000	69.610	90.05
31	-62.000	69.421	96.03
32	-69.000	67.421	106.86
33	-76.000	65.211	115.50
34	-84.000	60.726	121.54
35	-89.000	57.527	123.67
36	0.000	-7.000	0.00
37	0.000	-22.000	0.00
38	-0.116	-30.000	0.00
39	-1.573	-40.000	13.06
40	-4.824	-50.000	22.97
41	-9.560	-59.000	32.56
42	-19.000	-65.390	66.87
43	-29.000	-68.318	79.74
44	-39.000	-69.400	87.05
45	-49.000	-69.620	89.82
46	-55.000	-69.620	90.05
47	-62.000	-69.430	96.03
48	-69.000	-67.977	106.86
49	-76.000	-65.221	115.50
50	-84.000	-60.736	121.54
51	-89.000	-57.537	123.67

UNLESS OTHERWISE SPECIFIED: DIMENSIONS ARE IN MILLIMETERS SURFACE FINISH: TOLERANCES: LINEAR: ±0.01 ANGULAR: ±0.01°
FINISH:
DEBUR AND BREAK SHARP EDGES
DO NOT SCALE DRAWING
REVISION 1
Third Angle Projection
TITLE: Shoulder Pressure Taps
DWG NO. WHEEL03
A3
SCALE:1:5
SHEET 3 OF 4

	NAME	SIGNATURE	DATE
DRAWN	D. Angland		15/10/06
CHK'D			
APP'V'D			
MFG			
Q.A.			
MATERIAL:			

(b) Shoulder pressure taps

FIGURE 3.14: Location of pressure taps on the wheel

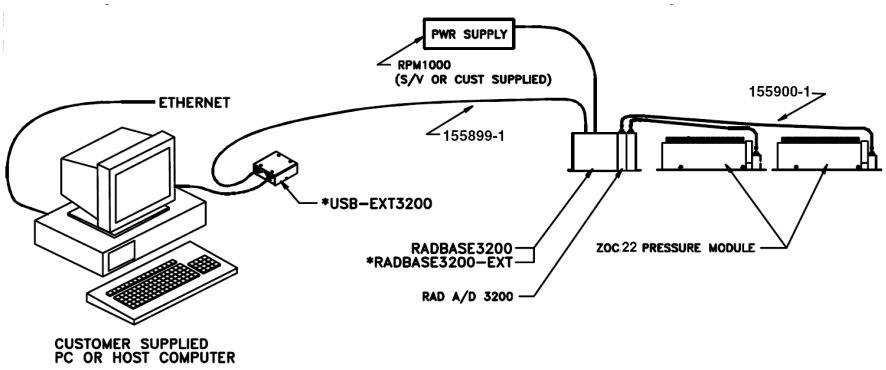

FIGURE 3.15: Visualization of the measurement set-up for the ZOC, taken from Scanivalve website.

pressure distribution, the wheel is rotated in 4 steps of 90 ° increment. The rotation of the wheel in steps of 90 ° increment yields 4 locations for measurement of the shoulder taps. Since the model is inclined parallel to the streamwise xz-plane, left and right wheels should yield identical pressure distributions. Therefore only the pressures on the front and rear wheels located in the half space with positive y-coordinate (see Figure 3.13) are measured.

The total of 51 taps are connected to a Scanivalve ZOC22B/32PxX2 - 20' H20 pressure scanner via tubing inside the wheel. The measurement setup is visualized in Figure 3.15. The ZOC module inside the wheel contains piezoresistive pressure sensors (capable of measuring up to 64 channels) and a pressure scanner temperature sensor. This data is then digitized in the RADBASE3200 and passed to the PC for temperature corrected unit conversion. Using the internal calibration, the system readily gives a pressure output and an individual calibration is not deemed necessary.

The normalized pressure coefficient can be defined as

$$Cp = \frac{p - p_\infty}{0.5\rho {U_\infty}^2} \quad , \tag{3.11}$$

where p_∞ is the static pressure of the tunnel pitot-static tube and ρ is derived from barometer and temperature readings in the tunnel using the ideal gas law. Since the reference pressure of the recording instrumentation is connected to the static pressure port of the tunnel pitot-static tube, the output is a measure for $p - p_\infty$.

In each frame, the channels are sampled at a rate of 50 μs and averaged over 32 samples. For each run, 50 frames of data are acquired and averaged to obtain time averaged pressure. To minimize the influence of drifting of the signal, a zero run

was performed before each measurement, which was subtracted before conversion to Cp values.

Uncertainty The fixed error consists of the accuracy of the data acquisition system and it's calibration. Scanivalve claims an accuracy of the current system of $\pm 0.12\%$ of the full scale range, which converts into $\Delta Cp = \pm 0.006$ at $U_\infty = 40$m/s. The variable error is estimated by comparing the values of the 50 frames. The average standard deviation at $U_\infty = 40$ m/s equals 0.013, indicating an uncertainty of 0.002 for the 50 frames. Therefore the total uncertainty adds up to 0.006 at this velocity.

3.4.3.3 Unsteady pressure sensors

Unsteady pressure sensors have been placed on various positions flush with the gear surface. For the present test, sensors have been placed in positions 1, 4 and 5 indicated in Figure 3.16. Additionally 2 sensors have been placed on the wheel

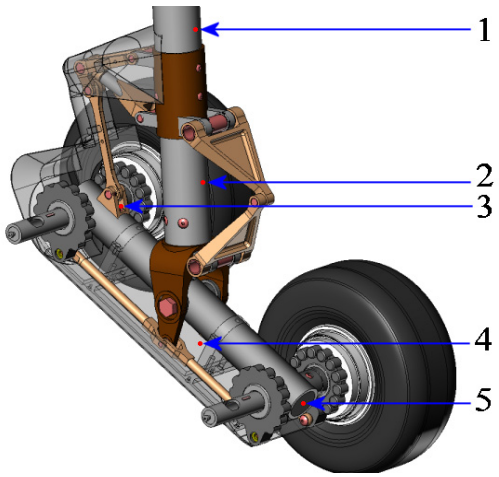

Nr	Location	x (mm)	y (mm)	z (mm)
1	Main leg (upper)	40	0	460
2	Main leg (lower)	40	0	213
3	Bogie-artlink junction	-143	0	136
4	Undertray surface (facing down)	40	0	-129
5	Rear bogie cap	237	0	-154

FIGURE 3.16: Pressure sensor locations.

centerline, spaced $\Delta\varphi = 180\,^\circ$ apart. Both front and rear wheel are rotated in 4 steps to obtain unsteady centerline pressures around the wheel circumference spaced $\Delta\varphi = 45\,^\circ$ apart using the 2 sensors.

The reference tubes of the pressure sensors are connected to the static pressure from the tunnel pitot-static tube, enabling real time measurement of the fluctuating surface pressure. The sensors used are 2.4 mm diameter Kulite XCQ-093 sensors with a range of 0.35 bar and a natural frequency of 150 kHz. They are powered by a 8 channel VISHAY model 2150 strain gauge amplifier. As for the

microphones, analog to digital conversion was performed using a National Instruments' PXI-4472 24 bit data acquisition card, controlled by a PC using LabView software.

To convert the output voltage to pressure units, a calibration was performed using a Druck DPI 601-F pressure calibrator for each individual Kulite, assuming a linear relationship between voltage and pressure.

To minimize the influence of drifting of the signal, a zero run was performed before each measurement, which was subtracted before conversion to Cp values. The data were sampled at a frequency of $f = 24$ kHz and a block size of $n = 16384$, averaged over 100 blocks, giving a resolution of $\Delta f = 1.46$ Hz. Equation 3.11 was used to convert the pressures to Cp values with input from barometer and temperature readings in the tunnel documented for each run.

Uncertainty The fixed error consists of the accuracy of the sensors and the calibration. The quoted accuracy of the calibrator is $\pm 0.05\%$ of it's 0.5 bar range. The typical error of the Kulites due to combined non-linearity, hysteresis and repeatability is quoted at 0.1% of the 0.35 bar range. These combined figures add up to a fixed error of $\Delta Cp = \pm 0.04$ at a freestream velocity of $U_\infty = 40$ m/s.

The variable error is estimated by comparing the average values of the 100 blocks. For the time averaged pressure, the average standard deviation at $U_\infty = 40$ m/s equals 0.008, indicating an uncertainty of 0.0008 for the 100 blocks. For the time averaged value of Cp at $U_\infty = 40$ m/s, this yields a total uncertainty of ± 0.04.

3.4.3.4 Microphones

Various microphones have been placed on the model (flush with its surface). Referring to Figure 3.16, location 1,2,3 and 5 have been instrumented. Microphones, powering, data acquisition and calibration are identical to the on-surface microphone measurements on the basic model, hence the reader is referred to section 3.3.5.4 for more details.

3.4.3.5 Phased microphone array

Two similar phased arrays are positioned in the starboard side wall and the ceiling of the $7' \times 5'$ wind tunnel. They both consist of 56 microphones, spirally placed in

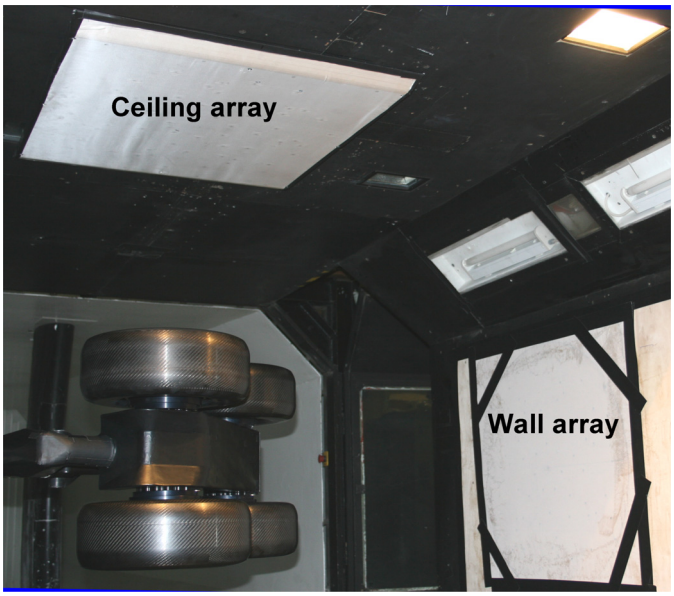

FIGURE 3.17: Set-up of microphone arrays in the $7' \times 5'$ tunnel.

a wooden board with a diameter of 700 mm, flush with its surface. The perpendicular distance between array and model center is 0.73 m for the ceiling array and 1.18 m for the side wall array. The different distance of the arrays to the model results in different resolution of the beamforming plot. Since the aperture of both arrays is the same and resolution varies linearly with distance, the side wall array resolution is 61% better than the ceiling array.

Setup and powering for both arrays is identical to the microphone array as described in section 3.3.5.5. The same holds for the data acquisition, which was done simultaneously for both arrays. However sampling frequency is set to $f = 48$ kHz, block size $n = 8192$ and the data were averaged over 120 blocks. The post-processing method is identical to the method described in section 3.3.5.5. However an attempt was made to reduce the influence of non-physical sidelobes on the beamforming plots by implementing an algorithm based on CLEAN-SC [87]. The effect was found to be minimal, except from a slight reduction (< 1 dB) in background noise level for the higher frequency beamforming plots. The computing effort for this algorithm was found to be significantly more time consuming ($> 50\%$ increase). Since for a quantitative comparison the 1/3-Octave band averaged beamforming plots are integrated over the source area, it was decided to postprocess using the conventional beamforming method [86].

The side view beamforming plots from the ceiling array are aligned in the xz-plane at y=0. However, the ground view plots from the side wall array are aligned with the bogie beam and rotated by 33° going through the model origin. For the

previously mentioned integration of the beamforming plots, squared pressures are summed between $x = \pm 0.2$ m and $z = -0.1$ m to $z = 0.3$ m for the ceiling array and between $x = -0.4$ m to $x = 0.3$ m and $y = \pm 0.15$ m for the side wall array. The uncertainty for both microphone arrays was found to be roughly the same as for the basic model array measurements (section 3.3.5.5).

Chapter 4

Basic Model Research

Flow and acoustics of the basic model featuring various configurations are investigated in this chapter. Firstly, time averaged flow behavior is researched. Since a two-dimensional RANS simulation is believed to provide a good qualitative image of the time averaged flow features, experimental results are complimented with results from a computational simulation. Following the research on the mean flow behavior, the influence of the various configurations on vortex shedding behavior is presented. Several high frequency noise features of the basic model are discussed thereafter.

4.1 Time-averaged Flow Features

4.1.1 On surface

An oil flow visualization was carried out as explained in section 3.3.5.1. The only shells suitable used for the visualization are the solid and the perf42($\pm 45\,^{\circ}$) shell, since the perf33 and perf55 shells are fully covered by the perforations. Entrapment of air bubbles while wrapping the black plastic cover around the curved strut surface resulted in surface irregularities. Holes for microphone positioning further distort the image. Therefore flow visualization on the strut (model rear view) should be interpreted with care, owing to influence of these surface irregularities on the flow field.

Pictures of flow visualization on the model front and rear are shown in Figure 4.1. The front views reveal two-dimensional flow behavior and attached flow for both

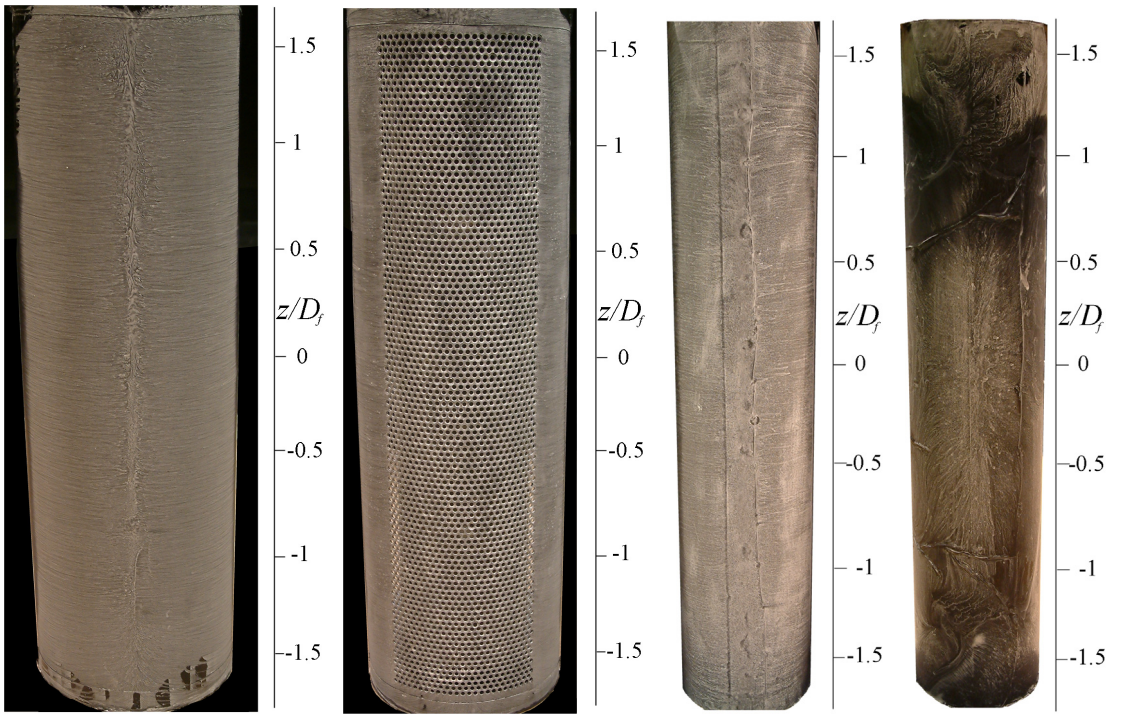

(a) solid+cylinder, front view of shell

(b) perf42(±45 °)+cylinder, front view of shell

(c) solid+cylinder, rear view of strut

(d) perf42(±45 °)+cylinder, rear view of strut

FIGURE 4.1: Front and rear view of basic model oil flow visualization ($U_\infty = 40$ m/s).

the solid and the perf42(±45 °) configuration. The stagnation line is clearly visible for the solid configuration and uniform in the spanwise direction. However, spanwise directed streaklines are visible close to the model ends dictated by junction flow phenomena (horseshoe vortices).

The rear views in Figure 4.1(c) and 4.1(d) reveal more of a difference between the configurations. A chaotic non-symmetrical structure is visible for the perf42(±45 °) configuration. Low near wake velocities without spanwise coherence are believed to be the cause for this random pattern. Additionally, the low velocities make the path of the oil susceptible for the earlier mentioned surface irregularities and gravity. The solid configuration shows a clear pattern with two-dimensional streaklines, uniform in spanwise direction. A strong vortex shedding mechanism with high reversed flow velocities on the rear of the strut instead of a random wake can explain the resulting pattern.

The visualization of the side view of the two different shells is depicted in Figure 4.2. For both configurations, separation occurs before the shell trailing edge, at an angular position of roughly $\varphi = 85\,°$. The separation lines are reasonably uniform in the spanwise direction. Reversed flow phenomena are visible aft of the

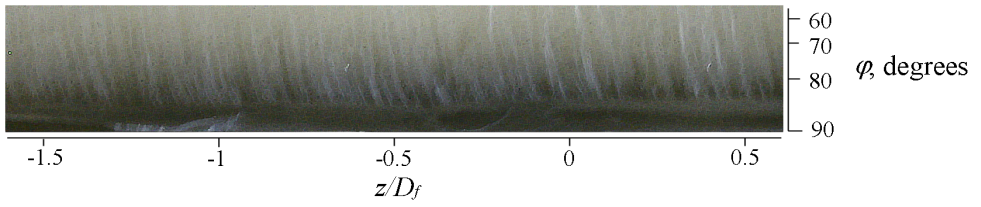

(a) solid+cylinder

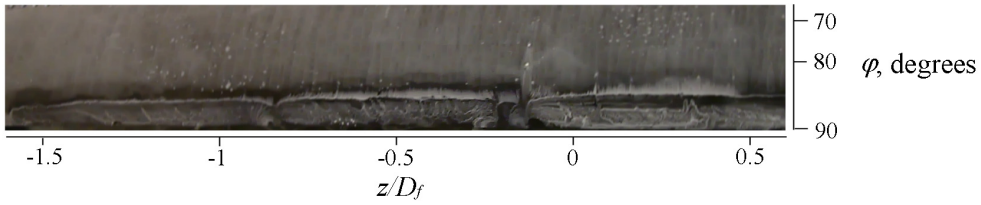

(b) perf42 (±45 °)+cylinder

FIGURE 4.2: Side view of basic model oil flow visualization at the shell trailing edge ($U_\infty = 40$ m/s, flow from top to bottom).

separation line, especially for the perf42(±45 °) configuration. For the solid configuration, the last 5 ° of the shell are mostly black, hardly showing the signature of the oil flow path. This points at strong shear sweeping the oil away in this region. A possible explanation conform with the model rear view visualization is the different nature of separation compared to the perf42(±45 °) configuration. A strong vortex shedding process involving a region of high shear could be responsible for sweeping away the oil. For the perf42(±45 °) configuration a similar coherent structure is absent, resulting in more conventional separation with low velocities as illustrated by the reversed flow pattern.

4.1.2 Off surface

Time averaged velocity contours obtained by PIV measurements in an xy plane at $z/D_f = 0$ are shown in Figure 4.3. A distinct stagnation point can be observed for the solid model in front of the shell ($x/D_f = -0.5, y/D_f = 0$). Aft of the shell trailing edge ($x/D_f = 0, y/D_f = -0.5$), a thin high gradient shear layer is present. The shear layer rapidly diffuses aft of the shell, thereby shortening the length of the wake downstream of the model. The time averaged streamlines clearly show the separated flow structure is related to the diameter of the shell.

For the perf42 model, a clear stagnation point is not present due to the air passing through the perforate. The accelerated flow that emerges from between the shell and strut significantly alters the wake structure compared to the solid model.

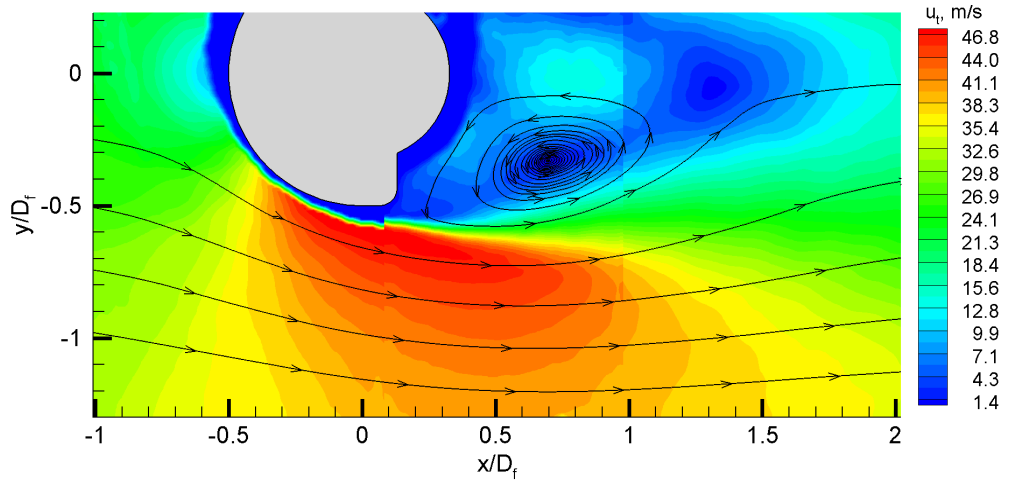

(a) solid+cylinder

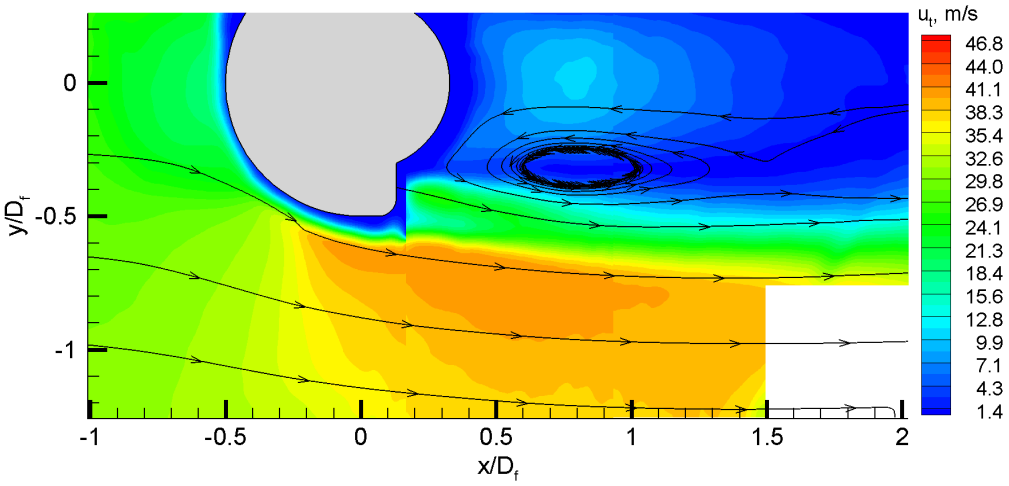

(b) perf42(±45 °)+cylinder

FIGURE 4.3: Time-averaged velocity contours and streamlines ($U_\infty = 30$ m/s, $z/D_f = 0$).

Two different shear layers relating to the strut and shell respectively merge and diffuse more slowly resulting in a downstream extended wake. The magnitude of the maximum velocity gradient relating to the shear layer is roughly 50% of the solid configuration. The time averaged streamlines indicate a smaller scale of the separated flow structure than the solid configuration.

The perf42 shell is the only perforated shell subject of PIV measurements, preventing a comparison of the time-averaged flow field between the different porosity shells. One could hypothesize that a large pressure drop over the shell results in the wake being pulled back towards the strut. According to Baines [2] the pressure drop over a flat plate scales with $1/\sigma^2$ and hence for larger porosities the wake size can be expected to increase. Hot wire measurements have been performed with the various porosity shells, indicating a similar wake structure (see also section 4.2.3).

However, a clear trend could not be discovered between the different porosities.

4.1.3 Deflected velocities

As visible from Figure 4.3(a), high speed velocities are deflected past the sides of the solid model, reaching values up to $u_t = 48.2$ m/s. The maximum value of deflected velocities is reduced by 18% for the perf42($\pm 45\,^\circ$) configuration in Figure 4.3(b). The maximum value of deflected velocities for different porosities is expected to be similar, based on a comparison between the time averaged flow fields of the perf33 and perf55 configuration obtained from CFD.

Slicing through the PIV-data at $x/D_f = 0.26$ yields Figure 4.4 and illustrates the different velocity profiles. For a comparison at this streamwise position, a

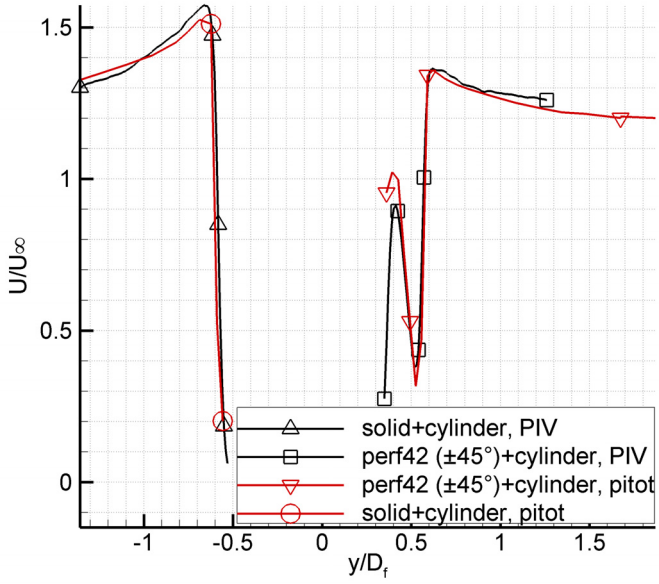

FIGURE 4.4: Lateral traverse of non-dimensional velocity in streamwise direction using pitot and PIV data ($U_\infty = 20$ m/s, $x/D_f = 0.26, z/D_f = 0$).

pitot-static tube is attached to the traverse post used for hot wire measurements (discussed in section 3.3.5.3). There is good agreement between PIV and pitot measurements, acting as a validation for the presented data.

Although the maximum deflected velocities are less for the perforated shell, the downstream extended wake prevents the flow spreading out in the lateral direction. As a consequence, the high velocity region to the side of the strut extends further downstream. Therefore velocity magnitudes for the perf42 shell at $x/D_f > 1.25$ and $y/D_f < -0.6$ exceed the values for the solid shell.

4.1.4 Bled mass flux

A rough estimate for the bled mass flux through the perforate can be obtained by integrating the velocity of the jet that results from the acceleration between the shell and strut. In Figure 4.4 the jet is represented by the hump between $y/D_f = 0.3$ and $y/D_f = 0.5$. Neglecting the small lateral velocity component in the jet, the bled mass flux m_b referenced to the freestream flux based on the frontal area of the perforated part of the shell can be defined as

$$m_b = \frac{\int_j u dy}{U_\infty D_f \sin\varphi} \quad , \tag{4.1}$$

where φ represents the angular exposure as defined in Figure 3.1 and the subscript j indicates integration over the jet area. Based on equation 4.1, the bled mass flux equals $m_b = 32\%$ for the perf42($\pm 45\,^\circ$) configuration.

It is the pressure difference between the upstream and downstream side of the shell that drives the flow through the perforate. Exposing the suction side of the shell ($\varphi > 45\,^\circ$) is therefore expected to bleed less or no flow depending on the pressure variation on the downstream side of the shell. Unfortunately experimental verification of this theory is hampered by the fact that only the perf42 and the solid shell have been the subject of PIV experiments. Therefore a two-dimensional computational study using the RANS equations to simulate the flow around a cross section of the basic model is employed. For more details on settings (e.g. grid, computational methods) of these simulations, the reader is referred to appendix A. The integrated bled mass fluxes for the various configurations are summarized in Figure 4.5. As expected, the bled mass flux follows a linear trend with varying porosity. Both the perf33 and perf55 shell have been run with $\varphi = \pm 45\,^\circ$ and $\varphi = \pm 90\,^\circ$ exposure. The coincidence of the different degrees of exposure for both cases indicates that exposing more than $\varphi = \pm 45\,^\circ$ does not yield additional bleeding.

Another observation regards the influence of hole edge radius on the bled air. From the literature review it appeared that application of an edge radius increases the vena contracta. A larger vena contracta implies a larger effective opening for each orifice and hence the bled air for the perf42 ($\pm 45\,^\circ$) case equals that for the *perf48* ($\pm 45\,^\circ$) case. Quantitatively, application of an edge radius of $r_{edge}/d_{or} = 0.14$ increases the effective porosity by 14%. Further more, the relative difference between the bled mass flux m_b obtained by PIV and CFD for the perf42($\pm 45\,^\circ$) configuration is 7%.

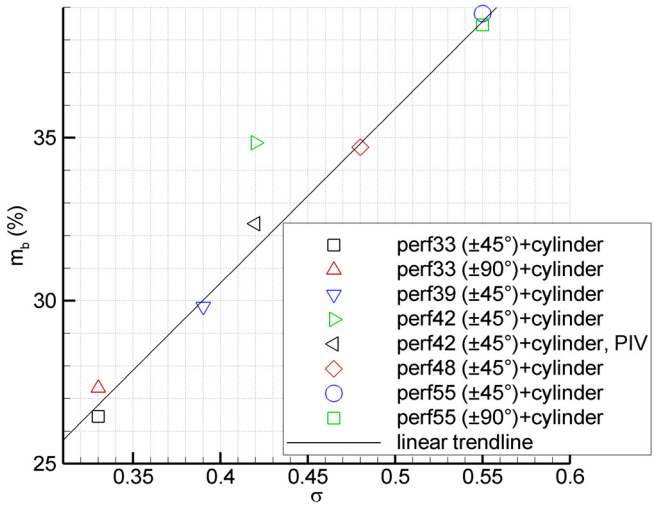

FIGURE 4.5: Bled mass flux m_b for different configurations obtained by CFD ($U_\infty = 30$ m/s).

4.1.5 Perforate flow

Flow physics around the perforate is investigated using CFD. A closer look at the flow field around holes with an edge radius is shown in Figure 4.6. The

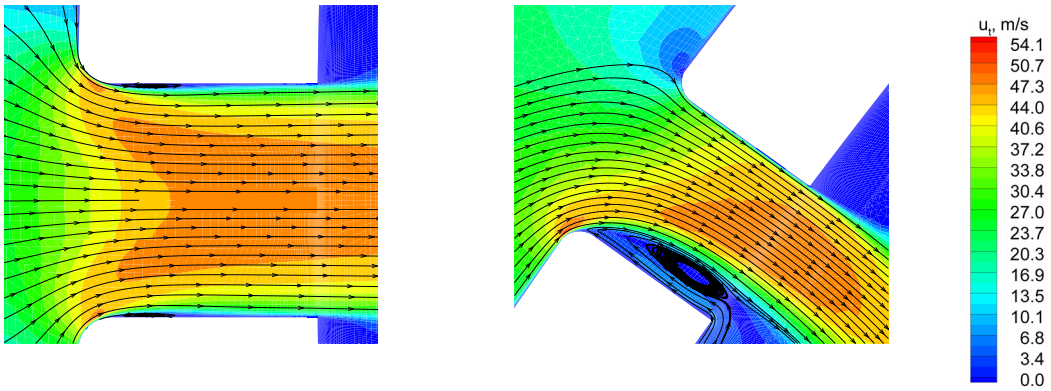

(a) center hole, $\varphi = 0\,^\circ$ (b) most outer located hole, $\varphi = 45\,^\circ$

FIGURE 4.6: Time averaged velocity distribution and streamlines around orifices rounded off edges (perf42 ($\pm 45\,^\circ$)+cylinder, $U_\infty = 30$ m/s).

flow funnels through the perforate resulting in a maximum velocity of about 1.5 times U_∞. Separation bubbles are present at both locations due to high adverse pressure gradients after the flow has been accelerated around the small edge radius. Shearing flow at $\varphi = 45\,^\circ$ increases the size of the separation bubbles and reduces the mass flow through the perforate.

Flow through sharp edged perforates is illustrated in Figure 4.7. At locations close

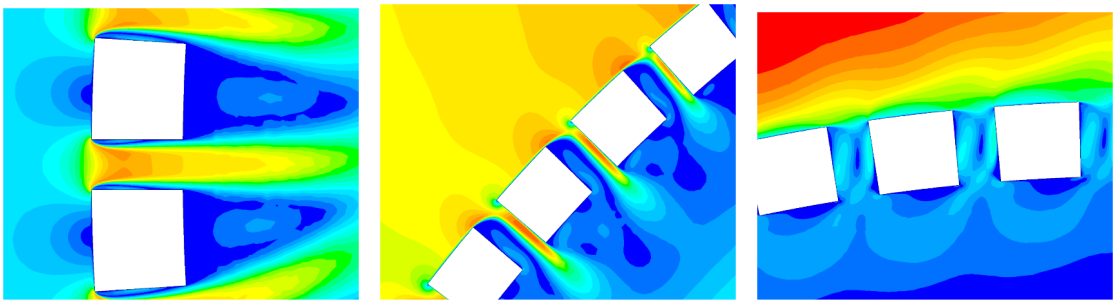

(a) $\varphi = 0\,^\circ$ (b) $\varphi = 45\,^\circ$ (c) $\varphi = 90\,^\circ$

FIGURE 4.7: Time averaged velocity distribution around sharp edged orifices (perf33 ($\pm 45\,^\circ$)+cylinder, $U_\infty = 30$ m/s, legend in Figure 4.6).

to $\varphi = 0\,^\circ$ there is a separate stagnation point for each hole as illustrated in Figure 4.7(a). At an angular position of $45\,^\circ$, flow separates from the hole leading edge and is forced in by the opposite side of the holes. This results in a narrow high velocity regime close to this side of the holes. This regime is less narrow if an edge radius is applied (Figure 4.6(b)), bending the flow around the corner. The effect of the sharp edges is thus to increase the separation pocket size and thereby reduce the vena contracta resulting in less bled air through the perforate as discussed in the previous section.

At an angular position close to the shell trailing edge (Figure 4.7(c)), the flow does not pass smoothly past the perforate. The boundary layer at this position has a relatively large thickness of the order of the shell thickness (t_f). The velocity contours outside the shell appear to waver between the holes. Inspection of instantaneous vector plots reveals an outflow through the perforate at this location. Apparently, high flow velocities past the strut are responsible for pushing away air through the perforate, acting as a blowing mechanism on the shell surface. This effect is observed for both the perf33 ($\pm 90\,^\circ$) and the perf55 ($\pm 90\,^\circ$) models.

The flow downstream of a perforate can be represented by a number of jets that form independently and then gradually spread and coalesce with neighboring jets [2]. The perforate will deflect the flow towards the longitudinal axis of each orifice, hence towards the projected shell center. The fully mixed jets result in isotropic turbulence [2] impinging on the strut.

4.2 Vortex Shedding

Instantaneous plots of the vorticity field obtained by PIV-measurements clarify the unsteady flow field in Figure 4.8. The velocity vectors show the existence of

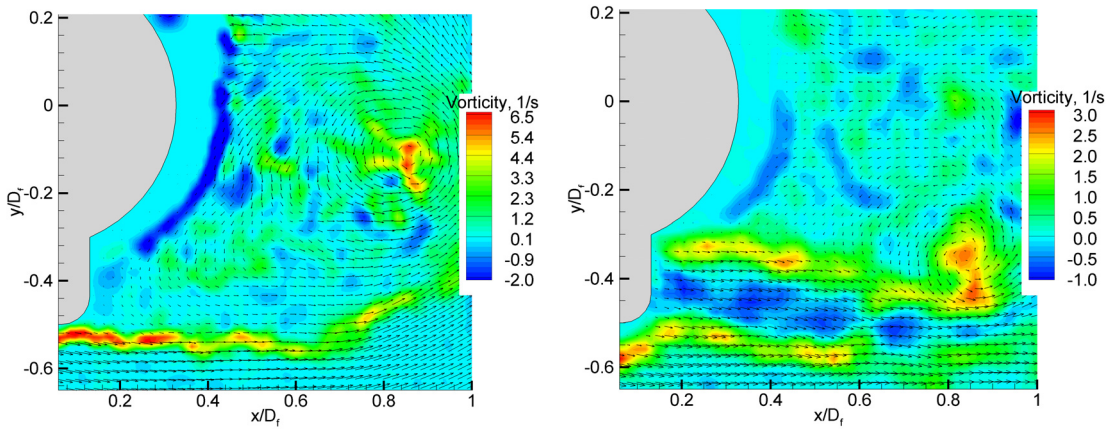

(a) solid+cylinder (b) perf42 (±45 °)+cylinder

FIGURE 4.8: Snapshots of vorticity combined with velocity vectors in the downstream region ($U_\infty = 30$ m/s, $z/D_f = 0$).

large vortex shedding for the solid model compared to a small vortex exhibiting approximately half the instantaneous vorticity value for the perf42 (±45 °) model. Turbulence statistics in the form of standard deviation of velocity in y-direction in Figure 4.9 agree with this observation. For the solid model, the two shear

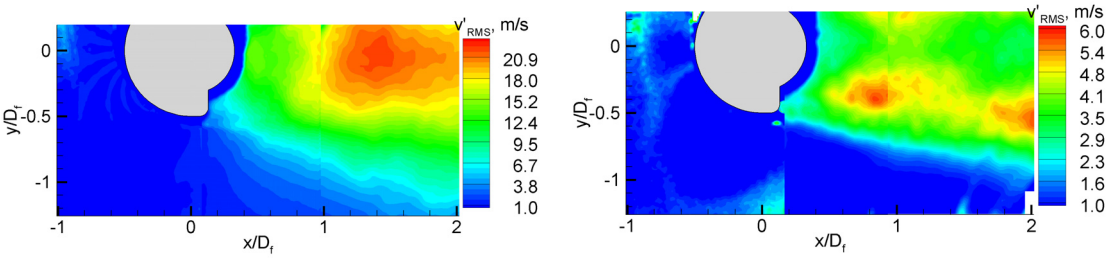

(a) solid+cylinder (b) perf42 (±45 °)+cylinder

FIGURE 4.9: Standard deviation of velocity in y-direction ($U_\infty = 30$ m/s, $z/D_f = 0$).

layers on the respective shell sides interact and roll up to result in high amplitude transverse velocity fluctuations peaking on the centerline of the wake ($y/D_f = 0$). The bled air through the perforate prevents the communication between both shear layers acting as a splitter plate and therefore this shedding does not take place. As a consequence, the transverse velocity fluctuations are of significantly lower amplitude and the maxima occur close to the shear layers instead of the centerline.

To investigate the spectral content of the unsteadiness, a hot wire is traversed in the wake of both models. Results of the traverse are shown in Figure 4.10. The

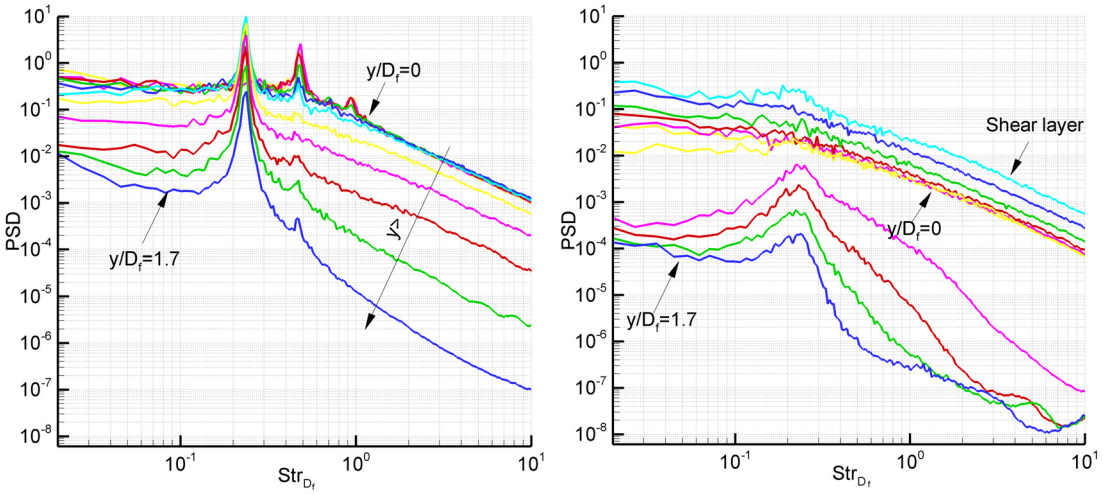

(a) solid+cylinder

(b) perf42 (±45 °)+cylinder

FIGURE 4.10: Transverse traverse of PSD of velocity ($U_\infty = 20$ m/s, $x/D_f = 1.44$ and $z/D_f = 0$).

wake area ($y/D_f = 0$) is characterized by a broadband spectrum, dominated by the breakdown of turbulence through the energy cascade. The side area ($y/D_f = 1.7$) is dominated by large scale velocity fluctuations associated with the shedding. Distinct peaks arise for the solid model, $Str_{D_f} = 0.24$ more pronounced laterally and $Str_{D_f} = 0.48$ more in the wake area. The first number is believed to correspond to the vortices being shed from the side of the shell. Because the shedding alternates between each side, double the frequency is more pronounced behind the strut. The dominant frequencies scale linearly with freestream velocity, conforming with the hypothesized nature of the fluctuations. The same traverse for the perf42 model yields a different graph. To the side a hump instead of a peak is present, indicating less distinct periodicity for this configuration. The fact that the dominant frequency is similar to the solid model indicates that this phenomenon is related to the shell instead of the strut. The level of the PSD is several magnitudes lower for the perforated shell. The largest values of the PSD are concentrated in the merged shear layers, agreeing with the PIV turbulence statistics.

The effect of the vortex shedding on the aerodynamic noise is investigated using on surface microphones and array measurements. 1/3 Octave band averaged spectra obtained from averaging microphone array beamforming plots are shown in Figure 4.11(a). A clear peak at $Str_{D_f} = 0.2$ arises for the solid shell (consistent for all velocities as shown in Figure 4.14(b)). The frequency is related to the vortex shedding from the shell as described above. The difference in Str_{D_f} opposed to the

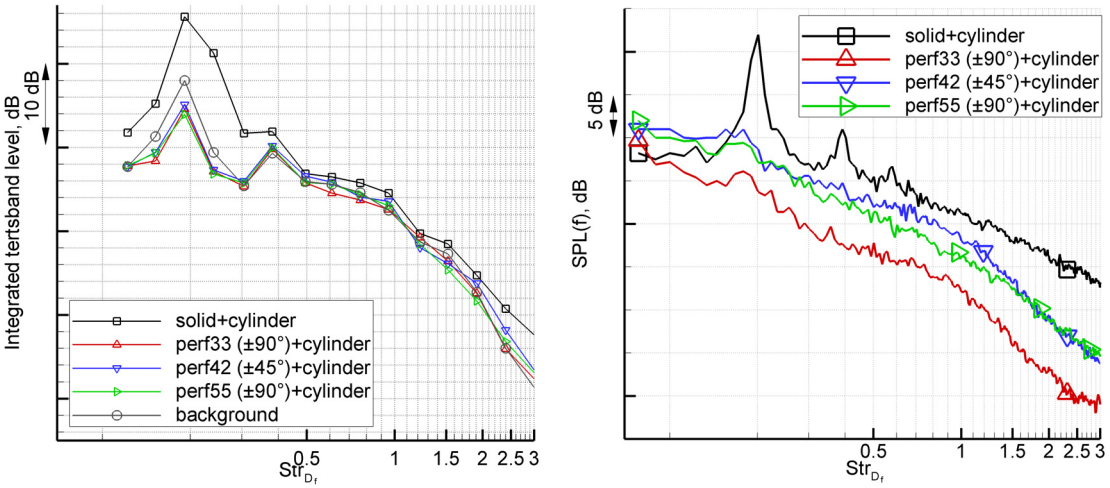

(a) Integrated 1/3 Octave band averaged beamforming plots ($x/D_f = \pm 1.0$ and $z/D_f = \pm 1.7$)

(b) Microphone k16 in the strut surface ($\varphi = 160\,°, z/D_f = -0.14$)

FIGURE 4.11: Measured acoustics in $7' \times 5'$ tunnel ($U_\infty = 40$ m/s).

dominant frequency of the velocity fluctuations from the hot wire measurements is attributed to the large blockage in the $3' \times 2'$ relative to the $7' \times 5'$ tunnel. The rest of the spectra hardly exceed tunnel empty noise and coincide in the displayed frequency range. The peaks visible in this part of the spectra are attributed to tunnel noise and scale with velocity as well.

Consistent with the microphone array are the data from on-surface microphone k16 in Figure 4.11(b). The vortex shedding peak appears for the solid model at the same Strouhal number Str_{D_f}. In agreement with the aerodynamic measurements, the application of perforations results in a breakdown of the periodic vortex shedding. The difference in level between the different perforate configurations in Figure 4.11(b) is caused by the difference in the local flow conditions in the proximity of the microphone.

As appeared in Figure 4.11, the quantification of vortex shedding noise in the wind tunnel is hampered by the high background noise levels and the impossibility of preventing flow impingement at the microphones. In order to quantify the vortex shedding noise and the effect of perforations, an anechoic chamber experiment is conducted as described in section 3.3.4.3. Results are shown in Figure 4.12 for both cylinder and H-beam as shielded objects. The distinct vortex shedding peaks for the solid and stand alone cylinder configurations are consistent with the wind tunnel measurements. Since the cylinder itself is not a noisy object, the level of the solid configuration exceeds the cylinder noise. As confirmed by wind tunnel measurements, the perforated fairing removes the spectral peak associated with the shedding. Additionally, the broadband noise level is reduced to below the

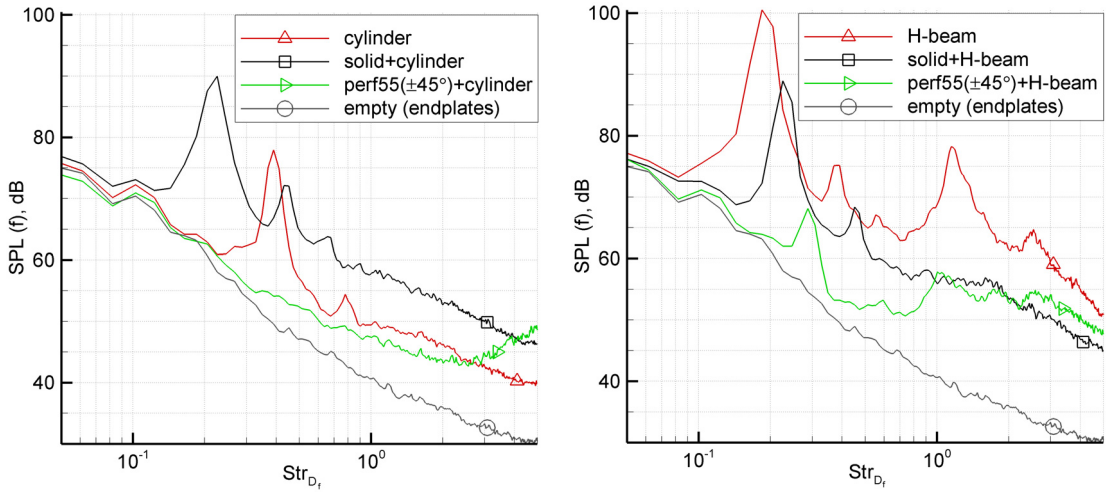

(a) Shielded cylinder

(b) Shielded H-beam

FIGURE 4.12: Measured acoustic in anechoic chamber (averaged over microphone 1 to 8, $d = 2$ m, $U_\infty = 40$ m/s).

cylinder noise.

Shielding the H-beam yields a different image, since this object features many sharp edges and a highly unaerodynamic shape. Therefore the H-beam unfaired configuration is far noisier than shielding the beam with the solid fairing. The spectrum shows two dominant spectral peaks at $Str_{D_f} = 0.18$ and $Str_{D_f} = 1.20$ that scale with velocity. A comparison of Figures 4.12(a) and 4.12(b) indicates that the noise signatures for the solid fairing shielding the cylinder or H-beam are nearly identical. Hence the noise in these cases is dominated by the large scale vortex shedding from the shell, independent of the shielded object. Application of perforations yields further noise decrease, most effectively for the lowest frequencies.

4.2.1 Reynolds number effects

The topology of two-dimensional bluff bodies is often compared to cylinder flow for which flow regimes are well documented [43] and summarized in section 2.5. The current wind tunnels limit the freestream velocity range between $U_\infty = 20$ m/s and $U_\infty = 40$ m/s, resulting in Reynolds numbers based on shell diameter D_f between $Re_{D_f} \epsilon [2 \times 10^5, 4 \times 10^5]$. In-flight Reynolds number will be approximately twice this value and hence in the supercritical regime. The proximity of Re_{D_f} to the critical Reynolds number for cylinder flow stresses the need for a sensitivity study on Reynolds number effects of the basic model.

4.2.1.1 Isolated cylinder

Firstly the flow around the isolated cylinder is investigated. Velocity traverses in the wake region $(x/D_f, y/D_f, z/D_f) = (1.44, 0, 0)$ are carried using hot wire apparatus. Results of the velocity traverse are shown in Figure 4.13(a). For the

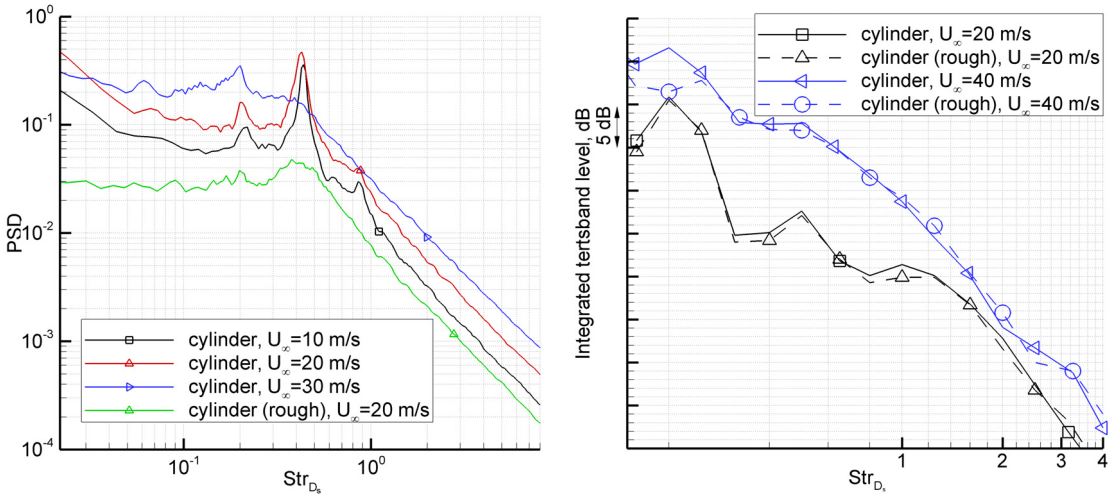

(a) hot wire, $x/D_f = 1.44$, $y/D_f = 0$, $z/D_f = 0$

(b) integrated 1/3 Octave band beamforming levels (integrated between $x/D_f = \pm 1.0$ and $z/D_f = \pm 1.7$)

FIGURE 4.13: Velocity traverse of isolated cylinder.

hot wire traverse, distinct peaks are present at $Str_{D_s} = 0.21$ and $Str_{D_s} = 0.42$ (Strouhal number is based on cylinder diameter D_s), except at $U_\infty = 30$ m/s. The absence of the distinct peak for $U_\infty = 30$ m/s indicates transition to the supercritical flow regime occurs before this velocity. Application of roughness strips is shown to artificially force transition to the supercritical regime. The roughness strips used consist of 12 mm wide double sided tape with 120 Grit Carborandum applied to one side. The *rough* configuration features two strips at $\varphi = \pm 45\,°$, applied uniform in the spanwise direction. The microphone array data in Figure 4.13(b) is taken in the $7' \times 5'$ tunnel, implying different flow conditions compared to the hot wire data, which influence transition phenomena. At $U_\infty = 20$ m/s, a distinct peak corresponding to the shedding arises at $Str_{D_s} = 0.20$ for both the clean and rough configurations. At $U_\infty = 40$ m/s however the peak is less distinct and the application of roughness strips reduces the maximum of the hump by a further 5 dB. Although the periodicity that causes the peak has disappeared at this velocity, the broadband levels of the clean and rough configurations coincide above $Str_{D_s} = 0.20$.

The above study illustrates the well-known transition phenomena for circular cylinders and it's sensitivity to roughness and turbulence level. For the basic model,

application of a porous shell yields flow around the downstream positioned cylinder. Since in that case the downstream cylinder is washed by turbulent airflow bled by the perforated fairing, transition effects are not expected to make their appearance.

4.2.1.2 Shells

A half-cylindrical shell is expected to exhibit a more fixed separation point, owing to the position of the shell trailing edge at $\varphi = \pm 90\,^\circ$. However, Figure 4.2 has shown separation to occur before the shell trailing edge at $\varphi \approx 85\,^\circ$. For the solid configuration, oil flow visualization at different freestream velocities ($U_\infty = 20$ m/s and $U_\infty = 40$ m/s) indicated no difference in separation point and pattern. A velocity traverse using both hot wire and microphones confirms these observations in Figure 4.14. Figure 4.14(a) shows that even application of roughness strips

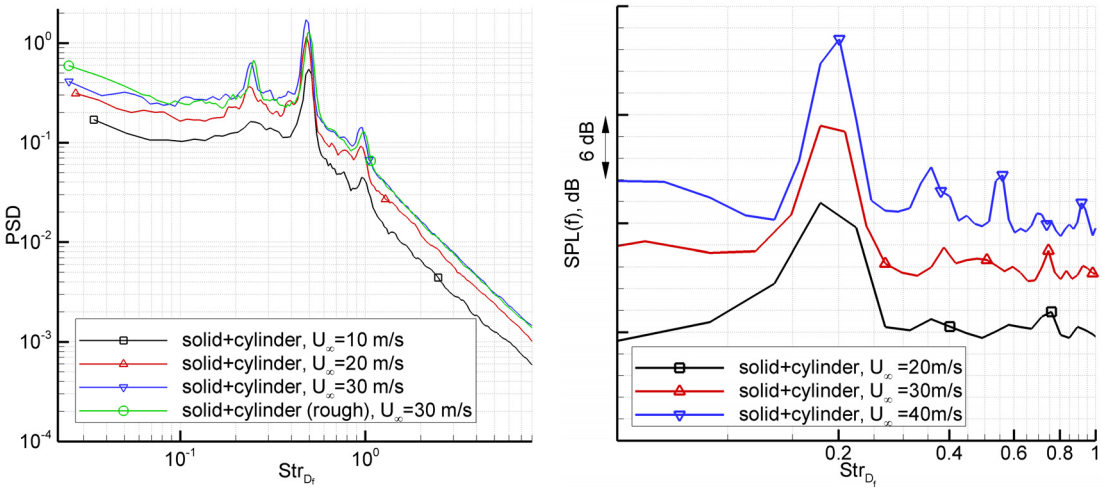

(a) hot wire, $x/D_f = 1.44$, $y/D_f = 0$, $z/D_f = 0$

(b) side wall microphone, $y/D_f = 6.89$

FIGURE 4.14: Velocity traverse of solid configuration.

(down to Grit 60 strips positioned at $\varphi = \pm 45\,^\circ$, uniform in spanwise direction) does not alter the shedding. Apparently the shell trailing edge at $\varphi = \pm 90\,^\circ$ and the presence of the strut fix the shell separation point to approximately $\varphi = \pm 85\,^\circ$ for the solid configuration, independent of freestream velocity and nature of the oncoming boundary layer. Although the solid configuration is insensitive for Reynolds number effects over the tested range, it is expected that like supercritical cylinder flow the shedding phenomenon will become less distinct for high Reynolds numbers ($Re_{D_f} > 10^6$) [43].

For the perforated shells, Reynolds number effects are not expected to influence the

current experimental results and their extrapolation to flight values. The presence of the holes can be expected to transition the shell boundary layer to a turbulent state. The distinct vortex shedding is readily broken down by the application of porosity. As highlighted in the previous section, the airflow washing the strut after bleeding through the perforate is already turbulent.

4.2.2 Effect of exposure

As illustrated in Figures 4.8 and 4.9, the bleeding of air through the fairing prevents large vortex formation associated with the shedding. The unsteadiness then consists of the individual shear layers flapping in lateral direction and rolling up into smaller vortices. This resulted in a hump shape in the velocity spectra as illustrated in Figure 4.10(b) for the perf42 (±45 °) configuration.

Increasing the exposure of the perf33 shell starting from an impermeable configuration yields the trends shown in Figure 4.15. For $\varphi = \pm 10\,°$, the distinct peak per-

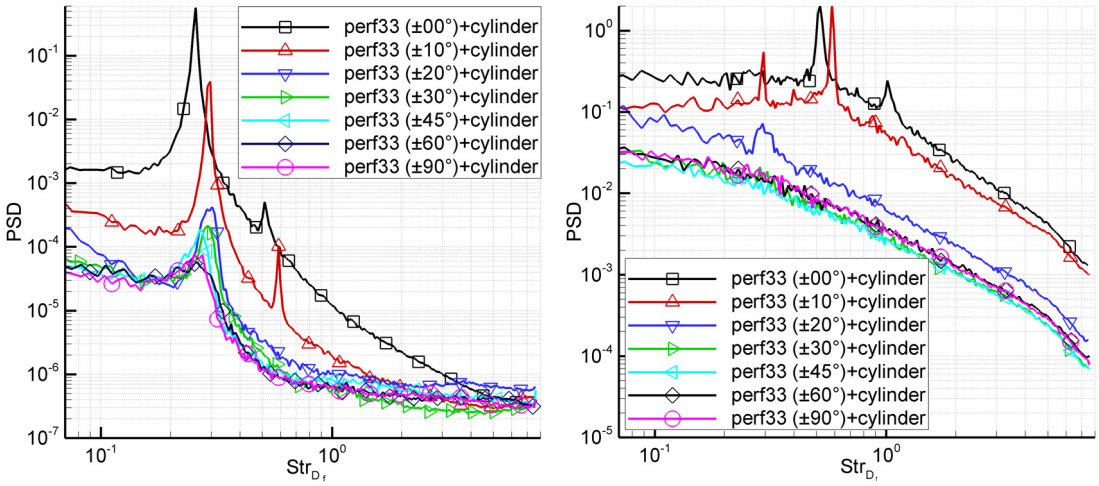

(a) $y/D_f = 1.7$ (b) $y/D_f = 0$

FIGURE 4.15: Influence of exposure on PSD of velocity ($U_\infty = 20$ m/s, $x/D_f = 1.44$, $z/D_f = 0$).

sists at a slightly higher frequency (increase from $Str_{D_f} = 0.24$ to $Str_{D_f} = 0.30$). To the side of the model, increasing exposure to $\varphi = \pm 20\,°$ yields a hump centered around the same frequency. For increasing exposure this humps starts to become less distinct and centered at slightly lower frequencies. This indicates that the flapping of the wake is less unsteady and position of the shear layers is more stable, due to an increase in the bled mass flux. However, the magnitude of the velocity fluctuations reduces with increasing exposure only up to $\varphi = 60\,°$. It is

likely that the pressure difference over the shell between $\varphi = 60\,°$ and $90\,°$ is too small to bleed extra air and reduce unsteadiness. The CFD results from section 4.1.4 readily indicated that exposing more than $\varphi = 45\,°$ does not yield extra bled air.

The wake data ($y/D_f = 0$) in Figure 4.15(b) shows a similar trend. After exposing more than $\varphi = 20\,°$, broadband fluctuations in the wake are dominant over more periodic features associated with the flapping of the wake. A lateral traverse at $x/D_f = 1.44$ (between $y/D_f = 0$ and $y/D_f = 1.7$) shows agreement in the wake structure after exposing more than $\varphi = 45\,°$.

The acoustic wind tunnel data is hampered by the high background noise levels as illustrated in Figure 4.11. Only the peak at $Str_{D_f} = 0.2$ associated with the vortex shedding exceeds the background noise in the low frequency domain. There is agreement with the aerodynamic measurements in the fact that this peak disappears by exposing $\varphi = 30\,°$ or more of the perforate. The results from the anechoic chamber experiment show that the same holds for the broadband noise level in Figure 4.16(a). However the shielded H-beam shows a different trend for

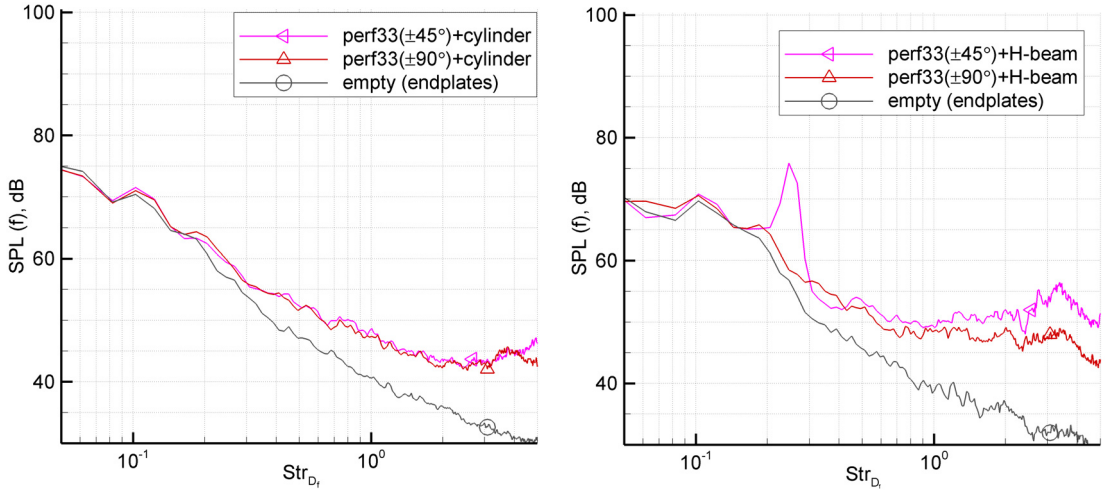

(a) Shielded cylinder

(b) Shielded H-beam

FIGURE 4.16: Influence of exposure on measured acoustic in anechoic chamber (averaged over microphone 1 to 8, $d = 2$ m, $U_\infty = 40$ m/s).

increasing exposure. The peak associated with the shedding is not fully broken down for the perf33 ($\pm 45\,°$) configuration. It is hypothesized that the difference in cross sectional geometry (Figure B.2(j)) is responsible for the discrepancy between cylinder and H-beam. For the cylinder configuration, the bled air is able to accelerate past the cylinder and form a jet exhibiting high streamwise velocities preventing the occurrence of large scale vortex shedding. For the H-beam, the

bled flow impinges on the flat surface of the beam, not allowing it to accelerate and develop in streamwise direction. It is plausible that the orientation of the flat surface in y-direction pushes air through the perforated shell between $\varphi = 45\,^\circ$ and $\varphi = 90\,^\circ$, a phenomenon that was readily observed in section 4.1.5 for the cylinder configuration. This 'blowing mechanism' could distort the shedding and be an explanation for the difference between the $\varphi = \pm 45\,^\circ$ and $\varphi = \pm 90\,^\circ$ cases, since the applied tape would prevent this phenomenon in the $\varphi = \pm 45\,^\circ$ configuration. The escape of bled flow through the perforate between $\varphi = 45\,^\circ$ and $\varphi = 90\,^\circ$ implies that the H-beam is washed by less mass flow and could therefore be responsible for the decrease in SPL for $Str_{D_f} > 1$. Both for the shielded cylinder as for the H-beam, the perf55 shell shows a similar trend compared to the perf33 configurations.

4.2.3 Effect of porosity

A comparison between the different porosity shells in Figure 4.17(a) shows few differences between the magnitude of the velocity fluctuations to the side of the model. This indicates that after a certain amount of air is bled through, bleeding

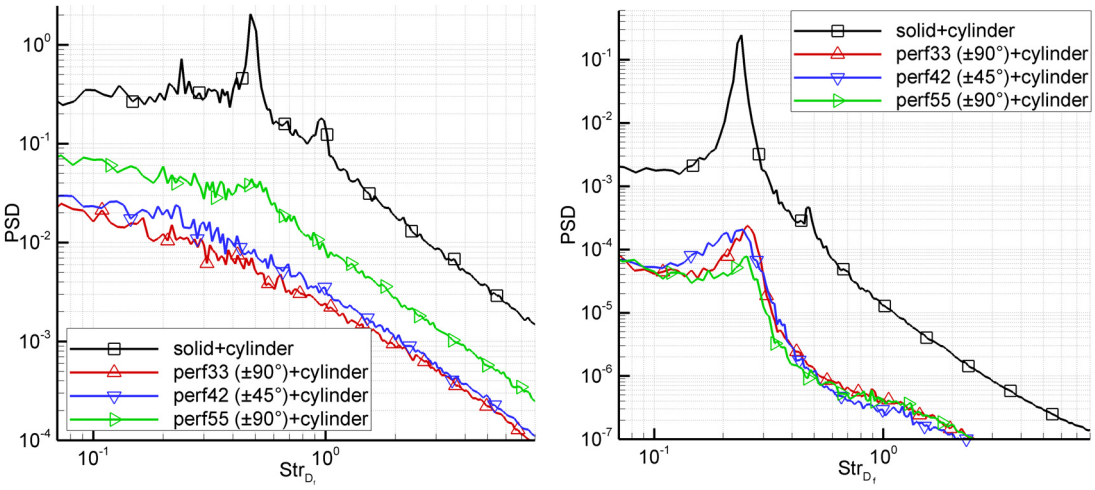

(a) $y/D_f = 1.7$ (b) $y/D_f = 0$

FIGURE 4.17: Influence of porosity on PSD of velocity ($U_\infty = 20$ m/s, $x/D_f = 1.44$, $z/D_f = 0$).

more air through the shell becomes less effective for reducing large scale velocity fluctuations. After enough air is bled to break down the vortex shedding, the unsteady flow field consists of the flapping of the wake in the lateral direction. It appears that this flapping is not significantly altered by increasing the porosity further.

The wake data in Figure 4.17(b) shows an increase in turbulence intensity at $x/D_f = 1.44$ with increasing porosity. Although the velocity fluctuations sideways of the model remain unaffected after a certain amount of bled air, the unsteadiness in the wake increases at this streamwise position. This indicates that the wake structure remains similar but wake size and the magnitude of associated flow variables might change slightly with varying porosity. Unfortunately it is impractical to map the total wake using a hot wire traverse and PIV with the perf33 and perf55 shell was not performed. Therefore a conclusion regarding the influence of porosity on wake size and associated flow variables cannot be given at this point.

For the effect of different porosity on the acoustics, the reader is referred to Figure 4.18. The increase in porosity increases the velocity of the bled air past the cylin-

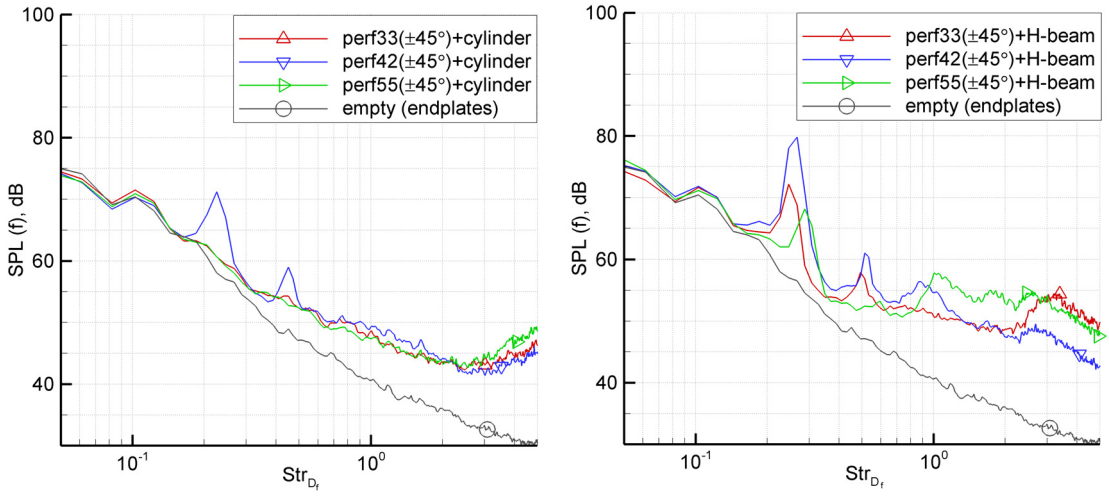

(a) Shielded cylinder

(b) Shielded H-beam

FIGURE 4.18: Influence of porosity on measured acoustic in anechoic chamber (averaged over microphone 1 to 8, $d = 2$ m, $U_\infty = 40$ m/s).

der. However, the resulting acoustics are not altered by this increase, illustrated by the coincidence of the spectra in Figure 4.18(a). The cylinder does not feature sharp edged or small scale details that can be responsible for noise creation by high velocity impingement. For the H-beam the increase in bled air does modify the related acoustics. Since the H-beam itself is a noisy structure, washing it with higher velocities increases total noise. As soon as the noise source associated with the shedding from the shell is broken down, the H-beam becomes the primary noise creation mechanism. This example illustrates the limitations to the perforated fairing concept. The initial purpose of the fairings is to prevent high speed flow past the landing gear components. Therefore one should be careful to apply high porosities for perforated fairings.

4.3 High Frequency Noise

The noise of the basic model in the solid configuration is shown to be dominated by vortex shedding at lower frequencies. For higher frequencies ($Str_{D_f} > 1$) however, several other phenomena exceeding background noise make their appearance.

4.3.1 Perforate noise

Model noise for several configurations at higher frequencies is displayed in Figure 4.19. For the perf33 and perf55 models, peaks occur in the high frequency do-

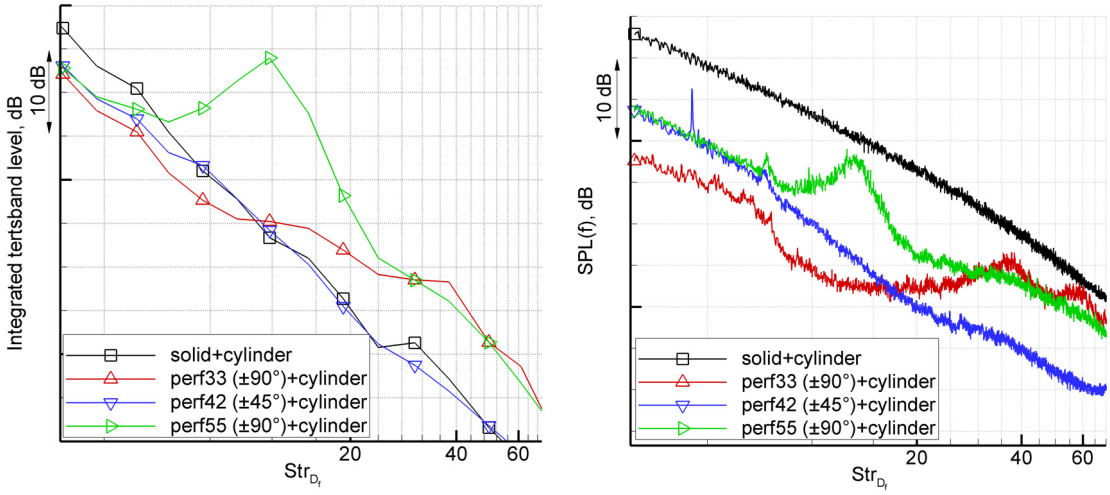

(a) Integrated 1/3 Octave band averaged beamforming plots ($x/D_f = \pm 1.0$ and $z/D_f = \pm 1.7$)

(b) Microphone k16 in the strut surface ($\varphi = 160\,°, z/D_f = -0.14$)

FIGURE 4.19: Measured acoustics at high frequencies in $7' \times 5'$ tunnel ($U_\infty = 40$ m/s).

main at respectively $Str_{D_f} = 35$ and $Str =_{D_f} 14$ for both nearfield and farfield measurements. The ratio of these two frequencies is 2.5, which equals the ratio of the orifice diameters of these shells. Comparing the $U_\infty = 40$ m/s data set to the $U_\infty = 20$ m/s and $U_\infty = 30$ m/s data set, shows scaling with velocity as well.

Source localization has been performed using the microphone array. Beamforming plots centered at $Str_{D_f} = 38$ for two different configurations are shown in Figure 4.20. The dashed vertical line represents the strut leading edge, the lower horizontal line the groundplate and the upper horizontal line the endplate. Noise sources are reflected by the groundplate, therefore contour plots show noise underneath the groundplate. The plots reveal the noise source location at the perforate. A closer look at the different tape configurations for the perf33 model shows the source

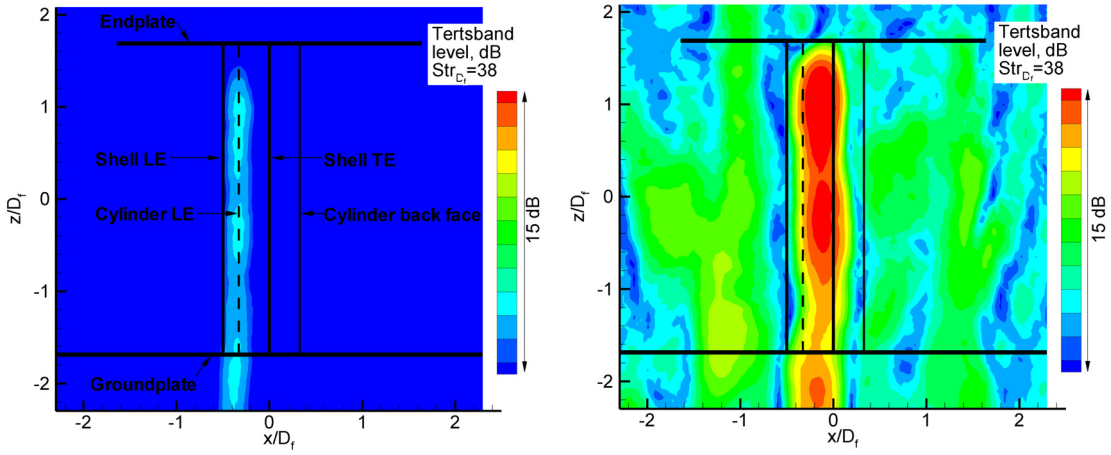

(a) perf33 (±30 °)+cylinder, $Str_{D_f} = 38$

(b) perf33 (±90 °)+cylinder, $Str_{D_f} = 38$

FIGURE 4.20: 1/3 Octave band averaged beamforming plots ($U_\infty = 40$ m/s).

moving more downstream from the $\varphi = \pm 30\,°$ to the $\varphi = \pm 90\,°$ configuration with a corresponding increment of 12 dB. These observations feed the hypothesis that the high frequency peaks are related to flow resonance ('whistling' or 'singing') of the perforate. Grazing flow past sharp edges is known to create an edgetone type noise as described by Brown [64, 65]. It is most probably this feedback mechanism that is responsible for the 'perforate noise'.

The perf55 model shows similar behavior at $Str_{D_f} = 15$ with a noise increment of 12 dB between $\varphi = \pm 30\,°$ and $\varphi = \pm 90\,°$. The difference between the various taped configurations for the perf55 model becomes clearly visible in Figure 4.21(a). The level of the maxima as well as the corresponding frequency of the perforate

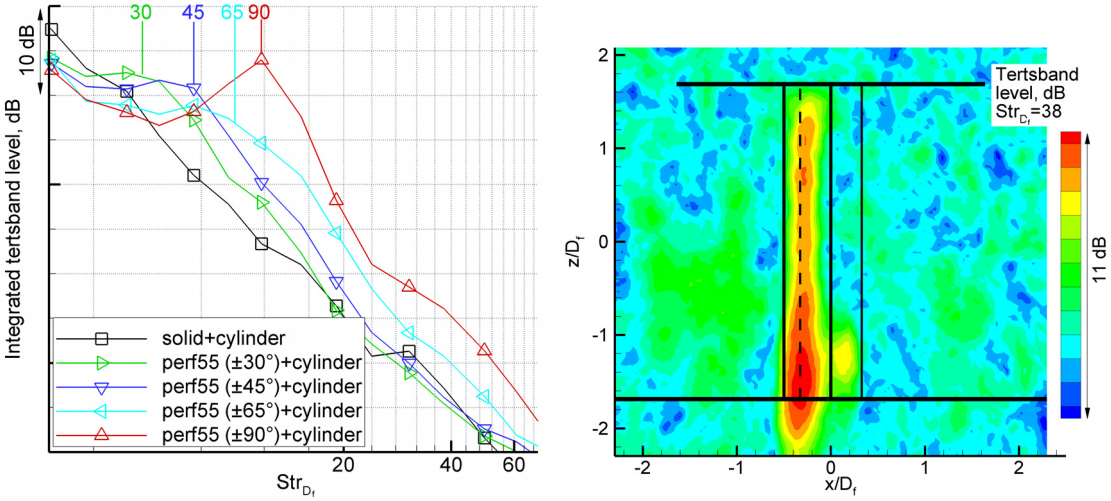

(a) Integrated 1/3 Octave band averaged beamforming plots ($x/D_f = \pm 1.0$ and $z/D_f = \pm 1.7$)

(b) 1/3 Octave band averaged beamforming plot, perf42(±45 °)+cylinder at $Str_{D_f} = 38$

FIGURE 4.21: Microphone array data ($U_\infty = 40$ m/s)

noise shifts with exposure angle for each configuration. This illustrates the scaling of the perforate noise with local shearing flow velocity past the perforate. To characterize the frequency content of the noise, the Strouhal numbers based on orifice diameter d_{or} and local velocity can be calculated using

$$Str_{d_{or}} = \frac{f d_{or}}{U} \quad . \tag{4.2}$$

The orifice diameter is known and the local velocity can be estimated using PIV and CFD. The frequencies are estimated from the maxima of the several configurations in Figure 4.21(a). This yields a rough estimate of $Str_{d_{or}} \approx 0.33$ for the frequency content of the perforate noise.

Although the perforate noise doesn't emerge for the perf42 ($\pm 45\,^{\circ}$) configuration in Figure 4.19, the beamforming plots do reveal it's presence in Figure 4.21(b). However, the level of the noise is 8 dB lower compared to the perf33($\pm 45\,^{\circ}$) model with a similar orifice diameter. The edge radius of the perf42 shell is expected to be responsible for the reduced intensity of the noise.

From the spectra it appears that the phenomenon is not purely tonal, which can be explained by the varying velocity magnitude across the shell responsible for the noise. Another contributor to the broadband feature in this noise can be the fluctuating volume flow through the orifices [61]. These fluctuations originate from a turbulent boundary layer passing over a perforated sheet and are known to create a broadband type noise scaling with orifice diameter as discussed in the literature review and the above referenced paper.

To extrapolate the frequency range to flight conditions, one should take into account size and velocity changes. Typical speed during approach is $U_\infty = 80$ m/s. Assuming the magnitude of the shearing flow component is $1.5U_\infty$ together with an orifice diameter of $d_{or} = 2$ mm results in frequencies close the upper limit of the audible range ($f \in [20, 20 \times 10^3]$ Hz). This illustrates the possibility for tailoring d_{or} to avoid the high frequency noise penalty. In addition to that atmospheric attenuation (along the path between airplane and receiver) will reduce high frequency noise relative to lower frequencies, since absorbtion increases with frequency. To provide the reader with a more quantitative impression, Figure 4.22 displays relative absorption of tertsband frequencies for various source-receiver distances calculated according to the procedure documented by ICAO [6]. Clearly noticeable is the increase in absorption above $f = 1000$ Hz, reducing the level of the unwanted perforate noise for the receiver on the ground.

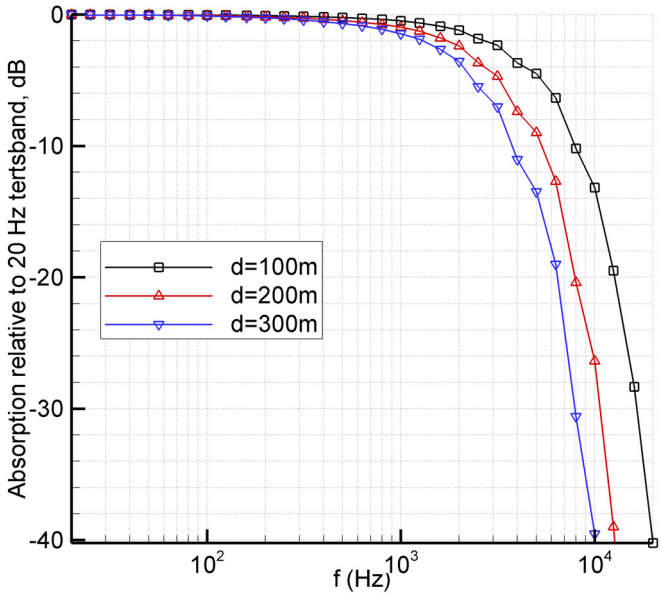

FIGURE 4.22: Relative atmospheric absorption according to ICAO [6] at a temperature of 15 ° C and humidity of 50%).

4.3.2 Other sources

Apart from the whistling noise of the perforate, several other high frequency noise sources were found. They are discussed below.

4.3.2.1 Trailing edge noise

The on-surface microphones located in the front half of the strut (k7, k8, k9, k10, k11, k12) pick up a high frequency tonal noise source for the solid configuration as illustrated in Figure 4.23. Localization in Figure 4.23(b) points at the shell trailing edge region responsible for the noise. Turbulence in the vicinity of a sharp trailing edge is a well known broadband noise generation mechanism [88]. The sound output of quadrupoles associated with turbulence is significantly increased when the motion is directed perpendicular to a sharp trailing edge. Both the solid and the perf42 shell feature a sharp 1.6 mm thick trailing edge. The perf33 and perf55 shells are perforated over the whole shell and a piece of tape is wrapped from the shell inside to the outside to cover the last 10 mm of the trailing edge area on both sides. Hence there is no sharp trailing edge present for these shells, which explains the absence of the phenomenon for these configurations, even when the perforations are taped.

Removal of the top endplate makes the trailing edge noise disappear for the solid

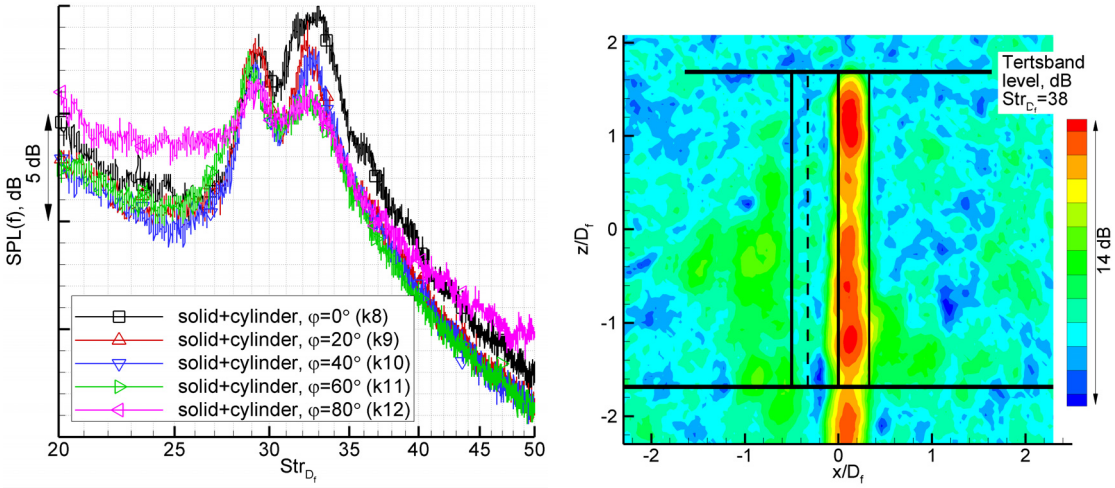

(a) On-surface microphones

(b) 1/3 Octave band averaged beamforming plot, solid+cylinder at $Str_{D_f} = 38$

FIGURE 4.23: Acoustics of trailing edge noise ($U_\infty = 40$ m/s)

configuration. Removal of the endplate introduces spanwise flow fields, hence the main direction of the flow is not perpendicular to the shell trailing edge anymore. This results in the loss of spanwise coherence and vanishing of the trailing edge noise phenomenon.

The clear peak in the spectra of Figure 4.23(a) indicates the presence of a periodic phenomenon. The Strouhal number based on trailing edge thickness and local velocity ($1.5U_\infty$) works out as 0.2, revealing vortex shedding from the trailing edge to be responsible for the periodicity. The reason for the fork-like shape of the spectral peak remains unclear. Although the on-surface microphones only indicate the presence of the noise at $Str_{D_f} > 25$, the microphone array beamforming plots show the noise from emerging from lower Strouhal numbers, illustrating the broadband character of the noise.

Both array and on-surface microphone measurements indicate the presence of trailing edge noise for the solid configuration only at $U_\infty = 40$ m/s. The absence of the phenomenon at $U_\infty = 20$ and $U_\infty = 30$ m/s could be caused by a reduced turbulence intensity in the vicinity of the trailing edge due to a change in the boundary layer state.

4.3.2.2 Horseshoe vortex

Noise contours of the bare strut (i.e. no shrouding shell employed) do not exceed background noise for $Str_{D_f} < 20$, illustrated by roughly uniform levels on the

beamforming plots. Above these frequencies flow interaction with ground- and endplate creates noise concentrated in these regions as shown in Figure 4.24. This

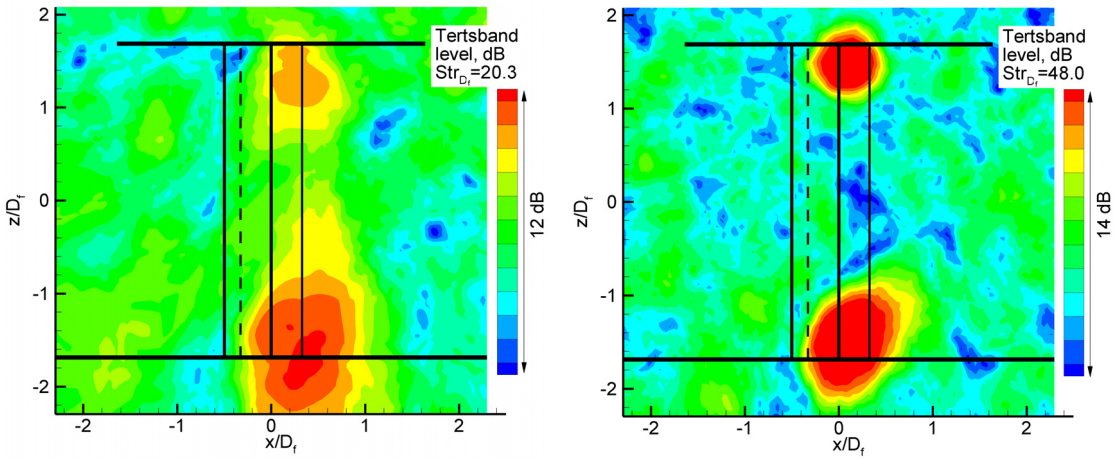

(a) solid+cylinder, $Str_{D_f} = 20.3$, $U_\infty = 30$ m/s (b) isolated cylinder, $Str_{D_f} = 24$, $U_\infty = 20$ m/s

FIGURE 4.24: 1/3 Octave band averaged beamforming plots

phenomenon is also present for the solid configuration. Comparison of the solid and isolated cylinder beamforming plots between $U_\infty = 20$ m/s and $U_\infty = 40$ m/s reveals Reynolds number dependency of this phenomenon. Expected flow physics is described in [89]. Ground- and endplate boundary layer are subjected to a streamwise adverse pressure gradient approaching the model. Following is a three dimensional separation with highly unsteady horseshoe vortices that wrap around the cylinder or solid shell. The shorter length of the endplate and corresponding thinner boundary layer can explain why the top end vortex is less noisy than the bottom one.

4.4 Summary

Experiments with a simplified fairing-cylindrical strut model have been performed to investigate the use of perforated fairings for passive noise control. Both aerodynamics and the related acoustics are studied employing two different wind tunnel facilities and an anechoic chamber.

Application of perforated fairings reduces the flow velocities to the side of the shell. Quantitatively, a fairing featuring 42% porosity reduces the maximum flow velocity sideways of the shell by 18% resulting in a reduction of unwanted high speed flow deflection. The bled mass flux through the perforate follows a linear trend with varying porosity. A dedicated two-dimensional RANS simulation predicts a

mass flux between 26% and 39% of the freestream flux (based on the perforated frontal area) for porosities between 33% and 55%. Application of an edge radius of $r_{edge}/d_{or} = 0.14$ increases the effective porosity by 14%. Exposing more than $\varphi = \pm 45\,^{\circ}$ of the perforate does not yield extra bled air.

With respect to the unsteady flow field, application of perforated fairings shows a dual shear layer exhibiting roughly half the vorticity of the solid fairing, resulting in weaker vortices of smaller scale. The distinct spectral peak of velocity fluctuations related to the vortex shedding of the solid model disappears. However it is expected that like supercritical cylinder flow the periodic shedding of the solid fairing will become less distinct for high Reynolds number flow ($Re_{D_f} > 10^6$). Exposing the perforate on the suction side of the shell bleeds less air and is therefore less effective in reducing the magnitude of the large scale velocity fluctuations.

Consistent with the aerodynamic measurements, application of the perforations results in breaking down of the vortex shedding noise at $Str_{D_f} = 0.2$ illustrated by a vanishing spectral peak of near field microphone measurements. The anechoic chamber test results show that the associated broadband level is reduced as well. Furthermore, a test with a noisy H-beam replacing the cylinder indicates that increasing porosity can result in adverse noise effects due to the bled mass flow washing the strut.

Finally, the perforate is shown to create noise at higher frequencies centered around $Str_{d_{or}} = 0.33$. This opens up the possibility for tailoring this noise phenomenon above the upper limit of the audible range. Since the shearing flow past the perforate is responsible for the high frequency noise, one should take into account that both intensity and spectral content are dictated by the local velocity past the perforate instead of freestream velocity. Other features making their appearance at higher frequencies include shell trailing edge noise and junction flow effects.

The research on the basic model has been presented at the 13^{th} AIAA/CEAS Aeroacoustics Conference in Rome [90] and is soon to be published in [91].

Chapter 5

Landing Gear Model Research

Flow and acoustics of the landing gear model featuring various configurations are investigated in this chapter. For details on test set-up, model and apparatus, the reader is referred to section 3.4. Most of the aerodynamic and acoustic tests were performed at freestream speeds U_∞ of 20, 30 and 40 m/s. This allows to distinguish physical features that scale with velocity and to discover Reynolds number effects in this range. Since the model is 0.25 scale and typical speed during approach is 80 m/s, testing at the maximum tunnel velocity will give an 8 times lower Reynolds number compared to real flight. According to Strouhal number scaling, frequencies in the wind tunnel will be twice the frequencies in flight for the maximum tunnel velocity ($U_\infty = 40$ m/s). To characterize the frequency domain, it is often decomposed into a low, mid and high frequency range as explained in the literature review. There is no official guideline stating the limits of these ranges. In the present work, low frequencies are below $f = 500$ Hz, the mid frequency ranges from this value to $f = 5$ kHz and the high frequencies exceed above $f = 5$ kHz. For the aerodynamic tests, 3 different configurations have been investigated; the plain landing gear (no fairings), fairings applied with perforations taped and fairings applied with all perforations exposed indicated respectively by LG, Solid and Perf in the figures.

Firstly, flow behavior around the fairings is researched predominantly using oil flow visualization. The following section investigates the influence of the different configurations on flow around the wheels by means of pressure measurements. Thereafter, the flow in the near wake of the landing gear is investigated by means of PIV and unsteady pressure sensors. Finally, acoustics of the landing gear model is researched employing two microphone arrays and on-surface microphone measurements.

5.1 Fairing Flow

This section describes time-averaged flow features on the fairings. A front view of oil flow visualization on the undertray and articulation link fairing is shown in Figure 5.1. The undertray stagnation line divides the flow in the upward and

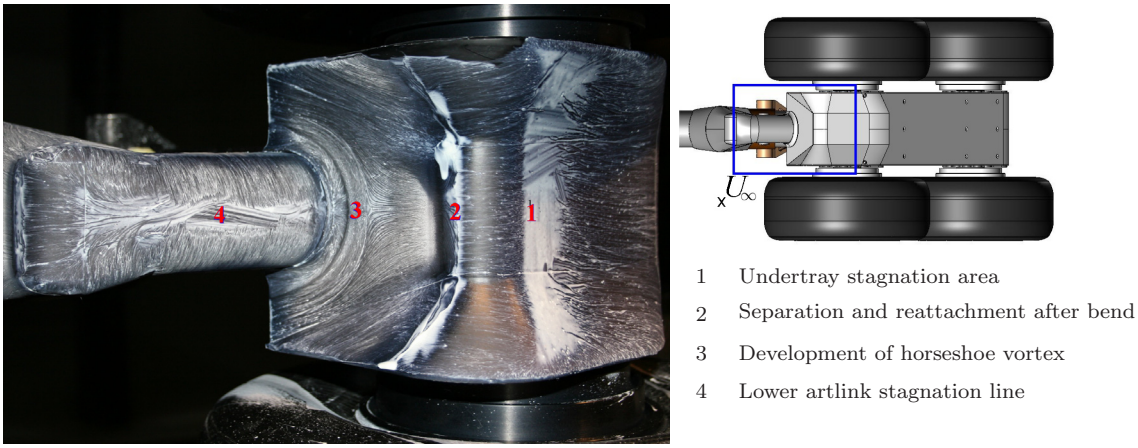

FIGURE 5.1: Front view of flow visualization of solid fairings ($U_\infty = 40$ m/s).

downward directions (z-direction). The upward deflected flow impinges on the lower articulation link fairing and forms a horseshoe vortex around it. The lower articulation link itself divides the flow in the transverse direction (y-direction), where it separates from the lower articulation sides as depicted in Figure 5.2. The streamlines on the upper articulation link indicate attached flow until the transition to the main leg is reached.

PIV is used to visualize the flow directly upstream of the articulation link fairing on the model centerline (y=0) in Figure 5.3. The effect of the fairing is to deflect the flow more in the upward direction, since it's cross sectional frontal area is large compared to the bare articulation link. The impact of perforations is relatively small. Noticeable is the increase in velocity in the stagnation point area between z=320 mm and z=380 mm caused by the bleeding of the air. However, the flow direction pattern remains largely unaltered, indicating that more porosity is needed if reduction of upward deflected velocities is desired.

Figure 5.4 visualizes the ground view of the downward directed flow by the un-

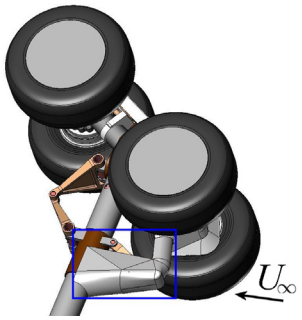

1 Separation on lower artlink side

2 Transition between lower and upper artlink: separation and reattachment

3 Separation and reattachment after bend on upper artlink

FIGURE 5.2: Side view of flow visualization of solid fairings ($U_\infty = 40$ m/s).

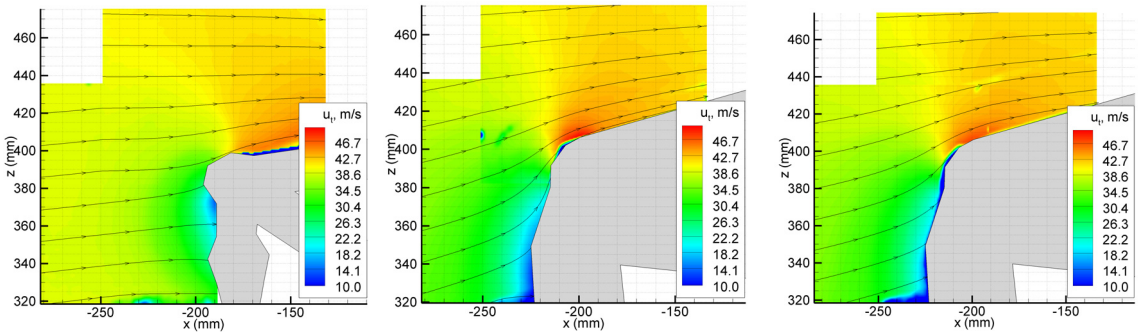

(a) LG (b) Solid (c) Perf

FIGURE 5.3: Time-averaged velocity contours and streamlines in the xz-plane at y=0 (artlink area, $U_\infty = 40$ m/s).

dertray. The flow remains attached to the fairing surface until the trailing edge apart from the laminar separation bubble at the sharp bend close to the stagnation line. Instead of leaving the undertray at the trailing edge, part of the flow escapes sideways between the wheels as visualized in Figure 5.4. After reaching the undertray side, a side edge vortex forms of which the path is visible in the figure. An unsteady pressure sensor is positioned flush with the undertray surface at location 4 (see Figure 3.16). The flow visualization readily revealed attached flow in this region. Hence large scale fluctuations are not present and pressure spectra are dominated by electronic noise and therefore omitted. The perforated

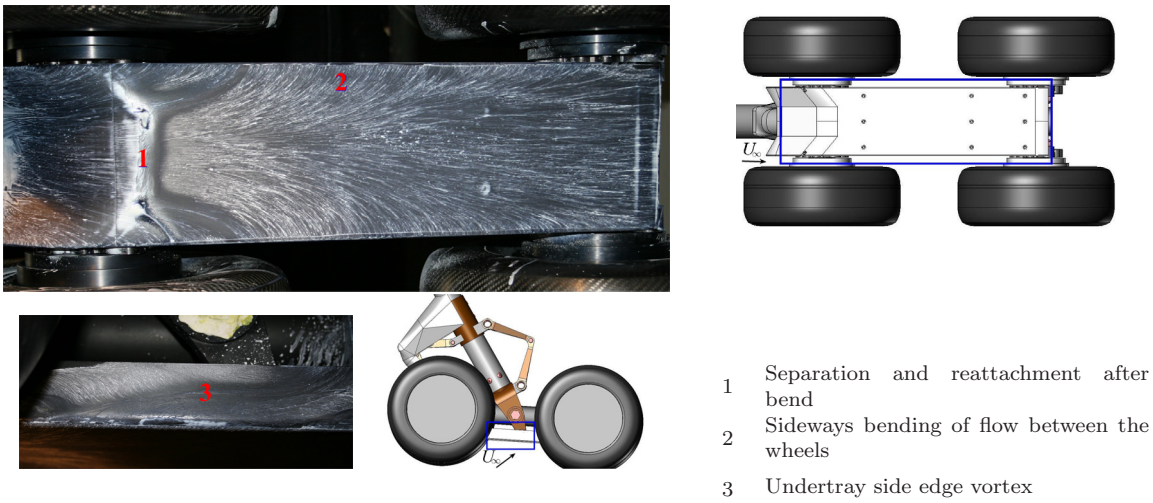

FIGURE 5.4: Ground view of flow visualization of solid fairings ($U_\infty = 40$ m/s).

and solid fairing configuration yield the same result, amounting to a mean pressure of $Cp = 0.22$ at this location.

There are several locations exhibiting laminar separation and turbulent reattachment after a small radius bend in the fairings. Application of roughness strips advances the transition to turbulent flow and thereby prevents the formation of laminar separation bubbles as depicted in Figure 5.5. The additional roughness of the perforations has also been confirmed to prevent the laminar separation bubble on the undertray bend (nr. 1 in Figure 5.4). A similar effect can be expected for the other fairing locations exhibiting laminar separation and turbulent reattachment. However, the influence of the described laminar separation on the noise signature is expected to be small since the microphone array results (section 3.4.3.5) for a configuration with and without roughness strips show identical beamforming plots.

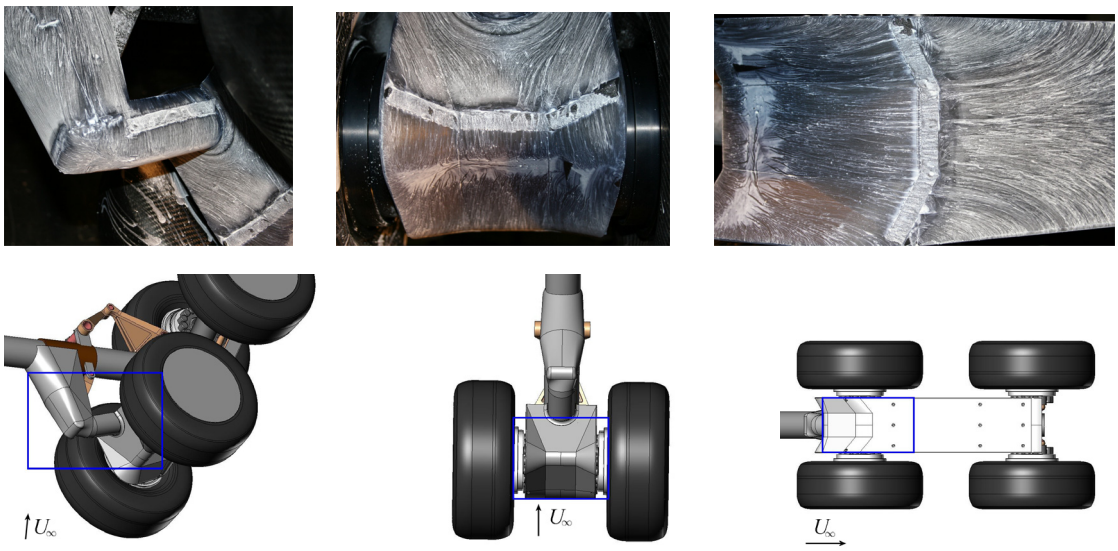

FIGURE 5.5: Flow visualization on application of roughness strips to fairings ($U_\infty = 40$ m/s).

5.2 Near Wake Flow

The flow conditions directly downstream of the gear (torque link, main leg and rear bogie area) have been investigated using PIV and unsteady pressure sensors. Time averaged velocity contours in the model centerplane are shown in Figure 5.6. As noticed before, the flow above z=340 mm in Figure 5.3(a) is not deflected upwards by the fairing, which results in a high streamwise velocity region in the top of Figure 5.6(a). The vectors illustrate that without fairings applied, the dominant wake flow direction is streamwise. An area of relatively high speed flow ($0.7U_\infty$) emerges between z=-100 and z=50 mm, resulting from the flow penetrating through the gear between the bogie beam and wheels. Application of the fairings alters the wake structure significantly. From the torque link junction, the flow is directed in the upward and downward direction. Apparently deflection of the air in z-direction by the fairings results in spanwise flow features in the wake. Since the undertray fairing prevents the air from penetrating through the gear, the high speed velocity region between z=-100 and z=50 mm partly disappears. Additionally, a dead flow area emerges below z=0 mm. The flow that manages to escape in the streamwise direction from the undertay side edge (Figure 5.4) results in a small area of higher streamwise flow velocities ($0.5U_\infty$) roughly between z=0 and z=50 mm.

The corresponding contours of standard deviation are shown in Figure 5.7. As expected, the application of the fairings yields very low values of u'_t in the dead flow area below z=0 mm. Apart from the dead flow area, the near wake generally

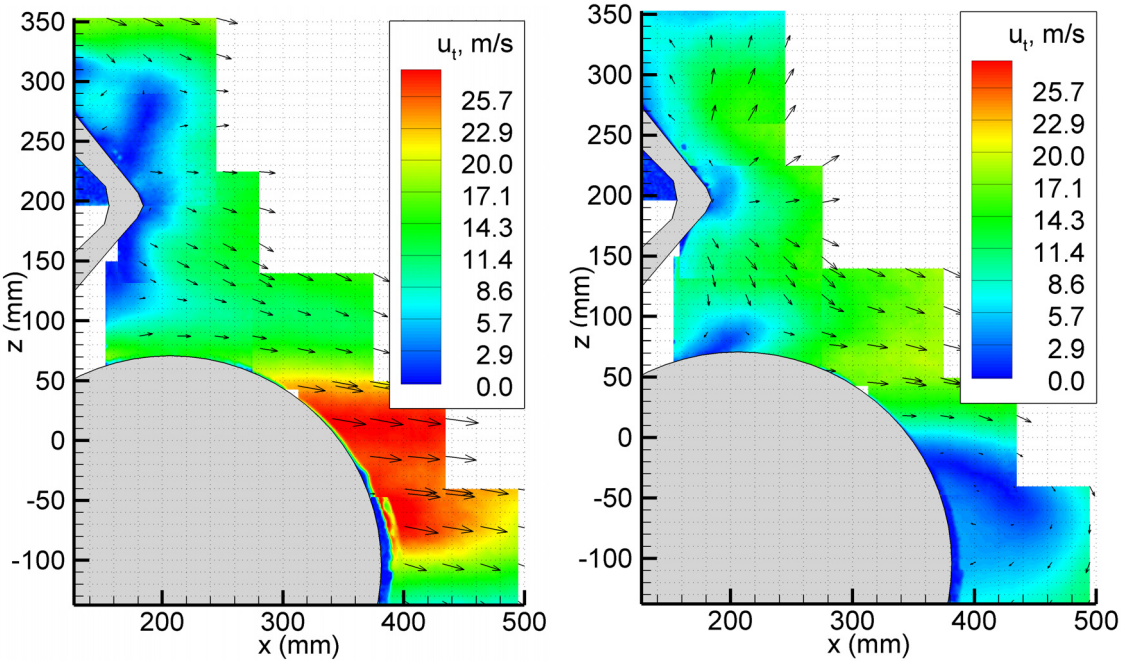

(a) LG (b) Solid

FIGURE 5.6: Time-averaged velocity contours and vectors in the xz-plane at y=0 (torque link area, $U_\infty = 40$ m/s).

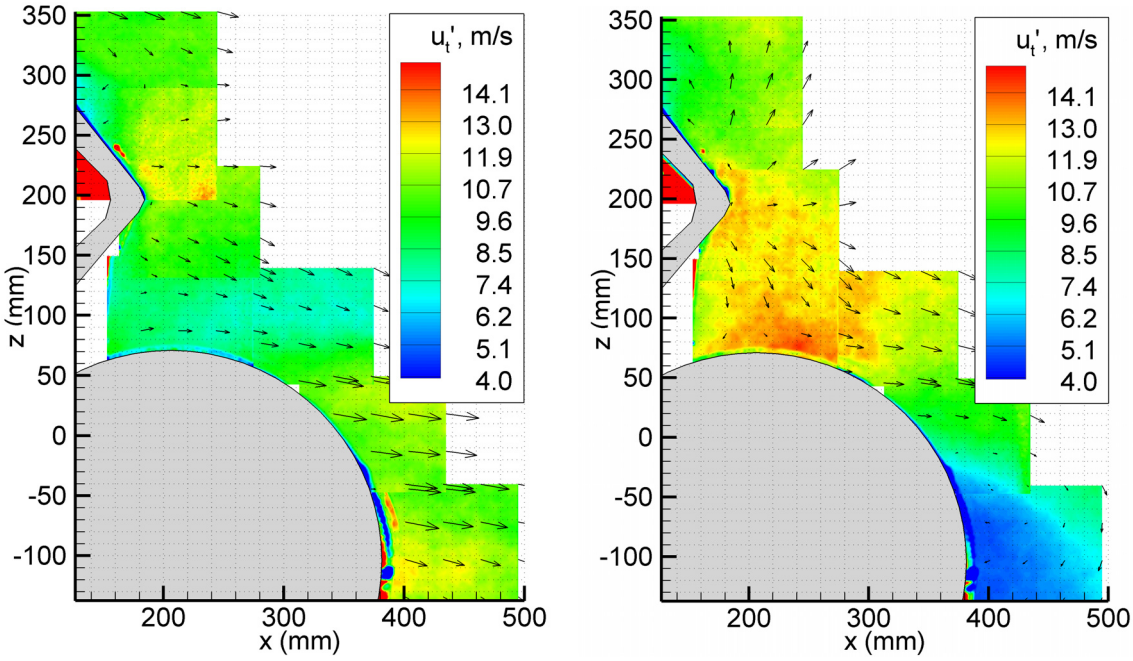

(a) LG (b) Solid

FIGURE 5.7: Contours of velocity standard deviation (u_t') combined with time-averaged velocity vectors in the xz-plane at y=0 (torque link area, $U_\infty = 40$ m/s).

exhibits lower values of u'_t without fairings applied. An explanation could be that the larger size of the fairings compared to the plain gear introduces large scale fluctuations and therefore higher values of u'_t.

The wake structures of the solid and perforated fairing configurations are very similar. To allow for a quantitative comparison between these configurations, the time averaged variables of these configurations are subtracted in Figure 5.8. Due to the similarity in wake structure, the direction of the subtracted vectors in

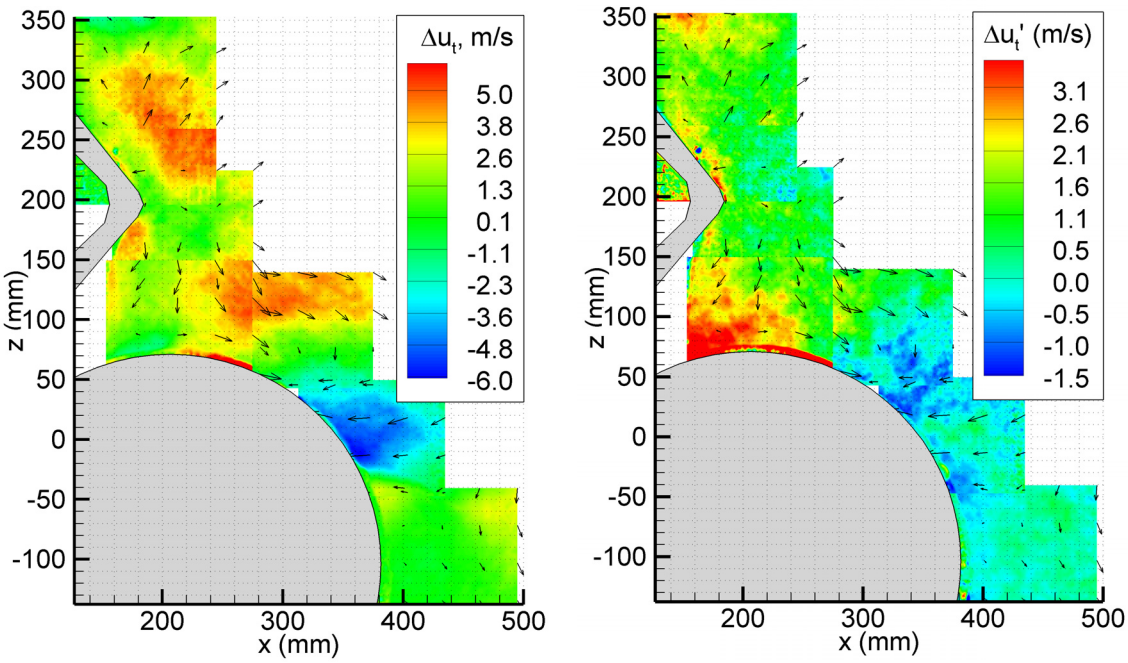

(a) Time-averaged velocity (contours and vectors)

(b) Contours of velocity standard deviation combined with time-averaged velocity vectors

FIGURE 5.8: Difference between solid and perforated fairings for contours an vectors in the xz-plane at y=0 (torque link area, $U_\infty = 40$ m/s).

Figure 5.8 aligns with the original flow direction in Figure 5.6(b). Downstream of the torque link area between z=100 and z=300 mm, wake velocities are up to 30 % lower for the perforated fairing. Plausibly, bleeding of air through the fairings reduces the high speed deflection past the fairing sides and thereby reduces wake velocities in the centerplane. The earlier hypothesized large scale fluctuations associated with fairing size would then also reduce in magnitude. This can explain the decrease in turbulence intensity reflected in the standard deviation in Figure 5.8(b).

The velocity decrease in the torque link area is opposed to a velocity increase in the small jet between z=0 and z=50 mm. It is likely that the bled air through the undertray mixes with the flow that escapes from the undertray side edge and

causes this velocity increase. Accompanied with the decrease of time averaged velocity comes a slight decrease in u' as depicted in the lower half of Figure 5.8(b).

Fluctuating surface pressures have been measured at several locations in the near wake (Figure 3.16). The data for location 1 and 5 are shown in Figure 5.9. The

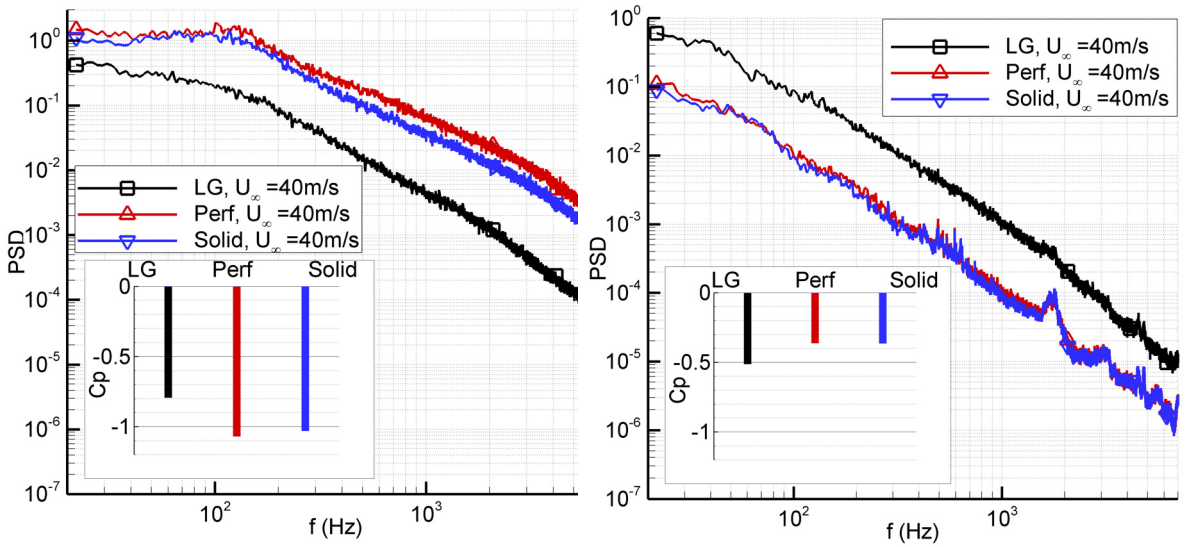

(a) Location 1, Main leg upper

(b) Location 5, Rear bogie cap

FIGURE 5.9: PSD and mean surface pressure on the gear ($U_\infty = 40$ m/s).

spectra in the back of the main leg are dominated by large scale turbulence and it's breakdown. With both solid and perforated fairings on, a hump is visible centered at $f \approx 104$ Hz. The frequency scales with freestream velocity and using the main leg diameter, the non dimensional frequency combines to $Str = 0.2$. The difference between solid and perforated fairings is small, although against expectations the perforated fairing configuration exhibits slightly higher amplitude fluctuations. Without the fairings on, the hump disappears and the magnitude of the pressure fluctuations is significantly lower. This is combined with a 23% increase in base pressure to $Cp = -0.79$. Although the freestream flow can directly impinge on the main leg at this z-coordinate, it seems that the vortex shedding is less intense than with fairings on. The fact that the application of the fairings increases the vortex shedding at this location probably lies in the overlay between the upper articulation link fairing and the main leg, allowing the fairing boundary layer to flow past the sides of the main leg and separate from it.

The sensor in the rear bogie cap shows the inverse image of the sensor in the upper main leg. The PIV-measurements revealed that the shielding of the bogie beam by the undertray results in a dead flow area at the rear of the bogie beam. Therefore fluctuations are of lower amplitude and base pressure is higher compared

to the configuration without fairings. The difference between solid and perforated fairings is small for both unsteady and steady pressures.

5.3 Wheel Flow

The flow around the landing gear wheels was investigated using (un)steady pressure measurements. The coincidence of the model centerplane with the freestream velocity vector enabled measuring wheel pressure on only one side of the gear. This reduces the number of plots per configuration to 2 (front and rear wheel) instead of all 4 wheels. The pressures are recorded at freestream velocities U_∞ of 20, 30 and 40 m/s. After inspection, Cp values for a specific configuration generally coincide for different velocities, indicating an absence of Reynolds number effects. Therefore the $U_\infty = 40$ m/s data set is displayed, since higher velocities use more of the range of the recording instrumentation and thus are more accurate.

5.3.1 Wheel centerline

A local polar coordinate system can be defined originating in the wheel axis to describe the location of the centerline tappings. The polar angle φ is defined in the inset in Figure 5.10 and starts at the most upstream wheel position.

5.3.1.1 Time averaged pressures

The centerline tappings show few differences between the configurations in Figure 5.10.

Front wheel The front wheel shows separated flow roughly between $\varphi = 100\,^\circ$ and $\varphi = 270\,^\circ$, similar for all three configurations. The average level of the base pressure differs slightly, the LG configuration displaying the highest value. The base pressure is not constant and shows a dip at $\varphi = 190\,^\circ$ with an amplitude of about $\Delta Cp \approx 0.3$ for all configurations.

Rear wheel The rear wheel is showing a similar distribution to the front wheel in Figure 5.10(b). The $33\,^\circ$ inclination of the bogie beam with respect to the freestream flow direction displaces the wheels and prevents the wake of the front

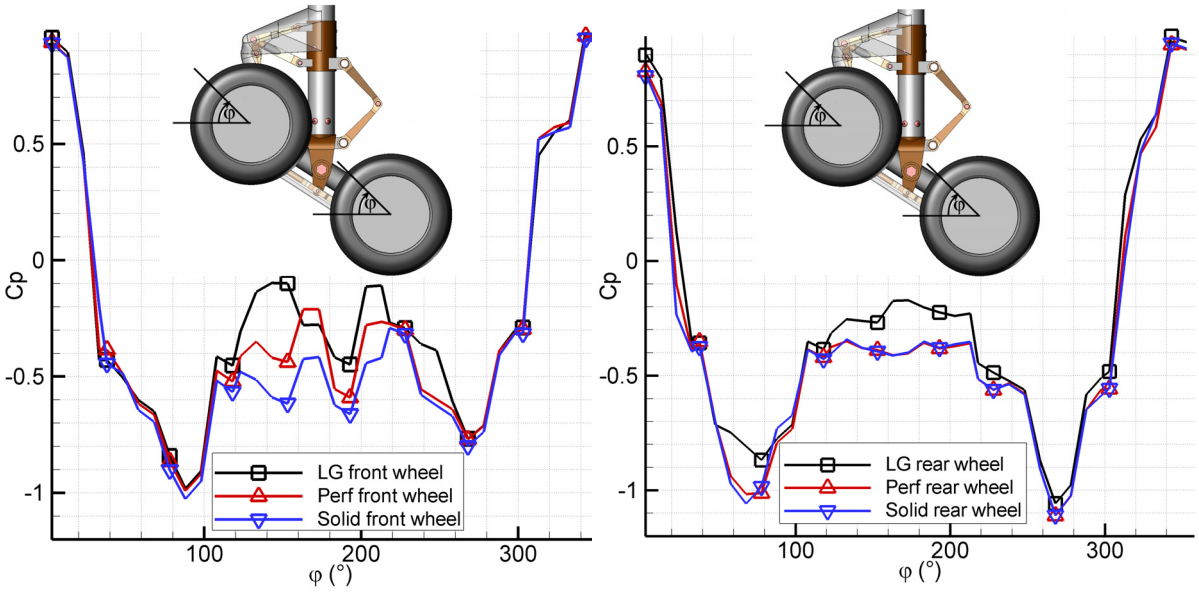

(a) Front wheel

(b) Rear wheel

FIGURE 5.10: Centerline surface pressures on landing gear wheels ($U_\infty = 40$ m/s).

wheel from impinging directly on the rear wheel. There are few differences between the configurations, apart from the LG configuration showing a 35% higher base pressure level. Base pressures are more constant in comparison to the front wheel. Also, suction is less on the lower wheel side ($\varphi > 270\,°$) illustrated by a minimum value of $Cp = -0.8$ opposed to $Cp = -1.1$ for the front wheel. Additionally, the point of minimum pressure on the upper wheel side shifts from $\varphi = 90\,°$ to $\varphi = 70\,°$, advancing the separation point.

The centerline mean pressure signatures of both front and rear wheels indicate that perforating the fairings is not significantly altering the time averaged flow around the wheels.

5.3.1.2 Unsteady pressures

The PSD of the fluctuating pressures are shown in Figure 5.11 for several angular stations. The landing gear configurations without fairings, with perforated fairings and solid fairings are indicated using black, red and blue color respectively. The front and rear wheels can be distinguished by a dashed and solid line respectively. For the attached flow regions at $\varphi = 348\,°$ and $\varphi = 303\,°$, the PSD displays a low value since large amplitude fluctuations are not present. There are very few differences between the various configurations and the front and rear wheel. A

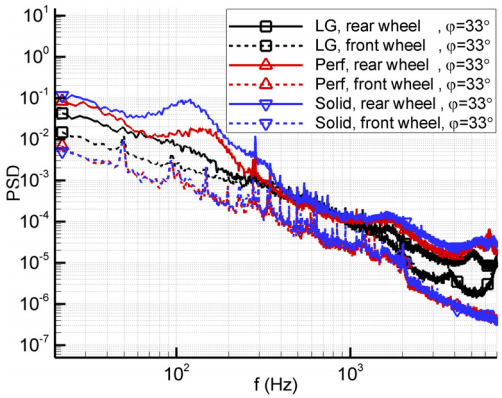

(a) $\varphi = 33\,^\circ$

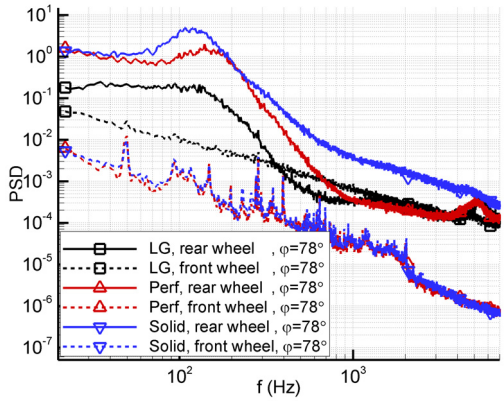

(b) $\varphi = 78\,^\circ$

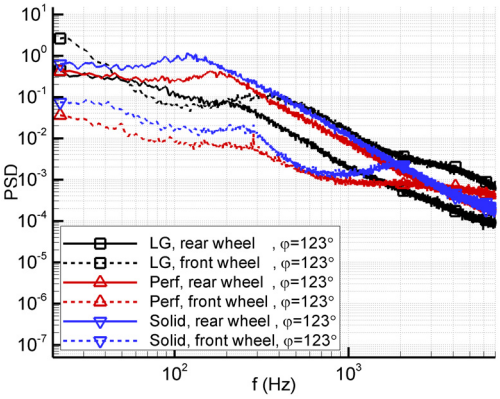

(c) $\varphi = 123\,^\circ$

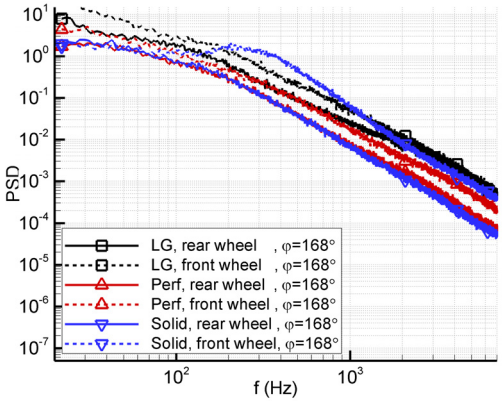

(d) $\varphi = 168\,^\circ$

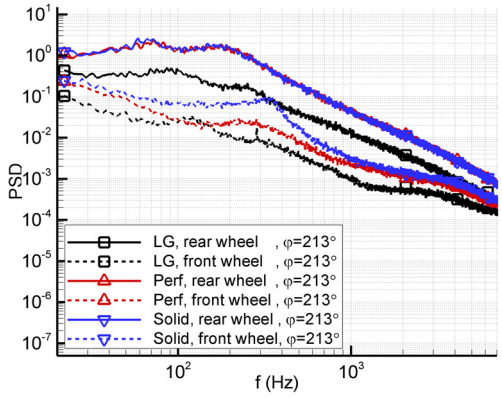

(e) $\varphi = 213\,^\circ$

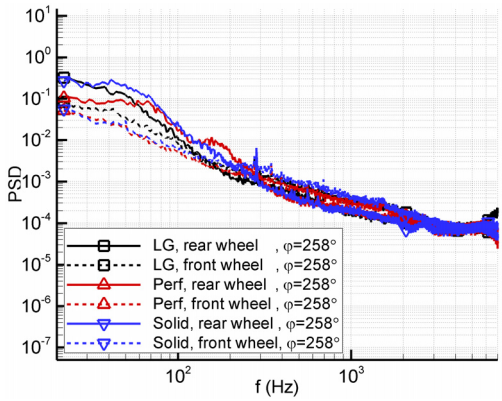

(f) $\varphi = 258\,^\circ$

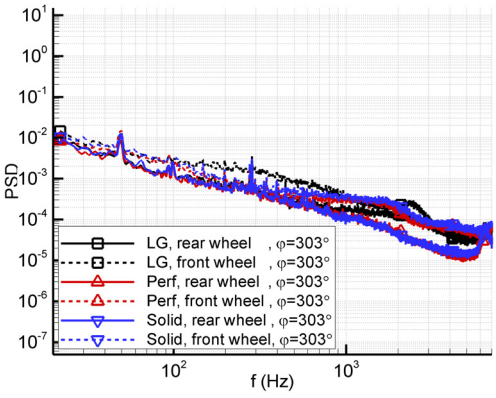

(g) $\varphi = 303\,^\circ$

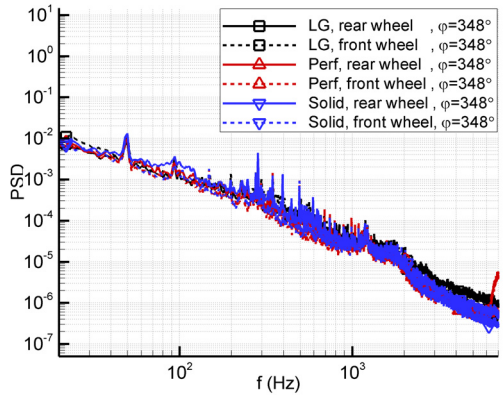

(h) $\varphi = 348\,^\circ$

FIGURE 5.11: PSD of surface pressure on landing gear wheels ($U_\infty = 40$ m/s).

low frequency tone is present at $f = 48$ Hz. The spectral content of the tone is found to scale linear with velocity, implying the physical background is related to a shedding phenomenon. However, the source location is not identified. For the other angular stations, this low frequency tone is swamped by separation induced pressure fluctuations. The high frequency content for the attached flow regions is dominated by peaks in the PSD due to electronic noise.

For the front wheel, the unsteady pressures for the solid and perforated fairing at $\varphi = 33\,^\circ$ and $\varphi = 78\,^\circ$ show a similar signature to the PSD's at $\varphi = 348\,^\circ$ and $\varphi = 303\,^\circ$. However, the rear wheel pressures show a low frequency hump centered roughly around $f = 125$ Hz, most pronounced for the solid fairing configuration. The application of perforations reduces the peak level of the fluctuations and shifts the centre slightly upward to $f = 150$ Hz. The absence of this phenomenon for the front wheel and the proximity of the angular stations to the front wheel points towards the unsteady front wheel wake responsible for the pressure fluctuations. However, the fact that the low frequency hump is hardly there for the plain landing gear configuration could also point in the direction of the undertray side edge vortex (visualized as nr.3 in Figure 5.4) impinging on the rear wheel tyre surface. The linear scaling of the humps with freestream velocity confirms the physical background of the phenomenon.

The high level of the PSD's for the rear wheel at $\varphi = 78\,^\circ$ agrees with the forward movement of the separation point between the front and rear wheel as measured in the centerline mean pressure distribution in Figure 5.10. The stations at $\varphi = 123\,^\circ$, $\varphi = 168\,^\circ$ and $\varphi = 213\,^\circ$ are located in the separated flow region, reflected by the increase in level of the PSD's. The fairing configurations appear to exhibit more unsteadiness than the landing gear configuration. The difference between porous or solid fairings is small. At $\varphi = 258\,^\circ$, the flow is on the verge of separation at the underside of both rear and front wheel, explaining the level decrease of the PSD. As for the attached flow regions at $\varphi = 348\,^\circ$ and $\varphi = 303\,^\circ$, the differences between configurations are small here.

Averaging the unsteady pressures yields the mean pressures around the wheel circumference. The obtained centerline pressure distributions in steps of $\Delta\varphi = 45\,^\circ$ largely agree with the centerline pressure distributions as measured by the tappings discussed in section 5.3.1.1.

5.3.2 Wheel shoulder

The rotation of the wheel yields 4 locations for measurement of the shoulder taps: $\varphi = 33\,^\circ, \varphi = 123\,^\circ, \varphi = 213\,^\circ$ and $\varphi = 303\,^\circ$. Pressure distributions are displayed in Figure 5.12, where the normal distance to the local tyre surface indicates the value for Cp. The stagnation area at $\varphi = 33\,^\circ$ is situated between the centerline and inboard side of the wheel, exhibiting a Cp close to 1. The entrapment of the impinging air between the bogie beam and wheel in the brake disc area appears to be a logical explanation for these high Cp's. The centerline locations at $\varphi = 123\,^\circ$ and $\varphi = 213\,^\circ$ are in the separated flow region.

Similar to the centerline pressures, the front and rear wheels largely give the same pressure distributions. The variation between configurations is minimal, agreeing with the image from the centerline pressures that perforating the fairings is not significantly altering the time averaged flow around the wheels.

5.4 Acoustics

The noise of the landing gear model has been investigated using microphone arrays and on-surface microphones. For more details on the apparatus and set-up, the reader is referred to sections 3.4.3.5 and 3.4.3.4.

5.4.1 Microphone array

Beamforming plots centered at $f = 2$ kHz for the different configurations are shown in Figure 5.13. The results reveal a decrease in noise source strength for this particular frequency by application of perforated fairings. From the ceiling view, the main source is located between the wheels and remains there for the different configurations. The ground view from the side wall array shows the noise source reduce in size and move downstream with solid fairings applied. The source further diminishes in strength by application of the perforations.

At higher frequencies the resolution becomes better. Figure 5.14 shows clearly discernible sources centered at 10 kHz. From the ceiling view perspective, the solid fairing configuration is the most quiet for this frequency, showing an almost uniform background noise level. Application of perforations gives perforate noise

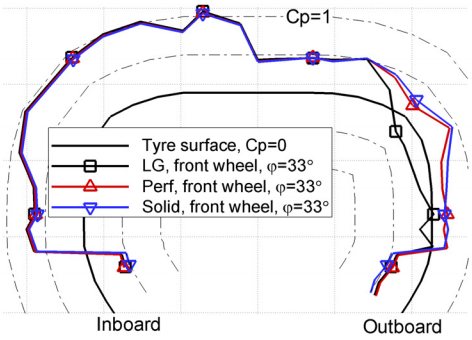

(a) Front wheel, $\varphi = 33\,^\circ$

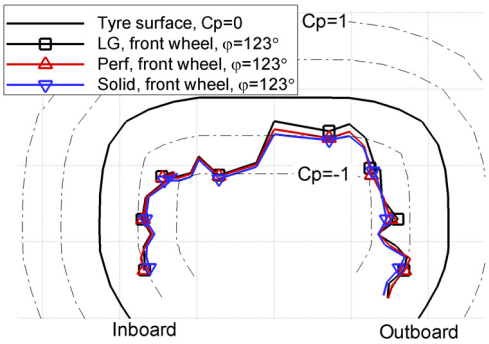

(b) Front wheel, $\varphi = 123\,^\circ$

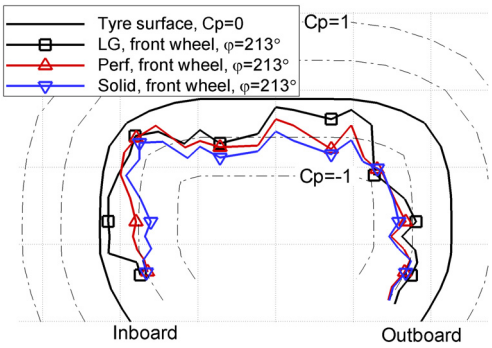

(c) Front wheel, $\varphi = 213\,^\circ$

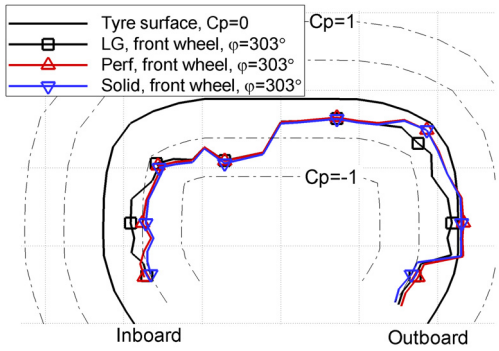

(d) Front wheel, $\varphi = 303\,^\circ$

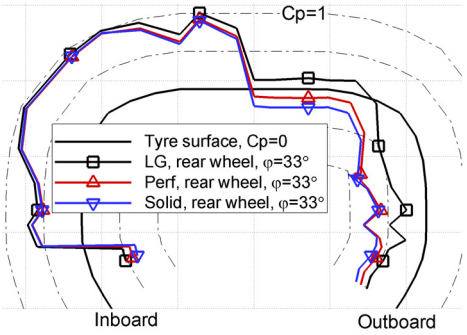

(e) Rear wheel, $\varphi = 33\,^\circ$

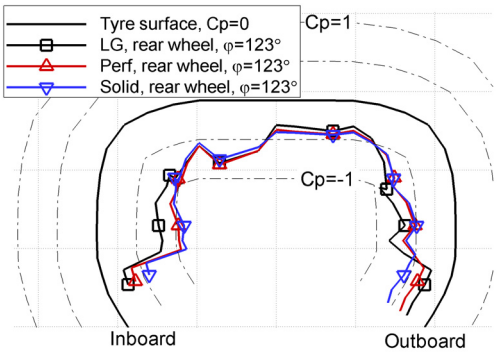

(f) Rear wheel, $\varphi = 123\,^\circ$

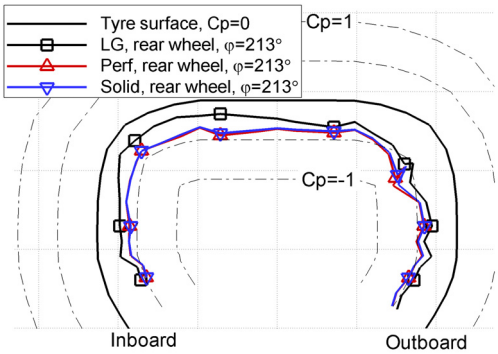

(g) Rear wheel, $\varphi = 213\,^\circ$

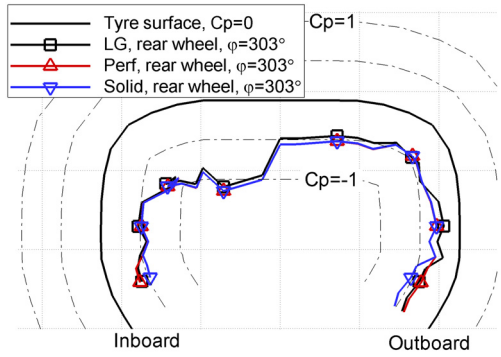

(h) Rear wheel, $\varphi = 303\,^\circ$

FIGURE 5.12: Shoulder pressures on landing gear wheels ($U_\infty = 40$ m/s).

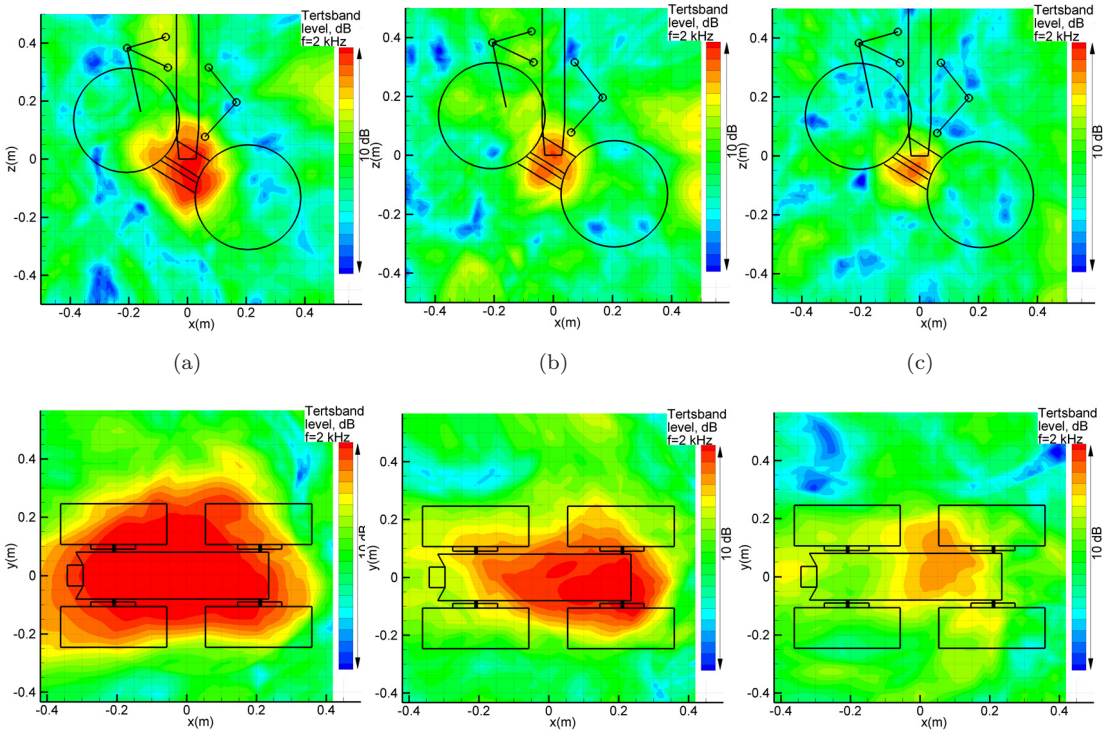

(a) (b) (c)

(d) LG (e) Solid (f) Perf

FIGURE 5.13: Beamforming plots at 2 kHz from ceiling array (above) and side wall array (below) ($U_\infty = 40$ m/s).

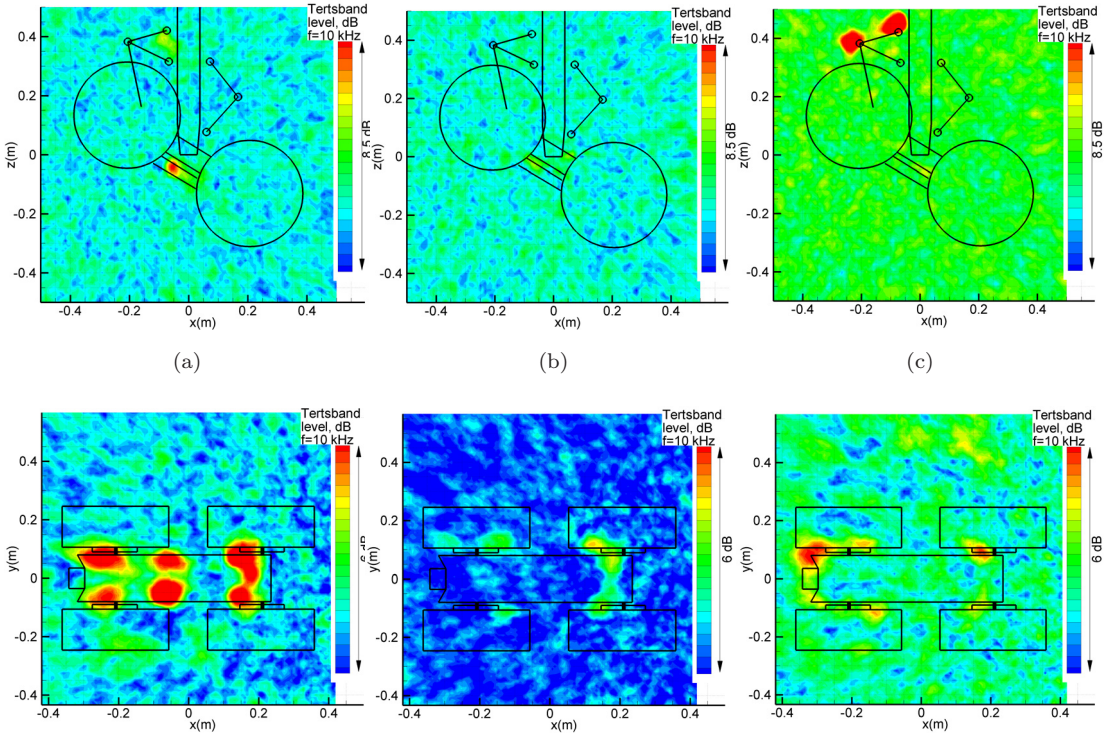

(a) (b) (c)

(d) LG (e) Solid (f) Perf

FIGURE 5.14: Beamforming plots at 10 kHz from ceiling array (above) and side wall array (below) ($U_\infty = 40$ m/s).

on the upper articulation link fairing, elevating the background noise level considerably. Without fairings a noise source emerges between the upper articulation link and the main leg. Additionally, a noise source appears at the brake rod junction with the yoke, plausibly because this item is not shielded anymore by the undertray. The location is confirmed by the ground view localization plot for this configuration in Figure 5.14(d). Shielded by the wheels for the ceiling view, noise sources emerge at the brake discs for the ground view. Application of fairings reduces the impingement velocity on the brake discs and hence the source strength decreases, especially for the front brakes. The perforated fairings in Figure 5.14(f) show the perforate noise again, together with the elevated background noise level. These results clearly show that especially for high frequencies, shielding sharp objects from high speed impingement yields considerable noise reduction.

In order to compare the results over the frequency domain, an area integration is performed over the different beamforming plots. For the ceiling array, values are added in the rectangle between $x = \pm 0.2$ m and $z = -0.1$ m to $z = 0.3$ m. For the side wall array, the rectangle comprises of $x = -0.4$ m to $x = 0.3$ m and $y = \pm 0.15$ m. By covering various parts of the perforated fairings with tape, a study is performed on the effectiveness of perforation location. Referring to drawing LG-400-100 in appendix C, the undertray stagnation area (deduced from the oil flow visualization in Figure 5.1) can be defined as surfaces u3 and u4 combined with the upper half of surfaces a5 and a6. For the articulation link fairing, the stagnation area is defined as the surface with the width of surface a5 (in y-direction) exposed over the total articulation link fairing (referring to drawing LG-400-200).

A comparison showing the effect of the main configurations referenced to the solid fairing configuration is illustrated in Figures 5.15(a) and 5.15(b) for the ceiling and side wall array respectively. The ceiling array shows a noise decrease by application of solid fairings in the mid frequency range and above $f = 10$ kHz. Lower frequencies (below $f = 600$ Hz) are noisier, but the application of perforations makes this low frequency increase disappear. However, exposing all perforations shows perforate noise emerging above $f = 8$ kHz. By exposing only the stagnation area of the perforations, the low frequency decrease persists while the perforate noise disappears. The side wall array corresponding to the ground view shows a similar trend. The plain landing gear configuration is noisier above $f = 1$ kHz instead of the smaller frequency range for the ceiling array. The dip for all presented configurations at the $f = 500$ Hz band indicates a sharp noise increase in this band for the referenced solid fairing configuration. Although

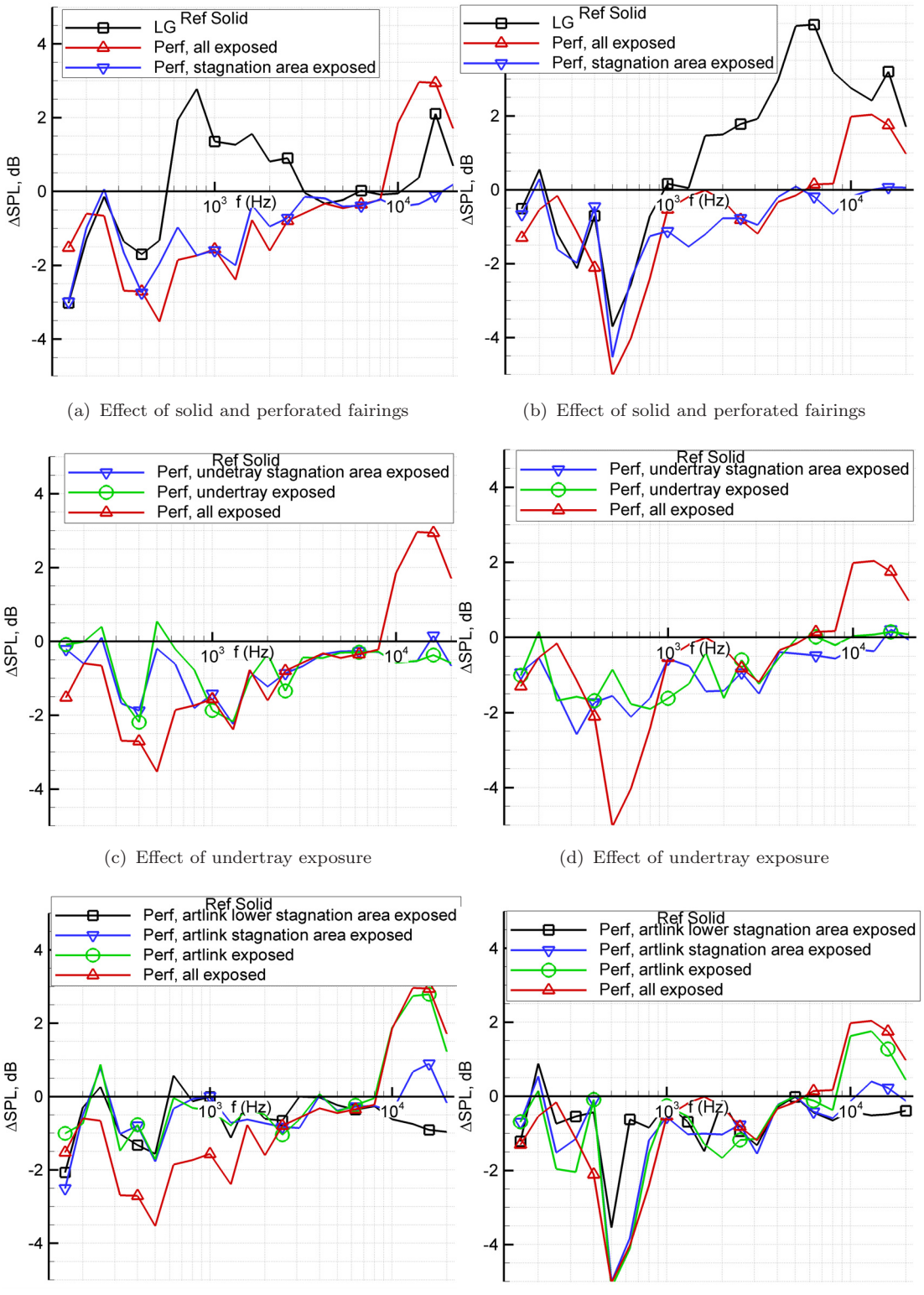

(a) Effect of solid and perforated fairings

(b) Effect of solid and perforated fairings

(c) Effect of undertray exposure

(d) Effect of undertray exposure

(e) Effect of artlink fairing exposure

(f) Effect of artlink fairing exposure

Ceiling array

Integrated between $x = \pm 0.2$ m and $z = -0.1$ m to $z = 0.3$ m

Wall array

Integrated between $x = -0.4$ m to $x = 0.3$ m and $y = \pm 0.15$ m

FIGURE 5.15: Comparison of levels from integrated beamforming plots (referenced to Solid configuration, $U_\infty = 40$ m/s).

the limited resolution of the beamforming plots at this frequency hamper source localization, inspection of the plots reveals a large noise source at the gear for the solid configuration opposed to wake noise sources for the plain landing gear and perforated fairing configuration.

Figures 5.15(c) and 5.15(d) show the effect of perforations on the undertray fairing, while Figures 5.15(e) and 5.15(f) show the effect of perforations on the articulation link fairing for ceiling and side wall array respectively. Referring to drawing LG-400-200 in appendix C, the lower part of the articulation link is defined as surfaces a1, a2 and a3. Interestingly, the sharp low noise decrease at the $f = 500$ Hz band for the ground view can be achieved by solely exposing the stagnation area of the articulation link fairing. Apparently the undertray fairing is not contributing to the sharp noise increase in the $f = 500$ Hz band. Furthermore, it appears that exposing more of the articulation link fairing than the stagnation area does not yield additional noise reduction for both views. The same holds for the undertray fairing. The porosity on both fairings seem to contribute to the total noise decrease in the low and mid frequency range compared to the solid fairing.

For both views, most of the perforate noise originates from the articulation link fairing, especially when areas outside the stagnation area are exposed. Although less dominant, localization plots indicate the presence of perforate noise also on the undertray fairing.

5.4.2 On-surface microphones

The narrowband spectra resulting from the on-surface microphone measurements for various locations (Figure 3.16) are shown in Figure 5.16. The microphones in location 1 and 2 in the back of the strut are swamped by the large scale velocity fluctuations impinging on the back of the strut. Therefore acoustic phenomena are difficult to observe in these spectra and the difference between configurations is hardly discernible. Unsteady pressure sensors are less sensitive than microphones, hence the PSD in Figure 5.9(a) for location 1 shows a different image to the narrowband spectrum in Figure 5.16(a).

At the lower main leg location, the LG configuration shows a hump at $f \approx 104$ Hz or $Str \approx 0.2$ based on freestream velocity and leg diameter. It is believed to correspond to vortex shedding noise from the main leg. Since the fairings upstream of this part of the strut prevent high speed impingement on the main leg, the hump is not visible with the fairings applied. Also, a peak corresponding to perforate

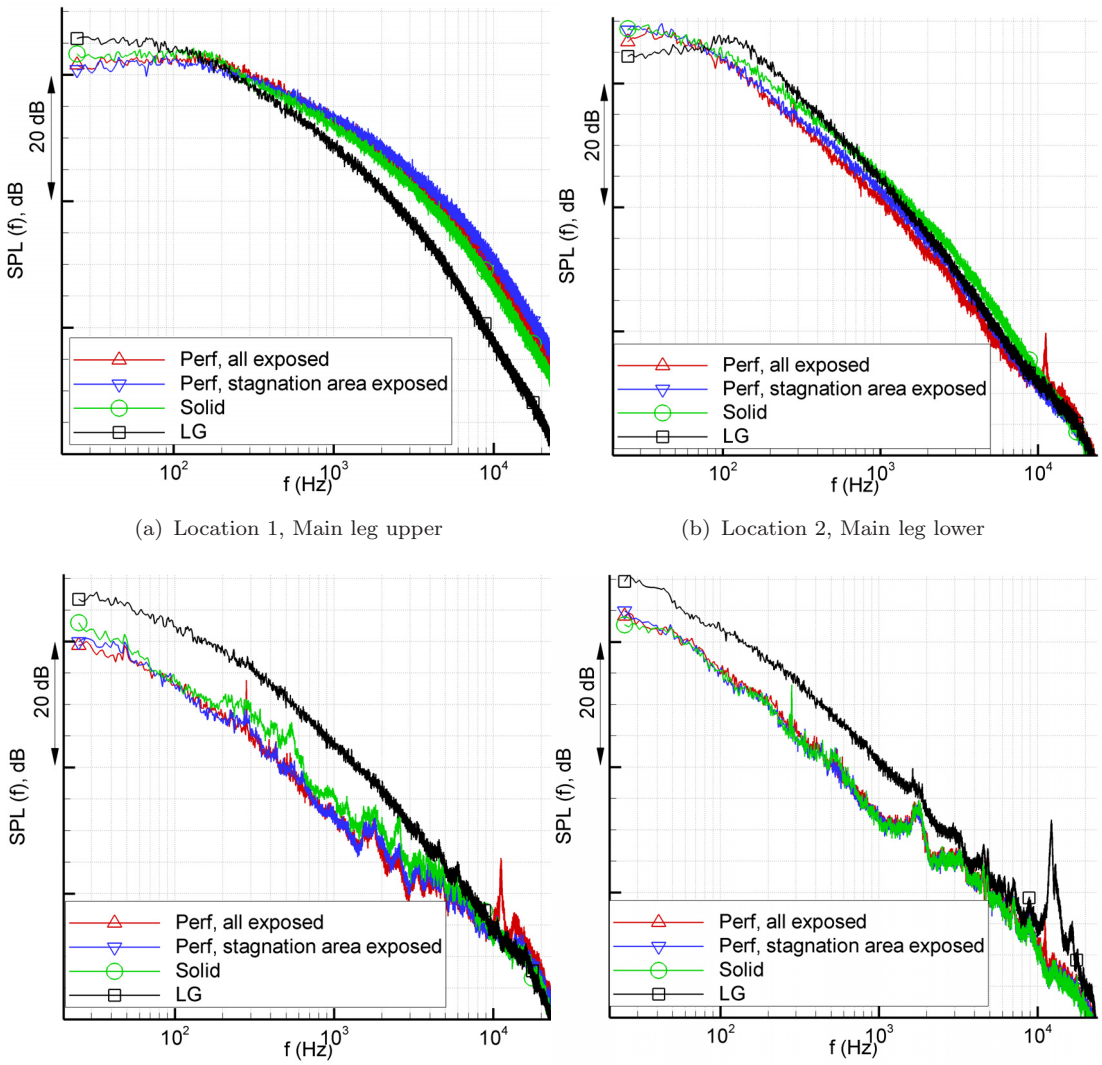

(a) Location 1, Main leg upper

(b) Location 2, Main leg lower

(c) Location 3, Bogie-artlink junction

(d) Location 5, Rear bogie cap

FIGURE 5.16: Narrowband spectra of on-surface microphones on the gear ($U_\infty = 40$ m/s).

noise is visible just above $f = 10$ kHz with all perforations exposed. The peak scales linearly with freestream velocity U_∞. The perforate noise is also picked up by the microphones in locations 3 and 5. The localization study utilizing tape mentioned in section 5.4.1 is also carried out for the microphone measurements. It reveals that the sides of the lower articulation link are responsible for the perforate noise peak just above $f = 10$ kHz. This conforms to the basic model experiment results, which have already showed that the shearing flow past the perforate is causing most of the noise. Comparing the non-dimensional frequency (referenced to local velocity and orifice diameter d_{or}, equation 4.2) with the basic model experiments is difficult since the local velocity in the present experiment is unknown. Estimating this variable at 1.5 times the freestream velocity U_∞ yields agreement between the Strouhal numbers for both experiments at $Str_{d_{or}} = 0.33$.

The spectra of the landing gear configuration at location 3 and 5 show a higher level compared to when the fairings are applied. Flow noise at the microphones is responsible for this higher level, since application of fairings prevents high speed flow in these areas. A clear difference between solid and perforated fairings is noticeable at location 3 above $f = 100$ Hz and almost up to $f = 10$ kHz. This elevated level of the solid fairing configuration in the low to mid frequency range agrees with the integrated wall- and ceiling array beamforming plot levels in Figure 5.15. Subtracting the tertsband averaged levels from this microphone further clarifies the difference between the configurations in Figure 5.17. A comparison to

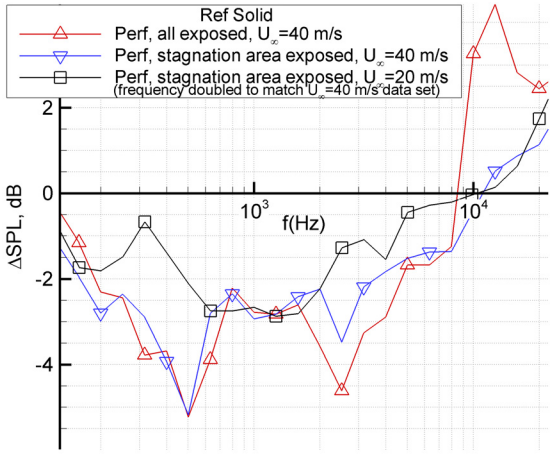

FIGURE 5.17: Subtracted tertsband averaged levels from microphone at bogie-artlink junction (referenced to Solid configuration).

different freestream velocity values shows the frequency content to scale linearly with velocity. Additionally, the difference in magnitude between both configuration increases with freestream velocity. Interaction of the separated flow from the fairings with the downstream gear components is believed to be responsible for the elevated noise level above $f = 100$ Hz. In this frequency range, the solid configuration displays a peak at $f = 560$ Hz which is believed to correspond to the dip in the integrated side wall array levels in Figure 5.15. The study on perforation location effectiveness in section 3.4.3.5 readily showed the articulation link fairing responsible for the noise. The microphone measurements confirm this, although the peak stands out better in the farfield wall array measurements than the nearfield on-surface microphone results.

Above $f = 1000$ Hz, the spectra in the dead flow areas (location 3 and 5) are far from smooth and electronic noise is dominant. Hence the several peaks in this part of the narrowband spectra show no scaling with freestream velocity and are not believed to represent physical phenomena. The difference between all perforations

exposed or only the stagnation point area perforations is hardly noticeable, except from the occurrence of the perforate noise above $f = 10$ kHz.

5.5 Summary

An aerodynamic and acoustic survey has been performed on a look alike A340 Main Landing Gear model to explore the influence of (perforated) fairings on the lower part of the gear.

The oil flow visualization combined with the PIV have clarified flow direction and magnitude around the fairings and in the wake centerplane. The undertray fairing exhibits largely attached flow and divides the airstream in up- and downward direction. The downward pushed flow partly escapes between front and aft wheels and produces a side edge vortex on the undertray side. The shielding of the bogie beam results in a dead flow area directly aft of the rear bogie end. The upward directed flow forms a horseshoe vortex around the lower articulation link fairing and pushes itself further upward on the upper articulation link fairing. The application of the fairings increases the frontal area and therefore bends the flow in the transverse and vertical direction, preventing the airstream from penetrating in the streamwise direction past the gear components. This influences the wake structure and hence the turbulence levels in the proximity of the downstream gear components. The application of the perforations does not significantly alter the flow structure in the wake or in front of the fairings, indicated by equal flow directionality between solid and perforated configurations. However, flow velocity and turbulence levels in the near wake of the torque link are lower than for impermeable fairings. It is hypothesized that by bleeding air, large scale unsteadiness associated with the fairings decreases, resulting in this reduction.

The flow around the wheels is studied by means of centerline and shoulder pressure taps on the tyre surface. The mean surface pressures show few differences between the various configurations, indicating that the time averaged flow around the wheels is largely unaltered by the application of (perforated) fairings. The unsteady surface pressures show increased unsteadiness on the upper side of the rear wheels with fairings applied, pointing towards the undertray side edge vortex and/or the front wheel wake impinging on the rear tyre surface.

Upward from the torque link, unsteady pressure sensor measurements indicate that application of the fairings enhances the vortex shedding from the main leg at this

position. By engineering judgement the overlay between upper articulation link fairing and the main leg is responsible for the enhanced shedding. Downward from this position the fairings prevent high velocities impinging on the main leg. Therefore vortex shedding features at this position of the main leg are only observed without fairings applied. The aerodynamic tests indicate that more porosity is needed ($\sigma > 0.4$) to induce more significant changes to the flow field by perforating the fairings.

The acoustics are studied employing several on-surface microphones and two microphone arrays to measure the ground- and side view noise signature. For both directions, the application of solid fairings has been shown to reduce the noise in the mid and high frequency domain compared to the plain landing gear configuration up to 4.5 dB. However a noise increase is measured in the low frequency domain. The application of perforations reduces the low frequency noise introduced by the solid fairings to values below the plain landing gear configuration for both arrays. Additionally, reduced levels are measured in the mid frequency domain by application of the perforations. The low to mid frequency noise reduction is confirmed by measurements of an on-surface microphone located in the bogie beam - articulation link junction. Combined with the linear velocity scaling of the noise, this points in the direction of large scale separation of the fairings interacting with the downstream gear components responsible for this phenomenon.

To investigate the effectiveness of perforation location, various parts of the fairing surfaces have been covered with tape. It appears that the stagnation area perforations are responsible for most of the noise decrease, for both the articulation link and undertray fairing. Agreeing with basic experiment results, most of the perforate noise is emitted from the lower articulation link sides at a Strouhal number based on orifice diameter d_{or} and local velocity of $Str_{d_{or}} = 0.33$.

The researched on the scaled landing gear model has been presented and published at the 14^{th} AIAA/CEAS Aeroacoustics Conference in Vancouver [92].

Chapter 6

Conclusions and Recommendations

The principle aim of the present research is to investigate and optimize the noise reduction potential by perforating landing gear fairings. The sparse knowledge about this new subject has necessitated a more fundamental study involving a basic fairing-strut configuration, followed by wind tunnel tests on a simplified landing gear configuration featuring perforated fairings. Conclusions that can be drawn from the basic model research are summarized in the first section. Thereafter conclusions from the landing gear model research will be summarized. Results from both cases are combined resulting in recommendations for application to landing gear. Most of the research in this thesis can be read in published format [90, 91, 92].

6.1 Basic Model Research

Wind tunnel tests of a simplified fairing-cylindrical strut model have been performed to investigate the use of perforated fairings for passive noise control. Both aerodynamics and the related acoustics are studied employing two different wind tunnel facilities and an anechoic chamber.

- Bled mass flux
  The bled mass flux through the perforate follows a linear trend with varying porosity. A dedicated two-dimensional RANS simulation predicts a mass flux between 26% and 39% of the freestream flux (based on the perforated

frontal area) for porosities between 33% and 55%. Application of an edge radius of $r_{edge}/d_{or} = 0.14$ increases the effective porosity by 14%. Exposing more than $\varphi = \pm 45\,^{\circ}$ of the perforate does not yield extra bled air.

- Deflected velocities
  Application of perforated fairings reduces the flow velocities to the side of the shell. Quantitatively, a fairing with 42% porosity reduces the maximum flow velocity sideways of the shell by 18% resulting in a reduction of unwanted high speed flow deflection.

- Vortex shedding
  With respect to the unsteady flow field, the application of perforated fairings shows a dual shear layer exhibiting roughly half the vorticity of the solid fairing, resulting in weaker vortices of smaller scale. The distinct spectral peak of velocity fluctuations related to the vortex shedding of the solid model disappears. The anechoic chamber test results show that the associated broadband noise level is reduced as well.

- Influence of exposure
  Exposing the perforate on the suction side of the shell bleeds less air and is therefore less effective in reducing the magnitude of the large scale velocity fluctuations. However, when the circular cylinder is replaced by an H-beam, it is hypothesized that the beam forces outflow through the perforate on the shell suction side and thereby further reduces the velocity fluctuations and related acoustics.

- Influence of porosity
  Varying the porosity of the shell does not significantly modify wake structure and associated acoustics. However, a test with a noisy H-beam replacing the cylinder indicates that increasing porosity can result in adverse noise effects due to the bled mass flow washing the strut.

- Perforate noise
  The perforate is shown to create noise at higher frequencies centered around $Str_{d_{or}} = 0.33$. This opens up the possibility for tailoring this noise phenomenon above the upper limit of the audible range. Since the shearing flow past the perforate is responsible for the high frequency noise, one should take into account that both intensity and spectral content are dictated by the local velocity past the perforate instead of freestream velocity.

- Other noise sources
  The microphone array measurements allowed for an inspection of other noise sources making their appearance at higher frequencies. The configurations featuring a sharp shell trailing edge were found to produce distinct trailing edge noise at a Strouhal number of 0.2 based on edge thickness and local velocity. Junction flow effects (horseshoe vortices) appear at the intersection between ground- and endplates and model for the solid fairing configuration.

6.2 Landing Gear Model Research

An aerodynamic and acoustic survey has been performed on a look alike A340 Main Landing Gear model to explore the influence of (perforated) fairings on the lower part of the gear.

- The oil flow visualization combined with the PIV have clarified flow direction and magnitude around the fairings and in the wake centerplane. The undertray fairing exhibits largely attached flow and divides the airstream in up- and downward directions. The downward pushed flow partly escapes between the front and aft wheels and produces a side edge vortex on the undertray side. The shielding of the bogie beam results in a dead flow area directly aft of the rear bogie end. The upward directed flow forms a horseshoe vortex around the lower articulation link fairing and pushes itself further upward on the upper articulation link fairing.

- The application of the fairings increases the frontal area and therefore bends the flow in transverse and vertical directions, preventing the airstream from penetrating in streamwise direction past the gear components. This influences the wake structure and hence the turbulence levels in the proximity of the downstream gear components. The application of the perforations does not significantly alter the flow structure in the wake or in front of the fairings, indicated by equal flow directionality between solid and perforated configurations. However, flow velocity and turbulence levels in the near wake of the torque link are lower than for impermeable fairings. It is hypothesized that by bleeding air, large scale unsteadiness associated with the fairings decreases resulting in this reduction.

- The flow around the wheels is studied by means of centerline and shoulder pressure taps on the tyre surface. The mean surface pressures show

few differences between the various configurations, indicating that the time averaged flow around the wheels is largely unaltered by application of (perforated) fairings. The unsteady surface pressures show increased unsteadiness on the upper side of the rear wheels with fairings applied, pointing towards the undertray side edge vortex and/or the front wheel wake impinging on the rear tyre surface.

- Upward from the torque link, unsteady pressure sensor measurements indicate that application of the fairings enhances the vortex shedding from the main leg at this position. By engineering judgement the overlay between upper articulation link fairing and the main leg is responsible for the enhanced shedding. Downward from this position the fairings prevent high velocities impinging on the main leg. Therefore vortex shedding features at this position of the main leg are only observed without fairings applied.

- The acoustics are studied employing several on-surface microphones and two microphone arrays to measure the ground- and side view noise signature. For both directions, the application of solid fairings has been shown to reduce the noise in the mid and high frequency domain compared to the plain landing gear configuration by up to 4.5 dB. However a noise increase is measured in the low frequency domain. The application of perforations reduces the low frequency noise introduced by the solid fairings to values below the plain landing gear configuration for both arrays. Additionally, reduced levels are measured in the mid frequency domain by application of the perforations. The low to mid frequency noise reduction is confirmed by measurements of an on-surface microphone located in the bogie beam - articulation link junction. Combined with the linear velocity scaling of the noise, this points in the direction of large scale separation of the fairings interacting with the downstream gear components responsible for this phenomenon.

- To investigate the effectiveness of perforation location, various parts of the fairing surfaces have been covered with tape. It appears that the stagnation area perforations are responsible for most of the noise decrease, for both the articulation link and undertray fairing. Agreeing with basic experiment results, most of the perforate noise is emitted from the lower articulation link sides at a Strouhal number based on orifice diameter d_{or} and local velocity of $Str_{d_{or}} = 0.33$.

6.3 Recommendations

The synthesis of the conducted studies has shed new light on the application of perforated fairings for landing gear noise control. The resulting guidelines for application to landing gear are summarized firstly, after which recommendations for future work are given.

6.3.1 Application to landing gear

The section summarizes how the findings of the discussed research can be applied to the landing gear and its fairings. Especially for the basic model research, one should be careful to translate findings directly onto the landing gear. Certain measured flow features are regarded as typical for the basic model geometry. For the landing gear model research, one should bear in mind that there are differences compared to real landing gear (level of detail, model scale, omittance of upper landing gear parts, gear inclination and freestream velocities).

Another issue not to be overlooked is the influence of modifications such as perforated fairings on the aerodynamic performance of the landing gear, see section 3.1. The application of perforations to the fairings will reduce the effective frontal area and is therefore expected to reduce the aerodynamic drag of the undercarriage. Although it has not been possible to incorporate balance measurements in the present test campaign, through the use of engineering judgement the drag reduction on the gear itself is not expected to exceed 20%. However, in the light of the real engineering application of noise reduction for landing gear the following recommendations can be made.

- Porosity
  Bleeding air through the fairing reduces the formation of large scale unsteadiness associated with the fairing. By bleeding too much air, high velocities past small scale landing gear components will reintroduce high frequency noise. The best solution should incorporate a compromise of these effects. The fairings used in the landing gear model experiments feature a porosity of 40%. The aerodynamic survey indicated few differences by application of these perforations, while there was no sign of high frequency noise increase. Therefore it is recommended to attempt higher porosities up to 50%. Trial and error seems to be the best way to determine the porosity that yields the quietest landing gear configuration.

- Location of porosity

  It has appeared that the bled mass flux does not significantly increase by perforating outside the stagnation area. This stagnation area can roughly be defined by non-dimensional pressures $Cp > 0$. For some cases (shielded H-beam in basic model research), perforations outside the stagnation area can be beneficial due to outflow past the perforate in this area. However, this finding is not regarded relevant for landing gears, since the frontal area of the shielded gear parts is significantly smaller. The landing gear model research has confirmed an identical noise decrease in the lower to middle frequency range for when all or only the stagnation area perforations are exposed. Additionally, the perforations outside the stagnation area are prone to create self-noise. Therefore it is recommended to apply perforations solely in the stagnation area of the fairings.

- Orifice geometry

  Orifice geometry influences the unwanted noise associated with the perforate. The perforate noise has been found to scale with orifice diameter around $Str_{d_{or}} = 0.33$. This indicates that hole diameters d_{or} smaller than 3 mm result in noise outside the audible range for approach conditions. Additionally, the higher the frequency of the noise, the more it is attenuated by atmospheric absorption before it reaches the receiver. Therefore it is recommended to employ orifice diameters smaller than 3 mm. However, one should realize that employing an orifice diameter of $d_{or} = 3$ mm or less yields few pitch between the holes and can thus result in unstable structures for high porosities ($> 50\%$).

  Further more it is recommended to round off the hole edges with an edge radius. In order to avoid a feedback mechanism for edge-tones, an edge radius of r_{edge}/d_{or} between 0.1 and 0.2 should be applied. One should bear in mind that application of a hole edge radius increases the effective porosity by enlarging the vena contracta.

- Fairing shape

  Fairing shape has readily been optimized to prevent interaction of high speed flow with landing gear components. The undertray shape is designed to deflect the air downwards to minimize interaction with wheels and articulation link fairing. High speed flow past sharp trailing edges can be an important source of high frequency narrow band noise, as was shown in the basic model experiments. Additionally, junction flow effects can also be significant noise contributors. It is recommended to redesign the fairings with these factors

in mind.

6.3.2 Future work

The recommendations for future work on the subject are highlighted below.

- As was pointed out above, it is recommended to optimize the fairings with respect to the porosity parameter. Trial and error is judged as the best method to achieve this. Hence several fairings featuring various porosities are to be tested on their acoustic performance.
- The landing gear model research in the current work has been restricted to the undertray and articulation link fairings. It is recommended to investigate the feasibility of perforations to the other fairings (such as the leg door fairing) and include the total landing gear in the research.
- In the anechoic chamber tests, the basic model research has been extended with an H-beam replacing a circular cylinder as a strut. The lack of complimenting aerodynamic measurements for this configurations has complicated finalizing the corresponding conclusions. Therefore it is recommended to extend the research on this configuration by performing aerodynamic measurements (PIV, HW) and computations (RANS).

Appendix A

Details of Computational Simulation

Spatial discretization of the volume around a perforate is an elaborate task, meshing the curving geometry of numerous holes. Switching from a three- to a two-dimensional geometry significantly reduces the amount of work needed. A modified cross section of the basic model experiment is suitable for a two-dimensional flow computation. A two-dimensional simulation would resemble the flow through slots instead of perforates. The effect of bleeding air through the shell is similar for both cases as long as the porosity is equal. Aerodynamic performance of a non-perforated and perforated shell-strut combination can be compared. The advantage of CFD is that the whole flow field is mapped and it therefore enables to interrogate all the modelled flow parameters. However since the flow is modelled, the validity of the computational data is sometimes questionable. If time-averaged flow behavior is sought after, the answer of present CFD can be satisfactory. Unsteady quantities should be interpreted with more care.

A.1 Preliminary Modelling Options

FLUENT 6.2.16 is used for the present computations, which can perform finite volume Reynolds Averaged Navier-Stokes (RANS) simulations as well as Large Eddy Simulations (LES). These are the main options for incorporating turbulence in the computation, since a Direct Numerical Simulation (DNS) that resolves the turbulence to its smallest scales is not regarded as a viable option.

The first option decomposes the variables in the Navier Stokes (N-S) equations into an ensemble-averaged and fluctuating part. This results in an extra term in the momentum equation, the Reynolds stress tensor. The models available to quantify the turbulent fluctuations in the Reynolds stresses can be divided into Boussinesq or the Reynolds Stress Transport Model. The first one relates the Reynolds stresses to a turbulent viscosity μ_t and the mean velocity gradients. Herein μ_t is treated as an isotropic scalar. The Reynolds Stress Transport Model solves transport equations for each of the terms in the Reynolds stress tensor, hence the fact that turbulence is not always isotropic is taken into account. However, often the additional computational expense of solving these transport model equations can not be justified.

Turbulence models employing the Boussinesq approach include the Spalart Allmaras model (one equation for solving $\tilde{\nu}_t$) and $k-\epsilon$ and $k-\omega$ models (two equations for solving $\tilde{\nu}_t$). The modified turbulent viscosity $\tilde{\nu}_t$ is a working variable related to μ_t. Different options are available for the latter two models. The SST $k-\omega$ model combines good performance in wall bounded flows with separated flow regions (wake areas), which is an important aspect of the flow to be simulated. The Spalart Allmaras model is designed to perform well in wall bounded, attached flow but also is known to be over dissipative. This model being computationally inexpensive with similar grid requirements as for the SST $k-\omega$ model makes both models a feasible option to try out.

The second option filters out the smaller eddies (usually smaller than the cell size) and uses subgrid scale models to model them. Because these small scale eddies are believed to be more isotropic than the larger ones, this makes it easier to find suitable subgrid scale models. Since the filtering process is not applied to all turbulent length scales like the averaging in the RANS approach, less of the turbulence is modelled and more is calculated. Generally speaking grid requirements are more severe for LES and high order spatial discretization is necessary for proper results, which makes this option computationally too expensive. The present computation is in two dimensions and three dimensions are needed to directly resolve the larger scale turbulence in LES. Therefore RANS simulations are carried out with the FLUENT 6.2.16 package and are discussed below. More details on turbulence modelling can be found in [93] and [94].

A.2 Computational Model

A preliminary choice of modelling options was discussed in section A.1. Employing an unsteady RANS simulation, still leaves a wide range of modelling options to choose from.

Although only time-averaged quantities are of interest for the computations, the corresponding basic model flow physics is essential unsteady. Therefore the unsteady solver is used and statistics are calculated to obtain mean values. The most important settings for perforate and solid simulations are summarized in Table A.1. The pressure far field boundary condition requires specification of

Table A.1: Settings for computational simulations.

Inflow/outflow boundary condition	Pressure far field
Side walls boundary condition	Symmetry
U_∞	30 m/s
Turbulence model	SST k-ω
Turbulent viscosity ratio	1
Turbulent intensity	10%
Numerical method	Segregated solver
Density evaluation	Ideal gas
Temporal discretization	Second order implicit

static conditions and free stream Mach number to model a free stream condition at infinity. In practice these values are used as input to calculate the outgoing or incoming Riemann invariant, depending on the boundary having respectively outflow or inflow. This Riemann invariant is combined with the complementary invariant based on the values of the cell adjacent to the boundary face to give the actual flow variables at the boundary. To take into account the blockage effect of the walls, a symmetry boundary condition has been imposed to the side walls. Not taking into account the displacement effect of the side wall boundary layer is expected to have a negligible influence on the results.

The segregated solver is used, which links the governing equations (e.g. momentum, continuity) using a pressure-velocity correction. The other option is the coupled solver which solves all the governing equations simultaneously. The segregated solver requires less memory and converges faster than the coupled solver. Density is evaluated by the ideal gas law instead of being treated like a separate

variable in the governing equations. This method of accounting for compressible flow effects can be justified, since no discontinuities like shock waves are expected to be present.

First simulations were carried out using the Spalart Allmaras turbulence model, this model being computationally the most inexpensive. The absence of the vortex shedding phenomenon in the solid configuration for this simulation is addressed to the overly dissipative nature of this model. The application of the SST k-ω model does yield the vortex shedding. This behavior is believed to conform more to reality and previous research [95] has indicated the superiority of this model for a similar geometry at comparable Reynolds numbers. Therefore this turbulence model is used for the present RANS-computations.

A.3 Geometry Construction

Because the perforate is essential three dimensional, some modifications will have to be made to the geometry. To keep the same porosity as the experimental model, spacing or hole sized has to be adjusted. For a hexagonal structure, porosity σ depends on hole diameter d_{or} and pitch p_{or} obeying equation 3.3.3, while for a two-dimensional arrangement $\sigma = \frac{d_{or}}{p_{or}}$. Hole size is adjusted for a constant spacing. Details of the simulated shells are given in Table A.2 together with a picture in Figure A.1. The rest of the geometrical parameters (fairing diameter D_f, fairing

Table A.2: Details of the simulated perforates.

Name	d_{or} (mm)	p_{or} (mm)	σ (%)	r_{edge}/d_{or}	Angular location of perforate (φ)
solid+cylinder	-	-	0	-	-
perf33 ($\pm 45\,^\circ$)+cylinder	1.65	5.00	33	0	$\pm 90\,^\circ$
perf33 ($\pm 90\,^\circ$)+cylinder	1.65	5.00	33	0	$\pm 90\,^\circ$
perf39 ($\pm 45\,^\circ$)+cylinder	2.15	5.50	39	0	$\pm 45\,^\circ$
perf42 ($\pm 45\,^\circ$)+cylinder	1.97	4.70	42	0.14	$\pm 45\,^\circ$
perf48 ($\pm 45\,^\circ$)+cylinder	2.88	6.00	48	0	$\pm 45\,^\circ$
perf55 ($\pm 45\,^\circ$)+cylinder	4.95	9.00	55	0	$\pm 90\,^\circ$
perf55 ($\pm 90\,^\circ$)+cylinder	4.95	9.00	55	0	$\pm 90\,^\circ$

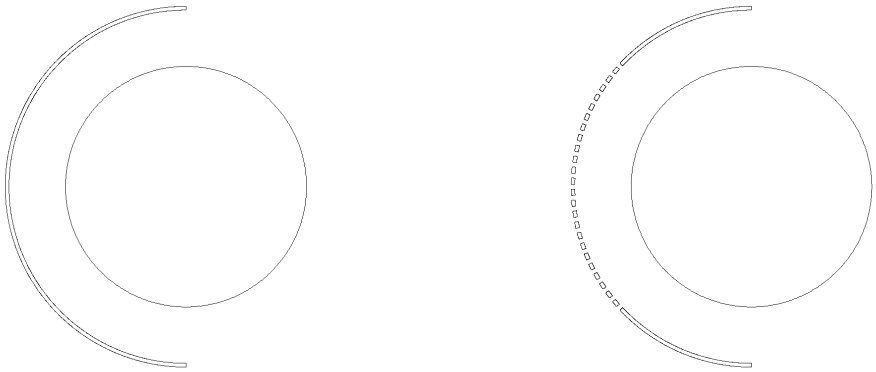

(a) solid+cylinder (b) perf42(±45 °)+cylinder

FIGURE A.1: Geometry of two simulated configurations.

thickness t_f, strut diameter D_s and relative distance between the two components) is conform the basic model experiment.

Instead of performing a free field computation, it is chosen to take into account the presence of the walls. This enables a more direct comparison to experimental results, since they are subject to a significant blockage of 17%. Therefore walls are placed at a distance of 300 mm from the model center to incorporate this effect.

A.4 Grid Construction

A hybrid grid approach is employed, using a structured grid for sufficient resolution in the boundary layers and wake area. Unstructured blocks link these areas together, preventing highly skewed and high aspect ratio cells and also reducing the total number of cells. Care is taken to have rectangular cells of equal size at these interfaces to prevent distortion of the flow field.

The area around one hole is meshed and then copied radially, using the symmetry of the holes. A visualization of the grid is present in Figure A.2. The flow inlet and outlet are set at 20 shell diameters from the model center. The first cell of the wall is set at $y^+ = 1$, corresponding to grid requirements for the turbulence models used. For a definition of y^+, the reader is referred to Nieuwstadt[96]. A first estimation for y^+ is obtained from Blasius' flat plate boundary layer analysis using diameter of the shell as the length scale. This value is refined using the values of the first simulation. It appeared that while the estimation gave $y = 1 \times 10^{-5}$ mm for $y^+ = 1$, this value could be adjusted to $y = 3 \times 10^{-3}$ mm leading to a

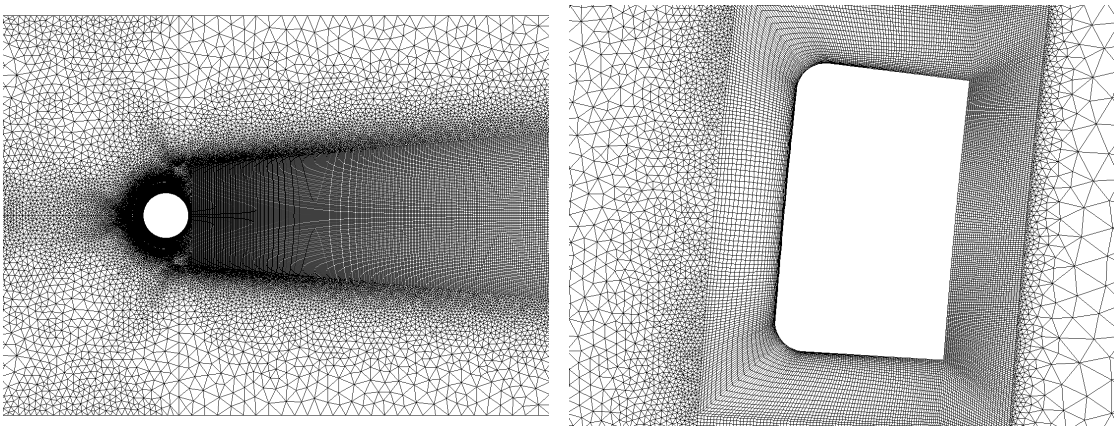

(a) Mesh topology (b) Mesh around a hole

FIGURE A.2: Grid details

large reduction in number of cells.

A.4.1 Grid density

A grid convergence study is performed to determine if the grid is fine enough to capture the relevant flow physics. The perf42 ($\pm 45\,^{\circ}$) case is chosen to evaluate grid resolution around the perforate and the wake area behind the model. Coarse, medium and fine grids are constructed. Spacing details for the structured parts of the medium case are summarized in Table A.3. The number of cells on each edge

TABLE A.3: Structured grid spacing for perf42 ($\pm 45\,^{\circ}$) case (medium refinement).

structured grid area	tangential/streamwise direction			normal/lateral direction		
	nr cells	begin spacing (mm)	end spacing (mm)	nr cells	begin spacing (mm)	end spacing (mm)
Hole BL	338	roughly equidistant		20	$3 \times 10^{-}3$	$1 \times 10^{-}1$
Strut BL	1000	equidistant		24	$3 \times 10^{-}3$	$1 \times 10^{-}1$
Wake	750	1.5	6	150	equidistant	

is increased with $\sqrt{2}$ per refinement step, resulting in $0.41 \times 10^6, 0.77 \times 10^6$ and

1.46×10^6 number of cells for the coarse, medium and fine grid respectively. Time averaged pressure distribution is monitored for the different grids in Figure A.3. For both shell and strut it appears that refinement from the coarse grid yields a

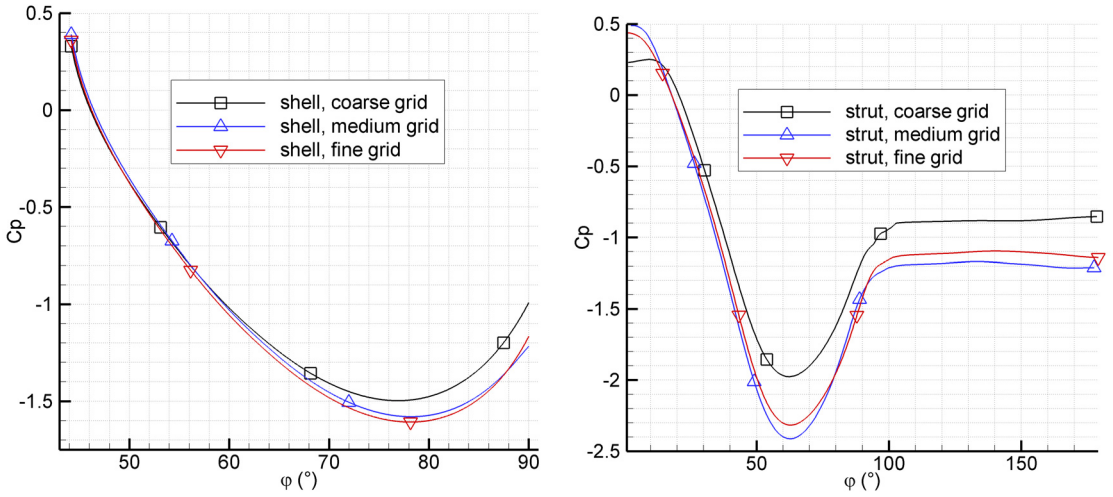

(a) Shell (b) Strut

FIGURE A.3: Grid convergence on time-averaged pressure distribution of the perf42 ($\pm 45\,^\circ$)+cylinder model, $U_\infty = 30m/s$.

considerable variation (a decrease of 33% on the base pressure of the strut), while refinement from medium to fine grid hardly yields changes (a maximum variation of $\Delta Cp \approx 0.05$ on the strut). This indicates that the essential flow physics is captured by the medium grid and time averaged flow quantities are accurately represented. Therefore it is chosen to use the tangential and normal grid spacing settings of the medium grid for the various cases in Table A.2.

A.5 Temporal and Iterative Convergence

Previous studies on cylinder flow [95] indicate that about 300 time steps per shedding cycle are sufficient to ensure adequate temporal resolution. In this case that would yield a time step size of $\Delta t = 5 \times 10^{-5}$ s. The perforate is causing a high frequency modulation on top of the large scale shedding fluctuation. To resolve this phenomenon would require an even smaller time step. However, the aim of the present calculations is to quantify the time-averaged flow behavior and therefore it is not required to resolve the modulation. Therefore a time step size of $\Delta t = 5 \times 10^{-}5$ s is employed for the present computations. The number of sub-iterations is fixed to 30 to ensure that the residuals drop around three orders of magnitude or more for each sub-iteration.

Iterative convergence is assessed using non-dimensional time t_D

$$t_D = \frac{tU_\infty}{D_f} \tag{A.1}$$

The physical significance can be interpreted as the number of shell diameters that are travelled through the domain. Rule of thumb is one streamwise travel through the domain plus 10 to 20 non-dimensional times to obtain a 'dynamically' steady state, resulting in $t_D \approx 60$.

Current computations are carried out on the *Iridis2* network of the University of Southampton. In order to obtain $t_D = 60$ for the perf42($\pm 45\,^\circ$) medium grid using 4 double processor nodes would take 40 days. The perf33 and perf55 configurations feature perforations up to $\pm 90\,^\circ$ instead of $\pm 45\,^\circ$ and grid size is predominantly influenced by the dense mesh around the perforate. The strategy for these simulations is to run $t_D \approx 40$ employing a larger time step to capture the large scale vortex shedding and then refine the time step for 10 non-dimensional times. Since temporal resolution can be lower for the solid configuration, faster convergence is possible for this configuration.

A.6 Validation

Any attempt to numerically model flow around a bluff body at higher Reynolds numbers is complicated by the fact that the flow is three dimensional, raising doubts about the applicability of two-dimensional simulations. Additionally, RANS turbulence modelling for separated flows is known to be too dissipative, reducing the amount of unsteadiness [95]. Nonetheless, two-dimensional unsteady RANS simulations can be regarded as an important tool, since it may yield deeper insight into the physics at a relatively low cost. In the present case, the cost of alternative options is too high, taking into account the complexity and number of cells needed to resolve the flow around numerous holes. Since only time-averaged quantities are sought after, a validation is performed based on time-averaged velocity.

A comparison is performed with data from the basic model experiments. The time averaged flow velocity of the solid and the perf42($\pm 45\,^\circ$) model is compared to PIV-data in Figure A.4. The wake in the PIV-data extends further downstream compared to the computations for both configurations. However there is good agreement between the wake structures, illustrated by the shape and relative position of the low velocity regions in the wakes. Stretching the CFD-data

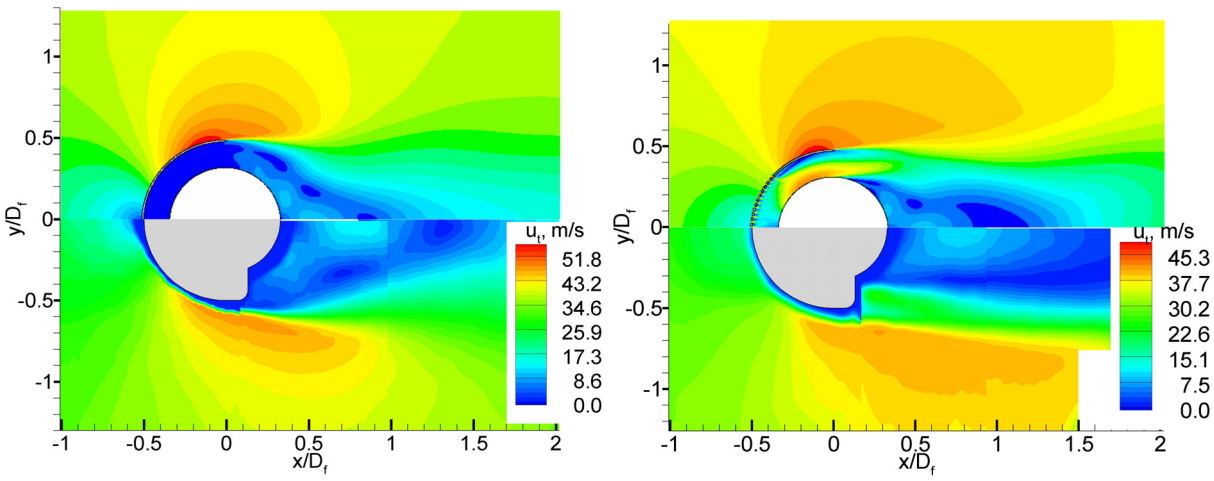

(a) solid+cylinder

(b) perf42 (±45 °)+cylinder

FIGURE A.4: Comparison of time-averaged velocity distribution between CFD (upper) and PIV (lower), $U_\infty = 30m/s$.

by 33% in streamwise direction would yield good agreement for the solid model, the perf42 model seems to need even more stretching. A possible explanation for this difference is the dissipative nature of the CFD shortening the wake. In addition to that, discrepancies can arise due to the fact that wind tunnel flow is not strictly two-dimensional and the vortex shedding is influenced by aspect ratio and end effects. However, qualitatively the prediction of the difference between the perf42 and solid configuration is satisfactory. There is an overall agreement in the prediction of the time averaged flow features.

Appendix B

Technical Drawings of the Basic Model Experiment

Item no.	Description	Drawing nr.	Figure nr.
1	Cylindrical shell, perforated and non-perforated edition	CB-SU-PP-1001	B.2(a)
2	Small and big strut	CB-SU-PP-1002	B.2(b)
3	Inserts for small and big strut	CB-SU-PP-1003-U, CB-SU-PP-1003-L	B.2(c), B.2(d)
4	Dummy part	CB-SU-PP-1004	B.2(e)
5	Dummy part flange for ceiling suspension	CB-SU-PP-1005	B.2(f)
6	Upper brackets	CB-SU-PP-1006	B.2(g)
7	Lower bracket	CB-SU-PP-1007	B.2(h)
8	Suspension pin	CB-SU-PP-1008	B.2(i)
9	Ceiling plate	-	-
10	Lower bracket	-	-
-	Cross sectional view of basic model	-	B.2(j)

TABLE B.1: Parts list corresponding to Figure B.1

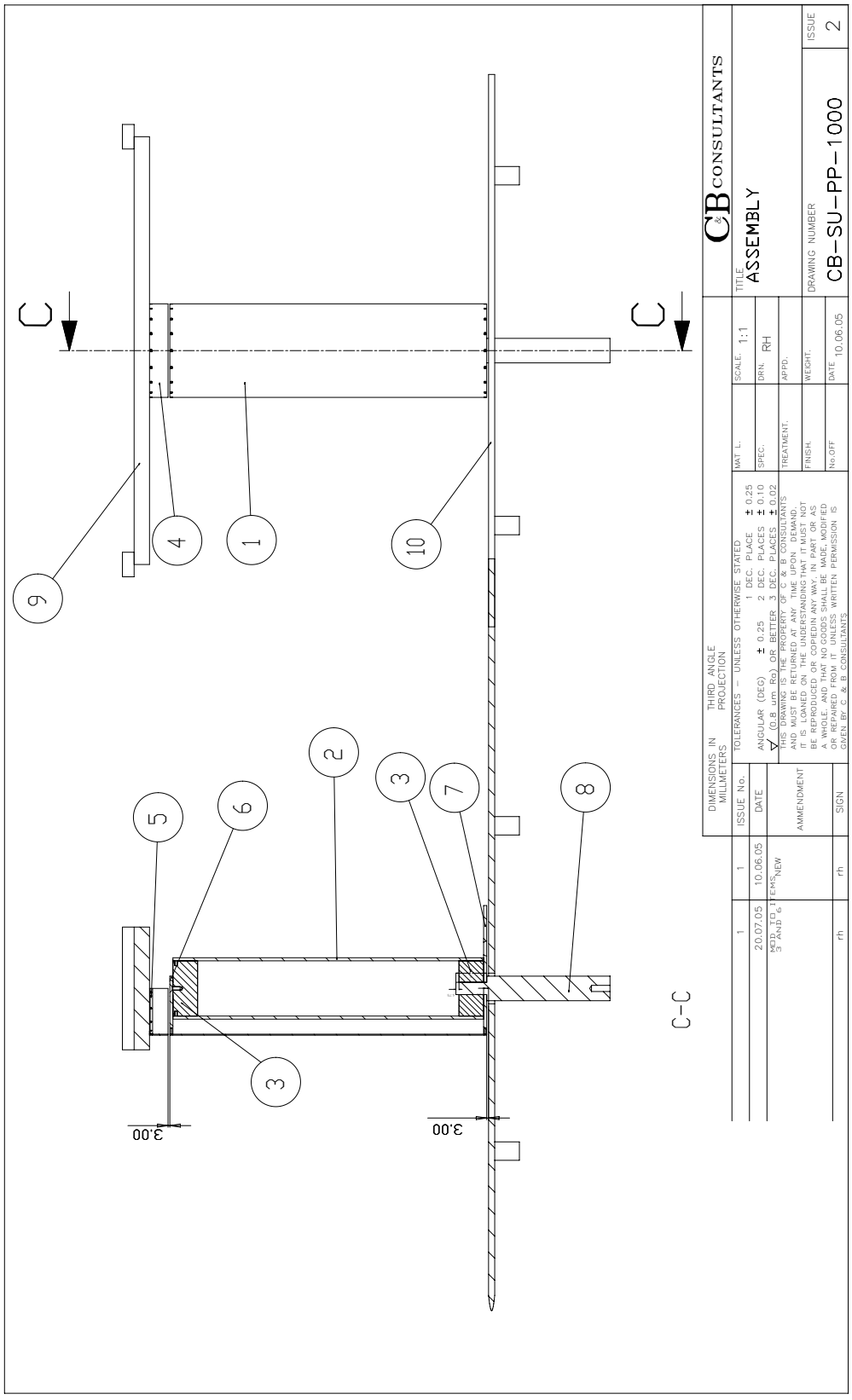

FIGURE B.1: Drawing of parts and test set-up.

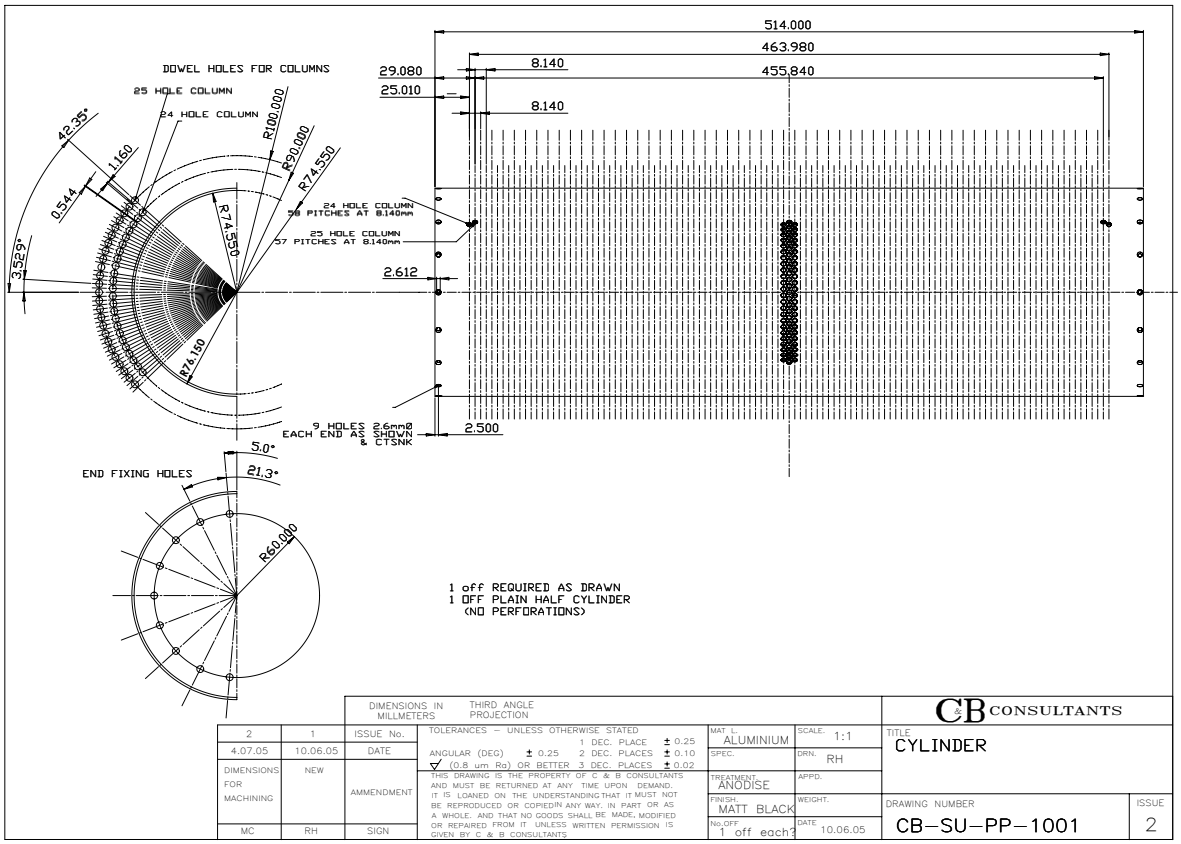
514.000
463.980
455.840
29.080
25.010
8.140
8.140
DOWEL HOLES FOR COLUMNS
25 HOLE COLUMN
24 HOLE COLUMN
42.35°
1.160
0.544
R100.000
R90.000
R74.550
R74.550
24 HOLE COLUMN
38 PITCHES AT 8.140mm
25 HOLE COLUMN
37 PITCHES AT 8.140mm
3.529°
2.612
R74.150
9 HOLES 2.6mmØ
EACH END AS SHOWN
& CTSNK
2.500
5.0°
END FIXING HOLES
21.3°
R60.000
1 off REQUIRED AS DRAWN
1 OFF PLAIN HALF CYLINDER
(NO PERFORATIONS)
DIMENSIONS IN MILLMETERS
THIRD ANGLE PROJECTION
TOLERANCES – UNLESS OTHERWISE STATED
1 DEC. PLACE ± 0.25
ANGULAR (DEG) ± 0.25 2 DEC. PLACES ± 0.10
(0.8 um Ra) OR BETTER 3 DEC. PLACES ± 0.02
THIS DRAWING IS THE PROPERTY OF C & B CONSULTANTS AND MUST BE RETURNED AT ANY TIME UPON DEMAND. IT IS LOANED ON THE UNDERSTANDING THAT IT MUST NOT BE REPRODUCED OR COPIEDIN ANY WAY, IN PART OR AS A WHOLE, AND THAT NO GOODS SHALL BE MADE, MODIFIED OR REPAIRED FROM IT UNLESS WRITTEN PERMISSION IS GIVEN BY C & B CONSULTANTS
2 | 1 | ISSUE No.
4.07.05 | 10.06.05 | DATE
DIMENSIONS FOR MACHINING | NEW | AMMENDMENT
MC | RH | SIGN
MAT'L. ALUMINIUM
SPEC.
TREATMENT. ANODISE
FINISH. MATT BLACK
No.OFF. 1 off each?
SCALE. 1:1
DRN. RH
APPD.
WEIGHT.
DATE 10.06.05
C&B CONSULTANTS
TITLE. CYLINDER
DRAWING NUMBER CB–SU–PP–1001
ISSUE 2

(a)

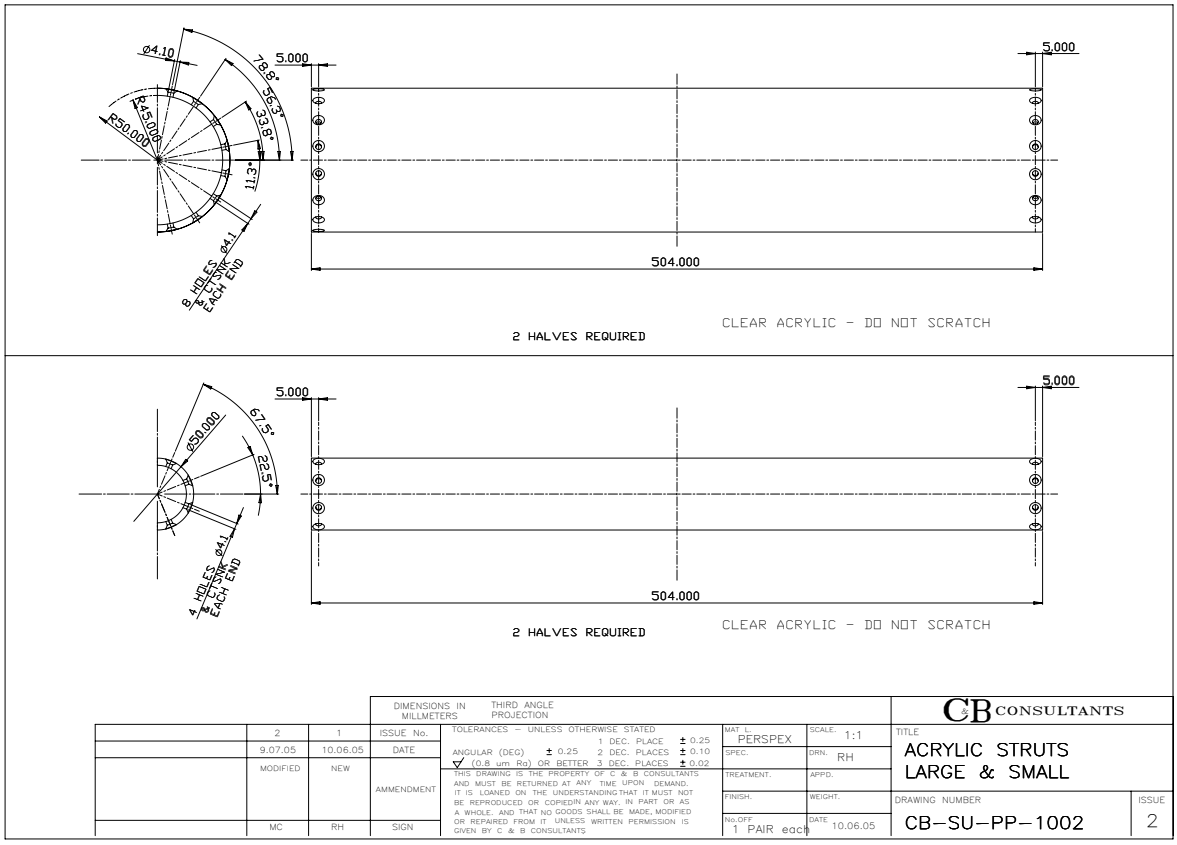
Ø4.10
5.000
78.8°
35.3°
33.8°
11.3°
R45.000
R50.000
8 HOLES Ø4.1
& CTSNK
EACH END
5.000
504.000
CLEAR ACRYLIC – DO NOT SCRATCH
2 HALVES REQUIRED
5.000
67.5°
Ø50.000
22.5°
4 HOLES Ø4.1
& CTSNK
EACH END
5.000
504.000
CLEAR ACRYLIC – DO NOT SCRATCH
2 HALVES REQUIRED
DIMENSIONS IN MILLMETERS
THIRD ANGLE PROJECTION
TOLERANCES – UNLESS OTHERWISE STATED
1 DEC. PLACE ± 0.25
ANGULAR (DEG) ± 0.25 2 DEC. PLACES ± 0.10
(0.8 um Ra) OR BETTER 3 DEC. PLACES ± 0.02
THIS DRAWING IS THE PROPERTY OF C & B CONSULTANTS AND MUST BE RETURNED AT ANY TIME UPON DEMAND. IT IS LOANED ON THE UNDERSTANDING THAT IT MUST NOT BE REPRODUCED OR COPIEDIN ANY WAY, IN PART OR AS A WHOLE, AND THAT NO GOODS SHALL BE MADE, MODIFIED OR REPAIRED FROM IT UNLESS WRITTEN PERMISSION IS GIVEN BY C & B CONSULTANTS
2 | 1 | ISSUE No.
9.07.05 | 10.06.05 | DATE
MODIFIED | NEW | AMMENDMENT
MC | RH | SIGN
MAT'L. PERSPEX
SPEC.
TREATMENT.
FINISH.
No.OFF. 1 PAIR each
SCALE. 1:1
DRN. RH
APPD.
WEIGHT.
DATE 10.06.05
C&B CONSULTANTS
TITLE. ACRYLIC STRUTS LARGE & SMALL
DRAWING NUMBER CB–SU–PP–1002
ISSUE 2

(b)

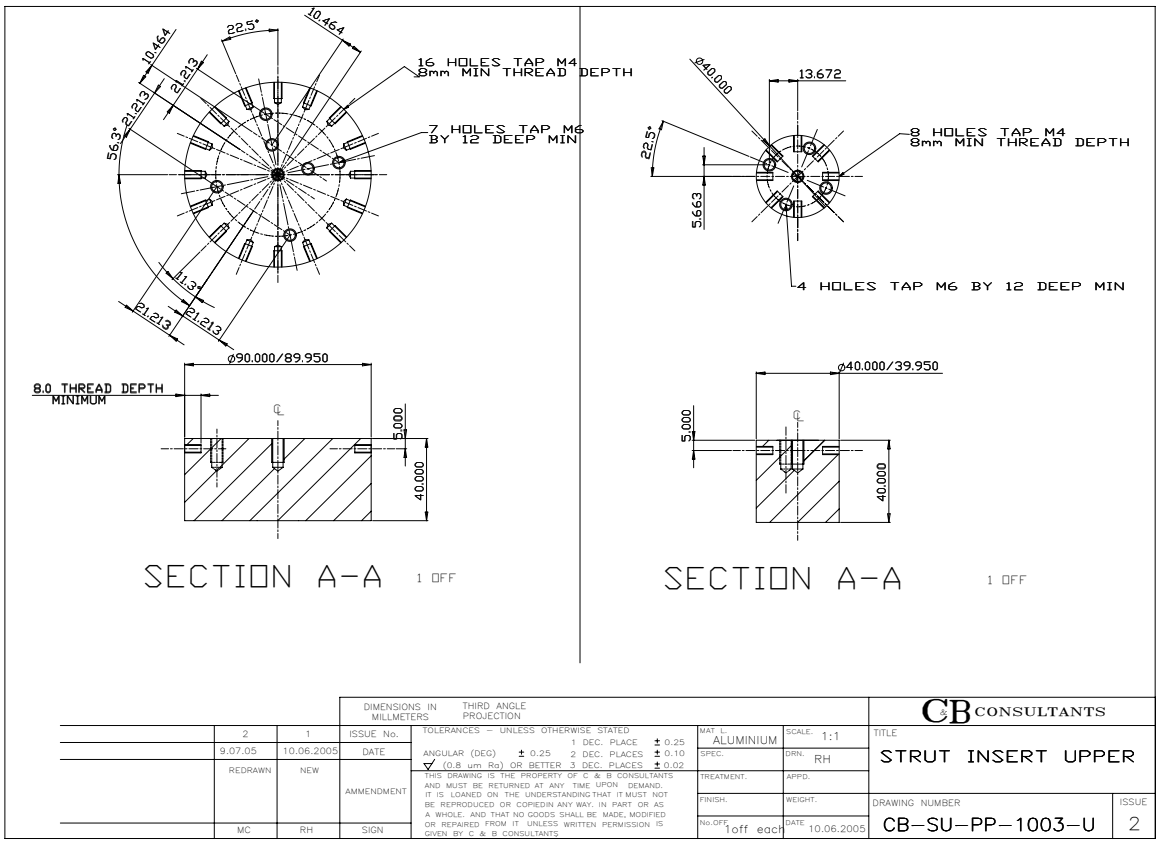
22.5°
10.464
10.464
2.213
2.213
56.3°
16 HOLES TAP M4
8mm MIN THREAD DEPTH
7 HOLES TAP M6
BY 12 DEEP MIN
11.31
21.213
21.213
ø40.000
13.672
22.5°
8 HOLES TAP M4
8mm MIN THREAD DEPTH
5.663
4 HOLES TAP M6 BY 12 DEEP MIN
ø90.000/89.950
8.0 THREAD DEPTH
MINIMUM
5.000
40.000
SECTION A-A 1 OFF
ø40.000/39.950
5.000
40.000
SECTION A-A 1 OFF
DIMENSIONS IN MILLMETERS
THIRD ANGLE PROJECTION
CB CONSULTANTS
ISSUE No. 2 1
DATE 9.07.05 10.06.2005
AMMENDMENT REDRAWN NEW
SIGN MC RH
TOLERANCES – UNLESS OTHERWISE STATED
1 DEC. PLACE ± 0.25
ANGULAR (DEG) ± 0.25 2 DEC. PLACES ± 0.10
(0.8 um Ra) OR BETTER 3 DEC. PLACES ± 0.02
THIS DRAWING IS THE PROPERTY OF C & B CONSULTANTS AND MUST BE RETURNED AT ANY TIME UPON DEMAND. IT IS LOANED ON THE UNDERSTANDING THAT IT MUST NOT BE REPRODUCED OR COPIEDIN ANY WAY, IN PART OR AS A WHOLE, AND THAT NO GOODS SHALL BE MADE, MODIFIED OR REPAIRED FROM IT UNLESS WRITTEN PERMISSION IS GIVEN BY C & B CONSULTANTS.
MAT'L. ALUMINIUM
SPEC.
TREATMENT.
FINISH.
No.OFF. 1off each
SCALE. 1:1
DRN. RH
APPD.
WEIGHT.
DATE 10.06.2005
TITLE
STRUT INSERT UPPER
DRAWING NUMBER CB–SU–PP–1003–U
ISSUE 2

(c)

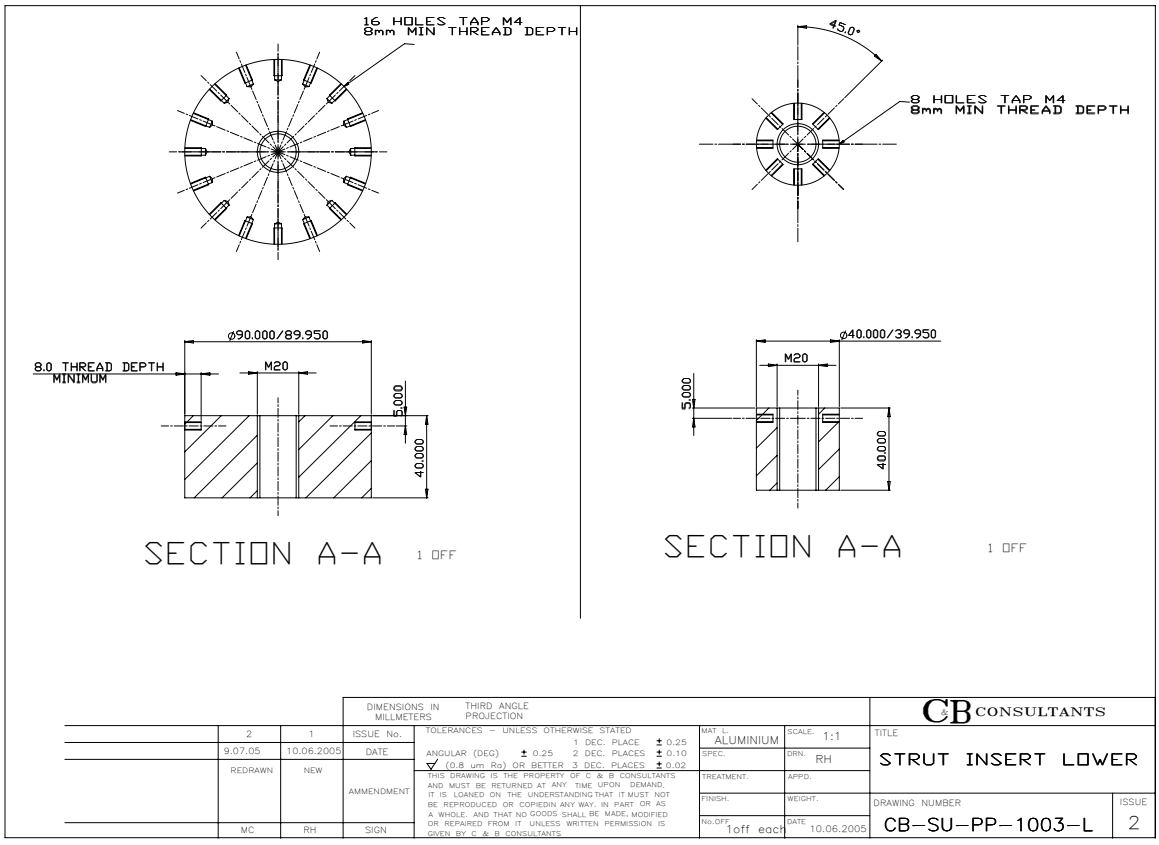
16 HOLES TAP M4
8mm MIN THREAD DEPTH
45.0°
8 HOLES TAP M4
8mm MIN THREAD DEPTH
ø90.000/89.950
8.0 THREAD DEPTH
MINIMUM
M20
5.000
40.000
SECTION A-A 1 OFF
ø40.000/39.950
M20
5.000
40.000
SECTION A-A 1 OFF
DIMENSIONS IN MILLMETERS
THIRD ANGLE PROJECTION
CB CONSULTANTS
ISSUE No. 2 1
DATE 9.07.05 10.06.2005
AMMENDMENT REDRAWN NEW
SIGN MC RH
TOLERANCES – UNLESS OTHERWISE STATED
1 DEC. PLACE ± 0.25
ANGULAR (DEG) ± 0.25 2 DEC. PLACES ± 0.10
(0.8 um Ra) OR BETTER 3 DEC. PLACES ± 0.02
THIS DRAWING IS THE PROPERTY OF C & B CONSULTANTS AND MUST BE RETURNED AT ANY TIME UPON DEMAND. IT IS LOANED ON THE UNDERSTANDING THAT IT MUST NOT BE REPRODUCED OR COPIEDIN ANY WAY, IN PART OR AS A WHOLE, AND THAT NO GOODS SHALL BE MADE, MODIFIED OR REPAIRED FROM IT UNLESS WRITTEN PERMISSION IS GIVEN BY C & B CONSULTANTS.
MAT'L. ALUMINIUM
SPEC.
TREATMENT.
FINISH.
No.OFF. 1off each
SCALE. 1:1
DRN. RH
APPD.
WEIGHT.
DATE 10.06.2005
TITLE
STRUT INSERT LOWER
DRAWING NUMBER CB–SU–PP–1003–L
ISSUE 2

(d)

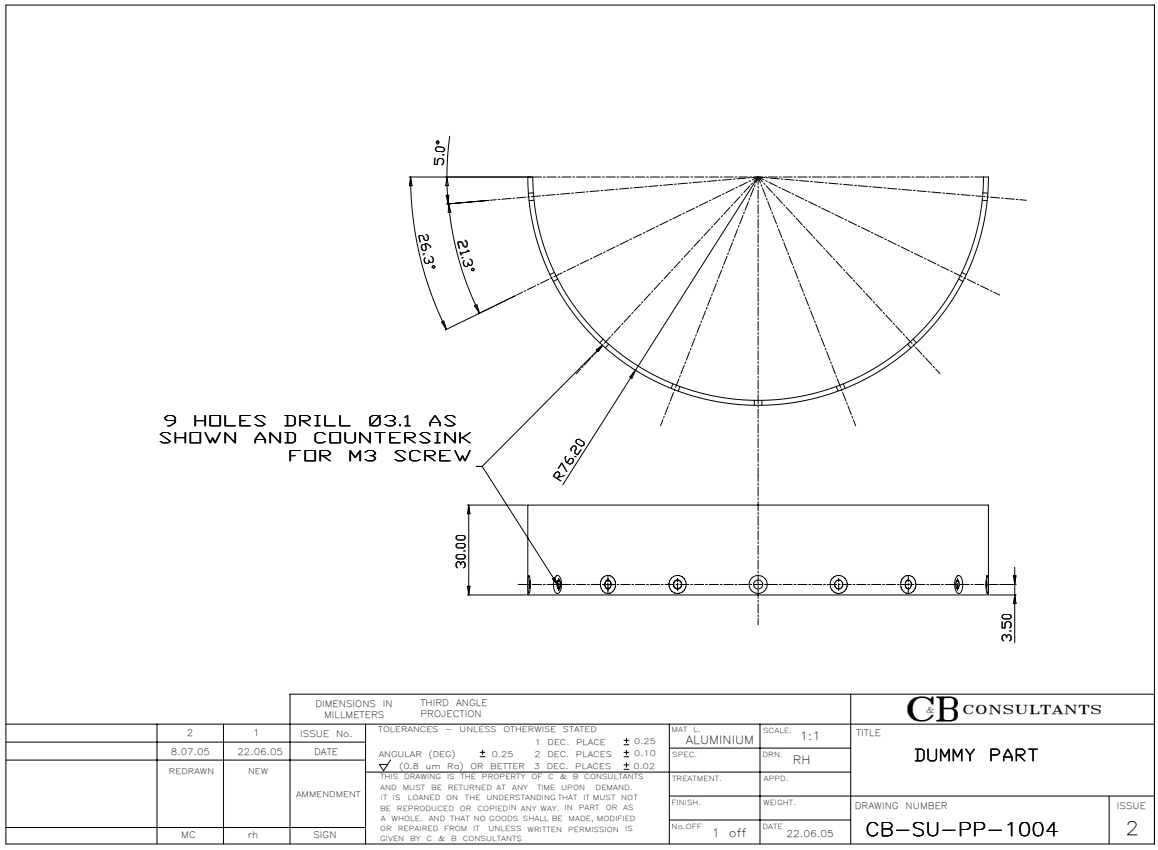
5.0°
26.3°
21.3°
9 HOLES DRILL Ø3.1 AS
SHOWN AND COUNTERSINK
FOR M3 SCREW
R76.20
30.00
3.50
DIMENSIONS IN MILLMETERS
THIRD ANGLE PROJECTION
CB CONSULTANTS
2
1
ISSUE No.
8.07.05
22.06.05
DATE
REDRAWN
NEW
AMMENDMENT
MC
rh
SIGN
TOLERANCES – UNLESS OTHERWISE STATED
1 DEC. PLACE ± 0.25
ANGULAR (DEG) ± 0.25
2 DEC. PLACES ± 0.10
(0.8 um Ra) OR BETTER
3 DEC. PLACES ± 0.02
THIS DRAWING IS THE PROPERTY OF C & B CONSULTANTS AND MUST BE RETURNED AT ANY TIME UPON DEMAND. IT IS LOANED ON THE UNDERSTANDING THAT IT MUST NOT BE REPRODUCED OR COPIEDIN ANY WAY. IN PART OR AS A WHOLE. AND THAT NO GOODS SHALL BE MADE, MODIFIED OR REPAIRED FROM IT UNLESS WRITTEN PERMISSION IS GIVEN BY C & B CONSULTANTS
MAT L. ALUMINIUM
SPEC.
TREATMENT.
FINISH.
No.OFF 1 off
SCALE. 1:1
DRN. RH
APPD.
WEIGHT.
DATE 22.06.05
TITLE
DUMMY PART
DRAWING NUMBER
CB–SU–PP–1004
ISSUE
2

(e)

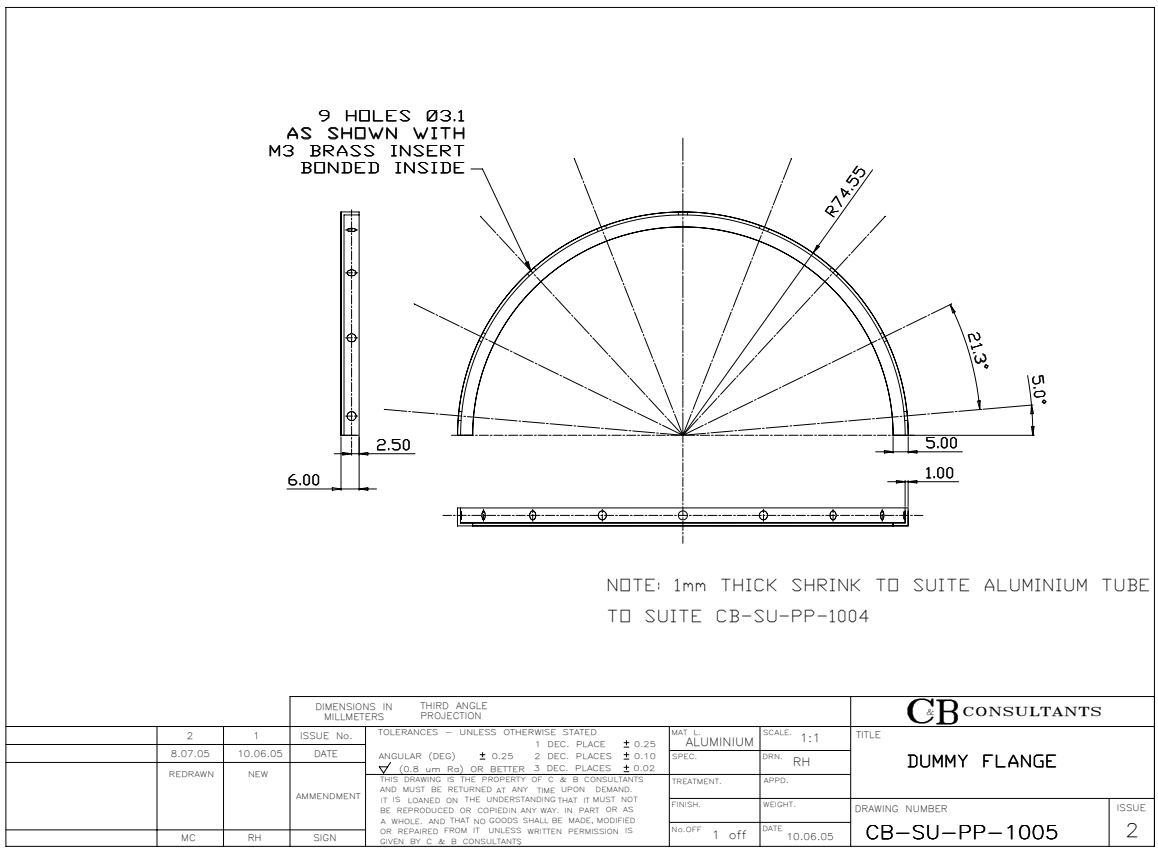
9 HOLES Ø3.1
AS SHOWN WITH
M3 BRASS INSERT
BONDED INSIDE
R74.55
21.3°
5.0°
2.50
6.00
5.00
1.00
NOTE: 1mm THICK SHRINK TO SUITE ALUMINIUM TUBE
TO SUITE CB–SU–PP–1004
DIMENSIONS IN MILLMETERS
THIRD ANGLE PROJECTION
CB CONSULTANTS
2
1
ISSUE No.
8.07.05
10.06.05
DATE
REDRAWN
NEW
AMMENDMENT
MC
RH
SIGN
TOLERANCES – UNLESS OTHERWISE STATED
1 DEC. PLACE ± 0.25
ANGULAR (DEG) ± 0.25
2 DEC. PLACES ± 0.10
(0.8 um Ra) OR BETTER
3 DEC. PLACES ± 0.02
THIS DRAWING IS THE PROPERTY OF C & B CONSULTANTS AND MUST BE RETURNED AT ANY TIME UPON DEMAND. IT IS LOANED ON THE UNDERSTANDING THAT IT MUST NOT BE REPRODUCED OR COPIEDIN ANY WAY. IN PART OR AS A WHOLE. AND THAT NO GOODS SHALL BE MADE, MODIFIED OR REPAIRED FROM IT UNLESS WRITTEN PERMISSION IS GIVEN BY C & B CONSULTANTS
MAT L. ALUMINIUM
SPEC.
TREATMENT.
FINISH.
No.OFF 1 off
SCALE. 1:1
DRN. RH
APPD.
WEIGHT.
DATE 10.06.05
TITLE
DUMMY FLANGE
DRAWING NUMBER
CB–SU–PP–1005
ISSUE
2

(f)

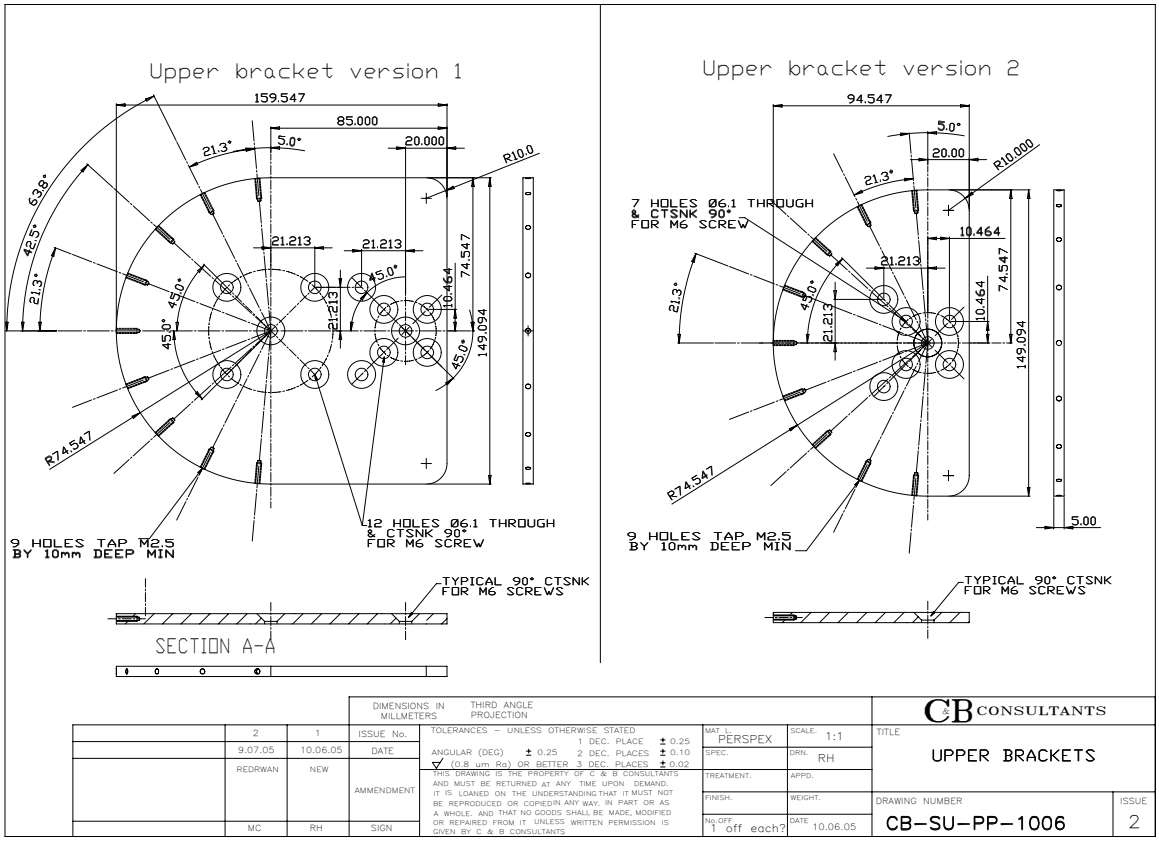
Upper bracket version 1
159.547
85.000
21.3°
5.0°
20.000
R10.0
6.38°
42.5°
21.3°
21.213
21.213
15.0°
10.464
74.547
45.0°
45.0°
21.213
45.0°
149.094
R74.547
9 HOLES TAP M2.5
BY 10mm DEEP MIN
12 HOLES Ø6.1 THROUGH
& CTSNK 90°
FOR M6 SCREW
TYPICAL 90° CTSNK
FOR M6 SCREWS
SECTION A-A
Upper bracket version 2
94.547
5.0°
20.00
R10.000
21.3°
7 HOLES Ø6.1 THROUGH
& CTSNK 90°
FOR M6 SCREW
10.464
21.213
74.547
21.3°
45.0°
21.213
10.464
149.094
R74.547
9 HOLES TAP M2.5
BY 10mm DEEP MIN
5.00
TYPICAL 90° CTSNK
FOR M6 SCREWS
DIMENSIONS IN MILLMETERS
THIRD ANGLE PROJECTION
CB CONSULTANTS
2
1
ISSUE No.
9.07.05
10.06.05
DATE
REDRWAN
NEW
AMMENDMENT
MC
RH
SIGN
TOLERANCES – UNLESS OTHERWISE STATED
1 DEC. PLACE ± 0.25
ANGULAR (DEG) ± 0.25 2 DEC. PLACES ± 0.10
(0.8 um Ra) OR BETTER 3 DEC. PLACES ± 0.02
THIS DRAWING IS THE PROPERTY OF C & B CONSULTANTS AND MUST BE RETURNED AT ANY TIME UPON DEMAND. IT IS LOANED ON THE UNDERSTANDING THAT IT MUST NOT BE REPRODUCED OR COPIEDIN ANY WAY, IN PART OR AS A WHOLE, AND THAT NO GOODS SHALL BE MADE, MODIFIED OR REPAIRED FROM IT UNLESS WRITTEN PERMISSION IS GIVEN BY C & B CONSULTANTS
MAT'L. PERSPEX
SPEC.
TREATMENT.
FINISH.
No.OFF 1 off each?
SCALE. 1:1
DRN. RH
APPD.
WEIGHT.
DATE 10.06.05
TITLE
UPPER BRACKETS
DRAWING NUMBER
CB–SU–PP–1006
ISSUE
2

(g)

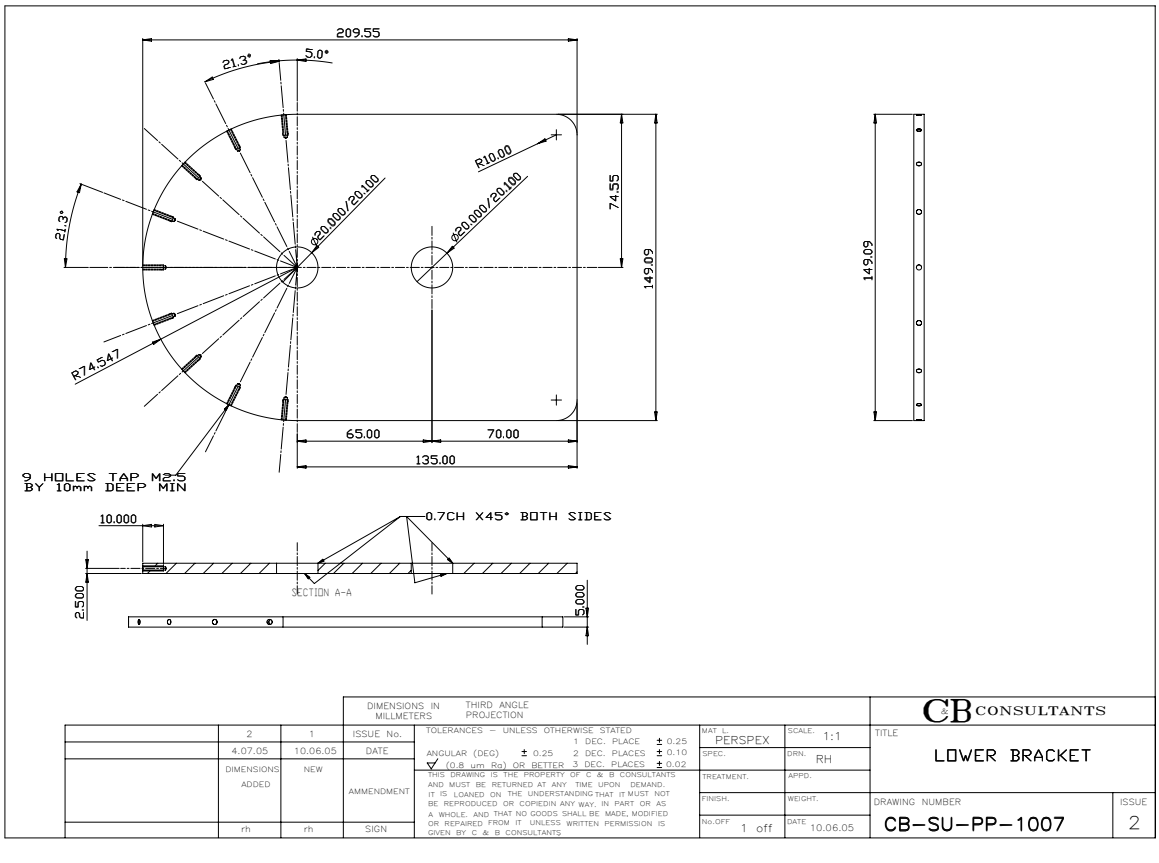
209.55
21.3°
5.0°
R10.00
ø20.000/20.100
ø20.000/20.100
74.55
149.09
21.3°
R74.547
65.00
70.00
135.00
9 HOLES TAP M2.5
BY 10mm DEEP MIN
149.09
10.000
0.7CH X45° BOTH SIDES
SECTION A-A
2.500
5.000
DIMENSIONS IN MILLMETERS
THIRD ANGLE PROJECTION
CB CONSULTANTS
2
1
ISSUE No.
4.07.05
10.06.05
DATE
DIMENSIONS ADDED
NEW
AMMENDMENT
rh
rh
SIGN
TOLERANCES – UNLESS OTHERWISE STATED
1 DEC. PLACE ± 0.25
ANGULAR (DEG) ± 0.25 2 DEC. PLACES ± 0.10
(0.8 um Ra) OR BETTER 3 DEC. PLACES ± 0.02
THIS DRAWING IS THE PROPERTY OF C & B CONSULTANTS AND MUST BE RETURNED AT ANY TIME UPON DEMAND. IT IS LOANED ON THE UNDERSTANDING THAT IT MUST NOT BE REPRODUCED OR COPIEDIN ANY WAY, IN PART OR AS A WHOLE, AND THAT NO GOODS SHALL BE MADE, MODIFIED OR REPAIRED FROM IT UNLESS WRITTEN PERMISSION IS GIVEN BY C & B CONSULTANTS
MAT'L. PERSPEX
SPEC.
TREATMENT.
FINISH.
No.OFF 1 off
SCALE. 1:1
DRN. RH
APPD.
WEIGHT.
DATE 10.06.05
TITLE
LOWER BRACKET
DRAWING NUMBER
CB–SU–PP–1007
ISSUE
2

(h)

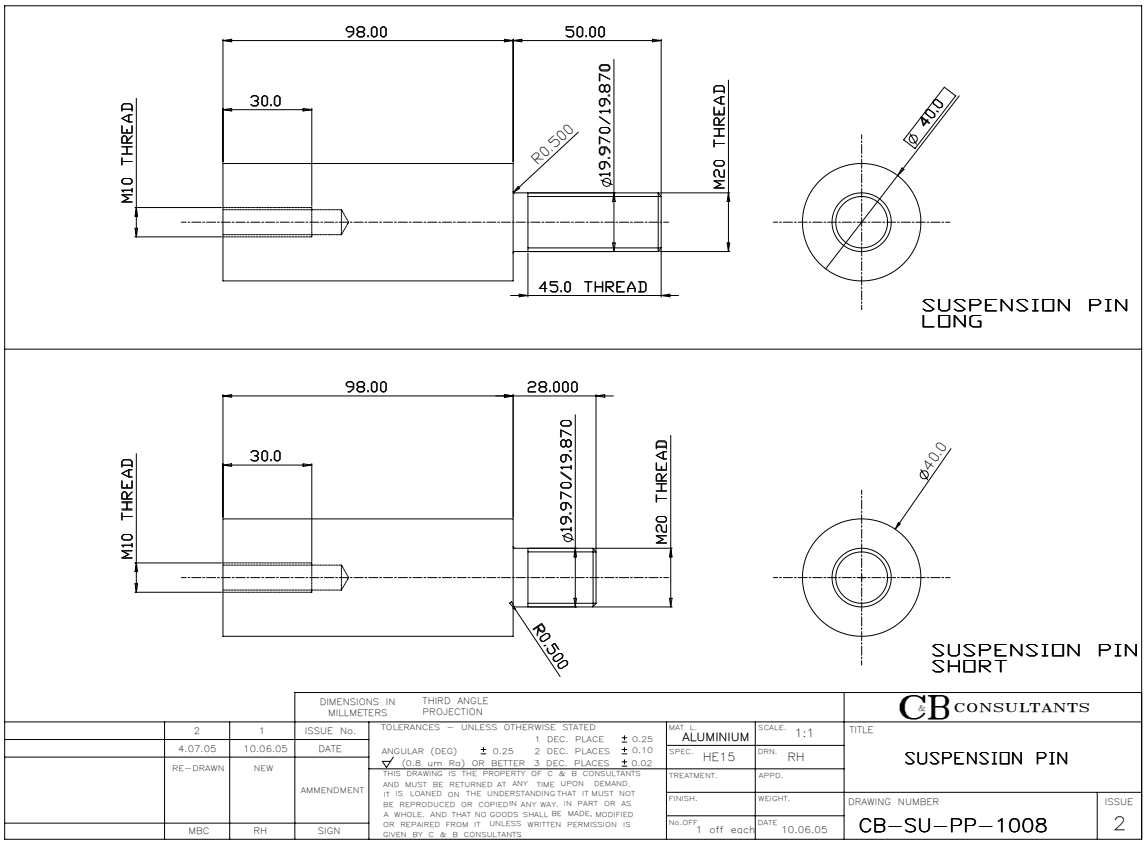
98.00
50.00
30.0
M10 THREAD
R0.500
ø19.970/19.870
M20 THREAD
45.0 THREAD
Ø 40.0
SUSPENSION PIN LONG
98.00
28.000
30.0
M10 THREAD
ø19.970/19.870
M20 THREAD
Ø40.0
R0.500
SUSPENSION PIN SHORT
DIMENSIONS IN MILLIMETERS
THIRD ANGLE PROJECTION
CB CONSULTANTS
ISSUE No. 2 1
DATE 4.07.05 10.06.05
AMMENDMENT RE-DRAWN NEW
SIGN MBC RH
TOLERANCES – UNLESS OTHERWISE STATED
1 DEC. PLACE ± 0.25
ANGULAR (DEG) ± 0.25 2 DEC. PLACES ± 0.10
(0.8 um Ra) OR BETTER 3 DEC. PLACES ± 0.02
THIS DRAWING IS THE PROPERTY OF C & B CONSULTANTS AND MUST BE RETURNED AT ANY TIME UPON DEMAND. IT IS LOANED ON THE UNDERSTANDING THAT IT MUST NOT BE REPRODUCED OR COPIED IN ANY WAY, IN PART OR AS A WHOLE, AND THAT NO GOODS SHALL BE MADE, MODIFIED OR REPAIRED FROM IT UNLESS WRITTEN PERMISSION IS GIVEN BY C & B CONSULTANTS
MAT'L ALUMINIUM
SPEC. HE15
TREATMENT.
FINISH.
No.OFF. 1 off each
SCALE. 1:1
DRN. RH
APPD.
WEIGHT.
DATE 10.06.05
TITLE
SUSPENSION PIN
DRAWING NUMBER CB-SU-PP-1008
ISSUE 2

(i)

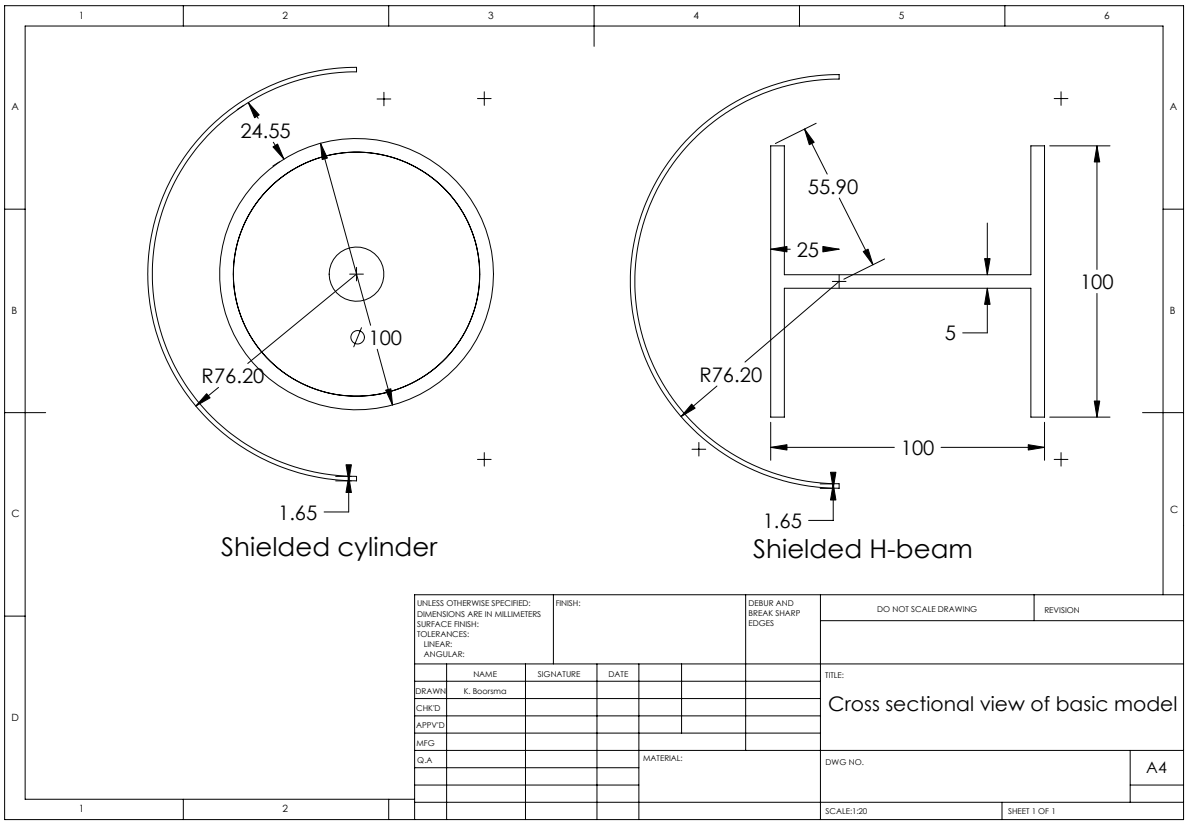
24.55
Ø100
R76.20
1.65
Shielded cylinder
55.90
25
100
5
R76.20
100
1.65
Shielded H-beam
UNLESS OTHERWISE SPECIFIED:
DIMENSIONS ARE IN MILLIMETERS
SURFACE FINISH:
TOLERANCES:
LINEAR:
ANGULAR:
FINISH:
DEBUR AND BREAK SHARP EDGES
DO NOT SCALE DRAWING
REVISION
NAME SIGNATURE DATE
DRAWN K. Boorsma
CHK'D
APPV'D
MFG
Q.A
MATERIAL:
TITLE:
Cross sectional view of basic model
DWG NO.
A4
SCALE:1:20
SHEET 1 OF 1

(j)

Appendix C

Technical Drawings of the LG Model Experiment

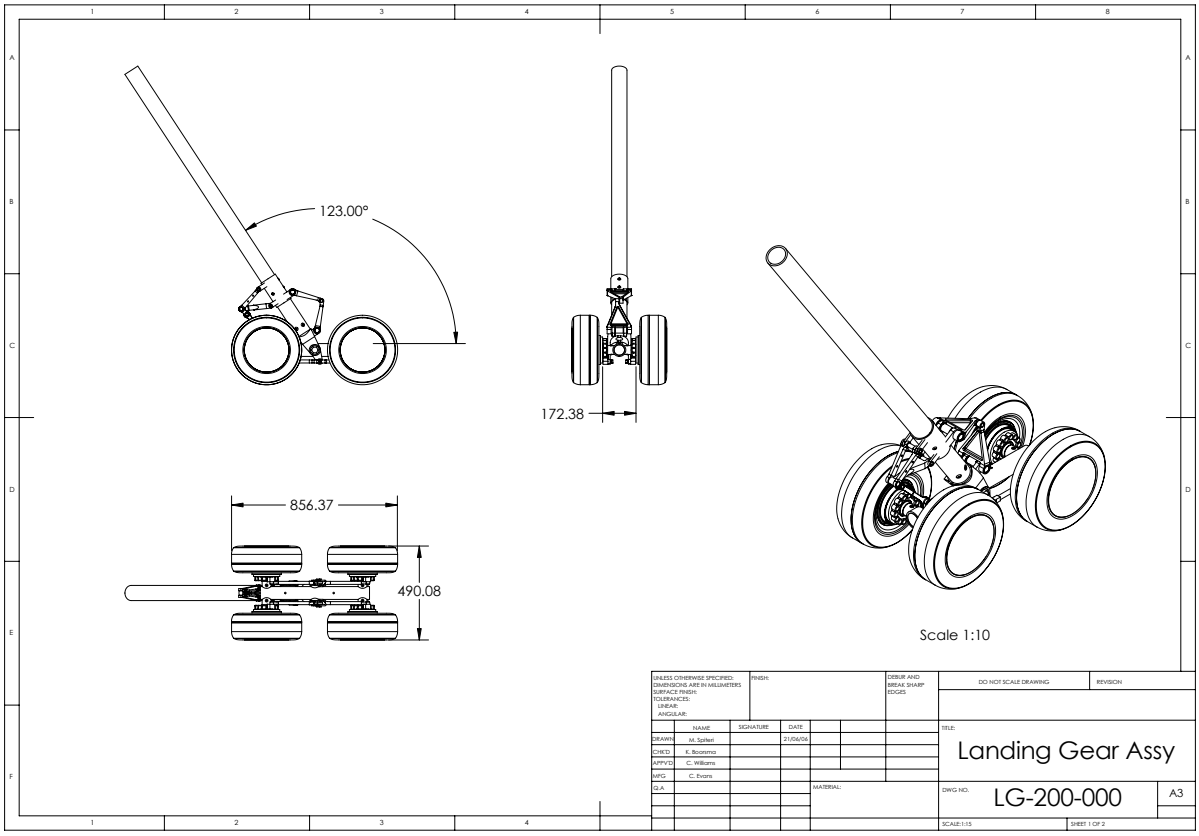

UNLESS OTHERWISE SPECIFIED: DIMENSIONS ARE IN MILLIMETERS SURFACE FINISH: TOLERANCES: LINEAR: ANGULAR:	FINISH:	DEBUR AND BREAK SHARP EDGES	DO NOT SCALE DRAWING	REVISION
	NAME	SIGNATURE	DATE	TITLE: Landing Gear Assy
DRAWN	M. Spiteri		21/06/06	
CHK'D	K. Boorsma			
APP'D	C. Williams			
MFG	C. Evans			
Q.A.				DWG NO. LG-200-000 A3
MATERIAL:				SCALE:1:5 SHEET 1 OF 2

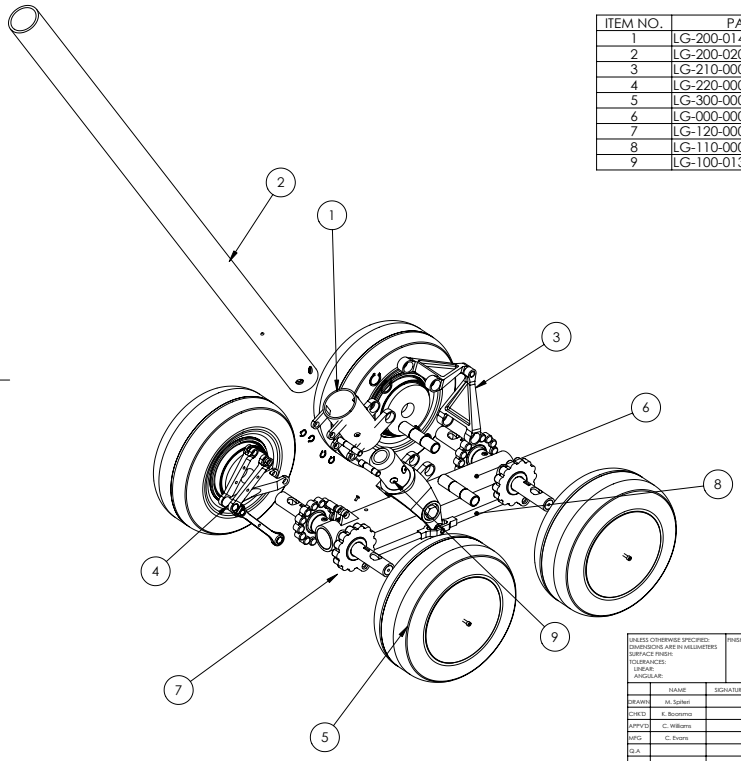

ITEM NO.	PART NUMBER	DESCRIPTION	QTY.
1	LG-200-014	Torque Bracket Assy	1
2	LG-200-020	Main Strut	1
3	LG-210-000	Torque Link Assy	2
4	LG-220-000	Articulation Link Assy	1
5	LG-300-000	Wheel Assy	4
6	LG-000-000	Bogie Assy	1
7	LG-120-000	Brake Assy	4
8	LG-110-000	Brake Link Assy	2
9	LG-100-013	Yoke Assy	1

UNLESS OTHERWISE SPECIFIED: DIMENSIONS ARE IN MILLIMETERS SURFACE FINISH: TOLERANCES: LINEAR: ANGULAR:	FINISH:	DEBUR AND BREAK SHARP EDGES	DO NOT SCALE DRAWING	REVISION
	NAME	SIGNATURE	DATE	TITLE: Landing Gear Assy
DRAWN	M. Spiteri		21/06/06	
CHK'D	K. Boorsma			
APP'D	C. Williams			
MFG	C. Evans			
Q.A.				DWG NO. LG-200-000 A3
MATERIAL:				SCALE:1:20 SHEET 2 OF 2

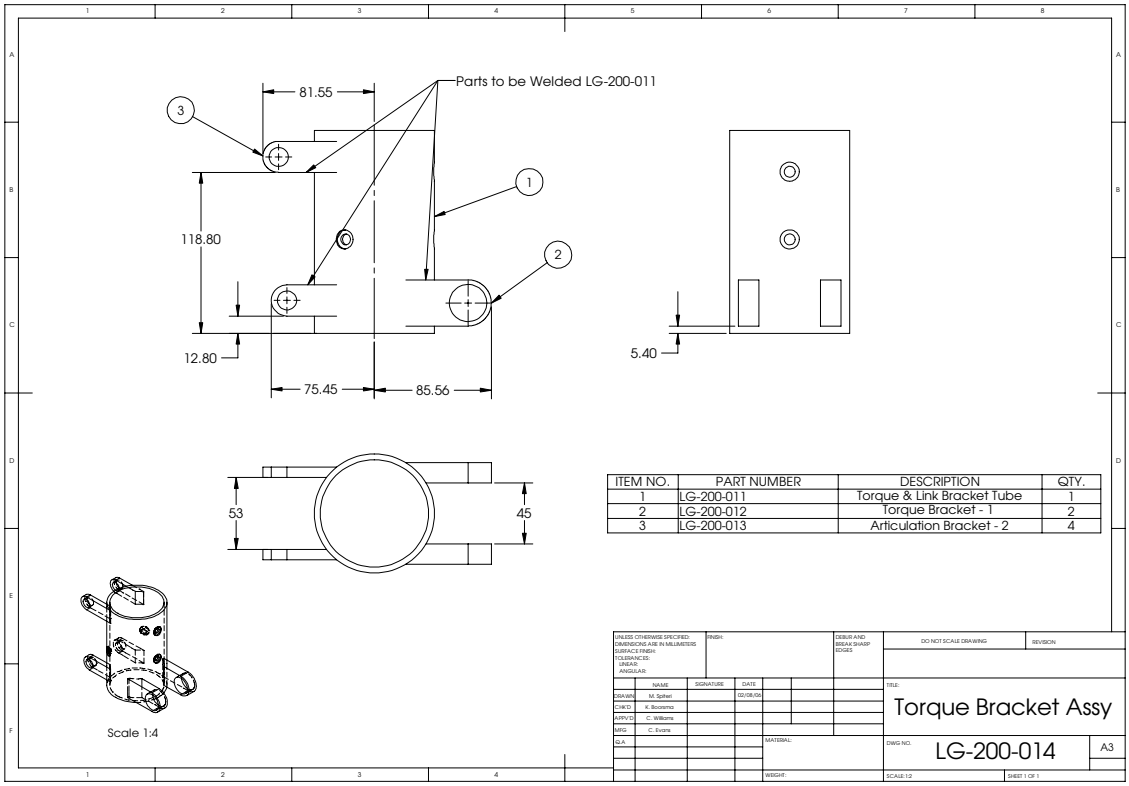
Parts to be Welded LG-200-011
81.55
118.80
12.80
75.45
85.56
5.40
53
45
Scale 1:4
ITEM NO. | PART NUMBER | DESCRIPTION | QTY.
1 | LG-200-011 | Torque & Link Bracket Tube | 1
2 | LG-200-012 | Torque Bracket - 1 | 2
3 | LG-200-013 | Articulation Bracket - 2 | 4
Torque Bracket Assy
LG-200-014
A3

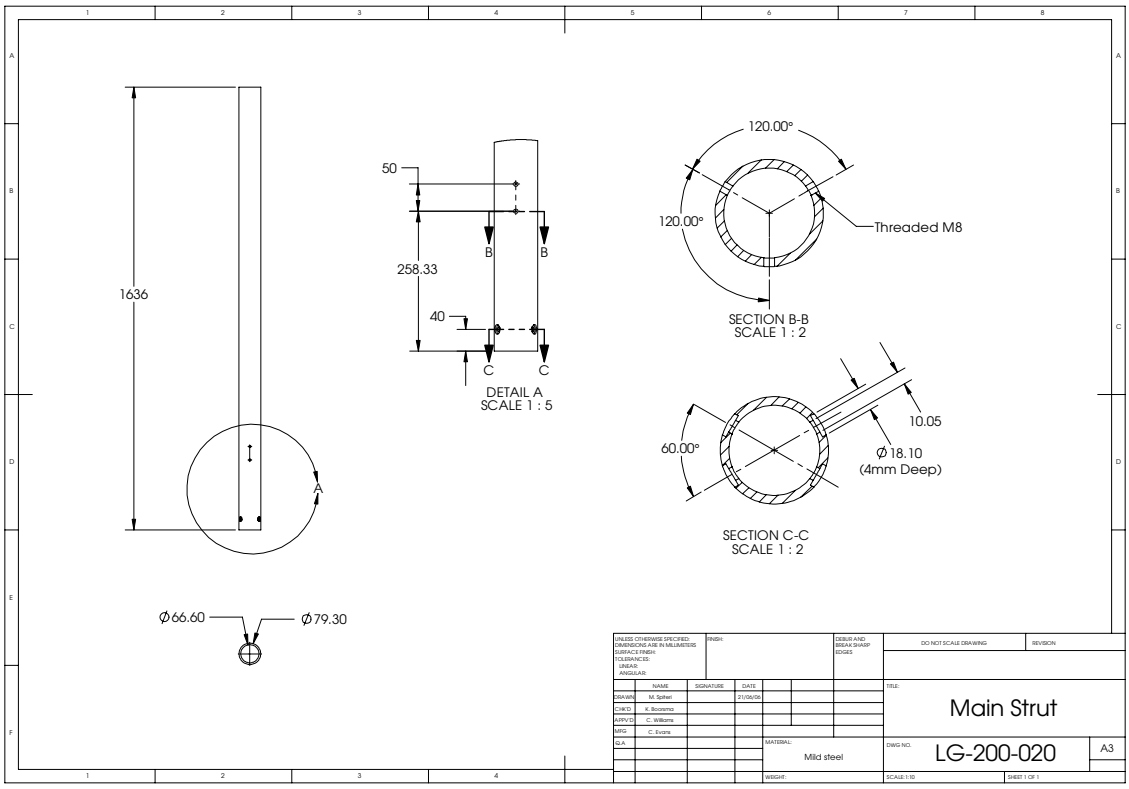
1636
50
258.33
40
DETAIL A
SCALE 1 : 5
120.00°
120.00°
Threaded M8
SECTION B-B
SCALE 1 : 2
60.00°
10.05
Ø18.10
(4mm Deep)
SECTION C-C
SCALE 1 : 2
Ø66.60
Ø79.30
Main Strut
Mild steel
LG-200-020
A3

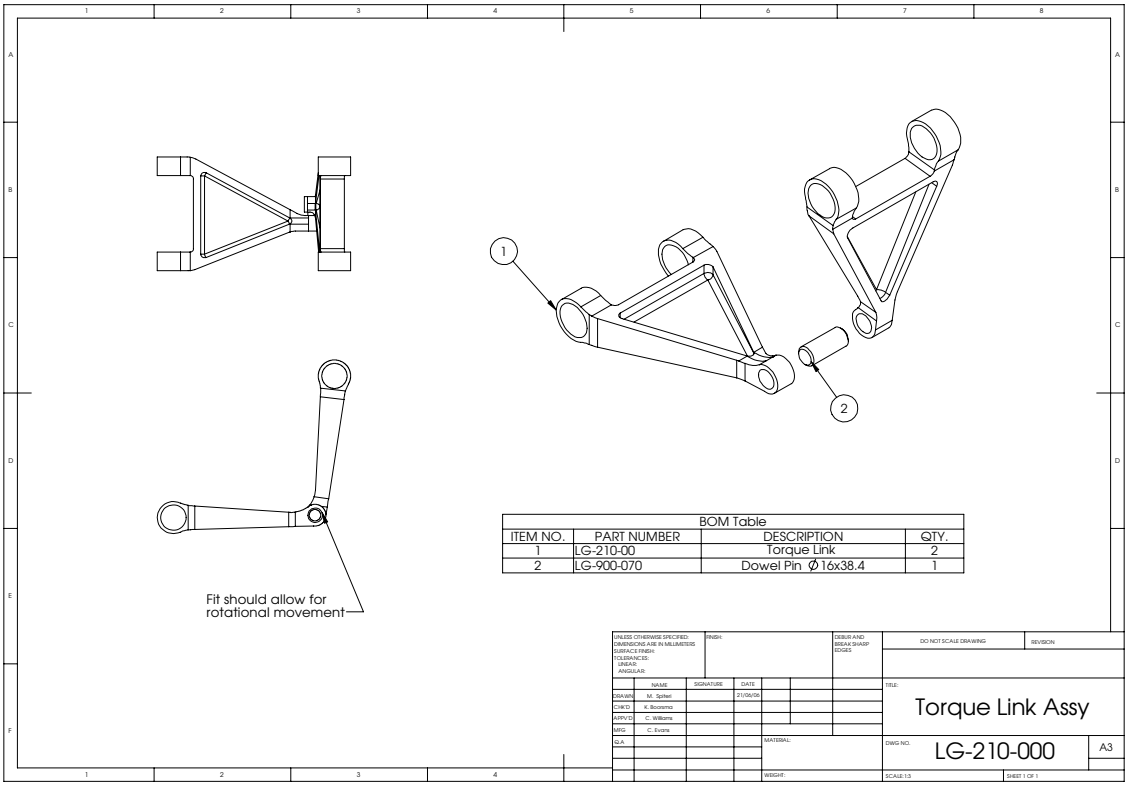

BOM Table			
ITEM NO.	PART NUMBER	DESCRIPTION	QTY.
1	LG-210-00	Torque Link	2
2	LG-900-070	Dowel Pin Ø16x38.4	1

UNLESS OTHERWISE SPECIFIED: DIMENSIONS ARE IN MILLIMETERS SURFACE FINISH: TOLERANCES: LINEAR: ANGULAR: | FINISH: | DEBUR AND BREAK SHARP EDGES | DO NOT SCALE DRAWING | REVISION:

	NAME	SIGNATURE	DATE
DRAWN	M. Spiteri		21/06/06
CHK'D	K. Boosma		
APPV'D	C. Williams		
MFG	C. Evans		
Q.A			

MATERIAL: | WEIGHT: | TITLE: Torque Link Assy | DWG NO. LG-210-000 | A3 | SCALE:1:3 | SHEET 1 OF 1

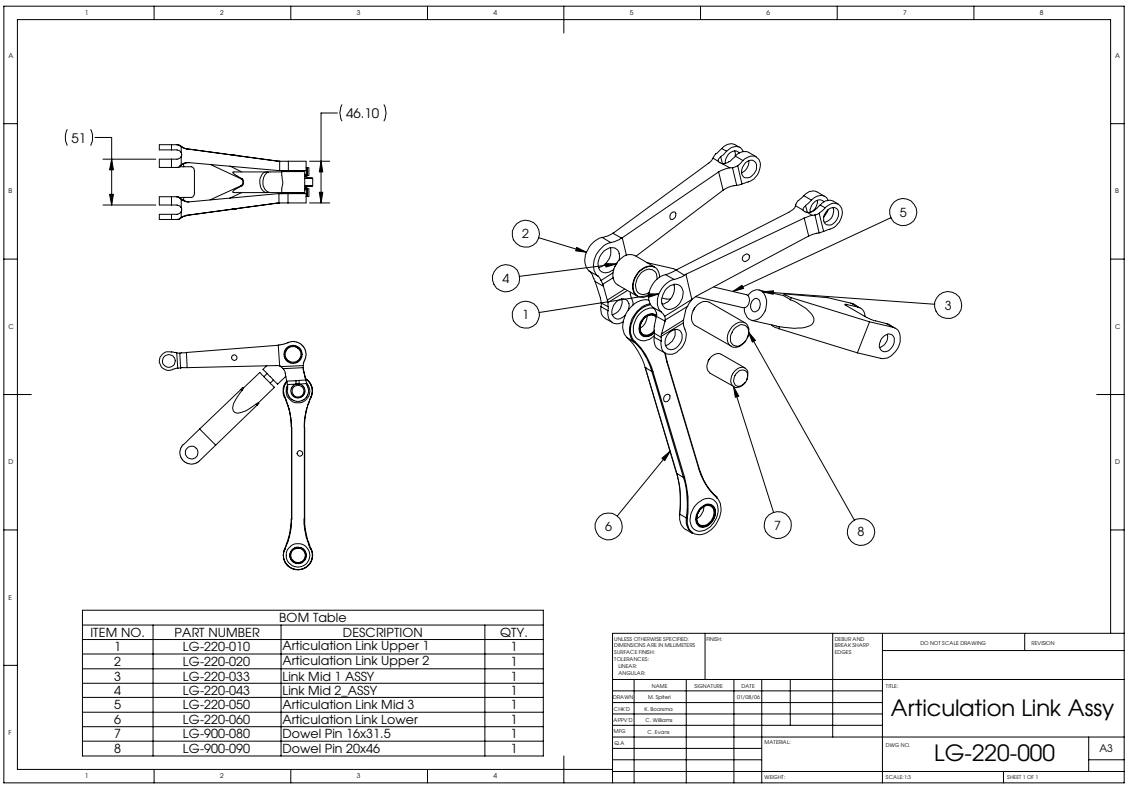

BOM Table			
ITEM NO.	PART NUMBER	DESCRIPTION	QTY.
1	LG-220-010	Articulation Link Upper 1	1
2	LG-220-020	Articulation Link Upper 2	1
3	LG-220-033	Link Mid 1 ASSY	1
4	LG-220-043	Link Mid 2_ASSY	1
5	LG-220-050	Articulation Link Mid 3	1
6	LG-220-060	Articulation Link Lower	1
7	LG-900-080	Dowel Pin 16x31.5	1
8	LG-900-090	Dowel Pin 20x46	1

UNLESS OTHERWISE SPECIFIED: DIMENSIONS ARE IN MILLIMETERS SURFACE FINISH: TOLERANCES: LINEAR: ANGULAR: | FINISH: | DEBUR AND BREAK SHARP EDGES | DO NOT SCALE DRAWING | REVISION:

	NAME	SIGNATURE	DATE
DRAWN	M. Spiteri		01/08/06
CHK'D	K. Boosma		
APPV'D	C. Williams		
MFG	C. Evans		
Q.A			

MATERIAL: | WEIGHT: | TITLE: Articulation Link Assy | DWG NO. LG-220-000 | A3 | SCALE:1:3 | SHEET 1 OF 1

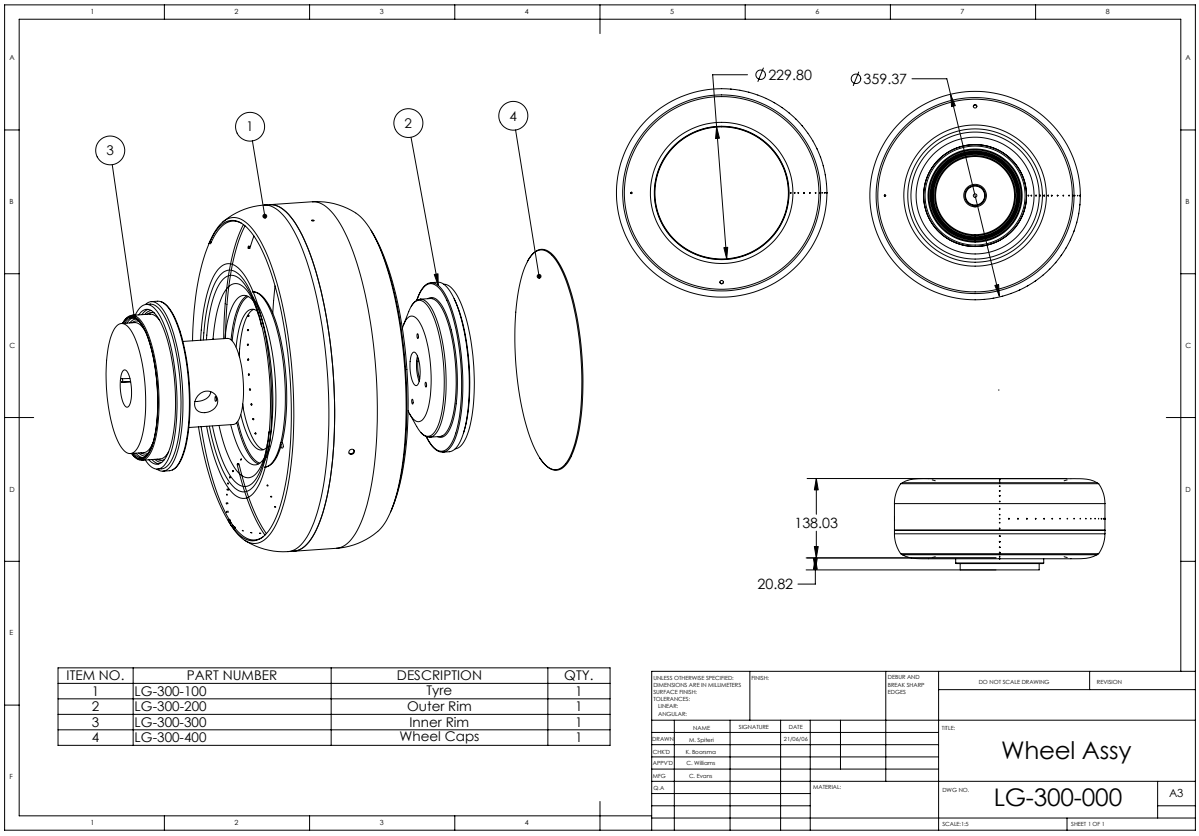

ITEM NO.	PART NUMBER	DESCRIPTION	QTY.
1	LG-300-100	Tyre	1
2	LG-300-200	Outer Rim	1
3	LG-300-300	Inner Rim	1
4	LG-300-400	Wheel Caps	1

UNLESS OTHERWISE SPECIFIED: DIMENSIONS ARE IN MILLIMETERS SURFACE FINISH: TOLERANCES: LINEAR: ANGULAR: | FINISH: | DEBUR AND BREAK SHARP EDGES | DO NOT SCALE DRAWING | REVISION

	NAME	SIGNATURE	DATE
DRAWN	M. Spiteri		21/06/06
CHK'D	K. Boorsma		
APPV'D	C. Williams		
MFG	C. Evans		
Q.A.			

MATERIAL:

TITLE: Wheel Assy

DWG NO. LG-300-000 | A3

SCALE:1:5 | SHEET 1 OF 1

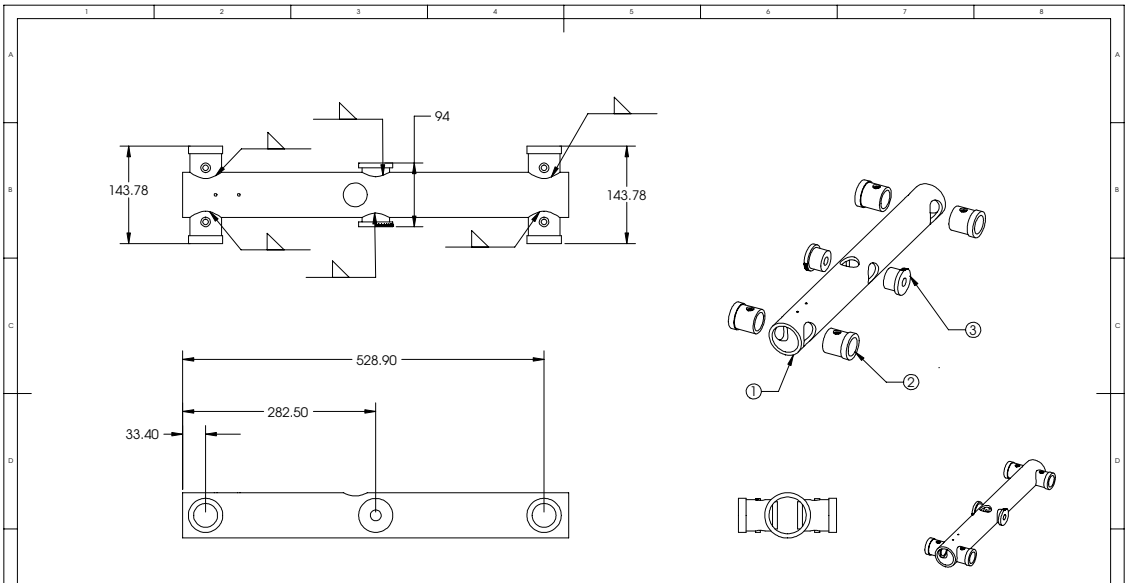

BOM Table			
ITEM NO.	PART NUMBER	DESCRIPTION	QTY.
1	LG-000-010	Main Bogie strut	1
2	LG-000-020	Axle Spacer	4
3	LG-000-030	Bogie Yoke Spacers	2

UNLESS OTHERWISE SPECIFIED: DIMENSIONS ARE IN MILLIMETERS SURFACE FINISH: TOLERANCES: LINEAR: ANGULAR: | FINISH: | DEBUR AND BREAK SHARP EDGES | DO NOT SCALE DRAWING | REVISION

	NAME	SIGNATURE	DATE
DRAWN	M. Spiteri		21/06/06
CHK'D	K. Boorsma		
APPV'D	C. Williams		
MFG	C. Evans		
Q.A.			

MATERIAL: | WEIGHT:

TITLE: Bogie Beam

DWG NO. LG-000-000 | A3

SCALE:1:5 | SHEET 1 OF 1

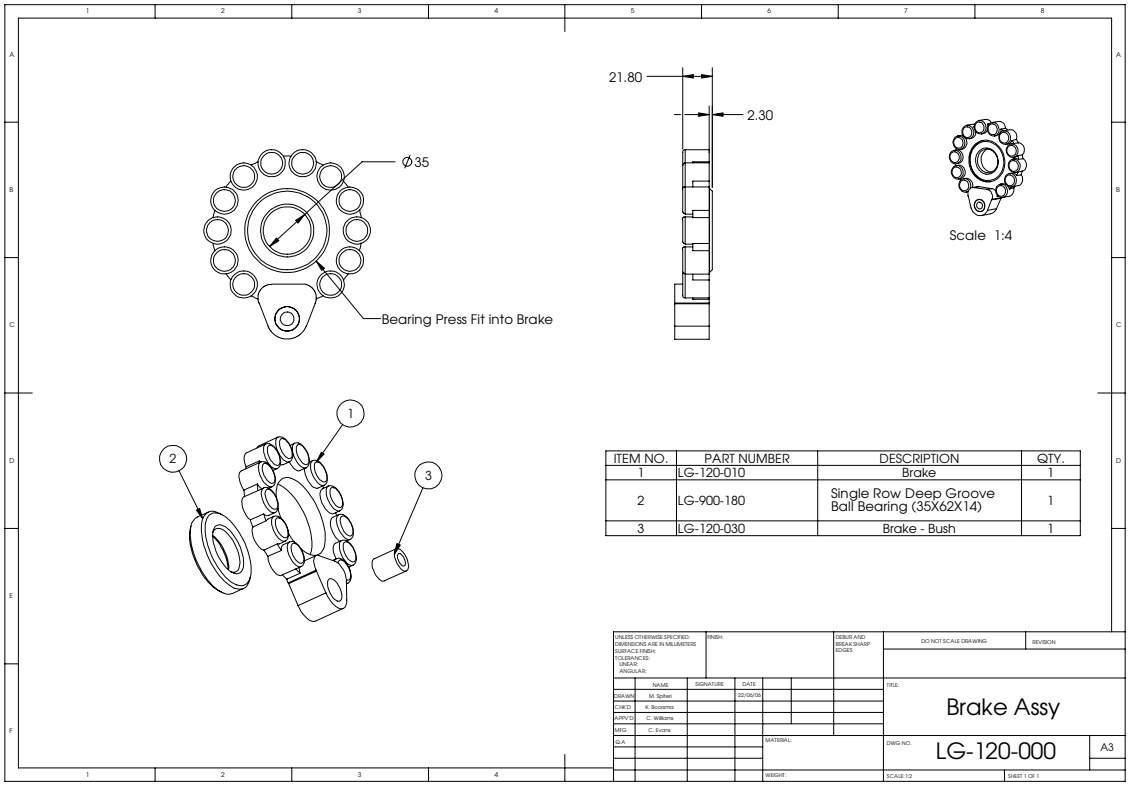

ITEM NO.	PART NUMBER	DESCRIPTION	QTY.
1	LG-120-010	Brake	1
2	LG-900-180	Single Row Deep Groove Ball Bearing (35X62X14)	1
3	LG-120-030	Brake - Bush	1

UNLESS OTHERWISE SPECIFIED: DIMENSIONS ARE IN MILLIMETERS SURFACE FINISH: TOLERANCES: LINEAR: ANGULAR: | FINISH: | DEBUR AND BREAK SHARP EDGES | DO NOT SCALE DRAWING | REVISION:

	NAME	SIGNATURE	DATE
DRAWN	M. Spheri		22/06/04
CHK'D	K. Boorsma		
APPV'D	C. Williams		
MFG	C. Evans		
Q.A			

MATERIAL: | WEIGHT: | TITLE: Brake Assy | DWG NO. LG-120-000 | A3 | SCALE:1:2 | SHEET 1 OF 1

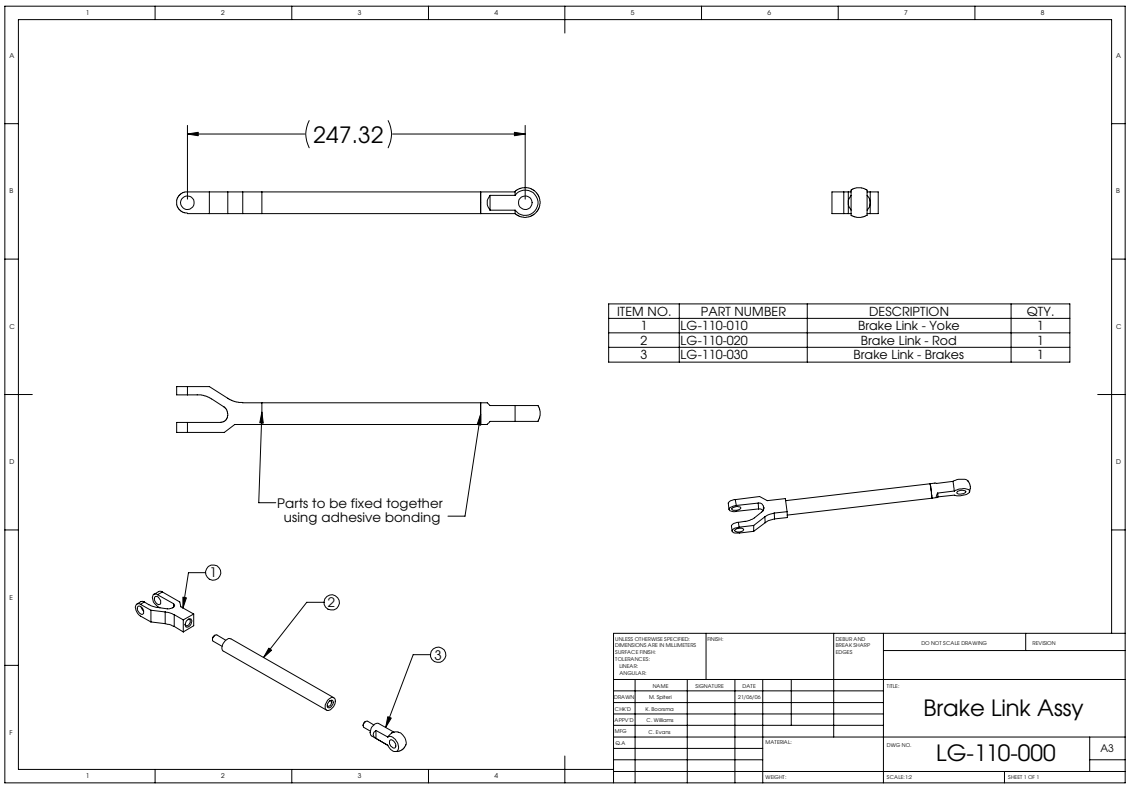

ITEM NO.	PART NUMBER	DESCRIPTION	QTY.
1	LG-110-010	Brake Link - Yoke	1
2	LG-110-020	Brake Link - Rod	1
3	LG-110-030	Brake Link - Brakes	1

UNLESS OTHERWISE SPECIFIED: DIMENSIONS ARE IN MILLIMETERS SURFACE FINISH: TOLERANCES: LINEAR: ANGULAR: | FINISH: | DEBUR AND BREAK SHARP EDGES | DO NOT SCALE DRAWING | REVISION:

	NAME	SIGNATURE	DATE
DRAWN	M. Spheri		21/06/04
CHK'D	K. Boorsma		
APPV'D	C. Williams		
MFG	C. Evans		
Q.A			

MATERIAL: | WEIGHT: | TITLE: Brake Link Assy | DWG NO. LG-110-000 | A3 | SCALE:1:2 | SHEET 1 OF 1

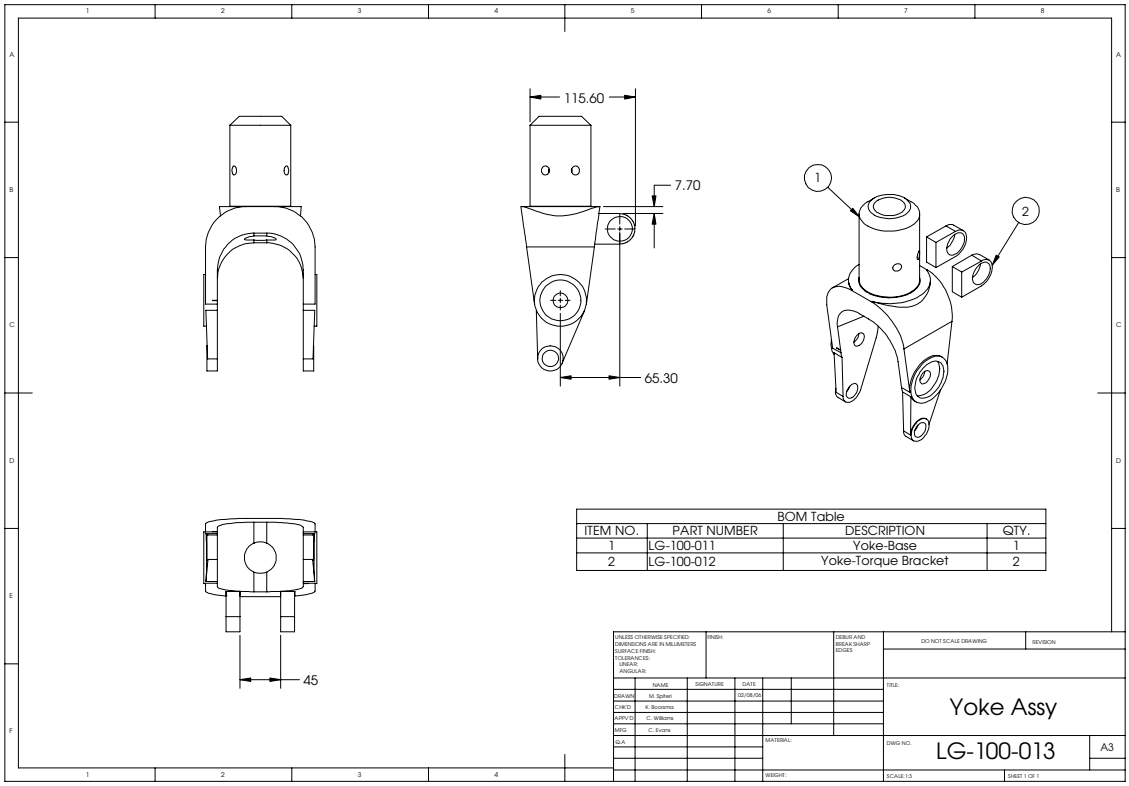

BOM Table

ITEM NO.	PART NUMBER	DESCRIPTION	QTY.
1	LG-100-011	Yoke-Base	1
2	LG-100-012	Yoke-Torque Bracket	2

UNLESS OTHERWISE SPECIFIED: DIMENSIONS ARE IN MILLIMETERS SURFACE FINISH: TOLERANCES: LINEAR: ANGULAR: | FINISH: | DEBUR AND BREAK SHARP EDGES | DO NOT SCALE DRAWING | REVISION

	NAME	SIGNATURE	DATE
DRAWN	M. Spiteri		02/08/06
CHK'D	K. Boorsma		
APPV'D	C. Williams		
MFG	C. Evans		
Q.A			

MATERIAL: | WEIGHT: | TITLE: Yoke Assy | DWG NO. LG-100-013 | A3 | SCALE:1:3 | SHEET 1 OF 1

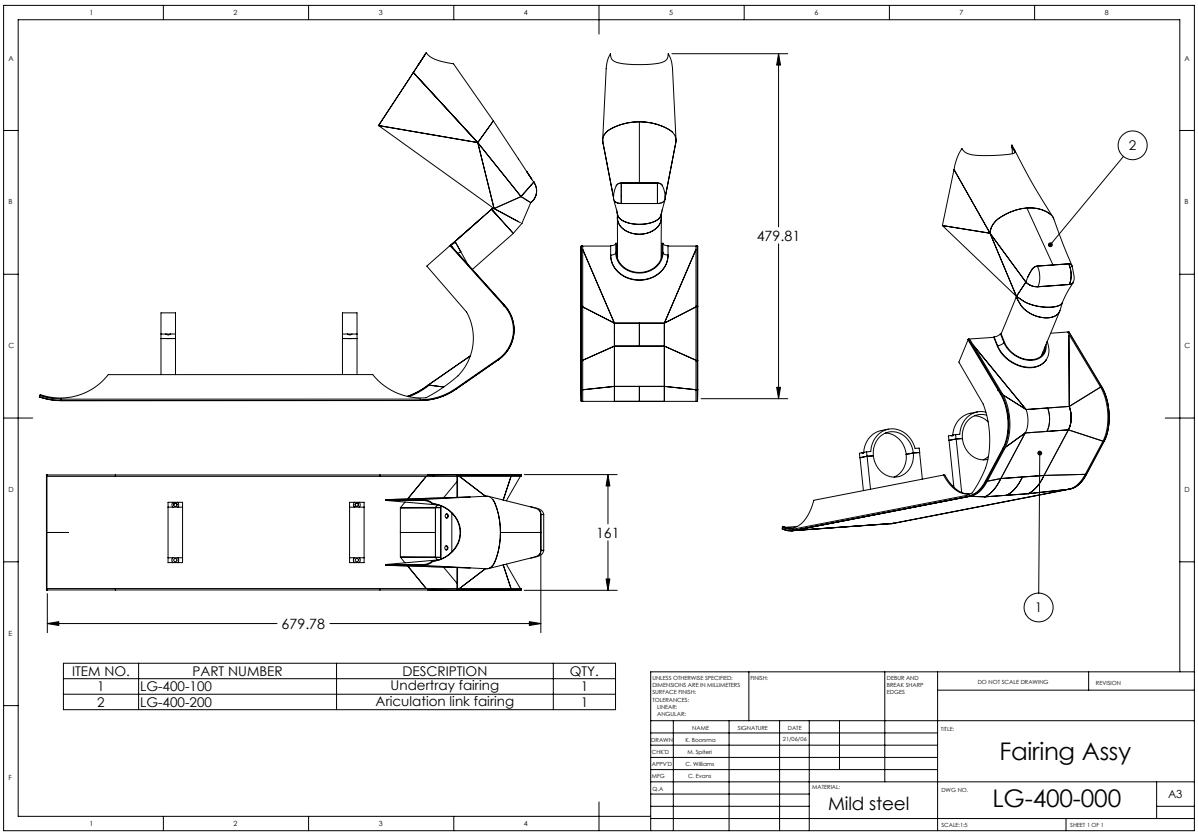

ITEM NO.	PART NUMBER	DESCRIPTION	QTY.
1	LG-400-100	Undertray fairing	1
2	LG-400-200	Ariculation link fairing	1

UNLESS OTHERWISE SPECIFIED: DIMENSIONS ARE IN MILLIMETERS SURFACE FINISH: TOLERANCES: LINEAR: ANGULAR: | FINISH: | DEBUR AND BREAK SHARP EDGES | DO NOT SCALE DRAWING | REVISION

	NAME	SIGNATURE	DATE
DRAWN	K. Boorsma		21/04/06
CHK'D	M. Spiteri		
APPV'D	C. Williams		
MFG	C. Evans		
Q.A			

MATERIAL: Mild steel | TITLE: Fairing Assy | DWG NO. LG-400-000 | A3 | SCALE:1:5 | SHEET 1 OF 1

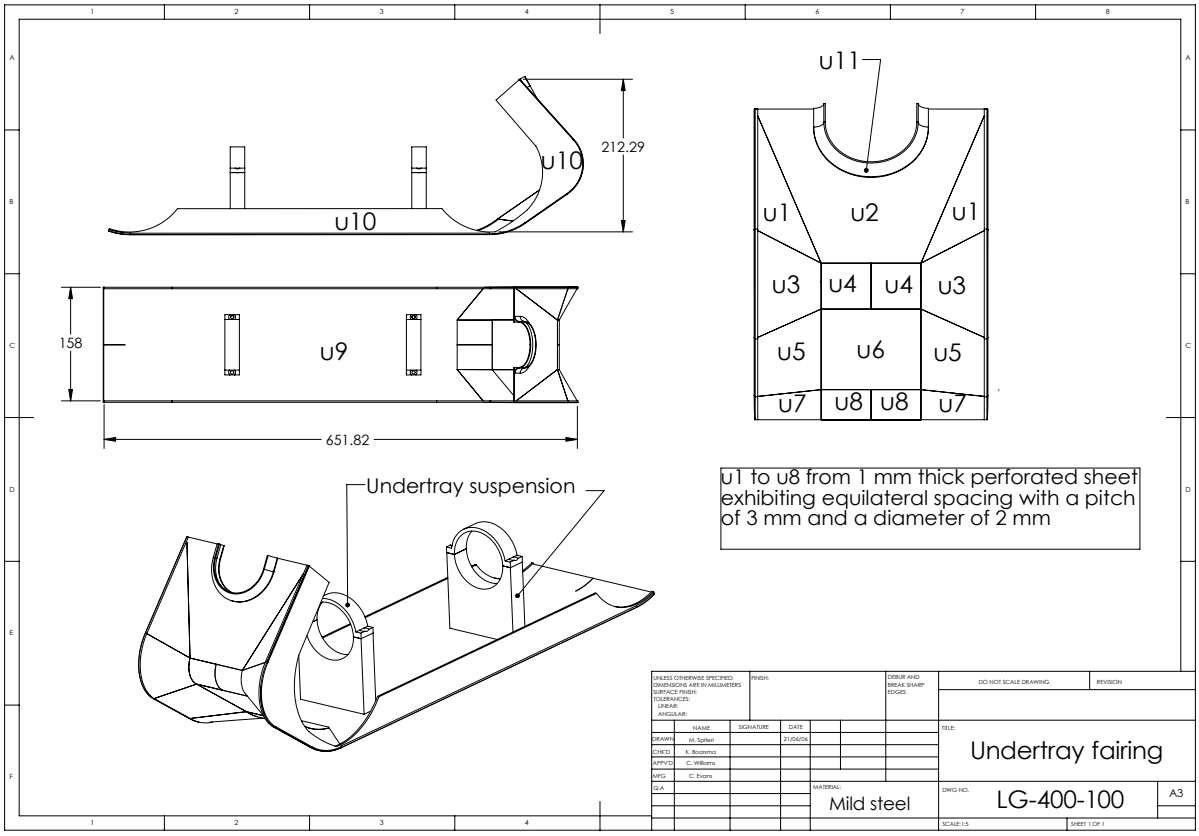
u11
212.29
u10
u10
u1
u2
u1
u3
u4
u4
u3
158
u9
u5
u6
u5
u7
u8
u8
u7
651.82
Undertray suspension
u1 to u8 from 1 mm thick perforated sheet exhibiting equilateral spacing with a pitch of 3 mm and a diameter of 2 mm
Undertray fairing
Mild steel
LG-400-100
A3

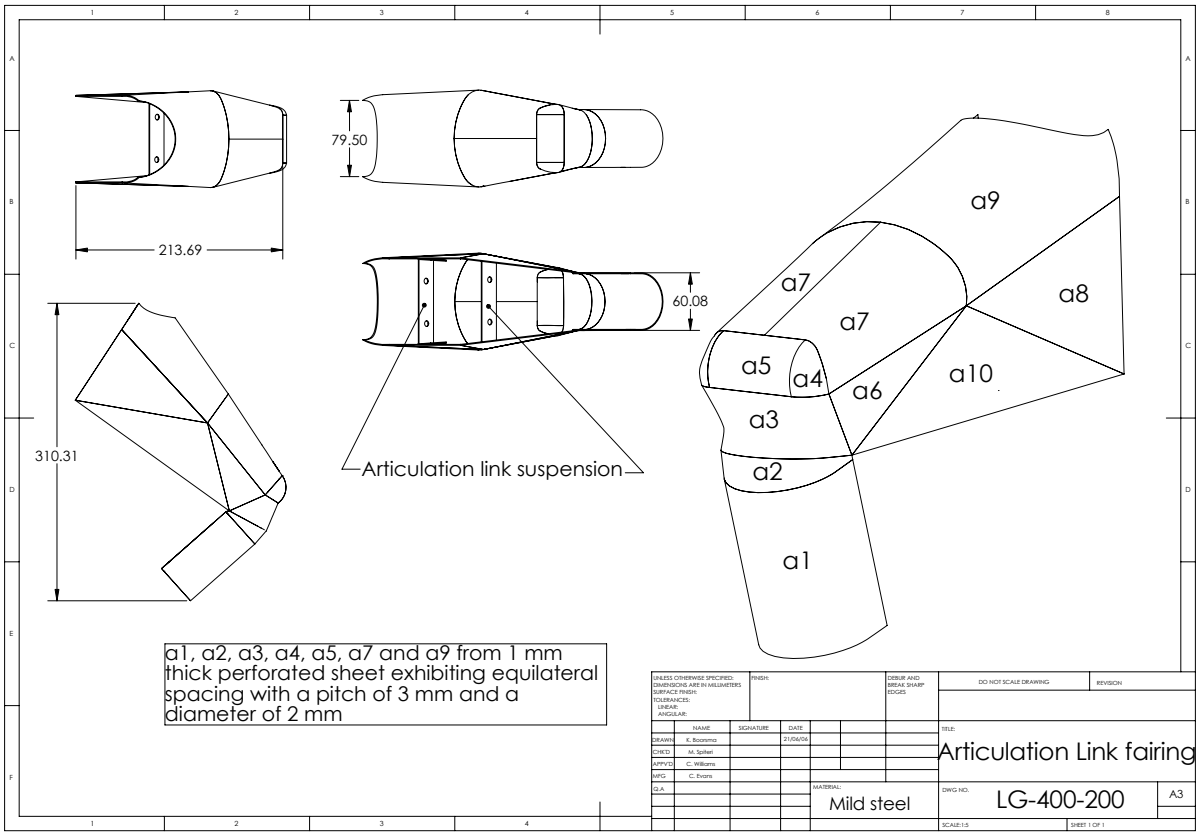
79.50
213.69
60.08
a9
a7
a8
a7
a5
a4
a6
a10
a3
310.31
Articulation link suspension
a2
a1
a1, a2, a3, a4, a5, a7 and a9 from 1 mm thick perforated sheet exhibiting equilateral spacing with a pitch of 3 mm and a diameter of 2 mm
Articulation Link fairing
Mild steel
LG-400-200
A3

References

[1] H.H. Heller and W.M. Dobrzynski. Sound radiation from aircraft wheel-well/landing gear configurations. *Journal of Aircraft*, 14(2):768–774, 1977.

[2] W.D. Baines and E.G. Peterson. An investigation of flow through screens. *Transactions of the ASME, Journal of Applied Mechanics*, 73:467–478, 1951.

[3] I.E. Idelchik. *Handbook of Hydraulic Resistance*. Second, revised and augmented edition, 1986.

[4] R. Liu, D.S. Ting, and G.W. Rankin. On the generation of turbulence with a perforated plate. *Experimental Thermal and Fluid Science*, 28:307–316, 2004.

[5] T.P. Chong, P. Joseph, and P. Davies. Design of a quiet open jet facility for the measurement of airfoil noise. AIAA Paper 2007–3437, 2007.

[6] Anon. *International Standards and Recommended Practices Environmental Protection; Annex 16 to the Convention of International Civil Aviation*, volume 1, Aircraft Noise. ICAO, Montreal, second edition, 1988.

[7] J.C. Ross. Progress in airframe noise reduction. In *Canadian Aeronautics and Space Institute Annual Conference*, 2001.

[8] W. Dobrzynski, L.C. Chow, P. Guion, and D. Shiells. A European study on landing gear airframe noise sources. AIAA Paper 2000–1971, 2000.

[9] W. Horne, K. James, and B.L. Storms. Flow survey of the wake of a commercial transport main landing gear. AIAA Paper 2002–2407, 2002.

[10] W. Dobrzynski and H. Buchholz. Full-scale noise testing on Airbus landing gears in the German Dutch wind tunnel. AIAA Paper 97–1597, 1997.

[11] L.V. Brentner Lopes, P.J. K.S., Morris, G.M. Lilley, and D.P. Lockard. Complex landing gear noise prediction using a simple toolkit. AIAA Paper 2005–1202, 2005.

[12] J.-F. Piet, L.C. Chow, F. Laporte, and H. Remy. Flight test investigation of high-lift devices and landing gear modifications to achieve airframe noise reduction. In *ECCOMAS 2004 conference*, Jyvaeskylae, Finland, July 2004.

[13] J.-F. Piet, R. Davy, G. Elias, H.A. Siller, L.C. Chow, C. Seror, and F. Laporte. Flight test investigation of add-on treatments to reduce aircraft airframe noise. AIAA Paper 2005–3007, 2005.

[14] M.G. Smith, B. Fenech, L.C. Chow, N. Molin, W. Dobrzynski, and C. Seror. Control of noise sources on aircraft landing gear bogies. AIAA Paper 2006–2626, 2006.

[15] Y. Li, M.G. Smith, X. Zhang, and N. Molin. Noise sources control of an aircraft landing gear. AIAA Paper 2007–3465, 2007.

[16] M.J. Lighthill. On sound generated aerodynamically i. general theory. *Proceedings of the Royal Society*, A(211):564–587, 1952.

[17] N. Curle. The influence of solid boundaries upon aerodynamic sound. *Proceedings of the Royal Society*, A(231):505–514, 1955.

[18] J.E. Ffowcs Williams and D.L. Hawkings. Sound generation by turbulence and surfaces in arbitrary motion. *Philosophical Transactions of the Royal Society of London*, 342:264–321, 1969.

[19] S.M. Jaeger and N.J. Burnside. Array assessment of an isolated, 26%-scale, high-fidelity landing gear. AIAA Paper 2002–2410, 2002.

[20] B.S. Lazos. Mean flow features around the inline wheels of a four-wheel landing gear. *AIAA Journal*, 40(2):193–198, 2002.

[21] T.J. Mueller. *Aeroacoustic Measurements*. Springer-Verlag, 2002.

[22] R.K. Amiet. Correction of open jet wind tunnel measurements for shear layer refraction. AIAA Paper 75–532, 1975.

[23] F.R. Grosche, G. Schneider, and H. Stiewitt. Windtunnel experiments on airframe noise sources of transport aircraft. AIAA Paper 97–1642, 1997.

[24] J. Piet and G. Elias. Airframe noise source localization using a microphone array. AIAA Paper 97–1643, 1997.

[25] S.M. Jaeger, W. Clifton Horne, and C.S. Allen. Effect of surface treatment on array microphone self-noise. AIAA Paper 2000–1937, 2000.

[26] G.J.J. Ruijgrok. *Elements of Aviation Acoustics*. Delft University Press, 1993.

[27] Y.P. Guo, K.J. Yamamoto, and R.W. Stoker. An empirical model for landing gear noise prediction. AIAA Paper 2004–2888, 2004.

[28] W. Dobrzynski, M. Pott-Pollenske, D. Foot, and M. Goodwin. Landing gears aerodynamic interaction noise. In *ECCOMAS 2004 conference*, Jyvaeskylae, Finland, July 2004.

[29] R.M. Fink. Airframe noise prediction method. Technical report 77-29, FAA-RD, 1979.

[30] L.C. Chow and M.C. Smith. Prediction method for aerodynamic noise from aircraft landing gear. AIAA Paper 98–2228, 1998.

[31] L.C. Chow and M.G. Smith. Validation of a prediction model for aerodynamic noise from aircraft landing gear. AIAA Paper 2002–2581, 2002.

[32] Y. Guo. A statistical model for landing gear noise prediction. AIAA Paper 2003–3227, 2003.

[33] F. Li, Khorrami M.R., and M.R. Malik. Unsteady simulation of a landing-gear flow field. AIAA Paper 2002–2411, 2002.

[34] L.S. Hedges, A.K. Travin, and P.R. Spalart. Detached-eddy simulations over a simplified landing gear. *Journal of Fluids Engineering*, 124:413–423, 2002.

[35] B.A. Singer and Y. Guo. Development of computational aeroacoustic tools for airframe noise calculations. *International Journal of Computational Fluid Dynamics*, 18(6):455–469, 2004.

[36] D.P. Lockard, M.R. Khorrami, and F. Li. High resolution calculation of a simplified landing gear. AIAA Paper 2004–2887, 2004.

[37] G.M. Lilley. The prediction of airframe noise and comparison with experiment. *Journal of Sound and Vibration*, 239(4):849–859, 2001.

[38] L.C. Chow, K. Mau, and H. Remy. Landing gears and high lift devices airframe noise research. AIAA Paper 2002–2408, 2002.

[39] R.W. Stoker, J.R. Underbrink, and G.R. Neubert. Investigations of airframe noise in pressurized wind tunnels. AIAA Paper 2001–2107, 2001.

[40] A. Iida, T. Otaguro, H. Nagarekawa, A. Torri, and I. Naruse. Similarity law of aerodynamic noise generation. AIAA Paper 2000–2012, 2000.

[41] W. Dobrzynski, L.C. Chow, P. Guion, and Shielss D. Research into landing gear airframe noise reduction. AIAA Paper 2002–2409, 2002.

[42] W. Dobrzynski, B. Schoning, L.C. Chow, C. Wood, M. Smith, and C. Seror. Design and testing of low noise landing gears. AIAA Paper 2005–3008, 2005.

[43] M.M. Zdrakovich. *Flow around Circular Cylinders*, volume 1:Fundamentals. Oxford Science Publications, 1997.

[44] M.M. Zdrakovich. *Flow around Circular Cylinders*, volume 2:Applications. Oxford Science Publications, 1997.

[45] S.F. Hoerner. *Fluid-Dynamic Drag*. published by the author, 1965.

[46] K. Shimizu and M. Kawamura. Spanwise correlation measurment behind a circular cylinder in subcritical Reynolds number region. *Journal of Physical Society of Japan*, 32:1454, 1972.

[47] B. Etkin, G.K. Korbacher, and R.T. Keefe. Acoustic radiation from a stationary cylinder in a fluid stream (aeolian tones). *The Journal of the Acoustical Society of America*, 29(1):30–36, 1957.

[48] F. Perot, X Gloerfelt, J. Auger, H. Giardi, and C. Bailly. Numerical prediction of the noise radiated by a cylinder. AIAA Paper 2003–3240, 2003.

[49] S. Szepessy and P.W. Bearman. Aspect ratio and end plate effects on vortex shedding from a circular cylinder. *Journal of Fluid Mechanics*, 234:191–217, 1995.

[50] J.D. Revell, R.A. Prydz, and A.P. Hays. Experimental investigation of aerodynamic noise versus drag relationship for circular cylinders. AIAA Paper 77–1292, 1977.

[51] C. Hahn, M. Kaltenbacher, R. Lerch, and S. Becker. Impact of geometry changes on noise radiated by a square cylinder in cross flow. AIAA Paper 2007–3430, 2007.

[52] D.P. Lockard, M.R. Khorrami, M.M. Choudhari, F.V. Hutcheson, T.F. Brooks, and D.J. Stead. Tandem cylinder noise predictions. AIAA Paper 2007–3450, 2007.

[53] W. Chen, F. Lee, and D. Chiang. On the acoustic absorption of porous materials with different surface shapes and perforated plates. *Journal of Sound and Vibration*, 237(2):337–355, 2000.

[54] S.S. Zabrodsky. *Hydrodynamics and Heat Transfer in Fluidized Beds*. The M.I.T. Press, american edition edition, 1966.

[55] I.F. Macdonald, M.S. El-Sayed, K. Mow, and F.A.L. Dullien. Flow through porous media-the Ergun equation revisited. *Ind. Eng. Chem. Fundamentals*, 18(3):199–208, 1979.

[56] P.G. Morgan. Fluid flow through screens of low solidity. *Journal of the Royal Aeronautical Society*, 66(613):54–56, 1962.

[57] M.D. Checkel. Measurements of turbulence generated by 60% solid perforated plates. In *The Winter Annual Meeting of ASME, Miami Beach, Florida*, 1985.

[58] I.P. Castro. Wake characteristics of two-dimensional perforated plates normal to an air-stream. *Journal of Fluid Mechanics*, 46(3):599–609, 1971.

[59] S. Akishita and I.D. Yahathugoda. Effect of surface impedance for reducing sound from circular cylinder. AIAA Paper 2005–2914, 2005.

[60] M. Ikeda and T. Takaishi. Perforated pantograph horn aeolian tone suppression mechanism. *Quarterly Report of Railway Technical Research Institute*, 45(3):169–174, 2004.

[61] P.A. Nelson. Noise generated by flow over perforated surfaces. *Journal of Sound and Vibration*, 83(1):11–26, 1982.

[62] J.E. Ffowcs Williams. The acoustics of turbulence near sound-absorbent liners. *Journal of Fluid Mechanics*, 51:737–749, 1972.

[63] C.Y. Tsui and G.A. Flandro. Self-induced sound generation by flow over perforated duct liners. *Journal of Sound and Vibration*, 50(3):315–331, 1977.

[64] G.B. Brown. The vortex motion causing edge tones. *Proceedings of the Physical Society*, 49(5):493–507, 1937.

[65] G.B. Brown. The mechanism of edge-tone production. *Proceedings of the Physical Society*, 49(5):508–521, 1937.

[66] G.F. McCanless Jr. and J.R. Boone. Noise reduction in transonic wind tunnels. *Journal of the Acoustical Society of America*, 56(5):1501–1510, 1974.

[67] M.O. Varner. Noise generation in transonic tunnels. *AIAA Journal*, 13(11):1417–1418, 1975.

[68] A.B.C. Anderson. A circular-orifice number describing dependency of primary pfeifenton frequency on differential pressure, gas density, and orifice geometry. *The Journal of the Acoustical Society of America*, 25(4):626–631, 1953.

[69] A.B.C. Anderson. A jet tone orifce number for orifices of small thickness-diameter ratio. *The Journal of the Acoustical Society of America*, 26(1):21–25, 1954.

[70] A.B.C. Anderson. Metastable jet-tone states of jets from sharp-edged, circular, pipe-like orifices. *The Journal of the Acoustical Society of America*, 27(1):13–21, 1955.

[71] A.B.C. Anderson. Structure and velocity of the periodic vortex-ring flow pattern of a primary pfeifenton (pipe tone) jet. *The Journal of the Acoustical Society of America*, 27(6):1048–1053, 1955.

[72] W.A. Olsen. Noise generated by impingement of turbulent flow on airfoils of varied chords, cylinders, and other flow obstructions. AIAA Paper 76–504, 1976.

[73] G.S. West and J. Apelt. The effects of tunnel blockage and aspect ratio on the mean flow past a circular cylinder with Reynolds numbers between 10^4 and 10^5. *Journal of Fluid Mechanics*, 114:361–377, 1982.

[74] Y.C. Fung. Fluctuating lift and drag acting on a cylinder in a flow at supercritical Reynolds numbers. *Journal of the Aerospace Sciences*, 27(11):801–814, 1960.

[75] C. Cant, N. Hankins, R. Mason, and E. Lait. Design, construction and commissioning of a multifunctional aerodynamic test facility. Meng group design project 2000, University of Southampton, School of Engineering Sciences, Ship Science Department, 2000.

[76] I.P. Castro. *Hot Wire Anemometry with the Newcastle, NSW bridges*. University of Southampton, School of Engineering Sciences, Aerodynamics and Flight Mechanics Research Group, November 2001.

[77] R. J. Pattenden. *An Investigation of the Flow Field around a Truncated Cylinder*. PhD dissertation, University of Southampton, Faculty of Engineering and Applied Science, School of Engineering Sciences, Fluid-Structure Interaction Research Group, April 2004.

[78] P.O.A.L. Davies. The new 7 by $5\frac{1}{2}$ ft. and 15 by 12 ft. low speed wind tunnel at the University of Southampton. Technical Report 202, A.A.S.U., 1961.

[79] Anonymous. *An information Booklet about the Test Laboratories (Lab Users Guide)*. ISVR consulting, University of Southampton.

[80] A.J. Smits and T.J. Lim. *Flow visualization: techniques and examples*. Imperial College Press, 2000.

[81] W. Merzkirch. *Flow Visualization*. Academic Press Inc.(London) Ltd, London, second edition, 1987.

[82] M. Raffel, C.E. Willert, and J. Kompenhans. *Particle Image Velocimetry, A Practical Guide*. Springer-Verlag, corrected 3rd printing edition, 2000.

[83] Dantec Dynamics A/S, Tonsbakken 18, DK-2740 Skovlunde, Denmark. *FlowManager Software and Introduction to PIV Instrumentation*, September 2002. Publication no. 9040U3625.

[84] R.J. Moffat. Describing the uncertainties in experimental results. *Experimental Thermal and Fluid Science*, 1:3–17, 1988.

[85] H.H. Bruun. *Hot-wire anemometry, principles and signal analysis*. Oxford University Press, 1995.

[86] B.A. Fenech and K. Takeda. Sotonarray: Southampton university wind tunnel microphone array system guide. Technical Report AFM 07/03, University of Southampton, School of Engineering Sciences, 2007.

[87] P. Sijtsma. CLEAN based on spatial source coherence. AIAA Paper 2007–3436, 2007.

[88] J.E. Ffowcs Williams and L.H. Hall. Aerodynamic sound generation by turbulent flow in the vicinity of a scattering half plane. *Journal of Fluid Mechanics*, 40(4):657–670, 1970.

[89] R.L. Simpson. Junction flows. *Annual Review of Fluid Mechanics*, 33:415–414, 2001.

[90] K. Boorsma, X. Zhang, and N. Molin. Perforated farings for bluff body noise control. AIAA Paper 2007–3462, 2007.

[91] K. Boorsma, X. Zhang, N. Molin, and L.C. Chow. Bluff body noise control using perforated fairings. *To be published in AIAA Journal*, -(-), 2008.

[92] K. Boorsma, X. Zhang, and N. Molin. Perforated farings for landing gear noise control. AIAA Paper 2008–2961, 2008.

[93] D.C. Wilcox. *Turbulence modeling for CFD*. D.C.W. Industries, 2nd edition edition, 1998.

[94] Fluent Inc., www.fluentusers.com. *Fluent 6.2 Documentation*, 2006.

[95] J.S. Cox, C.L. Rumsey, K.S. Brentner, and B.A. Younis. Computation of sound generated by viscous flow over a circular cylinder. Technical memorandum 110339, NASA, 1997.

[96] F.T.M. Nieuwstadt. *Turbulentie*. Epsilon Uitgaven, Utrecht, 1998.